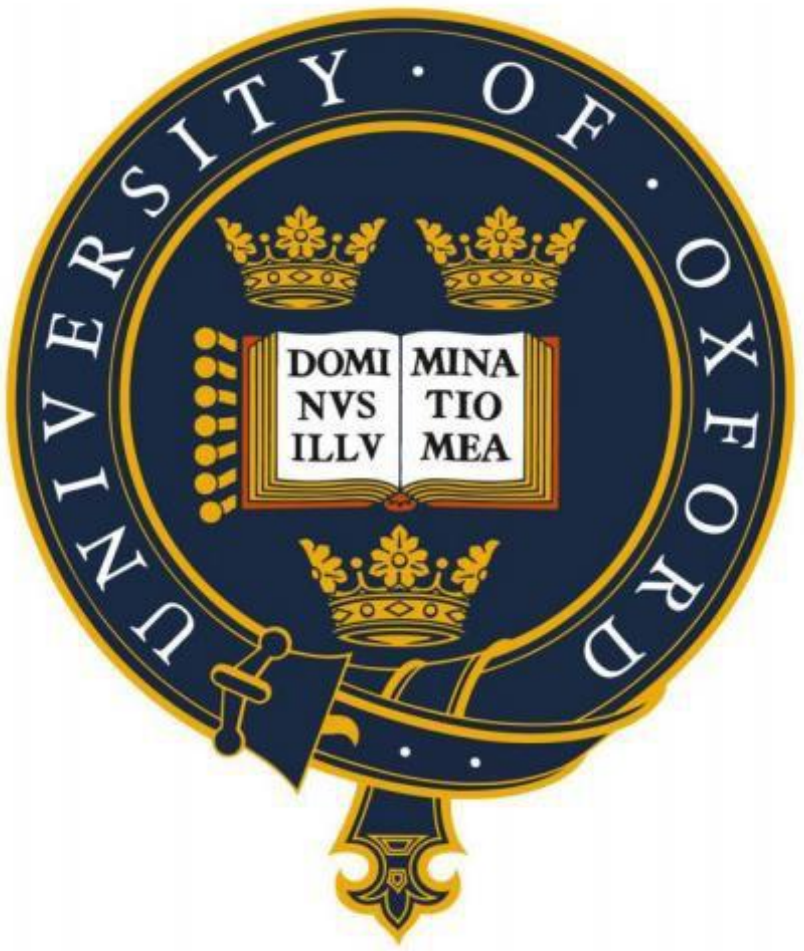
DEVELOPING AMMONIA AS A HYDROGEN SOURCE FOR GREEN ENERGY SUPPLY



Dongpei Ye

Wolfson College

Inorganic Chemistry Laboratary

A thesis submitted for the degree of Doctor of Philosophy

Trinity term 2025

Acknowledgements

First and foremost, I would like to express my deepest gratitude to my supervisor, Professor Edman Tsang, whose mentorship, wisdom, and encouragement were invaluable throughout my research. His passion for science and unwavering support shaped both the direction of this work and my development as a researcher. I am deeply saddened that he is no longer with us to see this thesis completed, but his influence remains a guiding force in my academic journey. It has been a privilege to have worked under his supervision.

I would also like to thank Dr. Yiyang Li and Professor John McGrady for their constructive comments and guidance, particularly during Edman's absence. Their support played a crucial role in helping me refine and complete this thesis. My sincere thanks go to my colleagues and friends in the Tsang group, especially, Leo Leung, Jiasi Li and Marvin Luo for the stimulating discussions, collaboration, and the enjoyable atmosphere we shared during our work on ammonia-related projects. I gratefully acknowledge the financial support from EPSRC, through the collaborative project with Oxford Green Innotech (OXGRIN), led by Dr. Simson Wu.

Throughout my DPhil studies, I have also benefited greatly from the support of my research collaborators. I would like to express my appreciation to Tai-Sing Wu (NSRRC, Taiwan) and Jingfeng Han (DICP, Dalian) for their unfailing support and technical assistance with XAS measurements. I also thank Dr. Baron Ho, Mrs. Mengqi Duan, and Mr. Xiaowei Liu (DICP, Dalian) for their help with TEM and SEM experiments. Special thanks to Mr. Marvin Luo for his contributions to the MACE and DFT calculations, and to Dr. Leo Leung and Dr. Xuelei Pan for their expertise in reactor design and experimental equipment set-up.

On a personal note, I am deeply thankful to my family and Luvian for their unwavering love, encouragement, and understanding throughout this journey. Their support has been a constant source of strength.

Lastly, I want to thank everyone who, in one way or another, contributed to the completion of this thesis.

Abstract

The catalytic decomposition of ammonia under mild conditions has emerged as a promising strategy for carbon-free hydrogen delivery. However, for traditional metal-supported catalysts that follow a dissociative mechanism, the trade-off between N–H bond cleavage and the desorption of strongly bound M≡N intermediates presents a significant kinetic challenge at low temperatures. According to Brønsted–Evans–Polanyi (BEP) scaling relations, strong nitrogen adsorption facilitates ammonia activation but simultaneously hinders nitrogen desorption due to unfavourable electron back-donation.

To overcome this limitation, inspiration has been drawn from the associative mechanism observed in enzyme-mediated nitrogen fixation. Where redox active nitrogen species, in particularly metal nitride has been considered as an active approach to circumvent the constraints via an alternative pathway and bypass the constraints of the dissociative route.

The first two chapters of this thesis aims to explore and develop nitrogen-containing catalysts that operate through such associative mechanisms, enabling efficient ammonia decomposition at lower temperatures.

The final chapter investigates the application of these catalysts in ammonia-coupled hydrogenation reactions, such as CO_2 methanation. This approach offers a pathway for direct hydrogen delivery via reactive intermediates, potentially eliminating the need for separate hydrogen storage and transportation.

Overall, this thesis highlights how catalyst design can result in a mechanistic shift in fundamental reaction mechanism, contributing to the broader goal of efficient, low-temperature hydrogen generation and utilization from ammonia.

List of Abbreviations

BET Brunauer-Emmett-Teller

BEP Brønsted-Evans-Polanyi

DFT Density Functional Calculations

EXAFS Extended X-ray Absorption Fine Structure

FTIR Fourier-Transform Infrared Spectroscopy

HAADF High-Angle Annular Dark Field

ICP Inductively Coupled Plasma

MACE Machine-learning Approach to Chemistry Emulation

MSI Metal Support Interaction

MvK Mars-van Krevelen

SEM Scanning Electron Microscopy

TEM Transmission Electron Microscopy

TPD Temperature-Programmed Desorption

TPR Temperature-Programmed Surface Reaction

WHSV Weight Hourly Space Velocity

XANES X-ray Absorption Near Edge Structure

XAS X-ray Absorption Spectroscopy

XPS X-ray photoelectron spectroscopy

XRD X-Ray Diffraction

List of Publications and Conferences

Publications:

1. Ye, D. & Tsang, S. C. E. Prospects and challenges of green ammonia synthesis. *Nat. Synth.* **2**, 612–623 (2023).
2. Leung, K. C. et al. Confined Ru Sites in a 13X Zeolite for Ultrahigh H_2 Production from NH_3 Decomposition. *J. Am. Chem. Soc.* **145**, 14548–14561 (2023).
3. Ye, D. et al. Active nitrogen sites on nitrogen doped carbon for highly efficient associative ammonia decomposition. *iScience* **27**, 110571 (2024).
4. Duan, M. et al. Synergistic Rh/La Codoping Enables Trap-Mediated Charge Separation in Layered Perovskite Photocatalysts. *J. Am. Chem. Soc.* **147**, 38599-38608 (2025).
5. Ye, D., Luo, M., Liu, X. et al. Unravelling the role of redox active sites in nitrogen doped cerium oxide for associative ammonia decomposition. *Nat. Commun.* **17**, 3892 (2026).
6. Li, J., Ye, D. & Leung, K. C. Construction of active centres and their contributions to mechanisms during thermocatalytic ammonia decomposition to generate hydrogen. *Appl. Catal. A Gen.* **724**, 121066 (2026).
7. Foo, C., et al. A Career in Catalysis: Shik Chi Edman Tsang. *ACS Catal.* **16**, 11678–11699 (2026).

Conference:

1. Ye, D. & Tsang, S. C. E. *Active Pyrrolic Nitrogen Sites with Low Activation Energy for Catalytic NH_3 decomposition.* Presented at 18th International Congress on Catalysis, Lyon, France (July 2024).
2. Ye, D. & Tsang, S. C. E. *Unravel The Role of Redox Active Site on Nitrogen Doped Cerium Oxide for Associative Ammonia Decomposition.* Presented at 12th World Congress of Chemical Engineering, Beijing, China (July 2025).

Declaration

All research works reported in this thesis have not previously been accepted in substance for any degree and is not being concurrently submitted in candidature for any degree. This thesis is conducted by the author unless stated otherwise. All materials from other sources have been properly and fully acknowledged.

Dongpei Ye

Table of content

Acknowledgement I

Abstract II

List of Abbreviation III

List of Publication and Conferences IV

Declaration V

Chapter 1 Introduction

1.1 General background of ammonia 1

1.2 Ammonia synthesis 3

1.2.1 Haber-Bosch process 3

1.2.2 Green ammonia synthesis 5

1.3 Ammonia as a green energy vector 7

1.3.1 Ammonia decomposition 10

1.4 Heterogenous catalyst design for ammonia decomposition 11

1.4.1 Sabatier principle: Ru - the most active metal catalyst for thermal decomposition and synthesis reactions of ammonia 14

1.4.2 Catalyst support 18

1.4.3 Reaction mechanism: associative 24

1.4.4 Ammonia coupling reaction 30

1.5 Aims and objectives 33

1.6 Thesis overview 34

Chapter 2 Characterisation Techniques and Experimental Methods

2.1 General characterisation techniques 40

2.1.1 X-ray diffraction (XRD) 40

2.1.2 Scanning electron microscopy (SEM) 41

2.1.3 Transmission Electron Microscopy (TEM) 42

2.1.4 X-ray adsorption spectroscopy (XAS) 44

2.1.5 X-ray photoelectron spectroscopy (XPS) 47

2.1.6 Brunauer-Emmett-Teller (BET) surface analysis 48

2.1.7 Temperature programmed reduction and desorption (TPR/TPD) 50

2.1.8 Fourier transform infrared spectroscopy (FTIR) 52
2.1.9 Mass spectrometry (MS) 55
2.2 Evaluation of catalytic performance 58
2.2.1 Ammonia decomposition reactor 58
2.2.2 Ammonia methanation reactor 59
2.2.3 Performance calculation and kinetic analysis 60
2.3 Catalyst synthesis 61
2.3.1 Synthesis of CNU_x 61
2.3.2 Synthesis of P-CNU_x 62
2.3.3 Synthesis of CeO_2 62
2.3.4 Synthesis of N-CeO_2 62
2.3.5 Metal impregnation 63

Chapter 3 Edge Site N on Nitrogen Doped Carbon for Efficient Ammonia Decomposition
3.1 Introduction 66
3.2 Results and discussion 72
3.2.1 Effect of nitrogen content 72
3.2.2 Effect of metal promotors 76
3.2.3 Effect of edge site nitrogen configuration control 78
3.2.4 Mechanistic understanding 86
3.3 Conclusion 97

Chapter 4 Enhanced Associative Ammonia Decomposition on Cerium Oxide via Inducing N Dopants
4.1 Introduction 101
4.2 Results and discussion 105
4.2.1 Support optimisation 105
4.2.2 Catalytic measurements 111
4.2.3 Metal support interaction 116
4.2.4 Mechanistic understanding 125
4.3 Computational modelling 132
4.3 Conclusion 136

Chapter 5 Direct Coupling of Ammonia and Carbon Dioxide for Methane Production

5.1 Introduction 143

5.2 Results and discussion 150

5.2.1 Catalyst screening 150

5.2.2 Reaction condition optimisation 154

5.2.3 Operando mechanism understanding 162

5.2.4 N doping evaluation 169

5.2.5 Techno-economic evaluation 173

5.3 Conclusion 176

Chapter 6 Conclusion

6.1 Summary of work 182

6.2 Future perspective 184

Chapter 1 Introduction

This chapter is adapted from the work by Dongpei Ye and Shik Chi Edman Tsang published in Nature Synthesis in 2023. Prospects and challenges of green ammonia synthesis. Nat. Synth ***2****, 612–623 (2023). The figures are reproduced with permission. Copyright 2023 Springer Nature Limited.*

1.1 General background of ammonia

Ammonia (NH_3) is the second highest chemical commodity produced among the world owning to its pivotal role in both the agriculture and the chemistry industry (**Fig. 1.1**).[1]

Nitrogen, phosphorus, and potassium are the three essential nutrients for plant growth, with nitrogen being the most consumed.[2] Unlike molecular nitrogen (N_2), which is abundant in the atmosphere but chemically inert, ammonia provides a more reactive and bioavailable form of nitrogen, facilitating its conversion into nitrogen-based fertilizers which can be further consumed by plants.[3] Thus, as a cornerstone of global food production, ammonia is primarily used in fertilizers to sustain crop yields and support the growth of global population. It has been estimated that ammonia-derived nitrogen fertilizers produce food that feeds 3.8 billion people or half of the global population, underscoring its vital role in food security and human development.[4]

Moreover, NH_3 also serves as an important precursor for various chemicals, including the production of polyimides, synthetic fibres, nitric acid, nylon, pharmaceuticals, explosive materials, refrigerants, dyes, cleaning solutions, and other industrial materials.[5] Its versatility and widespread applications make it a critical building block in the industrial manufacturing.

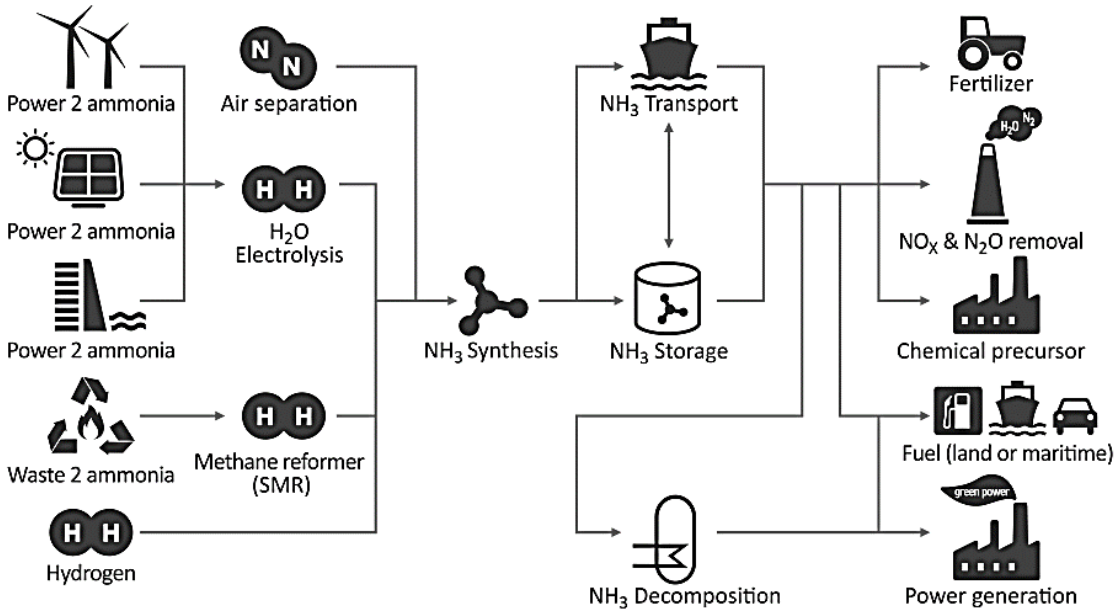


Fig. 1.1 Schematic illustration of the ammonia economy. Reprinted and adapted from reference[6].

It is only in recent years that increasing interest has been devoted to studying NH_3 as a hydrogen vector for carbon-free energy systems. Due to the intrinsic property of high hydrogen capacity (i.e., 17.8 wt.%) and ease of liquefication (i.e., 8 bars and room temperature), ammonia is considered as a perfect piece of the 'puzzle' that fits as a solution for hydrogen transportation and storage.[7–9] Besides, ammonia can be directly used as a fuel in combustion engines or converted to electricity via solid oxide fuel cells (SOFCs) further expanding its role in clean energy applications.[10,11]

Nevertheless, the widespread use of ammonia as a hydrogen carrier in day-to-day life would raise practical challenges due to its toxicity and pungent odor. Ammonia is corrosive and harmful to humans and ecosystems even at low concentrations. Its strong smell, detectable at very low levels, can serve as an early warning for leaks but also makes deployment in populated areas less appealing. Although ammonia has demonstrated technological feasibility as a hydrogen carrier in the transition toward a sustainable energy future, extra care is

required to ensure stringent handling, storage, and leakage prevention measures, along with robust safety protocols, before large-scale implementation can be realized.

1.2 Ammonia synthesis

In the nature world, NH_3 is synthesized by biological fixation, more specifically nitrogenase enzymes reduces nitrogen in air with hydrogen extracted from water to ammonium.[12] This pathway is environmentally friendly and cost-free, relying solely on biological processes. However, its low yield and slow reaction rate fall far short of the demands required to sustain the growing global population. Nowdays, around 180 million metric tonnes of ammonia are produced annually from the industrial sectors.[13] The energy consumption associated with it is estimated at approximately 2 % of the global energy utilisation.[14] As a result, the development of more sustainable and energy-efficient ammonia synthesis methods has become increasingly crucial.

1.2.1 Haber-Bosch process

The Haber-Bosch (HB) process describes the reaction that reduces dinitrogen into ammonia with the aid of hydrogen. Due to the strong nitrogen triple bond (dissociation energy 942 kJ mol^{-1}) and the exothermic reaction thermodynamics (see eq.1), extreme reaction conditions of 450-550 °C, 50-200 atm and an iron-based catalyst are required to yield a high ammonia production rate.[15,16]

$$N_2 + 3H_2 \leftrightarrow 2NH_3 \quad \Delta_f H_0 = -45.9\ kJ\ mol^{-1} \tag{1}$$

$$CH_4 + H_2O \leftrightarrow CO + 3H_2 \quad \Delta_f H_0 = 206\ kJ\ mol^{-1} \tag{2}$$

$$CO + H_2O \leftrightarrow CO_2 + H_2 \quad \Delta_f H_0 = -41.2\ kJ\ mol^{-1} \tag{3}$$

However, the process is far more complex than this single reaction suggests as illustrated in **Fig. 1.2**. Industrially, hydrogen is predominantly sourced from natural gas (CH_4) via steam methane reforming (SMR) (see eq.2), which produces a syngas mixture of H_2, CO, CO_2, and residual CH_4.[17] This is followed by separation and purification before further reacting to generate hydrogen via the water–gas shift reaction (WGSR) (see eq.3).[5]

This entire upstream hydrogen production chain is energy-intensive and carbon-emitting. With over 180 million tonnes of NH_3 produced annually, roughly 330–340 million tonnes of CO_2 per year are released as a by-product. This accounts for 2% of the world's total greenhouse gas emissions, which leads to severe climate change and environmental crisis like global warming.[9]

Given its environmental impact, the development of sustainable alternatives—such as electrochemical, photocatalytic, or plasma-assisted nitrogen fixation—is increasingly critical. These methods aim to operate under milder conditions, eliminate fossil fuel use, and ideally couple with renewable energy sources for hydrogen generation (e.g., water electrolysis using solar or wind power).

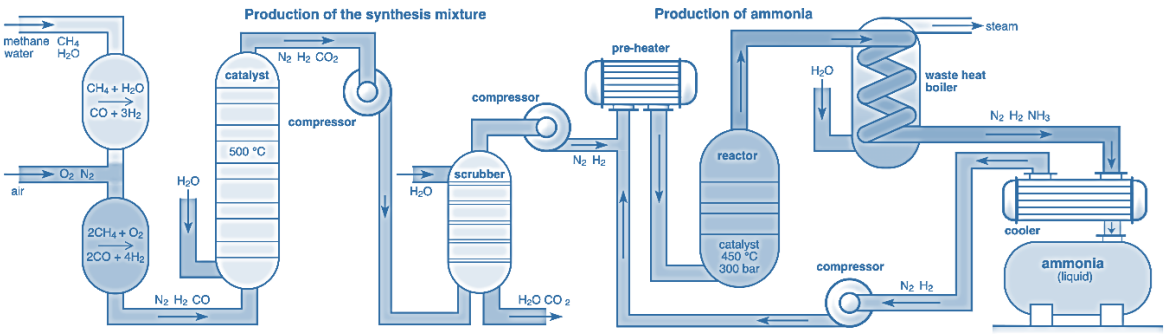


Fig. 1.2 Process flow diagram of the Haber-Bosch process for the production of ammonia. Reprinted from reference[18]

1.2.2 Green ammonia synthesis

Based on different hydrogen source and reaction conditions, the process of ammonia has been further classified in 5 different categories. The traditional HB process relies on natural gas and other fossil fuels as its mains source of hydrogen supply. Under this reactor unit, one tonne of ammonia can produce 1.9 tonnes of CO_2.[19] The ammonia produced via this route is classified as "brown" ammonia. It is not only energy intensive but also environmental unfriendly, and is therefore unsustainable (**Fig. 1.3a**).[20]

To mitigate its environmental impact, the conventional route can be modified by applying a carbon capture and storage (CCS) unit. This leads to a 'greener' approach of generating 'blue' ammonia (**Fig. 1.3b**). Based on today's CCS approach, a reduction of carbon dioxide emissions to ~0.5 kg per kg of ammonia can be achieved assuming that 90% of total green-house gas emission is captured.[19,21] However, the coupling of a CCS unit to the Haber-Bosch unit is accompanied by extra capital and energy costs.[17]

Looking toward future green ammonia synthesis, it is essential to eliminate unnecessary carbon emissions entirely. Rather than relying on fossil fuels or other carbon-containing precursors as the hydrogen source, water (H_2O) should be used to supply hydrogen for nitrogen reduction. Based on this concept, the green ammonia synthesis is further classified as either direct method or indirect method.

The direct method aims to generate ammonia from nitrogen and water, without the production of dihydrogen gas as an intermediate. Most current research and reviews focus on electrochemical or photochemical activation methods, where electrons excited by energy sources break the O–H bonds in water, generating highly activated hydrogen species that subsequently reduce N_2 to NH_3 (**Fig. 1.3e**).[22–26] However, the direct photo- or electroreduction of nitrogen for the production of ammonia, is still lacking in stability of rate production, economic feasibility and catalytic activity.[26]

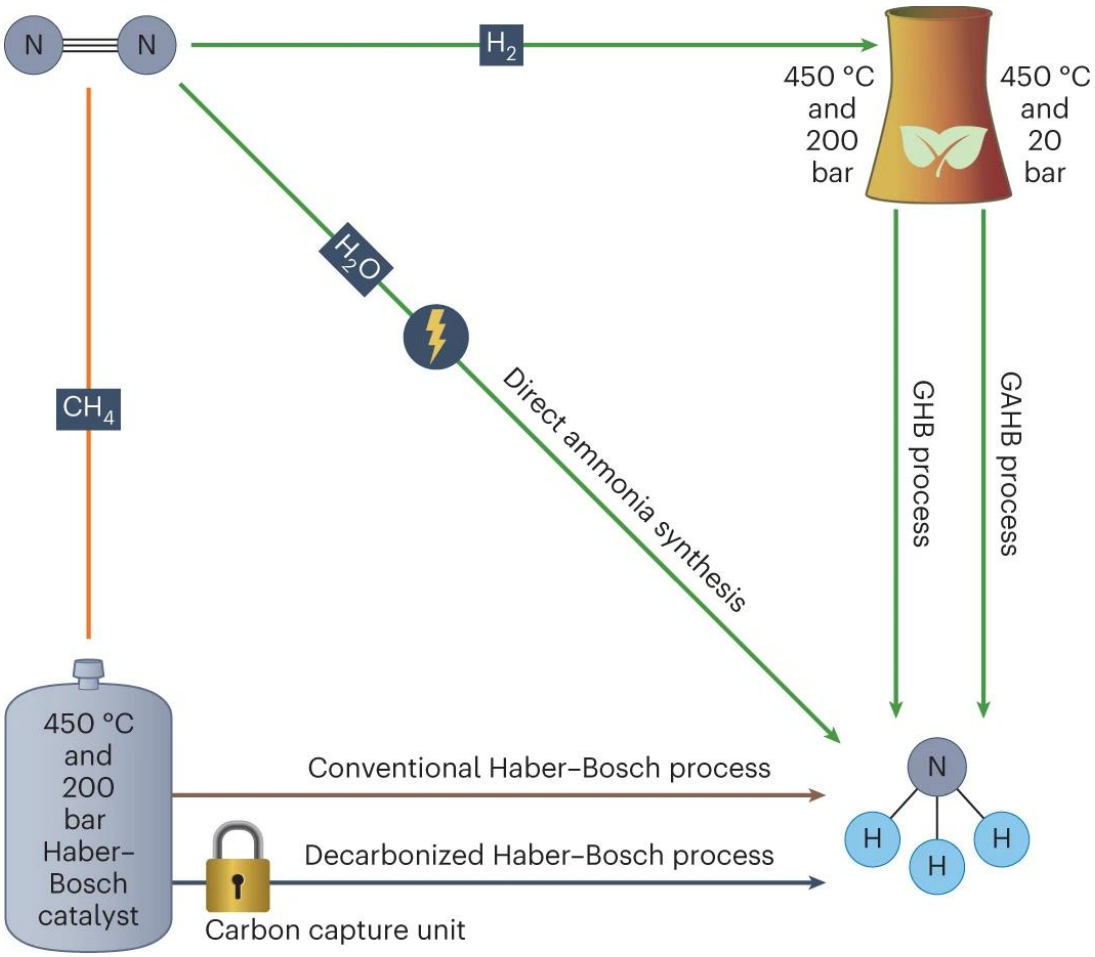


Fig. 1.3 Schematic illustration of different ammonia synthesis configurations. a Brown ammonia synthesis via conventional Haber-Bosch reaction using methane as H source; b Blue ammonia synthesis uses conventional Haber-Bosch process but with the aid of carbon capture unit for decarbonisation; c Green Haber-Bosch ammonia synthesis (GHB) where hydrogen comes from water electrolysis; d Green Agile Haber-Bosch ammonia synthesis (GAHB) where the reaction unit is operated at milder conditions with new catalyst and reactor design; e Direct green ammonia synthesis where water and nitrogen is directly reacted to produce ammonia via photo- or electro-catalysis. Reprinted from ref[5].

A more achievable route for large scale green ammonia synthesis in the near future would be the indirect method. This approach uses renewable energy sources like wind or solar to power electrolytic hydrogen unit associated with the HB plants. H_2 is generated from water splitting before combining with N_2 either in an unmodified Haber-Bosch reactor (green Haber-Bosch,

GHB, **Fig. 1.3c**) or in a green agile Haber-Bosch reactor, (GAHB, **Fig. 1.3d**). The GHB route uses conventional HB infrastructure, whereas the GAHB process operates under milder conditions with advanced catalysts and optimized reactor designs tailored for sustainable ammonia synthesis. Thanks to rapid advancements in renewable energy and water electrolysis technologies, both GHB and GAHB offer promising pathways to replace fossil-derived hydrogen with green hydrogen for nitrogen reduction. These systems can supply sufficient green hydrogen to replace fossil-derived hydrogen from methane, contributing significantly toward achieving net-zero carbon emissions by 2050.[21]

1.3 Ammonia as a green energy vector

Global rise in population has led to increasing needs to energy consumption. However, under current energy system, over 85% of primary energy consumed comes from unsustainable feed stock such as fossil fuels, coal, natural gasses etc.[11,27] These energy sources emit green-house gases and trigger severe environmental crises. The urgent need to transition away from carbon-intensive energy systems has driven global interest in alternative, sustainable, and low-emission energy carriers. Hydrogen has emerged as one of the most promising candidates for clean energy. It has the potential to decarbonize a wide range of applications owing to its high energy content (120 MJ kg^{-1} of hydrogen) and zero carbon emissions when used as a fuel. However, despite its advantages, hydrogen technology still faces considerable practical barriers, especially under mobile or decentralized conditions. Challenges such as the low volumetric energy density of hydrogen gas, its tendency to diffuse and escape from storage vessels, the need for high-pressure or cryogenic conditions, and the lack of widespread infrastructure for safe and efficient distribution have limited its widespread adoption in real-world applications, particularly for transportation and portable energy systems.[1]

To overcome these limitations, various chemicals have been studied as hydrogen carriers to fit in the hydrogen economy for future energy supply. Including organic molecules like

methanol and formic acid, metal hydrides such as lithium hydride (LiH) and potassium hydride (KH), and nitrogen-based compounds like ammonia and its derivatives.[28] Among these, ammonia (NH_3) has gained substantial attention due to its exceptional storage and transport properties.

As can be seen from **Fig. 1.4**, ammonia stands out as a promising candidate owing to its high gravimetric (17.8 wt. %) and volumetric (121 kg H_2 m^{-3}) hydrogen capacity at 10 bars.[29] Furthermore, ammonia can be readily liquefied at a relatively low pressure of 8 bar at room temperature, significantly reducing the energy and cost associated with storage and transportation compared to compressed or liquefied hydrogen. The global infrastructure for ammonia handling is already mature, as the chemical is widely used in agriculture and industry, with established protocols for storage, transportation, and leak detection. Its distinct pungent odour, detectable at concentrations as low as 5 ppm, provides an added safety mechanism, as leaks can be easily identified well before reaching its toxicity threshold of 50 ppm.[30] Moreover, ammonia is not highly flammable on its own (can only become flammable at concentration above 15% with air). Therefore, it does not pose the same explosive risks as hydrogen, making it a safer alternative for large-scale and long-distance distribution.

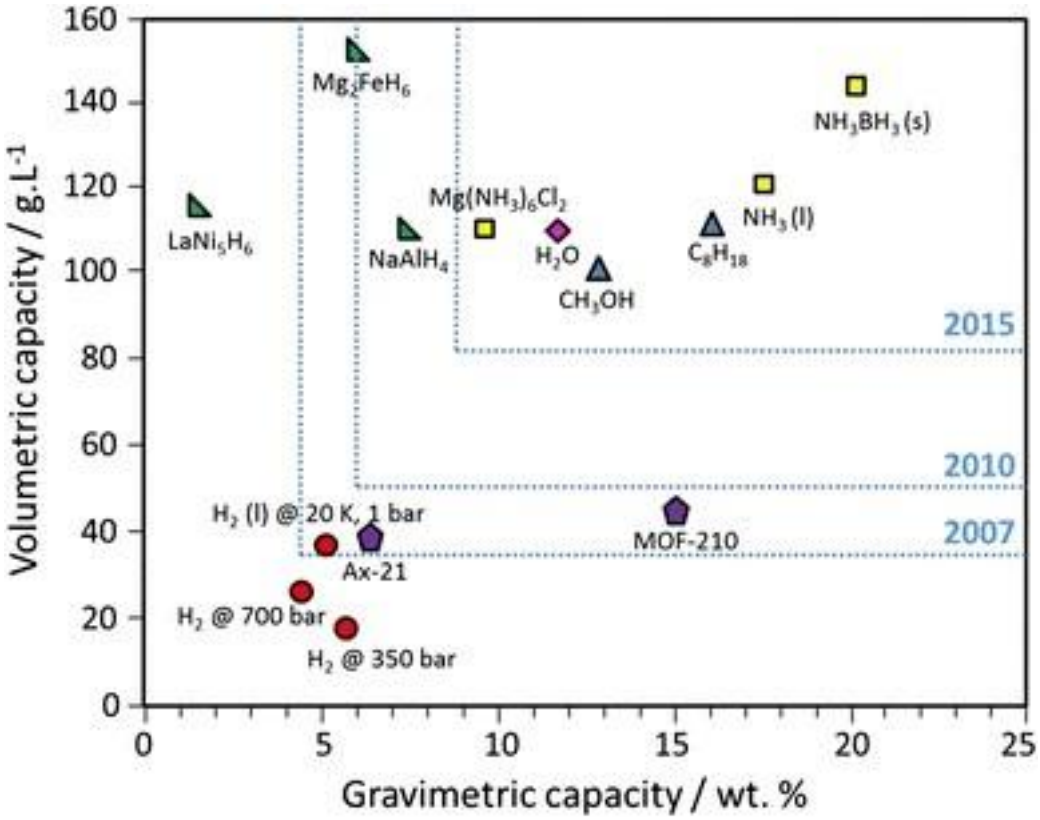


Fig. 1.4 Volumetric hydrogen capacity versus gravimetric hydrogen density for various hydrogen storage compounds. Reprinted from reference[28].

The green production of ammonia has given rise to new opportunities in utilisation of the chemical as a next-generation clean energy vector. Beyond its role as a hydrogen carrier, ammonia can be used directly as a fuel. It can be combusted in specially adapted gas turbines or engines, or it can be fed directly into solid oxide fuel cells (SOFCs) to generate electricity with low carbon emissions.[31,32]

These attributes make ammonia especially attractive as a viable alternative fuel for long-distance transportation and other heavy-duty applications. Like the maritime shipping sectors and off-grid power systems, where the process is energy-dense and hard to decarbonise, which makes easily transportable fuels more critical.[33–35] As the imminent need to cut down greenhouse gas emission intensifies, ammonia stands out as a viable and scalable solution in the global shift toward net-zero energy systems.

1.3.1 Ammonia decomposition

On the roadmap a using ammonia as a hydrogen carrier to power up energy plants, one essential task would be studying the process of catalytic decomposition of ammonia. This process is essential for releasing hydrogen stored in ammonia in a form that can be used for electricity generation. Similar to ammonia synthesis, ammonia decomposition is a multi-step elementary process where the ammonia molecule consecutively breaks its N-H bond followed by subsequent recombination of atomic nitrogen and atomic hydrogen to form N_2 and H_2.

$$2NH_3 \leftrightarrow N_2 + 3H_2 \quad \Delta_f H_0 = +45.9\ kJ\ mol^{-1} \tag{4}$$

In the context of establishing a completely carbon-free energy framework, ammonia decomposition must be effectively coupled with fuel cells such as proton exchange membrane fuel cells (PEMFCs) or SOFCs. This integration enables clean electricity generation without emitting greenhouse gases. Hydrogen for PEMFCs typically requires high purity >99.97% as impurities can damage the catalyst and reduce the fuel cell's efficiency and lifespans. Therefore, complete ammonia conversion is particularly crucial when ammonia is used to feed PEMFCs, even trace levels of unconverted ammonia (in the ppm range) can irreversibly degrade the proton-conducting membrane and poison the metal catalyst in the set-up.[36,37] Therefore, obtaining high purity hydrogen stream with low NH_3 residue is essential for completing an ammonia-fuelled energy system.

Ammonia decomposition is an endothermic reaction, meaning it requires continuous energy input to shift the equilibrium to hydrogen production (see eq.4). Despite being thermodynamically favourable at high temperatures, the ammonia decomposition reaction proceeds slowly in the absence of a catalyst.[38] Moreover, because the reaction is equilibrium-limited, it is not feasible to achieve 100% conversion under standard conditions. As a result, catalysts play a vital role in accelerating the reaction rate and improving hydrogen yield. This

makes the design of highly active and selective catalysts the critical bottleneck in enabling the efficient utilization of ammonia as a green hydrogen carrier.

Therefore, the overarching objective of this thesis is to rationally design and optimize catalytic systems and reaction mechanism pathways that enable high conversion rates and the production of high-purity hydrogen under relatively mild conditions for ammonia decomposition. Such advancements will play a pivotal role in establishing ammonia as a practical and sustainable energy vector for a carbon-neutral future.

1.4 Heterogenous catalyst design for ammonia decomposition

Catalysis is the process by which the rate of a chemical reaction is increased through the presence of a catalyst—a substance that provides an alternative reaction pathway with a lower activation energy, without being consumed in the overall reaction (see **Fig. 1.5**).[39] Among various types of catalysts, heterogeneous catalysts play a pivotal role in industrial chemistry. Given that over 90% of all chemical and fuel production processes involve heterogeneous catalysis, and an estimated 30% of the global gross product depends on catalytic technologies, the economic and societal impact of heterogeneous catalysis is profound.[40] In heterogeneous catalysis, the catalyst exists in a different phase than the reactants, typically as a solid interacting with gaseous or liquid reactants. This makes it particularly well-suited for reactions such as ammonia synthesis and ammonia decomposition, where the reactants are in the gas phase while the catalyst remains in the solid state.

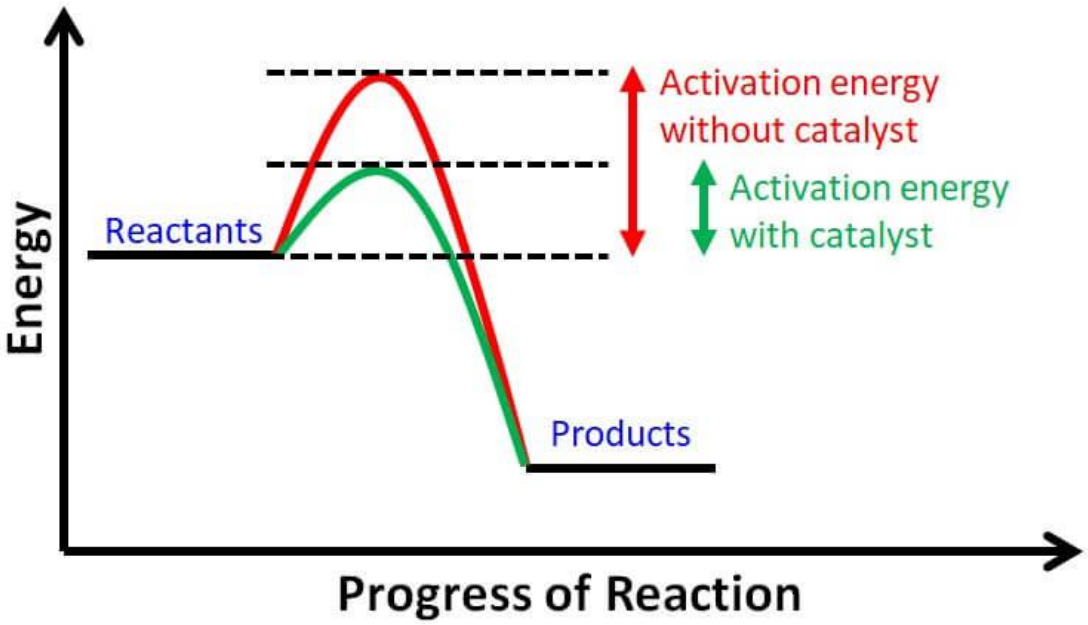


Fig. 1.5 illustration of the energy profile with and without a catalyst

The catalytic performance of a catalyst is influenced by a range of external and internal factors, including temperature, flow rates, pressure, and reactor design. These parameters impact both macroscopic mass transport (within the reactor) and microscopic transport (at the catalyst surface), as well as the adsorption strength of reactants, desorption of products, and the rate of surface reactions. Even slight variations in these conditions can significantly alter the catalytic behaviour by enhancing or weakening chemical bond interactions at the active sites.

To accurately assess catalytic activity, several key performance indicators are commonly used: ***1.*** Rate of reaction/conversion, quantifies the amount of reactant converted to product per unit time, it is commonly normalised to mass of catalyst, surface area of the catalyst or the mass of active metal dispersed on the catalyst support. Conversion which directly quantifies the fraction of reactants that has been reacted. ***2.*** Selectivity, a measure of the fraction of the converted reactant that forms the desired product. It is not less relevant for ammonia decomposition as it is an elementary reaction with N_2 and H_2 being the only products. However, this metric is crucial in complex reactions like CO_2 conversion, where multi-carbon products

are formed.[41] ***3.*** Weight hour space velocity (WHSV), measures the flow rate of the reactant per unit weight of catalyst. Especially useful in ammonia decomposition and synthesis as it helps to normalize across different reactor sizes and configurations. An extremely important factor used to evaluate catalytic efficiency under continuous flow conditions. ***4.*** Turnover frequency (TOF), which depicts the number of reactant molecule being turned to the product per active site per second. It is often further normalised to metal loading and dispersion for a fairer comparison between catalysts. ***5.*** Apparent activation energy (E_a), calculates the activation barrier of a reaction under experimental condition. It is obtained using the Arrhenius equation by plotting the Ln (r) verses 1/T, where r is the rate of reaction and T is the temperature at which the experiment is conducted (see eq.5 and 6). Accurate determination of E_a requires conducting experiments in the kinetic regime, minimizing the influence of external and internal mass transfer limitations on the measured rate.

$$\boldsymbol{k = A \times e^{-\frac{E_a}{RT}}} \quad \textbf{(5)}$$

$$\boldsymbol{Ln(k) = -\frac{E_a}{R} \times \left(\frac{1}{T}\right) + Ln(A)} \quad \textbf{(6)}$$

For a typical ammonia decomposition reaction, the mechanism over the catalyst proceeds through a series of elementary surface reactions, as illustrated in **Fig. 1.6**. The process begins with the adsorption of ammonia onto the catalyst surface. In this initial step, the nitrogen end of the ammonia molecule interacts with the active metal sites, forming an activated adsorbed NH_3 species. The activated ammonia would then stepwise dehydrogenate and dissociate the N-H bonds until it is left with a bare nitrogen atom adsorbed on the surface as described in ***R4*** **(Fig. 1.6)**. Simultaneously, the hydrogen atoms generated during dehydrogenation migrate on the surface and recombine to form dinitrogen molecules, which subsequently desorbs from the catalyst releasing H_2 gas. On the nitrogen side, two surface nitrogen atoms would associate to form molecular dinitrogen, which also desorbs from the surface, completing the catalytic cycle.[42–44]

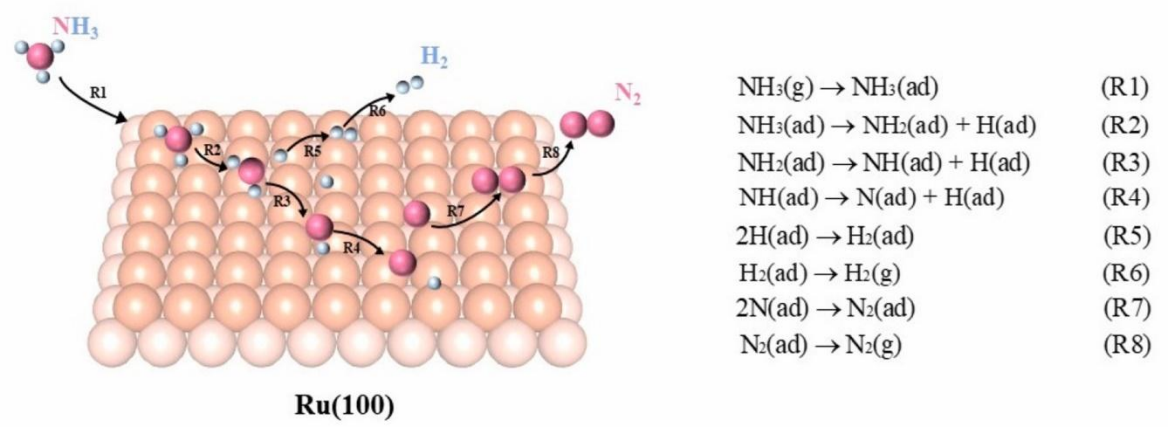


Fig. 1.6 illustration of ammonia decomposition on Ru (100) plane. Reprinted from reference[45].

Similar to ammonia synthesis technology, the catalytic technologies for ammonia decomposition mainly include thermal, photothermal, electrocatalytic, photoelectron-catalytic and microwave catalytic technologies. Among them, thermal catalysis is one of the many technologies widely studied because of its strong stability and industrialization basis. Thus, the aim of this thesis and introduction would only focus on the catalyst and reaction design of thermal ammonia decomposition.

1.4.1 Sabatier principle: Ru - the most active metal catalyst for thermal decomposition and synthesis reactions of ammonia

As previously discussed, decomposition of ammonia proceeds through a series of surface-mediated steps, involving the adsorption and desorption of nitrogen-containing intermediates. This makes the understanding and exploration on the key surface intermediates such as *N, *NH, and *NH_2 critical to unravelling the reaction mechanism and optimizing catalytic performance. From a thermodynamic point of view, highly active catalysts tend to bind *NH_x intermediates (where x = 0–2) less strongly to the surface. This weaker adsorption facilitates faster desorption of products and increases turnover. However, this benefit comes with a fundamental limitation governed by the Brønsted–Evans–Polanyi (BEP) relationship, which

imposes a linear scaling correlation between adsorption energies and activation barriers. Specifically, on stepped transition metal surfaces, the adsorption energy of the *N species correlates strongly with the activation energy for N–H bond cleavage, preventing the independent optimization of these two critical parameters.[46]

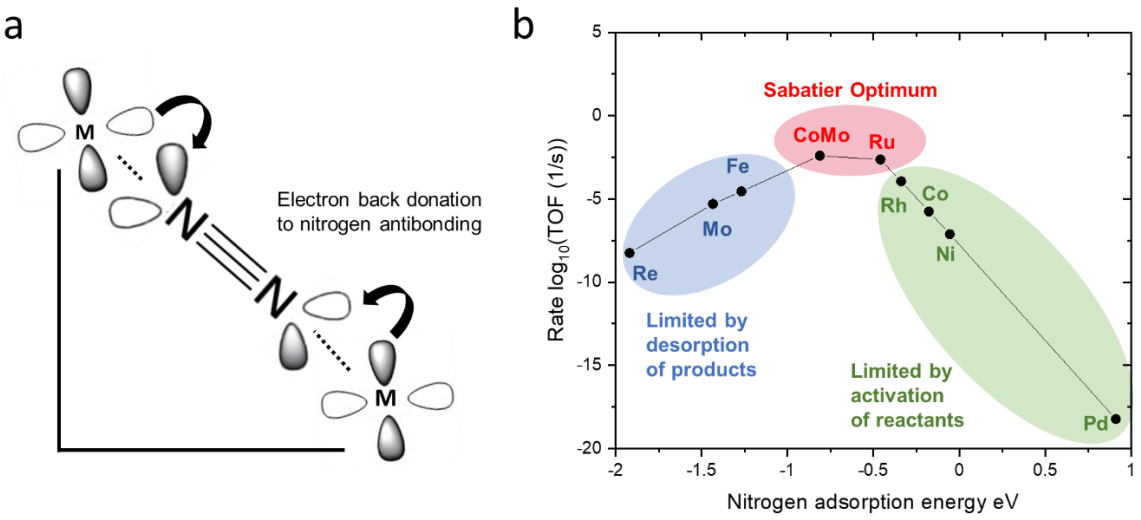


Fig. 1.7 a. Molecular bonding illustration of the origin of the Brønsted−Evans−Polanyi (BEP) constraints. b Volcano plot showing the turnover frequency against the nitrogen adsorption energy in which Ru was at the peak position.

As illustrated in **Fig. 1.7a**, the molecular orbital (MO) interactions that underpin the BEP scaling can be visualized through a bonding model involving two stepped metal atoms (M) and a bridging N_2 molecule forming a linear M–N=N–M configuration. Enhanced N adsorption energy by σ-interactions will simultaneously result in a weakened N≡N bond. Which is due to the back donation from M to the π* antibonding orbitals of N in this geometry. In contrast, lower π bonding and σ bonding interaction will weaken the adsorption energy of N but facilitate formation of the N≡N bond. This interplay reflects the fundamental challenge imposed by the BEP scaling: catalysts that bind nitrogen well enough to activate ammonia may also hold onto formation of dinitrogen intermediates too strongly, thereby inhibiting product desorption and active site regeneration.

For monometallic systems, achieving this balance under the constraints of BEP scaling is challenging. Thus, the optimal catalytic performance must be found where adsorption strength and dissociation barriers are appropriately balanced. This leads to the Sabatier principle, which postulates that an ideal catalyst should neither bind intermediates too weakly (resulting in insufficient activation) nor too strongly (leading to catalyst poisoning).[47,48]

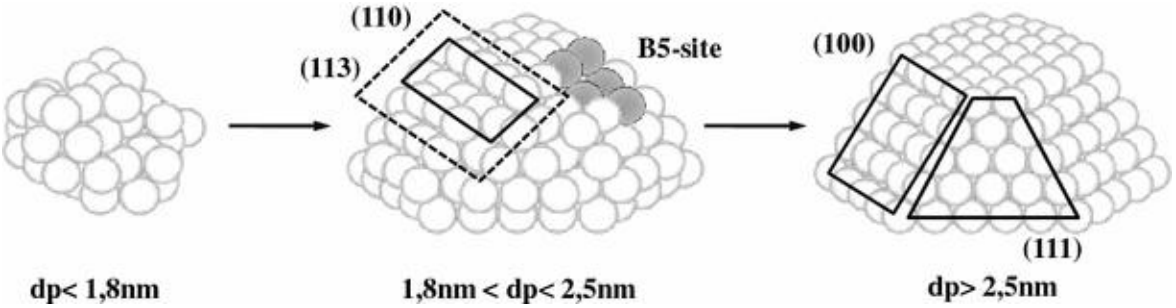


Fig. 1.8 Illustration of the dependency of size of Ru nanoparticles and the concentration of Ru-B5 site. Reprinted from reference[51].

These scaling relationships contribute to the characteristic volcano-type behaviour seen in the **Fig. 1.7b**, with nitrogen binding energy serving as a key descriptor.[49,50] As illustrated, the activity peaks for metals that strike a balance between too weak and too strong binding. Among transition metals, ruthenium (Ru) lies near the apex of the volcano plot, outperforming other candidates and thus being widely recognized as the state-of-the-art catalyst for ammonia decomposition.[28] From another point of view, Ru has an electron configuration of $[Kr]4d^7 5s^1$, with seven d-electrons in its outer shell. These active outer electrons possess relatively low ionization energy due to the strong shielding effect, which facilitates electron transfer during catalytic reactions. As a results, explains why Ru illustrates the highest activity for ammonia catalysis.

In depth research revealed that apart from the volcano plot described above, the exceptional performance of Ru in ammonia decomposition can be attributed to the presence of highly specific surface structures—namely, B5-type active sites located on single-atomic steps of the

Ru (0001) surface (see **Fig. 1.8**). The active site consists of three Ru atoms on the first layer and two Ru atoms above, forming a well-defined geometric allowing optimum interaction between the incoming reactant and metal surface.[51] However, it also means that only a limited fraction of the surface sites contribute to the overall reactivity. Indicating that the concentration of B5 sites has a direct impact on the ammonia decomposition activity. Studies by Garcia *et al*. suggest that the size of Ru nanoparticle (NPs) should be optimally controlled at 1.8 -2.5 nm for the highest concentration of B5 sites exposed (see **Fig. 1.8**).[51] Further investigations by Ayman *et al.* extended these findings by highlighting the influence of particle shape on site availability. It suggested that With hemispheric ruthenium particles, the highest TOF occurred in the size range of 1.8–3.0 nm, whereas with elongated nanoparticles, it occurred at ~7.0 nm.[52] These insights underscore the importance of precise morphological control in catalyst synthesis, as both particle size and shape critically dictate the density of catalytically active B5 sites, and thereby the overall performance of Ru-based catalysts in ammonia decomposition.

To advance the understanding of ammonia decomposition mechanisms and guide the rational design of future catalysts, it is crucial to identify the rate-determining step (RDS) of the reaction. RDS is typically referred to the step with the highest activation energy, and it is therefore slowest, determining the overall rate of reaction. Interestingly, the RDS of the decomposition reaction was found to be uncertain as it is sensitive to the metal catalysts. For non-noble metals including Fe, Co, and Ni, nitrogen recombination was the rate-limiting step, while the cleavage of N−H bond was the primary kinetic bottleneck for noble metals such as Pd, Rh, Pt, and Ir.[53] In the case of Ruthenium, the rate determining step is still debatable. Kulkarni *et al* reported a change in the rate determining step from N-H dissociation to N recombination after doping K onto the Ru/CaO catalyst, highlighting the sensitivity of mechanistic pathways to catalyst composition and surface modifiers.[54]

The overall process of hydrogen delivery from ammonia decomposition is endothermic with an enthalpy change of 46 kJ mol^{-1}.[55] This means that substantial external heat input is required

to drive the reaction forward. Which makes thermal ammonia decomposition a less feasible approach for hydrogen transportation and storage at this stage, especially under low-temperature or energy-limited conditions. Thus, development of more effective and yet economically sustainable catalysts is a goal with high priority.

1.4.2 Catalyst support

While monometallic catalysts can show high activity for catalytic ammonia decomposition, they often come with several limitations that reduce their effectiveness in real-world applications. This includes physical properties like low surface area and limited active site exposure and chemical properties like deactivation after over exposure to hydrogen and nitrogen leading to catalyst poisoning in ammonia decomposition.[50,56,57] Furthermore, noble metal such as Ru are scarce and expensive, which significantly reduce the economical tendency for industrial commercialisation.

Thus, over the past century, significant research has been dedicated on finding appropriate catalyst supports to promote catalytic activity of metals. The promotion effects offered by catalyst supports arise not only from their physical attributes—such as high specific surface area, thermal stability, and suitable electronic conductivity—but also from their chemical characteristics, including redox properties, surface basicity, metal-support interactions, and electron-donating capacity.[58–62] As being recently reviewed by van Deelen *et al*, the metal support phenomena is classified as charge transfer, interfacial perimeter, nanoparticle morphology, chemical composition and strong metal support interaction. This further result in approaches for tuning the interactions as illustrated in **Fig. 1.9**.[63,64] As shown, the treatments are divided at the three different stages of catalyst modification, that is, via solely the support or the nanoparticle or via treatments on the metal-support composite material.

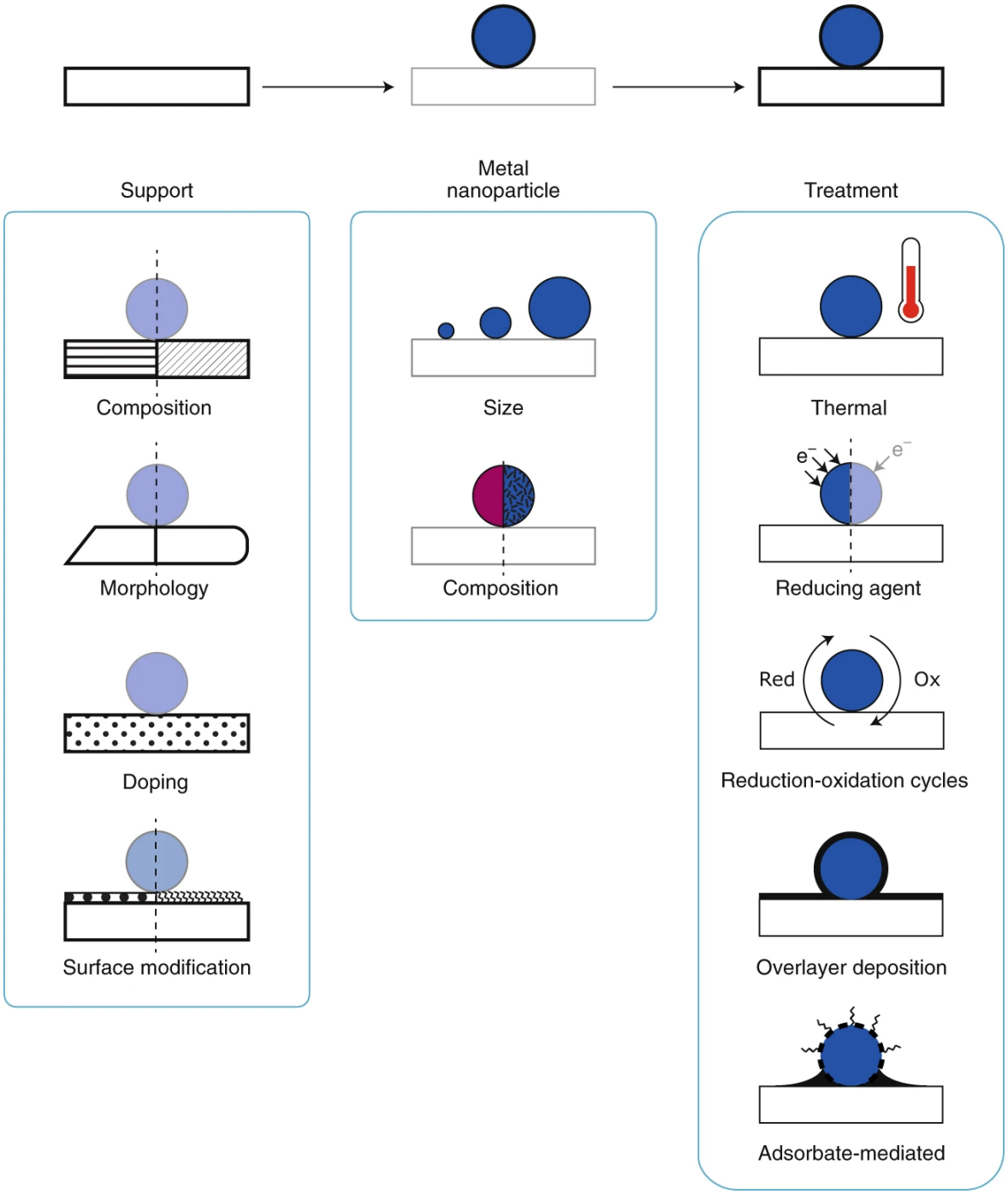


Fig. 1.9 Schematic illustration of the tuning strategies to achieve different metal support promotion effect at the three different stages. Reprinted from reference[63].

Catalyst modification is inherently a multifactorial and interdependent process. Altering one property often leads to unintended changes in others. For example, increased surface area of graphite support, which is commonly achieved through introduction of mesopores, would

result in better NPs distribution and reduced NPs size.[65] Leading to more exposed active sites and higher catalytic activity. On the other hand, excess porosity will reduce the crystallinity and disrupt the continuous π-electron system on graphitic materials. This would diminish electron transfer capabilities and lower catalytic activity.[66] These synergetic effects underscore the importance of rational catalyst design, where control over morphology, particle size, and support chemistry must be carefully balanced to optimize performance.

More specifically, Podila *et al* successfully synthesize a high surface area Co/MoN_2 catalyst which showed exceptional activity among other bimetallic systems.[67] It is proposed that the large surface area of the MoN_2 support favours the formation of well distributed NPs of Co, which greatly intensifies the metal support interaction and lead to the formation of a distinct Co_3Mo_3N phase. Similarly, Duan *et al*. investigated two Ru-based catalysts with comparable metal loadings on carbon nanotubes (CNTs) and carbon nanofibers (CNFs).[68] The Ru/CNFs catalyst exhibited a significantly higher turnover frequency for hydrogen production (TOF_H_2) of 0.16 s^{-1} at 450 °C—nearly an order of magnitude greater than that of Ru/CNT. This improvement was attributed to the intrinsic morphology of CNFs, where abundant edge sites could anchor Ru particles more stably and uniformly. Further studies concluded that the electron-donating ability of carbon-based supports plays a crucial role in ammonia decomposition, motivating research into the impact of functional groups with electron-donating properties.[69] This concept has been experimentally validated in various nitrogen-doped carbon supports (N-CNTs, N-CNFs, N-graphene etc.). It is widely acknowledged that substitution of carbon atoms by nitrogen increases the basicity of the support, thereby enhancing electron density at the metal interface. This promotes hydrogen desorption and improves overall catalytic activity.[55,70–72] Despite these insights, the fundamental nature of the metal–support interaction remains unclear—particularly the role of different nitrogen environments (e.g., graphitic, pyrrolic, and pyridinic nitrogen) during ammonia cracking (see **Fig. 1.10**). These open questions lead directly to the focus of Chapter 3: ***Edge Site N on Nitrogen Doped Carbon for Efficient Ammonia Decomposition***.

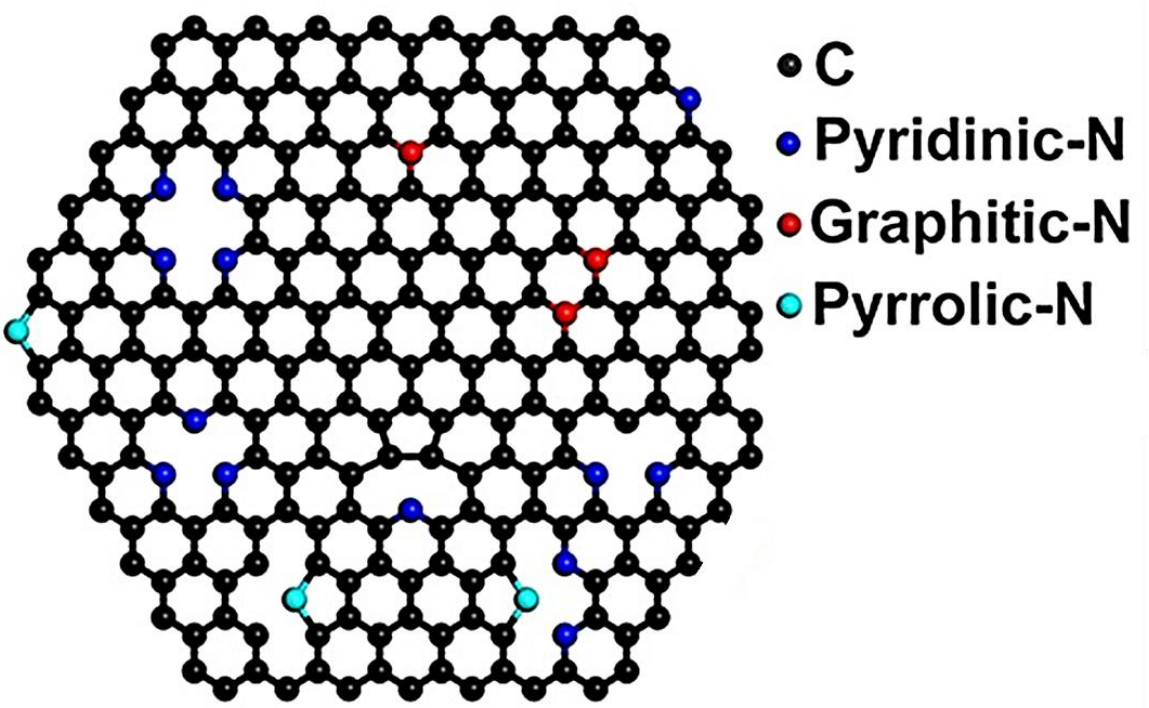


Fig. 1.10 illustration of the 3 main different nitrogen environments (graphitic, pyrrolic and pyridinic) on nitrogen doped carbon.

Apart from the discussion above, where the promotion effect from the support is mainly attributed to the dispersion of the metal NPs and the size control. Certain metal oxide support can induce non-physical effect to promote catalysis. For example, supports with redox-active surfaces like CeO_2 or TiO_2 can participate in electron exchange with metal particles, influencing their oxidation state and reactivity. Liu *et al.* proposed an inverse CeO_2/Ni catalyst with superior high hydrogen production rate of 79.6 mmol g_{cat}^{-1} min^{-1} at 500 °C.[73] The inverse structure significantly enhanced the metal–support interaction at the Ni-CeO_2 interface, which facilitate the generation of highly concentrated oxygen vacancies and abundant electron-rich Ni atoms under reduction conditions (see **Fig. 1.11a**). The generation of oxygen vacancies favours higher adsorption of gaseous NH_3 molecules, while the electron donation ability of the cerium support to the metal Ni facilitates stronger N-H dissociation ability. The dual effect led to the high activity of such catalyst reported.

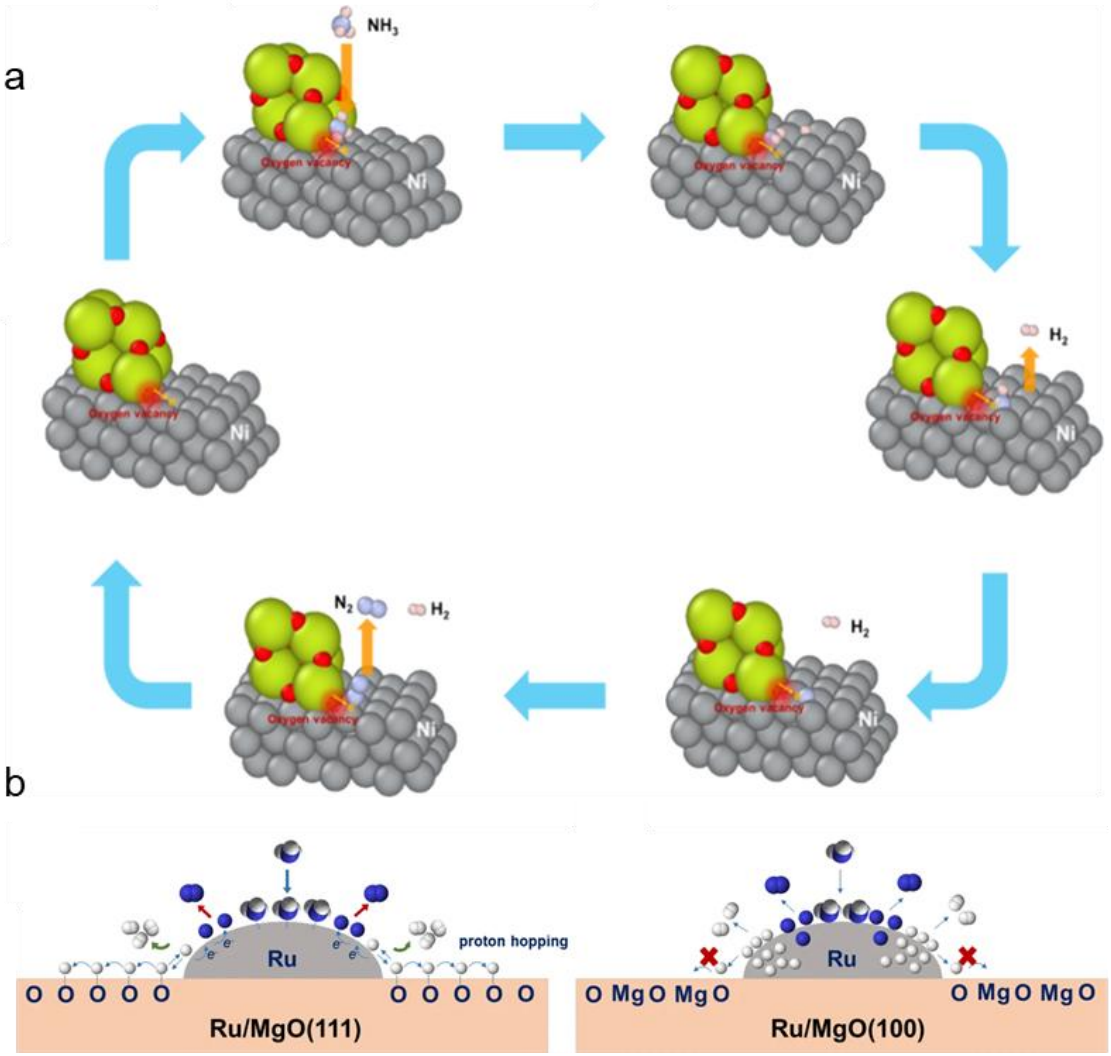


Fig. 1.11 Illustration of the ammonia decomposition reaction mechanism over various support a. CeO_2/Ni inverse catalyst b. Ru/MgO (111). Reprinted from reference[73,74].

Moreover, basic supports such as MgO or CaO can facilitate ammonia activation by stabilizing $*NH_x$ intermediates through acid-base interactions. It is recently found by our group that Ru embedded on polar MgO (111) facets shows an outstanding ammonia decomposition conversion of ca 99% (450 °C; WHSV=30,000) which is the best performance achieved by a single thermally catalytic technology in the field of ammonia decomposition at present.[74] The high activity was attributed to the distinct MgO (111) polar plane. The interface between Ru(II) with the support surface O^{2-} helps to break the dissociate N-H bond heterolytically. Furthermore, facile H^+ can 'hop' across the oxygen sites on the support surface, leaving proton

vacancy sites at the metal-support interface to remove extra H from Ru. This alleviates hydrogen poisoning on the metal phase therefore facilitating ammonia decomposition under low pressure conditions (see **Fig 1.11b**).[75,76]

To pursue catalysts with higher catalytic activity for NH_3 decomposition, many new carriers were utilized to support metal NPs. Hosono *et al* utilised an electride-cage structure to transfer electron density from the cage conduction band to the 4d orbital of Ru, thereby facilitating electron transfer into the antibonding orbital of Ru-N and promoting ammonia desorption.[44] Leung *et al* confined single atomic Ru within the 13X zeolite structure using ion exchange. This approach was found to amplify catalytic ammonia decomposition via a 'FLP' mechanism.[77] Where the N-H bond of ammonia is ruptured heterolytically by the frustrated Lewis pair of $Ru^{\delta+}$–$O^{\delta-}$ in the zeolite. Xiong *et al* reported a Tammann temperature guided strategy to synthesize core shell structured $Co@BaAl_2O_4$ which fully decomposes ammonia at 500 °C without Ru.[78] This exceptional activity was dedicated to the unconventional strong metal-support interaction.

In the case of ammonia decomposition, supports play a particularly important role in modulating metal-support interactions, tuning the electronic structure of the metal particles, and even contributing to the stabilization of specific active geometries—such as the Ru B5 sites—required for optimal catalytic performance. Therefore, the rational selection and engineering of support materials remains a critical strategy in the design of high-performance catalysts for hydrogen generation from ammonia.

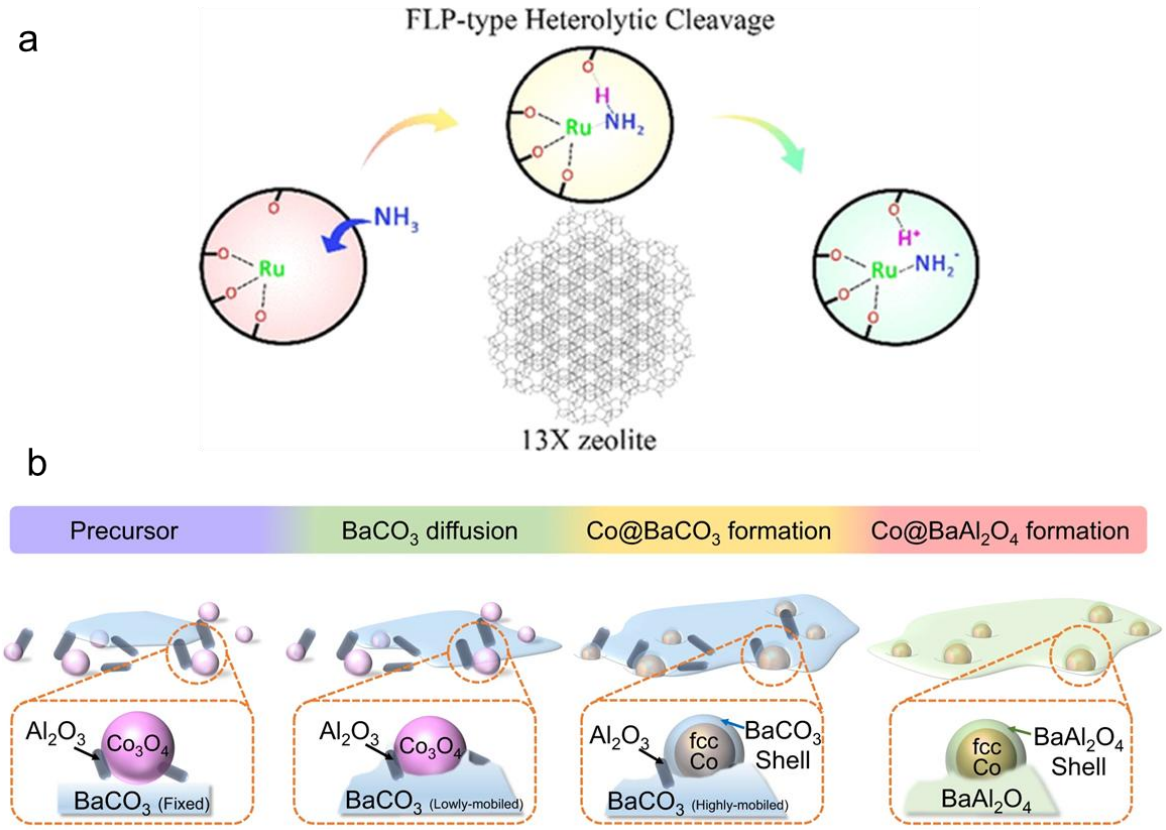


Fig. 1.12 Illustration of novel research in the field related to NH_3 cracking. a. A FLP type mechanism for NH_3 decomposition over Ru confined 13X zeolite. Reprinted from reference[77] b. Mechanism for the thermal-induced encapsulation strategy guided by Tammann temperature. Reprinted from reference[78].

1.4.3 Reaction mechanism: associative

The majority of the abovementioned metal-based catalysts follow a dissociative mechanism, where the strong N adsorption to metal subject to the BEP constraint is prevalent, making further tuning of metal catalysts for higher ammonia cracking nearly impossible (see **Fig. 1.13**). Thus, searching for new catalysts with different reaction mechanism(s) which are less affected by the thermodynamic BEP restrictions is required.

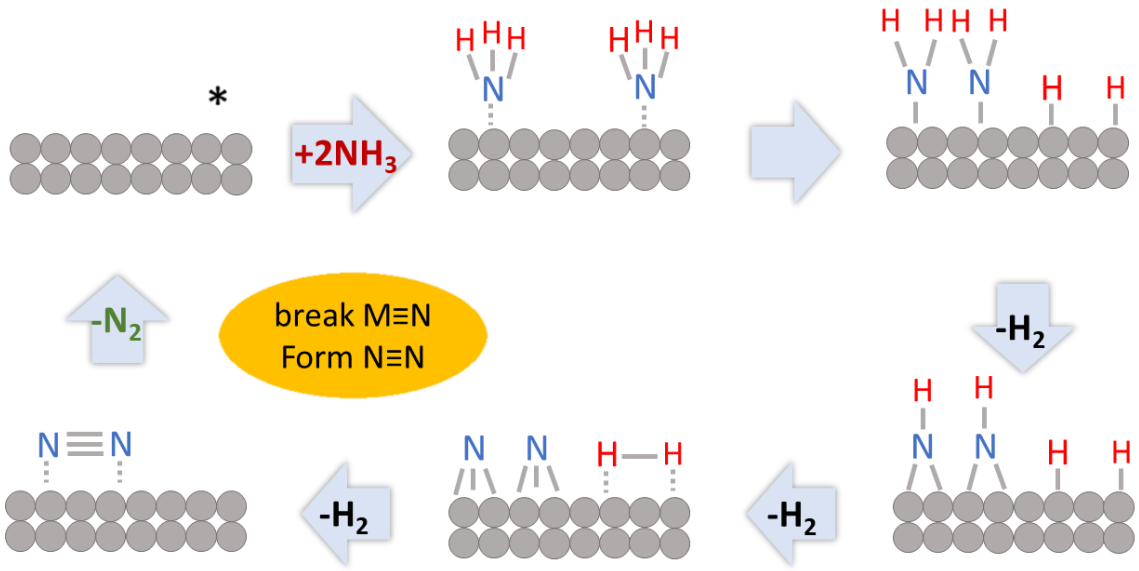


Fig. 1.13 Schematic illustration of the dissociative pathway of ammonia decomposition.

Inspired by biological enzymes for nitrogen fixation at mild conditions, an alternative Mars–van Krevelen (MvK) kinetic model is considered in the field of ammonia synthesis, where N_2 cleavage is not the rate limiting step.[15] This model describes ammonia synthesis as an associative mechanism, where gaseous nitrogen first binds to atomic nitrogen vacancies or receptive sites through a single end-on configuration without activation of N-N from both ends (no strong synergetic effect to activate the π bonds) (see **Fig. 1.14**).[8] The chemisorbed dinitrogen is then hydrogenated rapidly forming a M-N-N-H_2 intermediate. For traditional HB ammonia synthesis using Fe catalyst which follows the dissociated pathway, high temperatures and pressures are required to provide sufficient energy for direct nitrogen triple bond breakage and enhancement of the mobility of surface *N species from metal site (breaking N≡M). However, the associative mechanism does not involve the generation of mono-nitrogen surface intermediate species, instead, hydrogenation takes place on the adsorbed di-nitrogen molecule without the prior cleavage of N≡N or *N from the metal site. As a result, milder operating temperatures and pressures can be used due to the lower reaction barrier, allowing the development of novel catalysts for milder condition ammonia synthesis.

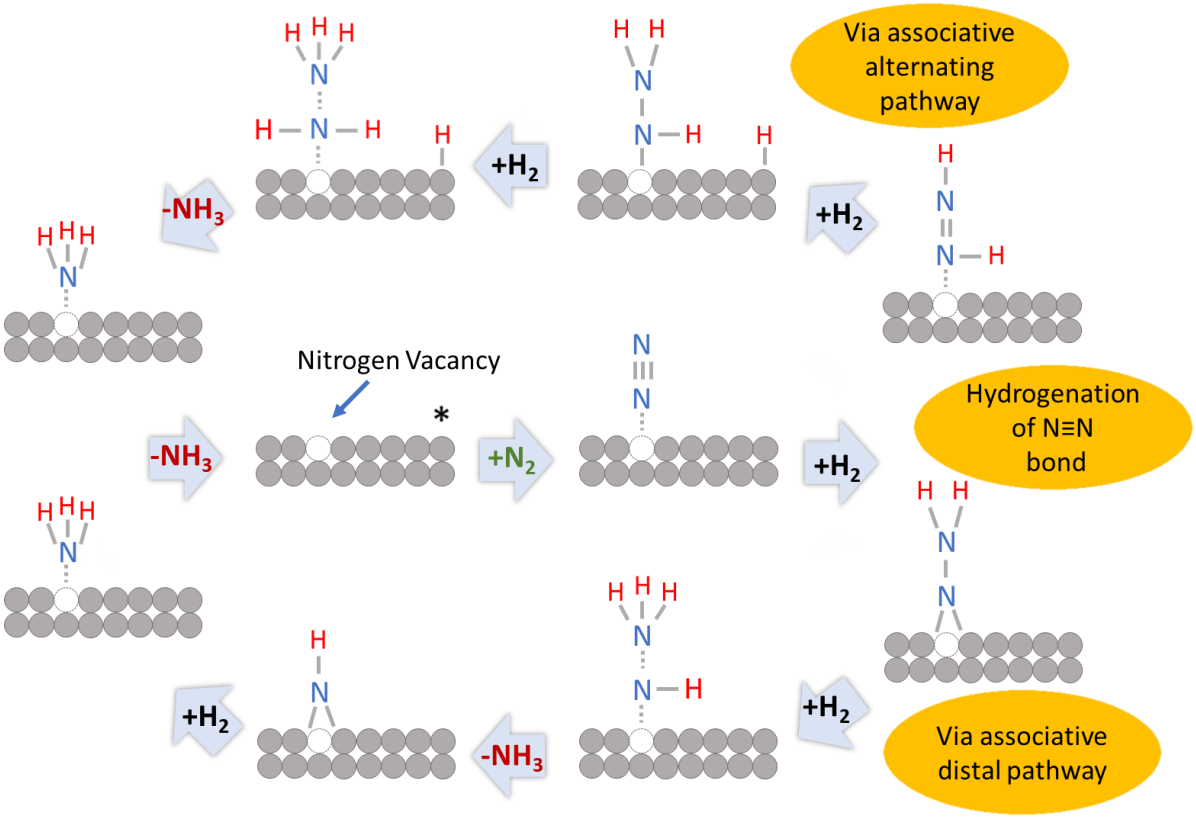


Fig. 1.14 Schematic illustration of the associative pathway of ammonia synthesis.

A novel cobalt molybdenum bimetallic nitride catalyst was reported by Kojima *et al* in 2000. The catalyst illustrated an outstanding catalytic activity of 15 mmol $h^{-1}g^{-1}$ at 673 K under 31 bars towards ammonia synthesis.[79] The reaction mechanism over CoMoN was investigated using $^{15}N_2$ gas and it was found that Lattice nitrogen was replaced by ^{15}N during the synthesis of ammonia. It dictates that nitrogen vacancies on the surface participate in the elementary step of ammonia formation.[80,81] This resulted in a lower activation barrier and explains the high activity observed. Associated new insights on the mechanism of this class of materials would lead to a step-change development on novel catalysts active under milder reaction conditions applicable to green ammonia production.

Over the past 25 years, novel catalysts have been developed favouring ammonia synthesis via an associative reaction mechanism. Metal hydrides, one major class of associative ammonia synthesis catalyst, could synchronously supply electrons and protons through the

conversion of H^- to H^0 and further to H^+.[82] The active hydrogen species on the support are directly involved in NH_3 formation via a hydride-mediated MvK mechanism, and with the supply of gaseous H_2, lattice hydrogen could be regenerated, hence accomplishing a NH_3 synthesis cycle.[83] Although the reaction mechanism over this material is not fully understood, it is proposed that the reaction proceeds through similar pathway like associative ammonia decomposition. Dinitrogen molecules are initially chemisorbed on a positively charged site. Instead of direct dissociating the nitrogen triple bond, the adsorbed species is stepwise hydrogenated by lattice hydrogen to form NH_3 (see **Fig. 1.15a**).[84] Direct nitrogen triple bond breaking is circumvented, lowering the activation barrier and thereby promotes the reaction.

Another class of material would be metal nitrides, particularly lanthanum nitrides.[85,86] Similar mechanism is observed as the CoMoN discussed above (see **Fig. 1.15b**). However, it is worth noting that a concerted mechanism of both associative and dissociative pathway has been observed on a cobalt catalyst on a nitride support (Co/CeN) over N_2 hydrogenation.[87] Incoming dinitrogen can rapidly interact with the nitrogen vacancies of the support to generate ammonia by the associative mechanism. The consumption of adsorbed positively charged hydrogen during hydrogenation leaves the remaining hydride-like species stabilising the surface nitrogen vacancies. This imparts high electron donation to the support which further activates and weakens nitrogen triple bonds though back-donation of electrons to the antibonding π* orbitals of N_2 on Co, favouring the dissociative mechanism on the metal site. Further introduction of Ni metal site helped to active dihydrogen dissociation whereas the vacant sites generated on CeN helped to activate dinitrogen and form ammonia at the metal-support interface. The synergy between the two sites, resulting in an ammonia synthesis activity that can compete with the existing Ru and Fe based catalysts.

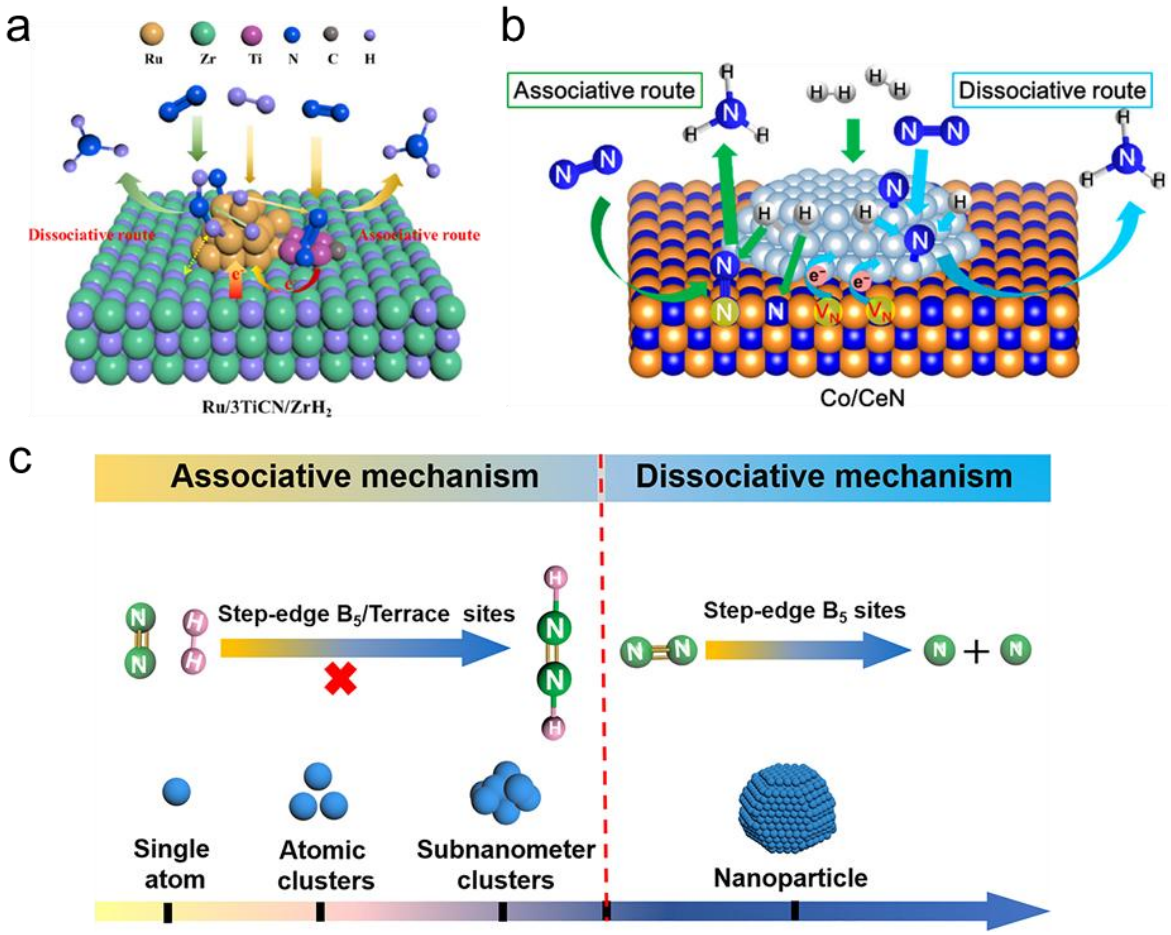


Fig. 1.15 illustration of associative mechanism over different catalyst. a. Metal hydride catalyst. Reprinted from reference[84]; b. Lanthanum nitride catalyst. Reprinted from reference[87]; c. Dependence between metal size and reaction mechanism over ammonia synthesis. Reprinted from reference[88].

Interestingly, it was found that associative mechanism would take place on non-redox active support by only tuning the size of the active metal (see Fig. 1.**15c**). Recently, different sizes of Ru supported catalyst were synthesised, ranging from single atoms, through atomic clusters and sub-nano-meter clusters to nano particles. It was claimed that when the size of Ru particles decreases to the sub-nano-meter cluster phase (<2 nm), ammonia synthesis could shift from a dissociative mechanism towards an associative mechanism due to the absence

of Ru B5 site.[89] This endowers a new strategy to escape the BEP constraints and also avoids hydrogen poisoning.

While the Nobel-recognized work established a dissociative mechanism for ammonia synthesis under typical Haber-Bosch conditions, recent identification of an associative mechanism has opened new avenues for catalyst development, particularly for operation under milder temperatures and pressures—conditions more suitable for future industrial applications.[90] Although the principle of equilibrium dynamics can guide the rational design of catalysts for both ammonia synthesis and decomposition, it is important to recognize that the optimal catalyst for one process may not necessarily be ideal for the other. This divergence arises from differences in optimal nitrogen-binding energies under varying reaction environments. As discussed earlier, from the MO point of view, the rate-determining steps for decomposition involves electron donation into the antibonding orbitals of metal–nitrogen triple bonds to promote the latter N recombination.[91] Nevertheless, in the scene of ammonia synthesis, it is required to transfer electron into the π* antibonding orbitals of the dinitrogen molecule to facilitate N triple bond breaking.[92] A notable example is Co_3Mo_3N, a highly effective bimetallic catalyst for ammonia synthesis, which demonstrates a significant drop in activity when exposed to ammonia concentrations as low as 5%.[93] This contrast underscores that the elementary steps of decomposition do not necessarily mirror those of the forward synthesis reaction, further justifying the need for separate catalyst development strategies.

With the limited literature reported on ammonia decomposition undergoing associative pathway, most of them are based on air sensitive alkali- metal oxynitrides. Ogasawara *et al* firstly reported a CaNH- supported Ni catalyst, where the generation of NH^- vacancies is the key for a MvK reaction mechanism.[94] Based on the experience gained for anion vacancy promoted associative ammonia decomposition. The same group further reported various Nickel supported barium titanium bimetallic oxynitride catalyst. The promoted activity by induced nitrogen to the plain bimetallic oxides were correlated to the nitrogen vacancies as

revealed by N_2- temperature programmed desorption measurements.[95,96] Further DFT revealed an anion vacancy mediated associative mechanism.

Despite their promising catalytic properties, nitride-based catalysts are highly sensitive to air and moisture, posing significant challenges for their practical application in industrial ammonia decomposition. Additionally, the synthesis of alkali metal-containing oxynitrides often requires stringent laboratory environments, such as the use of argon-filled glove boxes, liquid nitrogen cooling, and freeze-drying techniques.[86,97] The extreme synthetic conditions further limit their scalability and accessibility. These limitations raised the interest of the fourth chapter of my thesis: ***Enhanced Associative Ammonia Decomposition on Cerium Oxide via Inducing N Dopants***. Where I present an in-depth investigation of nitrogen-doped cerium oxide, a material that demonstrates catalytic activity comparable to state-of-the-art systems, while offering the advantage of straightforward and scalable synthesis.

1.4.4 Ammonia coupled reaction

In the context of sustainable and green chemistry, apart from being used in PEMFC for electricity generation, hydrogen has emerged as a pivotal reagent in several environmentally friendly processes. One notable example is its use in catalytic hydrogenolysis and hydrocracking of plastic waste, where hydrogen helps break down long polymer chains into valuable smaller hydrocarbons, thereby enabling chemical recycling of plastics into fuels or feedstocks.[98–100] Moreover, green hydrogen is intensively being explored in the reduction of CO_2 to produce syngas, methane, methanol and other carbon containing valuable products.[101–103] These applications not only highlight hydrogen's versatility but also underscore its growing importance in transitioning toward circular and low-carbon industrial systems.

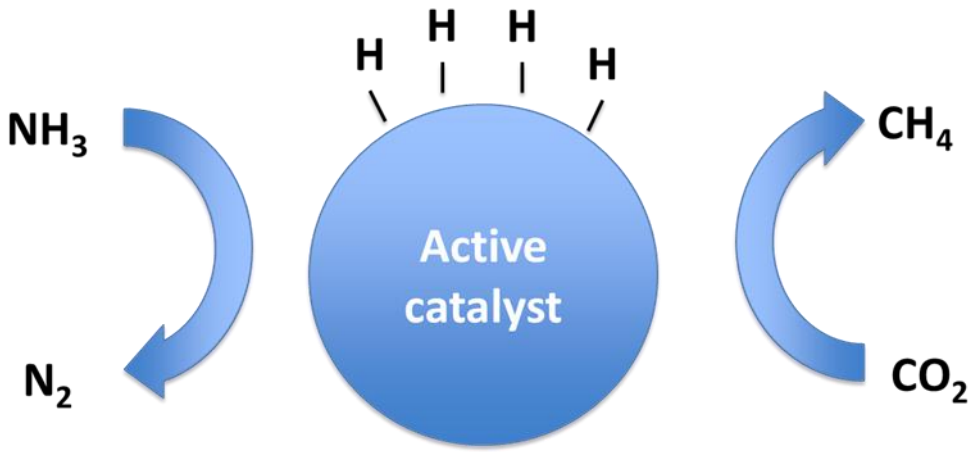


Fig. 1.16 schematic illustration of ammonia methanation process

Building on the knowledge discussed above, ammonia is a polar molecule with an N–H bond energy of 391 kJ mol^{-1}, which is notably lower than the H–H bond energy of 463 kJ mol^{-1} in molecular hydrogen.[104] Recent advances in catalysis have enabled the decomposition of ammonia at temperatures as low as 673 K, opening new avenues for its use in direct hydrogenation reactions. By coupling ammonia decomposition with downstream hydrogenation processes, it becomes possible to generate activated hydrogen adatoms *in situ*, eliminating the need for hydrogen storage or transportation. This approach not only simplifies the process chain but also allows the co-production of valuable hydrogenation products. Furthermore, nitrogen as the by-product of ammonia decomposition, offers a strong thermodynamic driving force that can shift the equilibrium forward. Moreover, integration of this system into industrial operations presents an opportunity to utilize available waste heat to meet the energy demands of the catalytic process, potentially lowering the overall energy input compared to operating the two reactions independently. This motivates further investigation that forms the fifth chapter: ***Direct Coupling of Ammonia and Carbon Dioxide for Methane Production***. In Chapter 5, ammonia decomposition is coupled with CO_2 hydrogenation for direct methane production and thereby enclosed the carbon cycle (see **Fig. 1.16**). That

chapter will extend the insights from chapters 3 and 4, with a particular emphasis on the active species presented at the catalytic interface via an associative reaction mechanism.

1.5 Aims and objectives

The catalytic decomposition of ammonia under mild conditions has emerged as a promising strategy for carbon-free hydrogen delivery. However, a major bottleneck in this reaction lies on the balance between the adsorption and activation of ammonia over the catalyst support, particularly the dissociation of N-H bond and desorption of the nitrogen molecule, which remains kinetically challenging at low temperatures. As previously discussed, this limitation is governed by BEP scaling relations, where strong nitrogen adsorption on one hand favours ammonia activation, however, on the other hand, inhibits effective nitrogen desorption due to unfavourable electron back-donation.

To address this challenge, inspiration has been drawn from the associative mechanism observed in enzyme-mediated nitrogen fixation. Where redox active nitrogen species, in particularly metal nitride has been considered as an active approach to circumvent the constraints via an alternative pathway. This thesis aims to explore and develop nitrogen-containing catalysts that operate through such associative mechanisms, enabling efficient ammonia decomposition at lower temperatures. In addition, the potential of these catalysts to drive ammonia-coupled hydrogenation reactions, such as CO_2 methanation, is explored. Offering a pathway for direct hydrogen delivery via active intermediates, thereby eliminating the need for hydrogen storage or transportation.

Comprehensive catalytic testing has been carried out under various operating conditions, including temperature, pressure, weight hourly space velocity, metal loading, and gas composition. Kinetic analyses, stability assessments, and apparent activation energy determinations have been performed to evaluate activity performance for the broader overview of these catalysts. A wide range of characterisation techniques have been employed to understand the structure–activity relationships. Furthermore, *in situ* and operando spectroscopy, isotopic labelling, and DFT simulations have been conducted to gain deeper insight into the reaction mechanisms and identify active intermediates.

1.6 Thesis overview

This thesis consists of sixth chapters. Chapters 3 to 5 are the results and discussions of the performed research projects during my DPhil study.

Chapter 1: Introduction on the background of ammonia as an energy vector. Literature review on the novel catalyst design for thermal ammonia decomposition.

Chapter 2: Introduces the principle of major used characterisation techniques, details of the experimental synthesis and reactor set-ups.

Chapter 3: Studies the effect of different nitrogen environments on nitrogen doped carbon for non-dissociative ammonia decomposition. Proposing the non-dissociative mechanism taking place over the catalyst using novel *in situ* techniques.

Chapter 4: Studies the associative mediated ammonia mechanism over synthesized nitrogen doped cerium oxide catalyst. Rationalise the MvK mechanism using isotopic labelling pulse experiments.

Chapter 5: Studies ammonia methanation reaction over various catalyst, perform further fundamental analysis of this reaction over previous nitrogen doped cerium oxide material. Investigate the effect of reaction intermediates on the nitrogen doped cerium oxide catalyst towards catalytic enhancement of the ammonia methanation reaction.

Chapter 6: Summarises the findings in the previous chapters and provides an outlook to future research.

References

1. Wu, S., Salmon, N., Li, M. M. J., Bañares-Alcántara, R. & Tsang, S. C. E. Energy Decarbonization via Green H_2 or NH_3? *ACS Energy Lett.* **7**, 1021–1033 (2022).
2. Rosa, L. & Gabrielli, P. Energy and food security implications of transitioning synthetic nitrogen fertilizers to net-zero emissions. *Environ. Res. Lett.* **18**, 014008 (2022).
3. Erisman, J. W., Sutton, M. A., Galloway, J., Klimont, Z. & Winiwarter, W. How a century of ammonia synthesis changed the world. *Nat. Geosci.***1**, 636–639 (2008).
4. Tonelli, D., Rosa, L., Gabrielli, P., Parente, A. & Contino, F. Cost-competitive decentralized ammonia fertilizer production can increase food security. *Nat. Food* **5**, 469–479 (2024).
5. Ye, D. & Tsang, S. C. E. Prospects and challenges of green ammonia synthesis. *Nat. Synth.* **2**, 612–623 (2023).
6. Blanco, H., Jinks, B., Bianco, E. & Sezer. Innovation Outlook: Renewable Ammonia, *International Renewable Energy Agency* (2022).
7. Morgan, E. R., Manwell, J. F. & Mcgowan, J. G. Sustainable Ammonia Production from U.S. Offshore Wind Farms: A Techno-Economic Review. *ACS Sustainable Chem. Eng.* **5**, 9554-9567 (2017).
8. Zeinalipour-Yazdi, C. D., Richard, C., Catlow, A., Hargreaves, J. S. J. & Laassiri, S. A comparative analysis of the mechanisms of ammonia synthesis on various catalysts using density functional theory. *R. Soc. Open Sci*. **8**, 210952 (2021).
9. Ghavam, S., Vahdati, M., Wilson, I. A. G. & Styring, P. Sustainable Ammonia Production Processes. *Front. Energy Res.* **9**, 34 (2021).
10. Liu, A. *et al.* Current Progress of Electrocatalysts for Ammonia Synthesis Through Electrochemical Nitrogen Reduction Under Ambient Conditions. *ChemSusChem* **13**, 3766–3788 (2020).
11. MacFarlane, D. R. *et al.* A Roadmap to the Ammonia Economy. *Joule* **4**, 1186–1205 (2020).
12. Bellenger R Darnajoux X Zhang A M L Kraepiel, J. P. Biological nitrogen fixation by alternative nitrogenases in terrestrial ecosystems: a review. *Biogeochemistry* **149** 53–73 (2020).
13. Energy Agency, I. Ammonia Technology Roadmap Towards more sustainable nitrogen fertiliser production. https://www.iea.org/reports/ammonia-technology-roadmap (2025)
14. Wang, Q., Guo, J. & Chen, P. Recent progress towards mild-condition ammonia synthesis. *J. Energy Chem.* **36**, 25–36 (2019).
15. Foster, S. L. *et al.* Catalysts for nitrogen reduction to ammonia. *Nat. Catal.* **1**, 490–500 (2018).
16. Walter, M. D. Ammonia formation revisited. *Nat. Chem.* **14**, 12–13 (2021).
17. Lee, K. *et al.* Techno-economic performances and life cycle greenhouse gas emissions of various ammonia production pathways including conventional, carbon-capturing, nuclear-powered, and renewable production. *Green Chem.* **24**, 4830–4844 (2022).
18. File:Haber-Bosch-En.svg - Wikimedia Commons. https://commons.wikimedia.org/wiki/File:Haber-Bosch-En.svg. (2025)
19. Wang, M. *et al.* Can sustainable ammonia synthesis pathways compete with fossil-fuel based Haber–Bosch processes? *Energy Environ. Sci.* **14**, 2535–2548 (2021).
20. Wang, T. & Abild-Pedersen, F. Achieving industrial ammonia synthesis rates at near-ambient conditions through modified scaling relations on a confined dual site. *Proc. Natl. Acad. Sci. U. S. A.* **118**, 2106527118 (2021).
21. Arnaiz del Pozo, C. & Cloete, S. Techno-economic assessment of blue and green ammonia as energy carriers in a low-carbon future. *Energy Convers. Manag.* **255**, (2022).

22. Shen, H. *et al.* Electrochemical ammonia synthesis: Mechanistic understanding and catalyst design. *Chem* **7**, 1708–1754 (2021).

23. Xiong, Y. *et al.* Electrochemical Nitrate Reduction: Ammonia Synthesis and the Beyond. *Adv. Mater.* **36**, 2304021 (2024).

24. Feng, C. *et al.* Photoexcitation Altered Reaction Pathway Greatly Facilitate Ammonia Synthesis Over Isolated Ru Sites. *Adv. Energy Mater.* **14**, 2303792 (2024).

25. Nayak-Luke, R. & Wilkinson, I. 'Green' Ammonia: Impact of Renewable Energy Intermittency on Plant Sizing and Levelized Cost of Ammonia. *Ind. Eng. Chem. Res.* **57**, 43, 14607–14616 (2018)

26. Soloveichik, G. Electrochemical synthesis of ammonia as a potential alternative to the Haber–Bosch process. *Nat. Catal.* **2**, 377–380 (2019).

27. Morlanés, N. *et al.* A technological roadmap to the ammonia energy economy: Current state and missing technologies. *Chem. Eng. J.* **408**, (2021).

28. Bell, T. E. & Torrente-Murciano, L. H2 Production via Ammonia Decomposition Using Non-Noble Metal Catalysts: A Review. *Top. Catal.* **59**, 1438–1457 (2016).

29. Lucentini, I., Garcia, nia, Vendrell, X. & Llorca, J. Review of the Decomposition of Ammonia to Generate Hydrogen. *Ind. Eng. Chem. Res* **60**, 18560–18611 (2021).

30. F. Schüth, R. Palkovits, R. Schlögl & S. Su, D. Ammonia as a possible element in an energy infrastructure: catalysts for ammonia decomposition. *Energy Environ. Sci.* **5**, 6278–6289 (2012).

31. Rathore, S. S., Biswas, S., Fini, D., Kulkarni, A. P. & Giddey, S. Direct ammonia solid-oxide fuel cells: A review of progress and prospects. *Int. J. Hydrogen Energy* **46**, 35365–35384 (2021).

32. Siddiqui, O. & Dincer, I. A review and comparative assessment of direct ammonia fuel cells. *Therm. Sci. Eng. Prog.* **5**, 568–578 (2018).

33. Al Baroudi, H., Awoyomi, A., Patchigolla, K., Jonnalagadda, K. & Anthony, E. J. A review of large-scale CO_2 shipping and marine emissions management for carbon capture, utilisation and storage. *Appl. Energy* **287**, (2021).

34. Machaj, K. *et al.* Ammonia as a potential marine fuel: A review. *Energy Strateg. Rev.* **44**, 100926 (2022).

35. Zhou, J. *et al.* Flexible design and operation of off-grid green ammonia systems with gravity energy storage under long-term renewable power uncertainty. *Appl. Energy* **388**, 125629 (2025).

36. Cinti, G., Liso, V., Sahlin, S. L. & Araya, S. S. System Design and Modeling of a High Temperature PEM Fuel Cell Operated with Ammonia as a Fuel. *Energies* **13**, 4689 (2020).

37. Zhou, X., Wang, Y. & Wu, W. Design and optimization of an ammonia fuel processing unit for a stand-alone PEM fuel cell power generation system. *Int. J. Energy Res.* **41**, 877–888 (2017).

38. Vegge, T. *et al.* Indirect hydrogen storage in metal ammines. *Solid-State Hydrog. Storage Mater. Chem.* **44**, 533–564 (2008)

39. Bashir, M. A. *et al.* Recent development of advanced processing technologies for biodiesel production: A critical review. *Fuel Process. Technol.* **227**, (2022).

40. Toulhoat, H. Heterogeneous Catalysis: Use of Density Functional Theory. in *Encyclopedia of Materials: Science and Technology* 1–7 (2010)

41. Yan, X. *et al.* Cooperatively tailored surface frustrated Lewis pairs and N-doping on CeO_2 for photocatalytic CO_2 reduction to high-value hydrocarbon products. *Appl. Catal. B Environ.* **343**, 123484 (2024).

42. Garcıá-Garcıá, F. R. *et al.* TAP studies of ammoniadecomposition over Ru and Ir catalysts. *Phys. Chem. Chem. Phys* **13**, 12892–12899 (2011).

43. Fang, H. *et al.* Challenges and Opportunities of Ru-Based Catalysts toward the Synthesis and

Utilization of Ammonia. *ACS Catal.* **12**, 7, 3938–3954 (2022)

44. Hayashi, F. *et al.* Ammonia decomposition by ruthenium nanoparticles loaded on inorganic electride C12A7:e^-. *Chem. Sci.* **4**, 3124–3130 (2013).

45. Su, Z. *et al.* Research progress of ruthenium-based catalysts for hydrogen production from ammonia decomposition. *Int. J. Hydrogen Energy* **51**, 1019–1043 (2024).

46. Liu, J.-C. *et al.* Heterogeneous Fe_3 single-cluster catalyst for ammonia synthesis via an associative mechanism. *Nat Commun* **9**, 1610 (2018).

47. Medford, A. J. *et al.* From the Sabatier principle to a predictive theory of transition-metal heterogeneous catalysis. *J. Catal.* **328**, 36–42 (2015).

48. Rod, T. H., Logadottir, A. & Nørskov, J. K. Ammonia synthesis at low temperatures*J. Chem. Phys* **112**, 5343 (2000).

49. Humphreys, J., Lan, R. & Tao, S. Development and Recent Progress on Ammonia Synthesis Catalysts for Haber–Bosch Process. *Adv. Energy Sustain. Res.* **2**, 2000043 (2021).

50. Jacobsen, C. J. H. *et al.* Catalyst design by interpolation in the periodic table: Bimetallic ammonia synthesis catalysts. *J. Am. Chem. Soc.* **123**, 8404–8405 (2001).

51. García-García, F. R., Guerrero-Ruiz, A. & Rodríguez-Ramos, I. Role of B5-type sites in Ru catalysts used for the NH_3 decomposition reaction. *Top. Catal.* **52**, 758–764 (2009).

52. Karim, A. M. *et al.* Correlating particle size and shape of supported Ru/γ-Al_2O_3 catalysts with NH_3 decomposition activity. *J. Am. Chem. Soc.* **131**, 12230–12239 (2009).

53. Ganley, J. C., Thomas, F. S., Seebauer, E. G. & Masel, R. I. A Priori Catalytic Activity Correlations: The Difficult Case of Hydrogen Production from Ammonia. *Catal. Lett.* **96**, 117–122 (2004).

54. Kulkarni, S. R. *et al.* Elucidating the rate-determining step of ammonia decomposition on Ru-based catalysts using ab initio-grounded microkinetic modeling. *Catal. Sci. Technol.* **13**, 2026–2037 (2023).

55. Chen, C. *et al.* Ru-Based Catalysts for Ammonia Decomposition: A Mini-Review. *Energy and Fuels* **35**, 11693–11706 (2021).

56. Hatta, A. H. *et al.* A review on recent bimetallic catalyst development for synthetic natural gas production via CO methanation. *Int. J. Hydrogen Energy* **47**, 30981–31002 (2022).

57. Hu, S. *et al.* Activity and stability of monometallic and bimetallic catalysts for high-temperature catalytic HI decomposition in the iodine–sulfur hydrogen production cycle. *Int. J. Hydrogen Energy* **41**, 773–783 (2016).

58. Sato, K. & Nagaoka, K. Boosting ammonia synthesis under mild reaction conditions by precise control of the basic oxideru interface. *Chem. Lett.* **50**, 687–696 (2021).

59. Sato, K. *et al.* Surface dynamics for creating highly active ru sites for ammonia synthesis: Accumulation of a low-crystalline, oxygen-deficient nanofraction. *ACS Sustain. Chem. Eng.* **8**, 2726–2734 (2020).

60. Lin, B. *et al.* Morphology Effect of Ceria on the Catalytic Performances of Ru/CeO_2 Catalysts for Ammonia Synthesis. *Ind. Eng. Chem. Res.* **57**, 9127–9135 (2018).

61. Marakatti, V. S. & Gaigneaux, E. M. Recent Advances in Heterogeneous Catalysis for Ammonia Synthesis. *ChemCatChem* **12**, 5838–5857 (2020).

62. Feng, J. *et al.* Sub-Nanometer Ru Clusters on Ceria Nanorods as Efficient Catalysts for Ammonia Synthesis under Mild Conditions. *ACS Sustain. Chem. Eng.* **10**, 10181–10191 (2022).

63. Van Deelen, T. W., Hernández Mejía, C. & de Jong, K. P. Control of metal-support interactions in heterogeneous catalysts to enhance activity and selectivity. *Nat. Catal.* **2**, 955–970 (2019).

64. Li, X. *et al.* Advances in heterogeneous single-cluster catalysis. *Nat. Rev. Chem.* **7**, 754–767 (2023).

65. Bueno-Ferrer, C., Parres-Esclapez, S., Lozano-Castelló, D. & Bueno-López, A. Relationship between surface area and crystal size of pure and doped cerium oxides. *J. Rare Earths* **28**, 647–653 (2010).

66. Maeda, K., Kuriki, R., Zhang, M., Wang, X. & Ishitani, O. The effect of the pore-wall structure of carbon nitride on photocatalytic CO_2 reduction under visible light. *J. Mater. Chem. A* **2**, 15146–15151 (2014).

67. Podila, S. *et al.* Hydrogen production by ammonia decomposition using high surface area Mo_2N and Co_3Mo_3N catalysts. *Catal. Sci. Technol.* **6**, 1496–1506 (2016).

68. Duan, X. *et al.* Carbon Nanofiber-Supported Ru Catalysts for Hydrogen Evolution by Ammonia Decomposition. *Chinese J. Catal.* **31**, 979–986 (2010).

69. Li, L., Zhu, Z. H., Yan, Z. F., Lu, G. Q. & Rintoul, L. Catalytic ammonia decomposition over Ru/carbon catalysts: The importance of the structure of carbon support. *Appl. Catal. A Gen.* **320**, 166–172 (2007).

70. Rizescu, C. *et al.* $RuCl_3$ Supported on N-Doped Graphene as a Reusable Catalyst for the One-Step Glucose Oxidation to Succinic Acid. *ChemCatChem* **9**, 3314–3321 (2017).

71. Ye, D. *et al.* Active nitrogen sites on nitrogen doped carbon for highly efficient associative ammonia decomposition. *iScience* **27**, 110571 (2024).

72. Shi, Z. *et al.* Metal-Nitrogen-Doped Carbon Materials as Highly Efficient Catalysts: Progress and Rational Design. *Adv. Sci.* **7**, 2001069 (2020).

73. Liu, H., Zhang, R., Liu, S. & Liu, G. CeO_2/Ni Inverse Catalyst as a Highly Active and Stable Ru-free Catalyst for Ammonia Decomposition. *ACS Catal.* **14**, 9927–9939 (2024).

74. Fang, H. *et al.* Dispersed surface Ru ensembles on MgO(111) for catalytic ammonia decomposition. *Nat. Commun.* **14**, 647 (2023).

75. Wu, S. *et al.* Removal of Hydrogen Poisoning by Electrostatically Polar MgO Support for Low-Pressure NH_3 Synthesis at a High Rate over the Ru Catalyst. *ACS Catal.* **10**, 5614–5622 (2020).

76. Wu, S. *et al.* Rapid Interchangeable Hydrogen, Hydride, and Proton Species at the Interface of Transition Metal Atom on Oxide Surface. *J. Am. Chem. Soc.* **143**, 9105–9112 (2021).

77. Leung, K. C. *et al.* Confined Ru Sites in a 13X Zeolite for Ultrahigh H_2 Production from NH_3 Decomposition. *J. Am. Chem. Soc.* **145**, 14548–14561 (2023).

78. Xiong, P. *et al.* Synthesis of core@shell catalysts guided by Tammann temperature. *Nat. Commun.* **15**, 420 (2024).

79. Kojima, R. & Aika, K. I. Cobalt Molybdenum Bimetallic Nitride Catalysts for Ammonia Synthesis. *Applied Catalysis A: General* **215** 514–515 (2003)

80. Zeinalipour-Yazdi, C. D., Hargreaves, J. S. J., Richard, C. & Catlow, A. Low-T Mechanisms of Ammonia Synthesis on Co_3Mo_3N. *J. Phys. Chem. C* **122**, 40 (2018).

81. Zeinalipour-Yazdi, C. D., Hargreaves, J. S. J., Laassiri, S., Richard, C. & Catlow, A. The integration of experiment and computational modelling in heterogeneously catalysed ammonia synthesis over metal nitrides. *Phys. Chem. Chem. Phys* **20**, 21803 (2018).

82. Zhang, Y. *et al.* Recent progress of thermocatalytic ammonia synthesis via an associative mechanism. *Fundam. Res.* 2667-3258 (2024)

83. Yan, H. *et al.* Lithium Palladium Hydride Promotes Chemical Looping Ammonia Synthesis Mediated by Lithium Imide and Hydride. *J. Phys. Chem. C* **125**, 6716–6722 (2021).

84. Zhou, Y. *et al.* Integrating Dissociative and Associative Routes for Efficient Ammonia Synthesis over a TiCN-Promoted Ru-Based Catalyst. *ACS Catal.* **12**, 2651–2660 (2022).

85. Ye, T.-N. *et al.* Vacancy-enabled N_2 activation for ammonia synthesis on an Ni-loaded catalyst. *Nature* **583**, 391-395 (2020).

86. Ye, T.-N. *et al.* Contribution of Nitrogen Vacancies to Ammonia Synthesis over Metal Nitride

Catalysts. *J. Am. Chem. Soc* **142**, 14374–14383 (2020).

87. Ye, T.-N. *et al.* Dissociative and Associative Concerted Mechanism for Ammonia Synthesis over Co-Based Catalyst. *J. Am. Chem. Soc* **143**, 12857–12866 (2021).

88. Li, L. *et al.* Size sensitivity of supported Ru catalysts for ammonia synthesis: From nanoparticles to subnanometric clusters and atomic clusters. *Chem* **8**, 749–768 (2022).

89. Zhou, Y. *et al.* Unraveling the size-dependent effect of Ru-based catalysts on Ammonia synthesis at mild conditions. *J. Catal.* **404**, 501–511 (2021).

90. Ertl, G. Reactions at Surfaces: From Atoms to Complexity (Nobel Lecture). *Angewandte Chemie International Edition*, **47** 3524-3535 (2007).

91. Wu, S. & Tsang, S. C. E. Renewable N-cycle catalysis. *Trends Chem.* **3**, 660–673 (2021).

92. Kitano, M. *et al.* Ammonia synthesis using a stable electride as an electron donor and reversible hydrogen store. *Nat. Chem.* **4**, 934–940 (2012).

93. Boisen, A., Dahl, S., Nørskov, J. K. & Christensen, C. H. Why the optimal ammonia synthesis catalyst is not the optimal ammonia decomposition catalyst. *J. Catal.* **230**, 309–312 (2005).

94. Ogasawara, K. *et al.* Ammonia Decomposition over CaNH-Supported Ni Catalysts via an NH_2--Vacancy-Mediated Mars-van Krevelen Mechanism. *ACS Catal.* **11**, 11005–11015 (2021).

95. Miyashita, K. *et al.* Effects of nitrogen vacancy sites of oxynitride support on the catalytic activity for ammonia decomposition. *NPG Asia Mater.* **16**, 54 (2024).

96. Ogasawara, K. *et al.* Ammonia Decomposition over Water-Durable Hexagonal $BaTiO_{3-x}N_y$ Supported Ni Catalysts. *Adv. Energy Mater.* **13**, 2301286 (2023).

97. Zhang, Z. *et al.* Anion vacancies activate N_2 to ammonia on Ba–Si orthosilicate oxynitride-hydride. *Nat. Chem.* **17**, 679–687 (2025)

98. Wang, H. & Edman Tsang, S. C. Recent advances in polyolefin plastic waste upcycling via mild heterogeneous catalysis route from catalyst development to process design. *Cell Reports Phys. Sci.* **5**, 102075 (2024).

99. Wang, H. *et al.* Ce-Promoted PtSn-Based Catalyst for Hydrocracking of Polyolefin Plastic Waste into High Yield of Gasoline-Range Products. *ACS Catal.* **13**, 15886–15898 (2023).

100. Wang, H., Huang, S. & Tsang, S. C. E. Heterogeneous catalysis strategies for polyolefin plastic upcycling: co-reactant-assisted and direct transformation under mild conditions. *Chem. Commun.* **61**, 1496–1508 (2025).

101. Guo, Y., Li, T., Li, D. & Cheng, J. Efficient reduction of CO_2 to high value-added *Sustain. Energy Rev.* **189**, 114053 (2024).

102. Bao, J., Yang, G., Yoneyama, Y. & Tsubaki, N. Significant Advances in C1 Catalysis: Highly Efficient Catalysts and Catalytic Reactions. *ACS Catal.* **9**, 3026–3053 (2019).

103. Zhong, J. *et al.* State of the art and perspectives in heterogeneous catalysis of CO_2 hydrogenation to methanol. *Chem. Soc. Rev.* **49**, 1385–1413 (2020).

104. Kim, S., Park, Y., Kim, J., Pabst, T. P. & Chirik, P. J. Ammonia synthesis by photocatalytic hydrogenation of a N_2-derived molybdenum nitride. *Nat. Synth.* **1**, 297–303 (2022).

Chapter 2 Characterisation Techniques and Experimental Methods

2.1 General characterisation techniques

The following subsections provide general background and working principles of the characterisation techniques employed through the thesis, followed by detailed explanation on experimental procedures.

2.1.1 X-ray diffraction (XRD)

X-ray diffraction (XRD) is a powerful technique to probe the crystallographic structure of the catalyst materials. Due to the similar wavelengths of X-rays and the interatomic spacing in crystallite materials (both in Angstrom region), the periodic electron density of such crystallographic planes can be scattered by incident X-rays. The resultant diffraction pattern can further derive information including phase identification, lattice constant calculation, particle size estimation and unit cell parameter determination.[1,2]

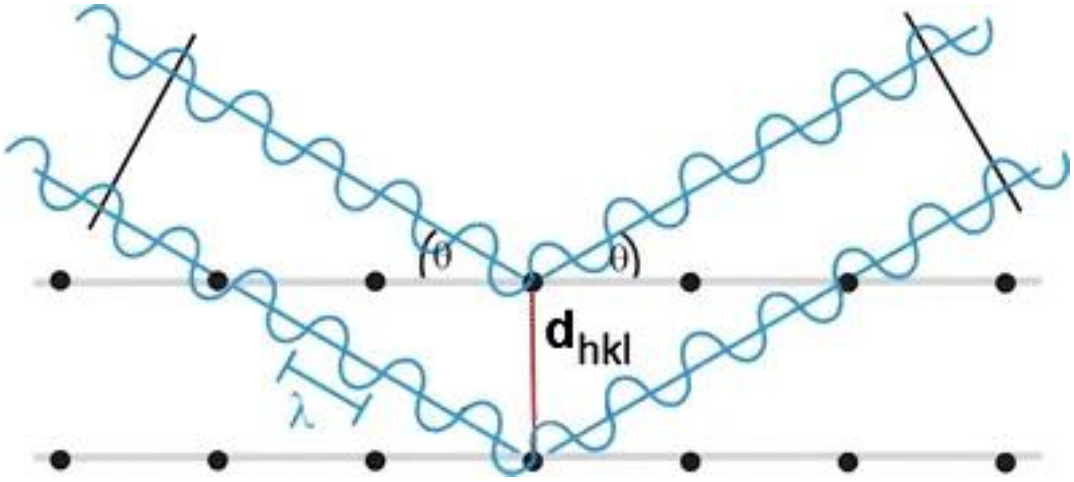


Fig. 2.1 Illustration on the principle of the Bragg's Law: relationship between interlayer spacing, diffraction angle, and wavelength of X-ray. Reprinted from reference[3].

More specifically, during constructive interference when the path difference between reflected X-rays from adjacent lattice planes equals an integer multiple of the wavelength, the scattered waves reinforce each other, producing a diffraction peak. This geometric condition, expressed as the Bragg's Law (see eq. 1), directly relates the angle θ between the incident X-ray and scattering plane, the crystal's atomic spacing d and the wavelength λ of the X-ray beam. Therefore, by measuring the diffraction angle for a known wavelength, the interplanar distance d can be precisely calculated, providing fundamental insight into the crystalline structure.

$$n\,\lambda = 2\,d\,sin\theta \qquad (1)$$

The XRD patterns measured in this thesis was performed on a Bruker D8 Advance X-ray diffractometer. Typically, high speed electrons are thermionically emitted from a heated filament (at 40 kV and 40 mA) of the cathode and targeted towards copper anode. The inner-shell electrons (K shell) are ejected forming vacant holes. Electrons from higher energy level (e.g. L shell) then drops down to fill the vacancy. The associated transition energy release forms the X-ray photon (Cu Kα radiation). The X-ray beam will then be mono-chromated and illuminated towards the sample material at different incident angles (2θ range of 5 to 90 °). If the sample is crystalline ordered, the X-ray beams will diffract through the interlayer spacing grating of the material and undergo constructive or destructive interference to produce a unique diffraction pattern.

2.1.2 Scanning electron microscopy (SEM)

The scanning electron microscope (SEM) is a common characterisation approach to investigate the surface morphology and microstructure of solid materials. In general, a finely focused beam of high-energy electrons probed through a series of electromagnetic lenses and scanned across the surface of a specimen. Interaction between the incident electron beam and the sample emits various, primary secondary electrons (SE) and backscattered electrons (BSE).[4] SE helps to produce high-resolution images with detailed topographical contrast, while BSE provide composition contrast based on the atomic number of the elements present

in the sample. Overall, SEM is mainly used to provide the high-magnification and high-resolution imaging of surface texture and structure.

In this thesis. *Mengqi Duan* (Tsang's group PhD student) performed all SEM experiments over two different sets instruments. For chapter 3, the morphology of carbon-based material was revealed on a JSM-6610LV with accelerated voltage of 24 kV and a working distance (WD) of 11 mm. For Chapter 4 and 5, the cerium-based catalysts were characterised on a Zeiss Sigma 300 FEG-SEM at 2 kV and 6.0 mm.

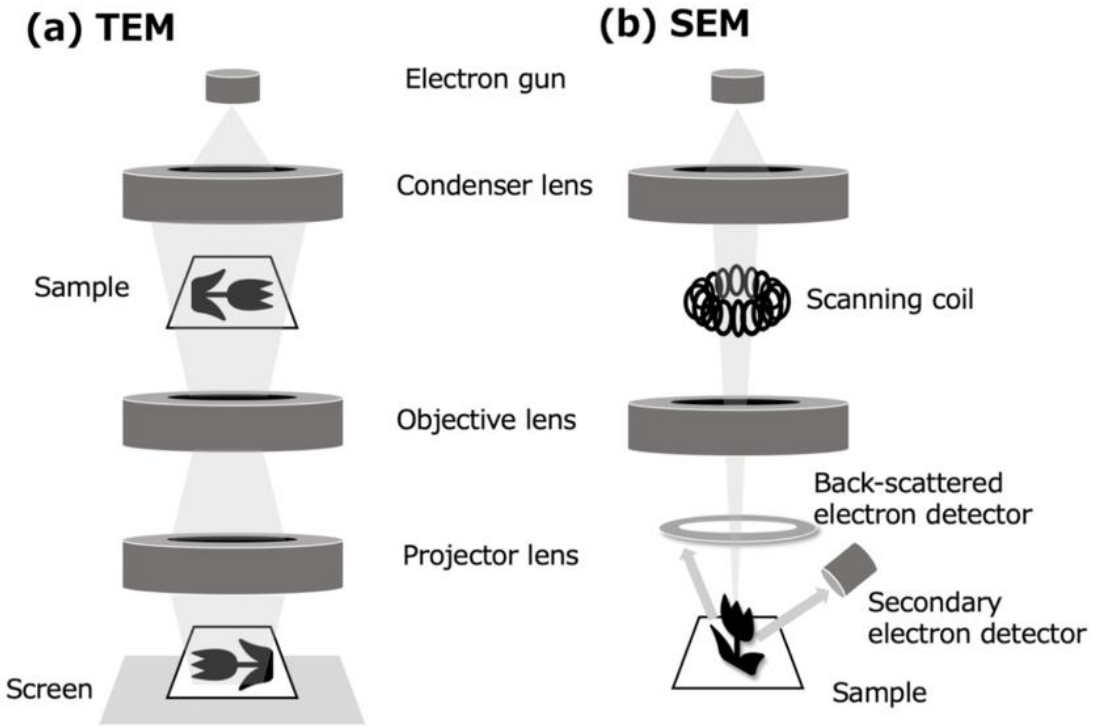


Fig. 2.2 Schematic illustration of the working principle of (a)TEM and (b)SEM. Reprinted from reference[5].

2.1.3 Transmission Electron Microscopy (TEM)

Transmission electron microscopy (TEM) is a similar technique as SEM which is used to visualise the morphology and structure of materials. However, unlike SEM which scans the surface of a specimen, TEM transmits a high-energy electron beam through the samples. This

does not only result in higher resolution, near atomic scale, but also provides detailed information about the internal structure of the material. The working principle is similar to SEM as illustrated in Fig. 2.2. In TEM, high-energy electrons interact with the atoms via scattering, absorption, and transmission processes. Imaging is thereby generated by processing the emitting signal from these interactions which are magnified by projector lenses and captured via an end on CCD camera, or direct electron detector.[6] Based on the different type of electrons emerged from the sample, the transmission electron microscopes can be classified into 2 modes, namely bright field and dark field. For the former, the un-scattered (transmitted) electron beam is being analysed and materials with high mass (or high electron density) appear darker whereas the background appears bright. Bright field imaging is particularly effective for visualizing overall morphology, grain boundaries, and thickness variations. On the other hand, in dark field mode, elastically scattered electrons are captured with the aperture instead, which means the material of interest will appear bright depending on the variation in electron density while the background is dark. Dark field imaging is particularly useful for studying crystal defects, phase boundaries, dislocations, and specific crystallographic orientations.[7]

In this thesis, two different TEM instruments were used to analyse the catalysts. In chapter 3, JEM2100 under the dark field mode was used to obtain the size of nanoparticles on the carbon support. The measurement was carried out by *Ping-Luen Ho* (Tsang's group senior PhD). For chapter 4 and 5, the measurements on cerium-based catalysts were acquired on a JEM-ARM300F, at 300 kV. The collection range of the STEM images were around 54−220 mrad. These data were collected by *Xiaowei Liu* (PhD student from DICP).

2.1.4 X-ray absorption spectroscopy (XAS)

X-ray absorption spectroscopy is an elemental specific technique that provides valuable information on the local electronic structure and coordination environment of selected atoms in a material.

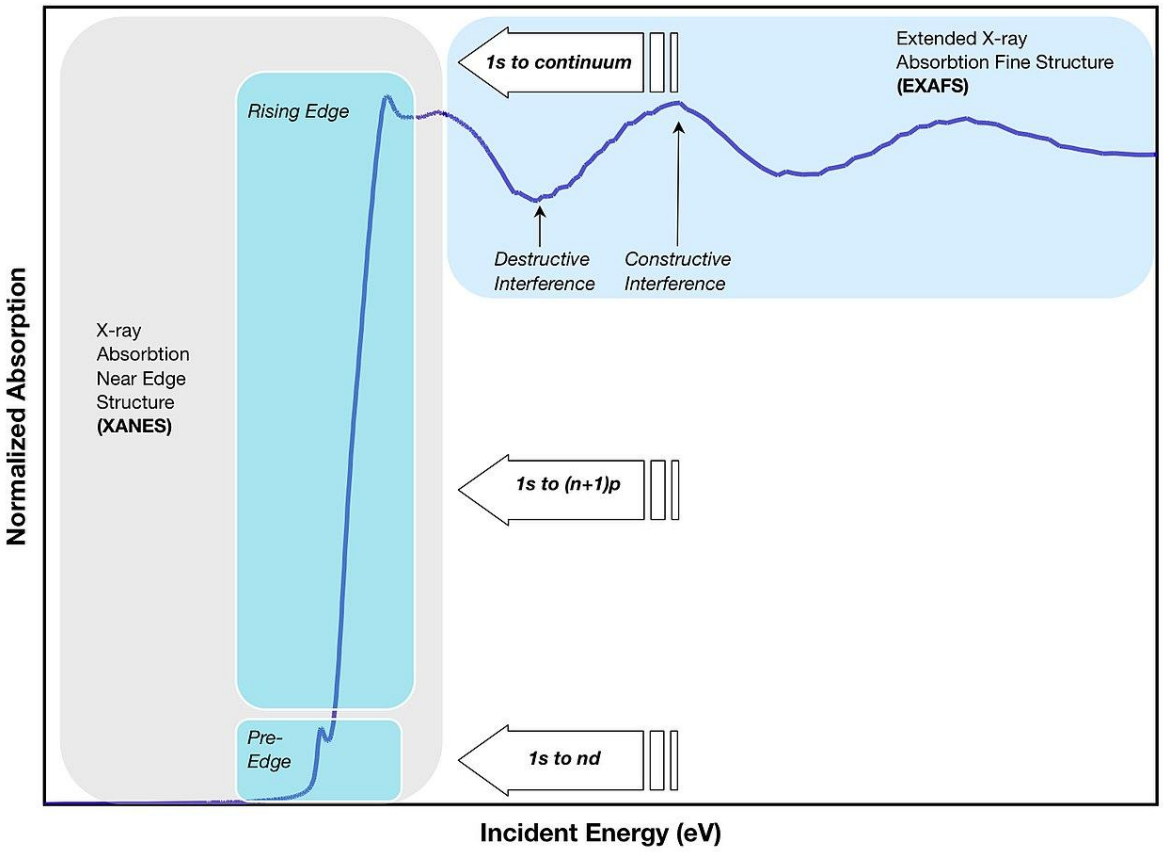


Fig 2.3 Schematic illustration of the XAS spectrum highlighting the Pre-edge, XANES, and EXAFS regions. Reprinted from reference[9].

Typically, incident X-ray energy is tuned across the binding energy of a core-level electron (such as the K, L, or M edge of an atom), resulting in a sharp increase in absorption which corresponds to the excitation of that electron into unoccupied states or into the continuum.[8] The final X-ray absorption spectrum is obtained by relating the absorption coefficient as a function of the X-ray energy followed by equation 2.

$$\mu = -\boldsymbol{Ln}\left(\frac{\boldsymbol{I}}{\boldsymbol{I_0}}\right)/\boldsymbol{t} \quad \textbf{(2)}$$

Where μ is the absorption coefficient, I_0 is the incident X-ray irradiation, I is the intensity of X-ray after transmitted through the sample and t is the thickness of the sample.

Based on the different strength of the photon energy, the spectrum is divided into three primary regions, the pre-edge, X-ray absorption near edge structure (XANES) and extended X-ray absorption fine structure (EXAFS). The pre-edge region corresponds to low-intensity features arising from electronic transfer from 1s electrons to unoccupied bound states such as metal 3d or ligand hybridized orbitals. Thereby providing information regarding the oxidation state, coordination geometry, and electronic structure of the absorbing atom.[10] The XANES region signifies the transition of a core electron to the continuum giving rise to a sharp energy edge, which is mainly determined by the oxidation state of the atom. The EXAFS shows oscillation which originates from interference between the outgoing photoelectron wave and the wave scattered back from neighbouring atoms (see **Fig. 2.4**). This region yields quantitative information including coordination number, interatomic distances, and disorder.[8]

Generally, XAS measurements are carried out at synchrotron radiation facilities due to its high intensity light source as well as its tuneable energies. The high-resolution raw data represents the variation in X-ray absorption as a function of photon energy. For EXAFS analysis, the oscillatory part of the spectrum is Fourier-transformed to obtain a radial distribution function that reveals distances, coordination numbers, and types of neighbouring atoms around the absorber. In contrast, XANES analysis focuses on the edge region to determine oxidation states, coordination geometry, and electronic transitions through comparison with reference compounds or theoretical simulations. Thus, XAS is used to determine quantitative structural and chemical information about the local atomic environment of the target element.

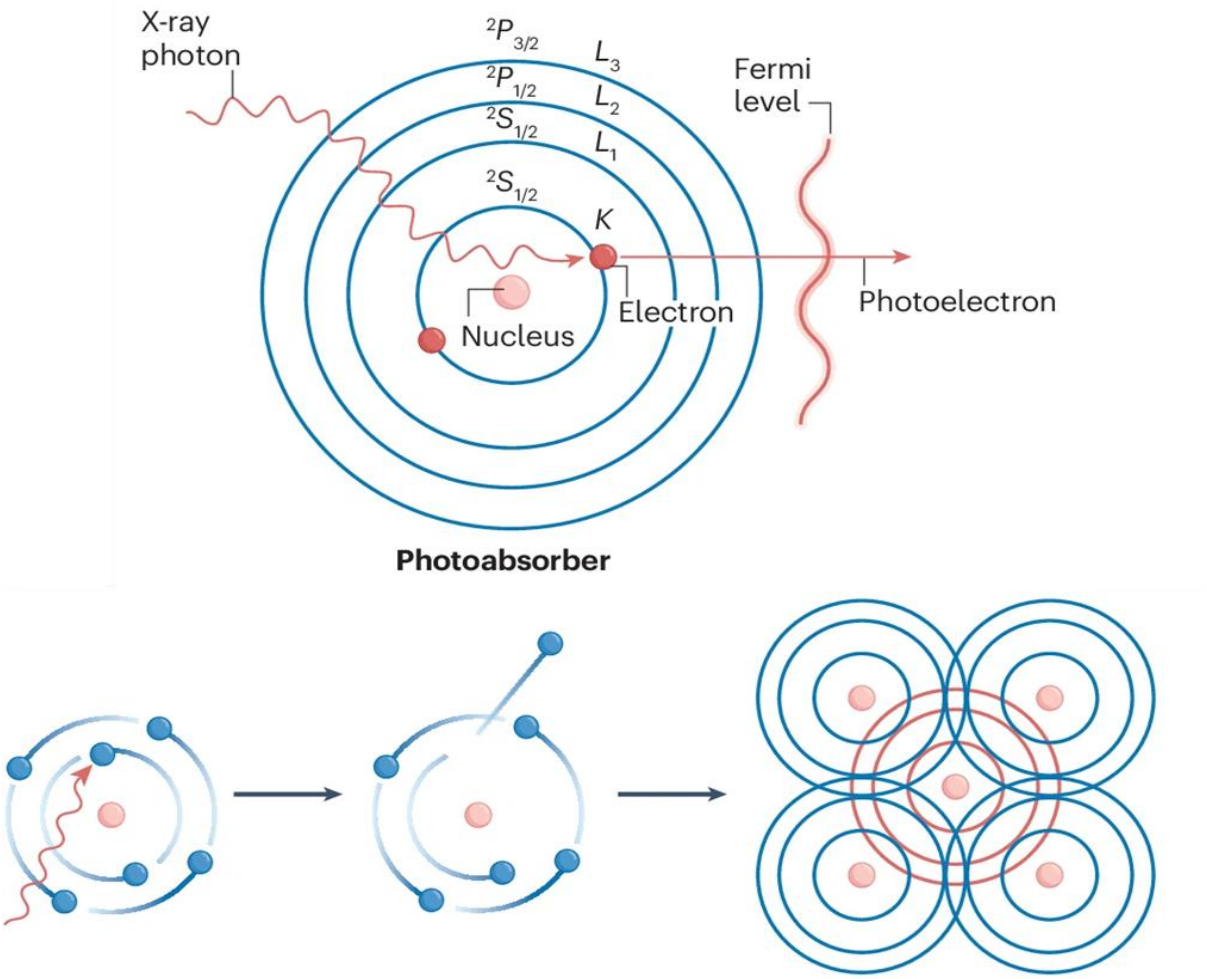


Fig. 2.4 Representation of excitation of electron to the continuum and how it results in interference between neighbouring atoms. Reprinted from reference[11].

In this thesis, XAS measurements were carried out at two different synchrotron light source facilities. For chapter 3, the XAS of Ru-K edge supported on carbon material were collected at Beamline BL07A at the Taiwan Light Source at National Synchrotron Radiation Research Centre by *Tai-Sing Wu and Yun-Liang Soo*. A Si (111) Double Crystal Monochromator (DCM) was used to scan the photon energy. For chapter 4 and 5, the Ru-K edge spectrum on ceria-based support was obtained at Shanghai Synchrotron Radiation Facility by *Prof. Jinfeng Han*.

2.1.5 X-ray photoelectron spectroscopy (XPS)

X-ray photoelectron spectroscopy is a surface-sensitive technique that is used to investigate on a material's surface chemical composition, oxidation state and electronic structure. It uses X-ray to excite the ground state of the studied material. When the core electron absorbs sufficient energy from the incident beam, it moves from its initial state and excites as a photoelectron. The kinetic energy of the emitted escaped electron is recorded by the spectrometer's energy analyzer. Using the known incident X-ray energy, the electron's binding energy in its unbound state can be derived based on the following equation:

$$E_{binding} = hv - E_{kinetic} - \varphi \quad (3)$$

Where $E_{binding}$ is the binding energy of the excited electron to its ground state, h is the Planck constant, v is the frequency of the X-ray radiation, which gives hv being the incident X-ray intensity, $E_{kinetic}$ is the kinetic energy of the photoelectron emitted and recorded by the instrument, φ is the work function of the spectrometer, which is a constant representing the amount of energy required for the electron to escape the energy analyzer of the spectrometer.

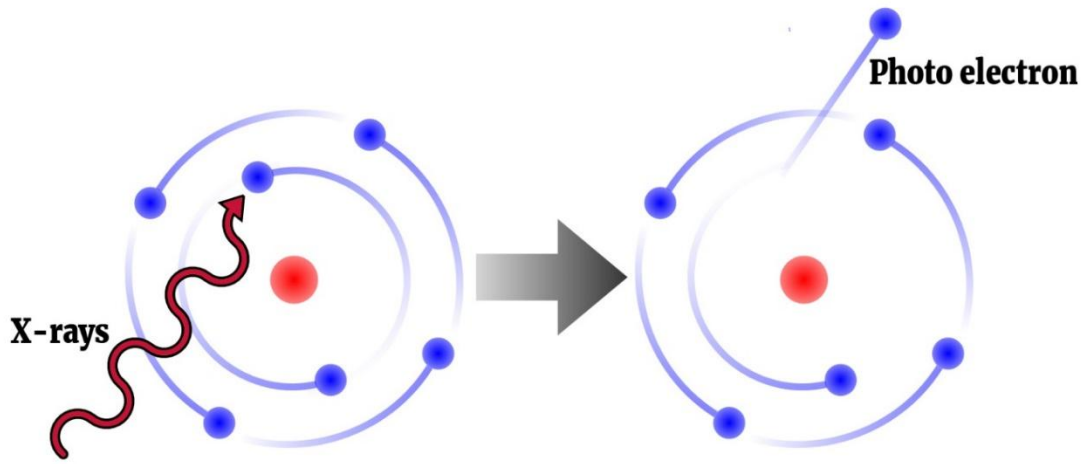


Fig. 2.5 Illustration on how photo electron is generated upon X-ray excitation.

Since the energy of the photoelectrons is directly related to the element's atomic number and the molecular environment from which they originated. XPS enables identification of elements and their oxidation states, as well as the presence of surface functional groups and chemical shifts due to bonding interactions.

In this thesis, all XPS spectra were collected at the EPSRC National Facility for XPS ("HarwellXPS"). In addition to routine scans of common elements such as C 1s and O 1s, particular attention was given to the N 1s orbital across all three chapters to investigate nitrogen incorporation and chemical states. Furthermore, high-resolution Ce 3d and Ru 3p spectra were acquired and analysed in chapters 4 and 5 to provide detailed insight into the oxygen vacancies on cerium oxide and surface interactions on Ru.

2.1.6 Brunauer-Emmett-Teller (BET) surface analysis

Brunauer-Emmett-Teller (BET) surface analysis is a widely applied method to determine the specific surface area, pore volume, pore size distribution of solid materials. It is based on physically adsorption and desorption of gaseous N_2 onto the material's surface.[12]

During measurement, the sample is first degassed under vacuum or inert gas at elevated temperatures to remove moisture and contaminants. It is then exposed to nitrogen gas at incremental relative pressures (P/P_0), and the volume of gas adsorbed is recorded (V). The result is fitted against the BET equation[13] (see eq. 4):

$$\frac{\boldsymbol{P}}{\boldsymbol{V(P_0-P)}} = \frac{\mathbf{1}}{\boldsymbol{V_m C}} + \frac{\boldsymbol{(C-1)P}}{\boldsymbol{V_m C P_0}} \qquad \textbf{(4)}$$

Where P is the equilibrium pressure, P_0 is the saturation pressure of absorbent gas, V stands for the volume of gas molecules adsorbed, V_m for the monolayer absorbed gas quantity and C being the BET constant related to the energy of adsorption.

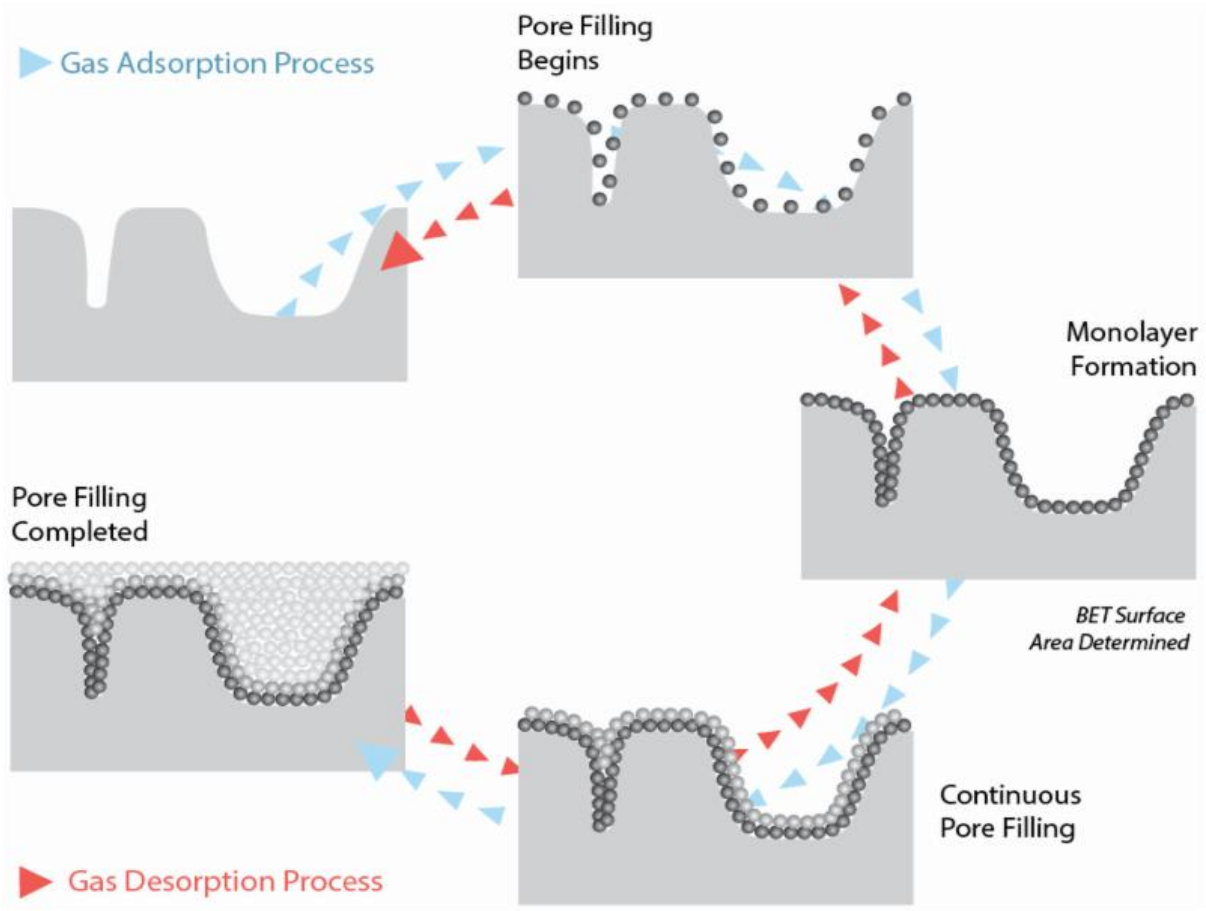


Fig. 2.6 Illustration of the absorption and desorption process during BET analysis. Reprinted from reference[14].

Using the monolayer capacity V is obtained, and the specific surface area can be calculated using the known cross-sectional area of the nitrogen molecule. Further information regarding the pore size, pore volume and pores size distribution could be calculated using the Barrett–Joyner–Halenda (BJH) method.[15] This method assumes all the pores within porous material are cylindrical and they are filled by absorbent gas via a layer-by-layer mechanism (see **Fig. 2.6**). Thus, by applying the Kelvin equation (see eq. 5), the pore size can be obtained.

$$Ln\left(\frac{P}{P_0}\right) = -\frac{2\gamma V_m}{rRT} \qquad \textbf{(5)}$$

Where γ is the surface tension of the absorbent gas, which typically is liquid nitrogen, r is the pore radius, R being the gas constant and T being the temperature.

Furthermore, according to the IUPAC classification, distinct shape of the hysteresis loop between the adsorption and desorption curve raise to six primary types of physisorption isotherms, each corresponding to different surface and pore characteristics.[15] Overall, BET analysis provides valuable information about the surface characteristics of porous and non-porous materials to assess textural properties of catalysts.

In this thesis, the Brunauer-Emmett-Teller (BET) surface area was obtained from N_2 adsorption/desorption isotherms at -196 °C and analysed by a Micromeritics TriStar II Plus instrument. All sorption isotherms were obtained using ultrahigh purity nitrogen gas (99.999%) to calculate the surface area and pore volume of the desired sample. The tested sample (approximately 100 mg) was loaded into a sample cell and pre-treated under vacuum of 10^{-5} Torr at 200 °C for 18 hours

2.1.7 Temperature programmed reduction and desorption (TPR/TPD)

Temperature programmed reduction (TPR) and desorption (TPD) are widely used techniques to obtain chemical properties regarding the catalyst. TPR is typically performed using H_2 as its reducing gas to examine the reducibility of the metal oxides within the catalysts. As for TPD, NH_3 is used to reveal the catalyst acidity while CO_2 is commonly used to observe the basic sites. The experiments are carried out over the same instrument as illustrated in Fig. 2.7.

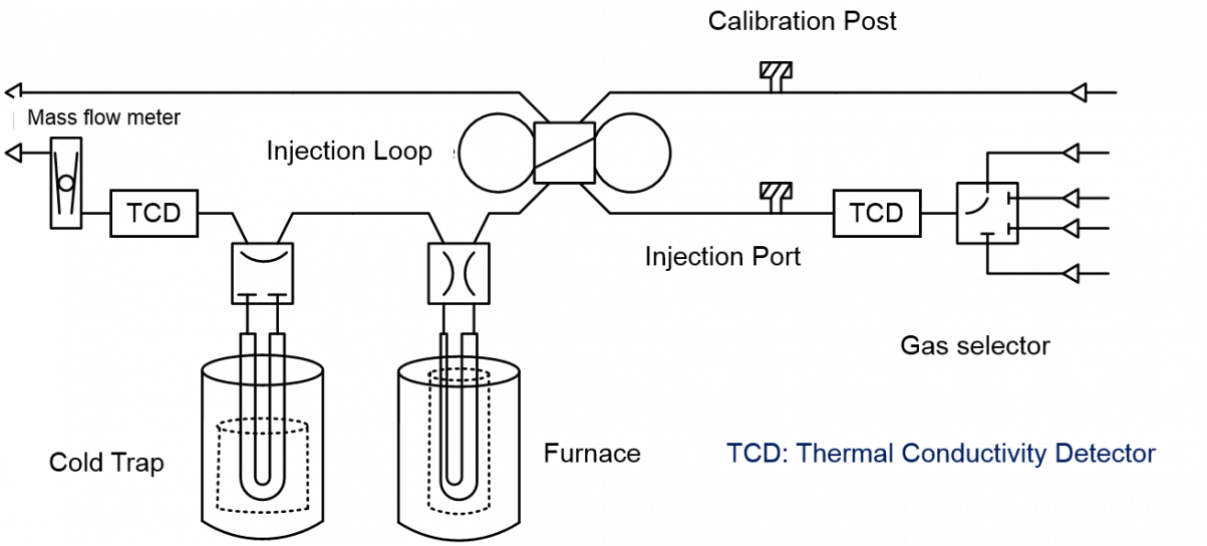


Fig. 2.7 Schematic illustration of a temperature programmed pulsar instrument. Reprinted from reference[16].

For TPR experiments, catalyst sample are held under a flow of a reducing gas while the temperature raises. The hydrogen consumption is monitored as a function of temperature using the end on thermal conductivity detector (TCD). Peaks in the TPR profile correspond to reduction events at specific temperatures, offering insights into the oxidation states and more importantly the strength of metal-support interactions. In TPD analysis, the experiment begins by adsorbing probed gas onto the catalyst at low temperature. After equilibrium has been reached, the excess absorbents are purged with reference gas until a set-point. The catalyst bed is then heated up, followed by monitoring the desorption of absorbed gas as a function of time. This will provide qualitative and quantitative insight on the acid and base strength of the catalyst.

In this thesis, all TPR and TPD measurements are carried out on an automated flow chemisorption analyser (ChemBET Pulsar). Around 100 mg of catalyst are placed in a U-shaped quartz tube and fixed to the reactor. The samples are pre-treated to 110 °C for 1 h under 20 ml min^{-1} He flow to remove moisture. In H_2-TPR, the catalyst bed is heated up to 700 °C under 20 ml min^{-1} 5%H_2/N_2 flow with a ramping rate of 5 °C min^{-1}. The H_2 consumption

is analysed as a function of time and temperature. In NH_3-TPD, the catalyst bed is treated with 20 ml min^{-1} 10% NH_3/He flow for 1 h. Temperature is then raised to 600 °C with the desorption of NH_3 being monitored. CO_2-TPD and N_2-TPD follows the same experimental method as NH_3-TPD, with CO_2 gas and N_2 gas being the probed gas instead. All TPD measurements share the same ramping rate of 5 °C min^{-1}.

2.1.8 Fourier transform infrared spectroscopy (FTIR)

Fourier transform infrared spectroscopy (FTIR) is a powerful analytical technique used to identify and study chemical bonds, functional groups, and molecular interactions in solid, liquid, or gaseous samples. When coupled with *in situ* or operando reaction cells, this approach becomes a valuable tool for probing catalytic mechanisms and providing insights into fundamental reaction pathways.

During a typical FTIR measurement, infrared radiation is passed through a system of optical lenses and reflected off the sample surface. Since molecules absorb IR light at characteristic frequencies corresponding to specific vibrational modes. The resulting reflected signal would carry such information regarding the chemical bonding. Fourier transform is applied to convert the raw signal into a frequency-domain spectrum, presenting absorbance (or transmittance) as a function of wavenumber.[17]

$$\boldsymbol{\nu = \frac{1}{2\pi c}\sqrt{\frac{k(m_1+m_2)}{m_1 m_2}}} \qquad \textbf{(6)}$$

The observed IR absorption bands are governed by the vibrational properties of molecular bonds and can be described using the harmonic oscillator model derived from Hooke's Law, as expressed in Equation (6).[18] Where ν is the vibrational frequency, c is the speed of light, k is the force constant, m_1 and m_2 are the atomic masses that forms the bond. Based on this relationship, isotopic substitution leads to a predictable shift in vibrational frequency, which

can be used to validate band assignments and gain mechanistic insight into bond formation and cleavage processes during catalytic reactions.

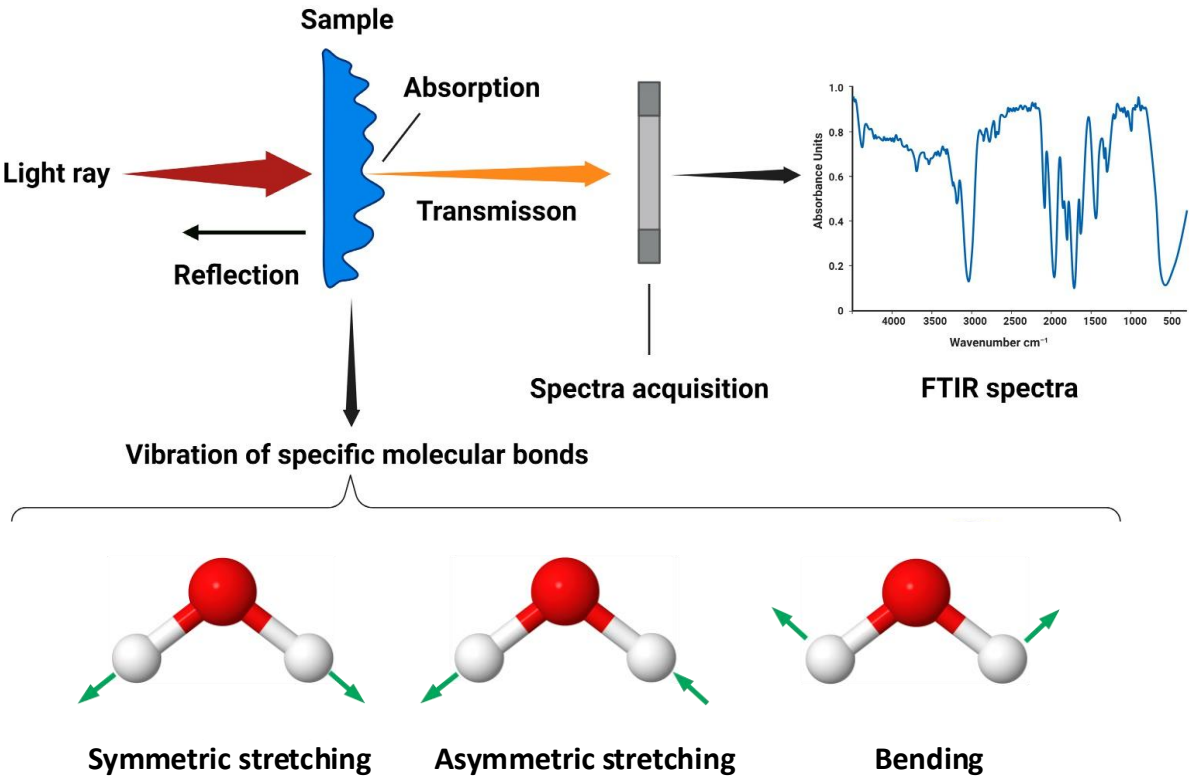


Fig. 2.8 schematic illustration of the working principle of Fourier transform infrared spectroscopy. Reprinted from reference[19].

In this thesis, FTIR and *in situ* FTIR experiments were carried out on a Nicolet iS50 FT-IR spectrometer equipped with a liquid nitrogen cooled MCT/A detector. For all experiments, ca. 150 mg of sample was loaded in the reactor cell. Prior to measurement, the catalyst was activated under 5% H_2/N_2 flow (10 ml min^{-1}) at 400 °C for 2 h, followed by Ar (10 ml min^{-1}) purging to remove excess residue gas. Unless otherwise specified, spectra were obtained by collecting 64 scans with a resolution of 4 cm^{-1}.

For *in situ* NH_3 FTIR, 10% NH_3 in helium (10 ml min^{-1}) was introduced over the sample cell for 1h at room temperature. Excess NH_3 was subsequently purged using Ar (10 ml min^{-1}). Spectra

were collected across a temperature range from room temperature to 400 °C in 50 °C increments under continuous Ar flow.

Operando NH_3 FTIR followed a similar procedure, except 10% NH_3/He was continuously flowed instead of Ar during the temperature ramp, allowing real-time monitoring of surface species under reaction conditions.

Isotopic pulsed experiments were operated at 400 °C using $^{14}NH_3$, $^{15}NH_3$ and $^{14}ND_3$. The specific designed gas-line were charged with targeted gas molecules to 0.6 bar. The reactants were then delivered into the reactor chamber under 10 ml min^{-1} Ar carrier flow. Spectra were recorded every 30 s by averaging 32 scans per acquisition.

Operando CO_2 methanation FTIR, pulsar CO_2 methanation FTIR and pulsar NH_3 methanation FTIR followed the same procedure. CO_2 and H_2 (molar ratio 1:4) gas mixture and CO_2 and NH_3 (molar ratio 3:8) was purged through the system instead. The flow rates of all the continuously flowing gasses remained the same.

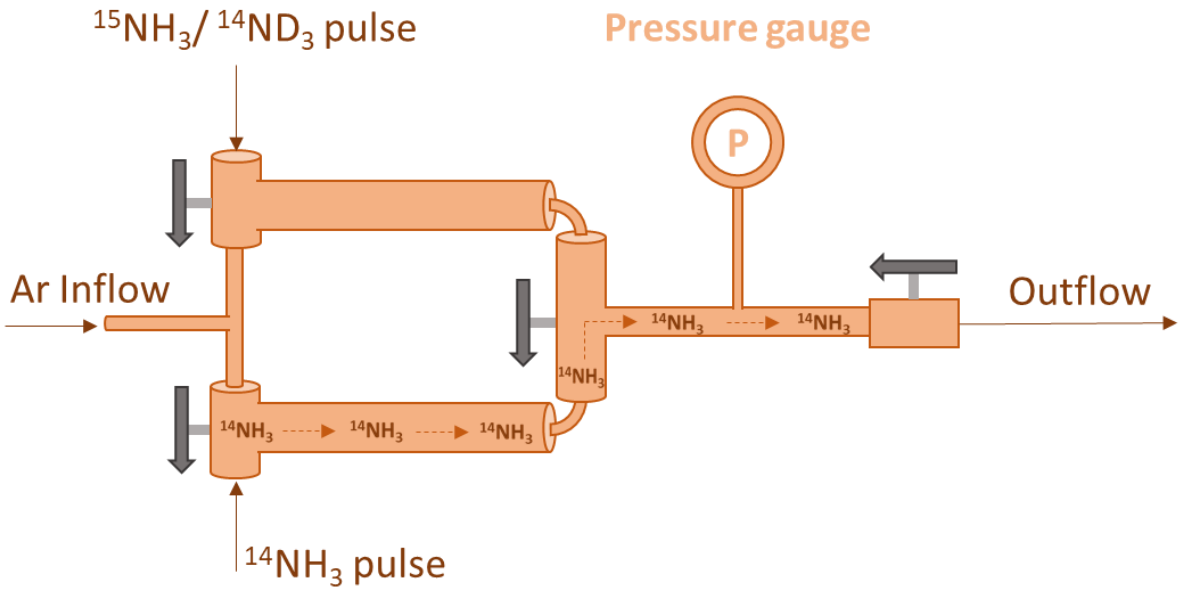


Fig. 2.9 Representation of the set-up design for $^{14}NH_3$, $^{15}NH_3$ and $^{14}ND_3$ pulse experiment.

2.1.9 Mass spectrometry (MS)

Mass spectrometry (MS) is a technique used to detect and quantify chemical species based on their mass-to-charge (m/z) ratio. The process begins with ionization, where the gaseous atom is ionised by knocking one or more electrons off to give a positive ion via electron impact. These ions are then accelerated in a positively charged chamber due to charge repelling to obtain uniform kinetic energy. It is worth noting that the ionisation chamber needs to be under vacuum to avoid ions colliding with air molecules. The ions are then deflected by a magnetic field according to their masses which separates them according to their m/z ratios. The final beam of ions is detected by a detector that records the abundance of each ion, generating a mass spectrum that reflects the composition of the gas mixture

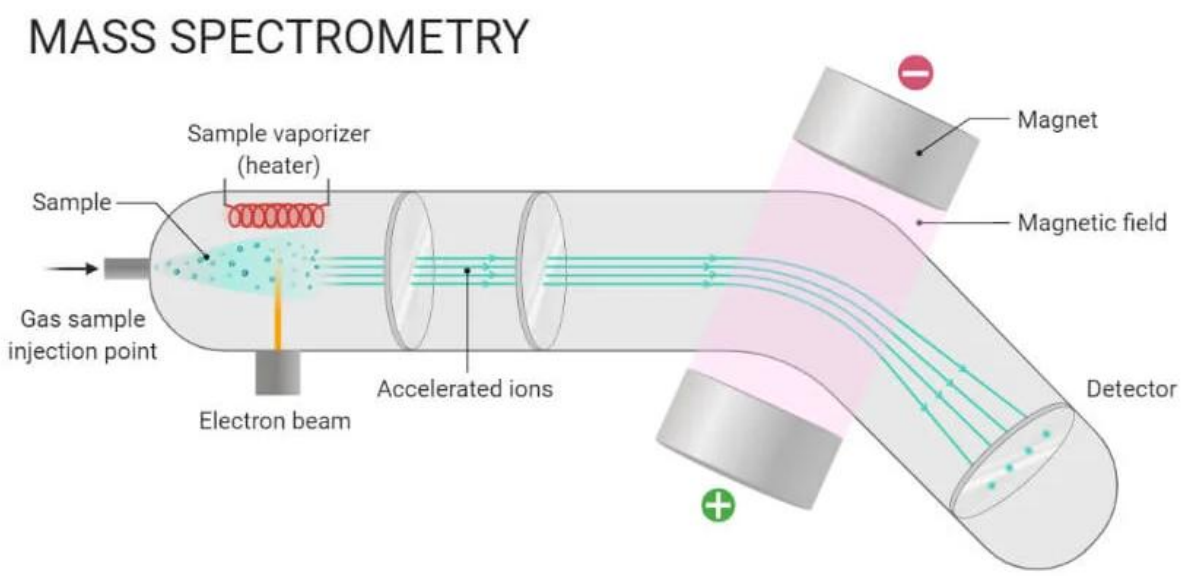


Fig. 2.10 schematic illustration of the working principle of mass spectrometry. Reprinted from reference[20].

In catalysis studies, MS is particularly valuable for real-time monitoring of gaseous reactants, intermediates, and products. It is coupled with the pulse experiment set-up shown in Fig. 2.9 and linked to a thermo-reactor for the investigation on the lattice nitrogen exchange effect during ammonia decomposition. More specifically, a stainless-steel gas chamber located in

the inflow gas system is preloaded with 0.6 bar of either $^{15}NH_3$ (>98 atom%, BOC Ltd) or $^{14}NH_3$, with pressure monitored by a gauge. The preloaded gas is pulsed into the reactor while the entire system is continuously being flushed with argon at 15 ml min^{-1}. The final reaction products are analysed by the inline mass spectrometer (Hiden HPR-20 QIC Gas Analysis System), with the electron beam energy set to 20 eV for optimal detection.

Apart from connecting the MS to the end on of the reactor to perform *in situ* experiments, it is also widely coupled with inductively coupled plasma to gather ICP-MS. This is a common technique used to determine the trace elemental composition inside the sample metrics.

Similar to conventional MS, ICP-MS starts with the nebulization of sample into a fine aerosol and introduced into an argon plasma chamber. This extremely high-temperature environment (~6000–10000 K) is capable of efficiently atomizing and ionizing almost all elements in the periodic table, converting them into positively charged ions. The plasma's primary role is to ensure near-complete ionization of the sample, which is critical for accurate and sensitive elemental analysis.

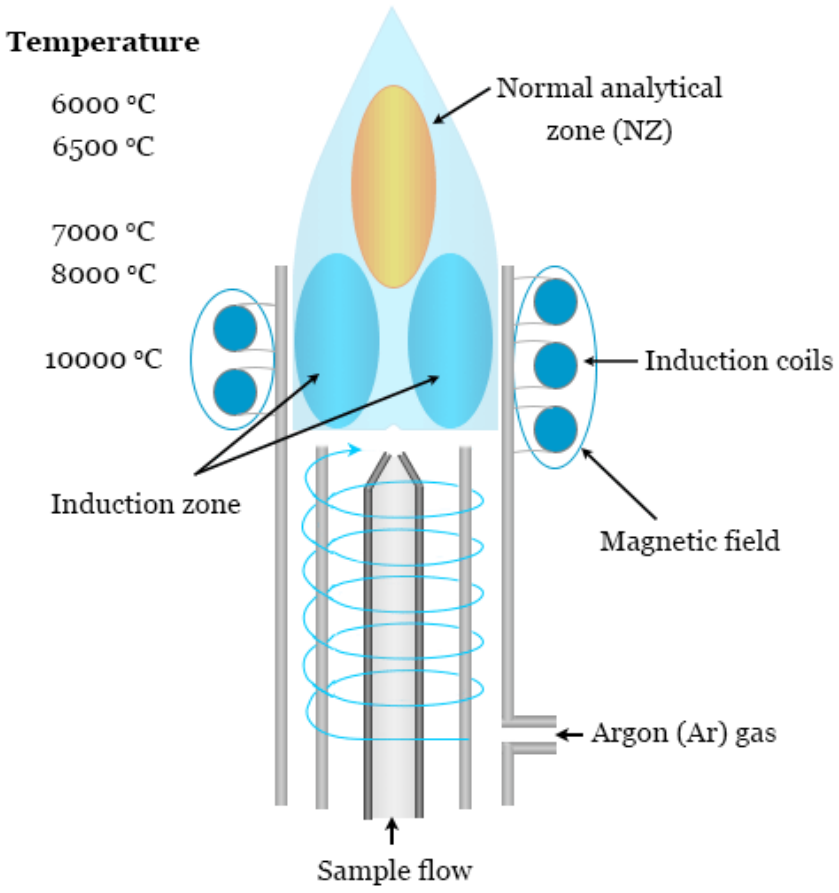


Fig. 2.11 Illustration diagram of the plasma induced ionisation section. Reprinted from reference[21].

Inductively Coupled Plasma Mass Spectrometry (ICP-MS) was employed in this thesis to determine the actual Ru loading on the catalyst supports. Prior to analysis, the catalyst samples were digested using concentrated HCl to ensure complete dissolution of the metal content. The resulting solution was then diluted with DI water to adjust the concentration of trace elements, ensuring they remained below 500 parts per billion (ppb) for optimal detection sensitivity and accuracy during ICP-MS measurement.

2.2 Evaluation of catalytic performance

The following subsections provide detailed descriptions of the reactor setup used for catalytic experiments, along with the methods employed to measure catalytic conversion and extract kinetic information.

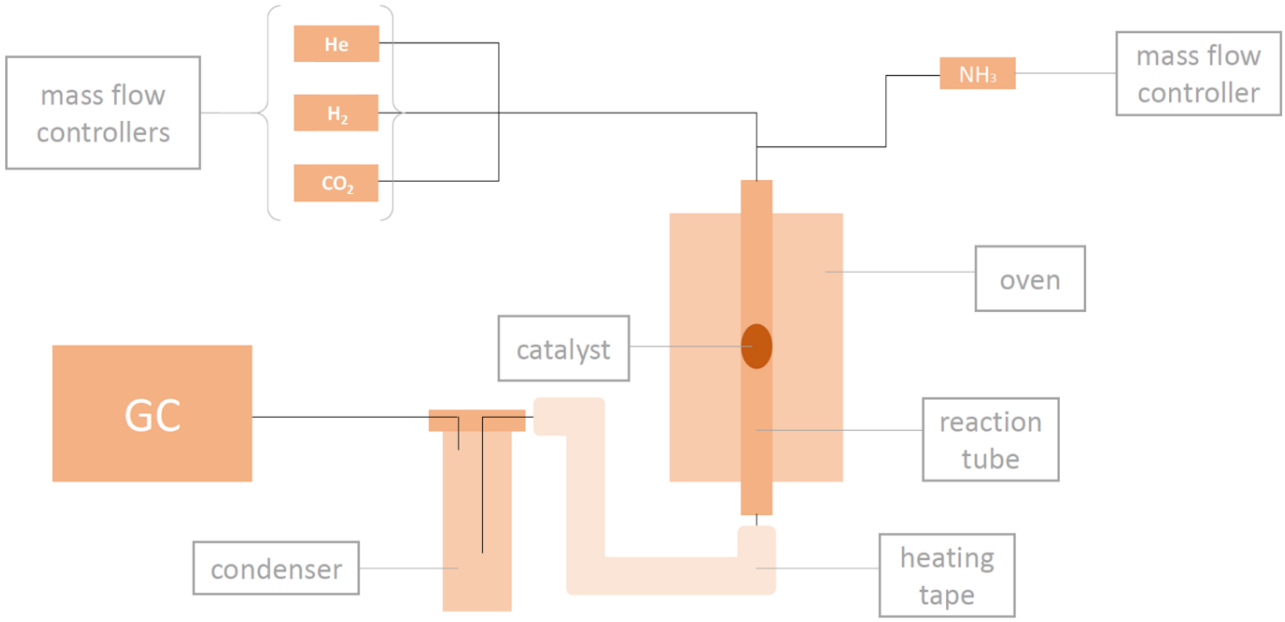


Fig. 2.12 Schematic illustration of the reactor set up for ammonia decomposition and ammonia methanation

2.2.1 Ammonia decomposition reactor

Ammonia decomposition was measured in a quartz-lined continuous flow reactor as described in **Fig. 2.12**. For a standard ammonia decomposition catalysis process, 50 mg of catalyst was packed in a quartz tube (4 mm i.d.) which was held vertically in the stainless steel fixed-bed flow reactor. Prior to the measurement, the catalyst was first pre-treated at 450 °C under 5% H_2/N_2 gas flow for 2 h. The gas was then switched to NH_3 feed and the catalyst bed was raised to a desired temperature accompanied by designated ammonia flow rate. All the catalytic performance measurements were measured at a range of temperature from 300 °C to 500 °C with weight hourly space velocity (WHSV) ranged from 6,000 to

72,000 mL g_{cat}^{-1} h^{-1} at ambient pressure. Once the catalytic rate has reached a steady state, the resultant gas compositions were analysed by an Agilent 7890A gas chromatography (GC) equipped with an 80/100 Porapak Q column and two thermal conductivity detectors (TCD).

2.2.2 Ammonia methanation reactor

For the ammonia methanation reaction, the same reactor setup used for ammonia decomposition was employed. Similarly, catalyst was loaded at the centre of a quartz tube with quartz wool sandwiched between both ends. The catalyst bed was heated to the desired temperature while a gas mixture of ammonia, carbon dioxide, and helium was introduced at various ratios. The reactor outlet was connected to a condenser, and the downstream stainless-steel lines were wrapped with heating tape to prevent condensation. The gas compositions were separated by an 80/100 Porapak Q column (for small molecules separation NH_3, N_2 etc.) and a HayeSep Q column (for hydrocarbon separation) followed by analysis using two thermal conductivity detectors (TCD). Helium served as the reference gas for quantifying the composition of the gaseous residue. Pure CO_2 methanation was also carried out over this set-up while having H_2 flowing instead of NH_3.

For a typical ammonia methanation reaction, 100 mg of catalyst was packed in to the micro-reactor, while maintaining the flow rates of CO_2 to NH_3 (3:8) constant. The catalytic performance measurements were measured at a range of temperature from 400 °C to 500 °C under ambient pressure. With pure CO_2 methanation, the ratio of CO_2 and H_2 is fixed at 1:4 unless otherwise stated

2.2.3 Performance calculation and kinetic analysis

As have previously mentioned, the gas composition of H_2, N_2, CO, CO_2, CH_4 and NH_3 were analysed by an online GC once a steady state of the reaction has reached. Based on the calibrated peak area to concentration ratio, the CO_2 conversion, CH_4 selectivity, CO selectivity and NH_3 conversion during reaction were calculated using the following equations:

$$\boldsymbol{X(NH_3) = 1 - (\frac{F_{NH_3,out}}{F_{NH_3,in}} \times 100\%)} \quad \textbf{(7)}$$

$$\boldsymbol{X(CO_2) = 1 - (\frac{F_{CO_2,out}}{F_{CO_2,in}} \times 100\%)} \quad \textbf{(8)}$$

$$\boldsymbol{S(CH_4) = \frac{F_{CH_4,out}}{F_{CO_2,in}} \times 100\%} \quad \textbf{(9)}$$

$$\boldsymbol{S(CO) = \frac{F_{CO,out}}{F_{CO_2,in}} \times 100\%} \quad \textbf{(10)}$$

Where F_x (with x referring to NH_3, CO_2, CH_4, or CO in inflow or outflow) represents the molar flow rates of the respective gaseous products and reactants. X(NH_3) and X(CO_2) denote the conversion of NH_3 and CO_2 respectively, while S(CH_4) and S(CO) refer to the selectivity of CH_4 and CO.

The apparent activation energy of the reaction was determined using the Arrhenius equation (see eq. 11 and 12). The temperature was varied between 300 °C to 400 °C (depending on catalyst) to ensure the rate of reaction is obtained under a kinetic controlled regime.

$$\boldsymbol{k = A \times e^{-\frac{E_a}{RT}}} \quad \textbf{(11)}$$

$$\boldsymbol{Ln(k) = -\frac{E_a}{R} \times \left(\frac{1}{T}\right) + Ln(A)} \quad \textbf{(12)}$$

To determine the reaction order, the partial pressures of NH_3, CO_2, and He (balance gas) were systematically varied while keeping the total flow rate and pressure constant. These

experiments were also performed under kinetically controlled conditions to ensure that the measured rates were far from thermodynamic equilibrium and unaffected by reverse reactions.

2.3 Catalyst synthesis

The following subsections provide detailed descriptions of the synthesis methods used to prepare the catalysts throughout this thesis. All catalyst synthesis procedures described in this work were repeated several times to ensure reproducibility of the preparation method and consistency of the material properties.

In addition to the catalysts described below, commercial Al_2O_3 (Sigma-Aldrich), SiO_2 (Sigma-Aldrich), ZSM-5 (Nankai University) and 5 wt.% Ru on carbon (Sigma-Aldrich) catalysts are used throughout this thesis.

Other supports like MgO, In_2O_3 and $BaAl_2O_4$ are provided by collaborators from the group. The synthesis of these metal oxide supports all follow a typical hydrothermal methods.[22–24]

2.3.1 Synthesis of CNU_x

Nitrogen doped carbon support was synthesized using a sol-gel method.[25,26] Typically, 1 g of chitosan (Sigma-Aldrich) was mixed with 0, 1:1, 1:3 and 1:5 ratios (0, 1, 3 and 5 g) of urea (Alfa Aesar). The mixture was dissolved in 40 mL of 5% acetic acid (Sigma-Aldrich) and subsequently dried at 80°C overnight. The desired nitrogen doped carbon powder (denoted as CNU_x x = Chitosan to Urea ratio) was synthesised by calcinating the precursor at 900°C for 2 h at a heating rate of 3 °C min^{-1} under N_2 atmosphere.

2.3.2 Synthesis of P-CNU$_x$

Controlled nitrogen doped carbon support with high content of edge site nitrogen (pyrrolic and pyridinic N) was prepared via a similar procedure. A mixture consisting of 1 g of chitosan (Sigma-Aldrich), 1 g of $MgCO_3$ (Sigma-Aldrich) and x g of urea (x = Chitosan to Urea ratio, Alfa Aesar) was dissolved in 40 mL of 5% acetic acid (Sigma-Aldrich). The solution was dried at 80°C overnight and subsequently calcined at 900°C for 2 h at a heating rate of 3 °C min^{-1} under N_2 atmosphere. The as-obtained carbon powder was immersed in 40 mL 0.5 M HCl (Fisher chemical) for 20 h, followed by washing with DI water until the pH value reached neutral. The final controlled nitrogen doped carbon support is denoted as P-CNU$_x$ where x is the chitosan to urea ratio.

2.3.3 Synthesis of CeO_2

Plain cerium oxide was synthesized using a soft-urea-glass method.[27,28] Typically, 3 g of cerium chloride (Fluorochem Ltd) was mixed with 3 g urea (Alfa Aesar) and stirred in 60 ml of ethanol (Alfa Aesar) for 2 h to form a colourless homogenous gel-like solution. The mixture was then dried at 80°C overnight to obtain a pink-red solid. Followed by calcinating at 800°C for 2 h with a heating rate of 5 °C min^{-1} in a tubular furnace under 30 ml min^{-1} air flow to produce CeO_2 support.

2.3.4 Synthesis of N-CeO_2

The nitrogen doped CeO_2 support were obtained by annealing the plain CeO_2 in 30 ml min^{-1} NH_3 flow for different temperatures (T = 500, 650, 800, 900 °C) and different duration (t = 2, 4, 6, 8, 10 h) at a constant heating rate of 5 °C min^{-1}. The final obtained nitrogen doped cerium oxide is denoted as N-CeO_2 (T-t) where T stands for the calcination temperature and t for the calcination time.

2.3.5 Metal impregnation

For carbon based materials, ruthenium was impregnated onto the support via a wetness impregnation method.[29] Typically, the carbon support was dispersed in a 0.1 M solution of ruthenium(III) chloride hydrate (Fluorochem Ltd), with the Ru-to-support weight ratio pre-calculated. The mixture was sonicated for 1h at 40 °C before drying at 80°C overnight, followed by reduction at 450 °C for 6 h at a heating rate of 5°C min^{-1} under 5% hydrogen/nitrogen atmosphere.

In Chapter 3, metal promoters were incorporated onto the support using an identical procedure. The catalyst was impregnated with a 0.1 M aqueous solution of the corresponding metal nitrate precursors (ie, $La(NO_3)_3$ (Lanthanum nitrate hexahydrate, Alfa Aesar); $Ce(NO_3)_3$ (Cerium nitrate hexahydrate, Alfa Aesar); KNO_3 (Potassium nitrate, Alfa Aesar); $LiNO_3$ (Lithium nitrate, Alfa Aesar) and $CsNO_3$ (Cesium nitrate, Alfa Aesar)). The mixture was sonicated for 1h at 40 °C before drying at 80°C overnight, followed by reduction at 450 °C for 6 h at a heating rate of 5 °C min^{-1} under 5% hydrogen/nitrogen atmosphere.

In Chapter 4 and 5, ruthenium was impregnated on the Ce-based supports using a modified wetness impregnation method to avoid direct interaction between water and the metal oxide.[30,31] In this case, the synthesized supports were wetness impregnated with 0.01 M of Tri-ruthenium dodeca-carbonyl in Tetrahydrofuran solution ($Ru_3(CO)_{12}$, Fisher Scientific UK Ltd; THF, Alfa Aesar) The mixture was gently stirred for 20 min until the solvent has evaporated. It is then dried at 80°C overnight, followed by reduction at 450 °C for 6 h at a heating rate of 5 °C min^{-1} under 5% hydrogen/nitrogen atmosphere. The same approach was applied for the preparation of Ru/Al_2O_3 and Ru/SiO_2 catalysts.

References

1. Holder, C. F. & Schaak, R. E. Tutorial on Powder X-ray Diffraction for Characterizing Nanoscale Materials. *ACS Nano* **13**, 7359–7365 (2019).
2. Hammond, C. The Basics of Crystallography and Diffraction. 4th edn, Oxford (2015)
3. Artioli, G. X-ray Diffraction (XRD). Springer Science+Business Media Dordrecht (2017)
4. Yoshida, A., Kaburagi, Y. & Hishiyama, Y. Scanning Electron Microscopy. *Mater. Sci. Eng. Carbon Charact.* 71–93 (2016)
5. Son, R. *et al.* Morphomics via next-generation electron microscopy. *J. Mol. Cell Biol.* **15**, (2023).
6. Bonnamy, S. & Oberlin, A. Transmission Electron Microscopy. *Mater. Sci. Eng. Carbon Charact.* 45–70 (2016)
7. Klein, N. D., Hurley, K. R., Feng, Z. V. & Haynes, C. L. Dark field transmission electron microscopy as a tool for identifying inorganic nanoparticles in biological matrices. *Anal. Chem.* **87**, 4356–4362 (2015).
8. Wang, M., Árnadóttir, L., Xu, Z. J. & Feng, Z. In Situ X-ray Absorption Spectroscopy Studies of Nanoscale Electrocatalysts. *Nano-Micro Lett.* **11**, (2019).
9. Extended X-ray absorption fine structure - Wikipedia. URL: https://en.wikipedia.org/wiki/Extended_X-ray_absorption_fine_structure.
10. Rehr, J. J. & Ankudinov, A. L. Progress in the theory and interpretation of XANES. *Coord. Chem. Rev.* **249**, 131–140 (2005).
11. Chantler, C. T., Bunker, G., Angelo, P. D. ' & Diaz-Moreno, S. X-ray absorption spectroscopy. *Nat. Rev. Methods Prim.* **4**, 1–25 (2024).
12. Foo, K. Y. & Hameed, B. H. Insights into the modeling of adsorption isotherm systems. *Chem. Eng. J.* **156**, 2–10 (2010).
13. Rodriguez-Reinoso, F., Martin-Martinez, J. M., Prado-Burguete, C. & McEnaney, B. A standard adsorption isotherm for the characterization of activated carbons. *J. Phys. Chem.* **91**, 515–6 (1987).
14. Gas Adsorption & Porosimetry Analyses at PTL - Particle Technology Labs. URL: https://particletechlabs.com/ptl-press/gas-adsorption-porosimetry-analyses-at-ptl/.
15. Ng, K. C., Burhan, M., Shahzad, M. W. & Ismail, A. Bin. A Universal Isotherm Model to Capture Adsorption Uptake and Energy Distribution of Porous Heterogeneous Surface. *Sci. Reports* **7**, 10634 (2017).
16. Chemisorption and Temperature Programmed Reactions (TPX) | Norlab. URL: https://www.norlab.com/library/overview-article/13201.
17. Colthup, N. B. Infrared Spectroscopy. *Encycl. Phys. Sci. Technol.* 793–816 (2003)
18. Beć, K. B., Grabska, J. & Huck, C. W. Physical principles of infrared spectroscopy. *Compr. Anal. Chem.* **98**, 1–43 (2022).
19. Muchaamba, F. & Stephan, R. A Comprehensive Methodology for Microbial Strain Typing Using Fourier-Transform Infrared Spectroscopy. *Methods Protoc.* **7**, 48 (2024).
20. Mass Spectrometry Explained: Principle, Steps & Uses. URL: https://microbenotes.com/mass-spectrometry-ms-principle-working-instrumentation-steps-applications/.
21. Inductively Coupled Plasma - ICP. URL: https://www.priyamstudycentre.com/2022/04/inductively-coupled-plasma.html.
22. Klubnuan, S., Amornpitoksuk, P. & Suwanboon, S. Structural, optical and photocatalytic properties of MgO/ZnO nanocomposites prepared by a hydrothermal method. *Mater. Sci. Semicond. Process.* **39**, 515–520 (2015).
23. Song, P. *et al.* Hydrothermal synthesis of porous In_2O_3 nanospheres with superior ethanol sensing properties. *Sensors Actuators B Chem.* **196**, 434–439 (2014).
24. Xiong, P. *et al.* Synthesis of core@shell catalysts guided by Tammann temperature. *Nat. Commun.* **15**, 420 (2024).
25. He, S. *et al.* Facile preparation of N-doped activated carbon produced from rice husk for CO_2 capture. *J. Colloid Interface Sci.* **582**, 90–101 (2021).
26. Chen, X., Oh, W. Da, Zhang, P. H., Webster, R. D. & Lim, T. T. Surface construction of nitrogen-

doped chitosan-derived carbon nanosheets with hierarchically porous structure for enhanced sulfacetamide degradation via peroxymonosulfate activation: Maneuverable porosity and active sites. *Chem. Eng. J.* **382**, 122908 (2020).

27. Tamizhdurai, P. *et al.* Environmentally friendly synthesis of CeO_2 nanoparticles for the catalytic oxidation of benzyl alcohol to benzaldehyde and selective detection of nitrite. *Sci. Reports* **7**, 46372 (2017).
28. Yuan, Y. *et al.* Zirconium nitride catalysts surpass platinum for oxygen reduction. *Nat. Mater.* **19**, 282–286 (2019).
29. Okal, J., Zawadzki, M., Kepiński, L., Krajczyk, L. & Tylus, W. The use of hydrogen chemisorption for the determination of Ru dispersion in Ru/γ-alumina catalysts. *Appl. Catal. A Gen.* **319**, 202–209 (2007).
30. Fang, H. *et al.* Dispersed surface Ru ensembles on MgO(111) for catalytic ammonia decomposition. *Nat. Commun.* **14**, 647 (2023).
31. Li, L. *et al.* Size sensitivity of supported Ru catalysts for ammonia synthesis: From nanoparticles to subnanometric clusters and atomic clusters. *Chem* **8**, 749–768 (2022).

Chapter 3 Edge site N on Nitrogen Doped Carbon for Efficient Ammonia Decomposition

This chapter is adapted from the work by Dongpei Ye, Kwan Chee Leung, Wentian Niu, Mengqi Duan, Jiasi Li, Ping-Luen Ho, Dorottya Szalay, Tai-Sing Wu, Yun-Liang Soo, Simson Wu and Shik Chi Edman Tsang published in iScience in 2024. Active nitrogen sites on nitrogen doped carbon for highly efficient associative ammonia decomposition iScience, ***27****, 8, 110571. The figures are reprinted with permission. Copyright 2024 Published by Elsevier.*

3.1 Introduction

Carbon-based materials have garnered significant attention due to their versatile properties and performance benefits in the field of heterogenous catalysis, including ammonia decomposition. They are highly favoured due to their ability to enhance reaction rates and control product selectivity. These materials full-fill many of the key criteria for an ideal support such as chemical inertness, thermal stability (particularly in the absence of molecular oxygen), mechanical strength, high surface area, and well-defined porosity.[1] Furthermore, the physicochemical properties of carbon materials can be readily tailored through surface functionalization or structural modifications, allowing for optimized metal-support interactions.[2] Their ease of synthesis, tunability, and widespread availability further contribute to their attractiveness for potential industrial-scale applications.[3] Given these advantages, carbon-based supports continue to be promising candidates in the design of next-generation catalysts for efficient and sustainable ammonia decomposition.

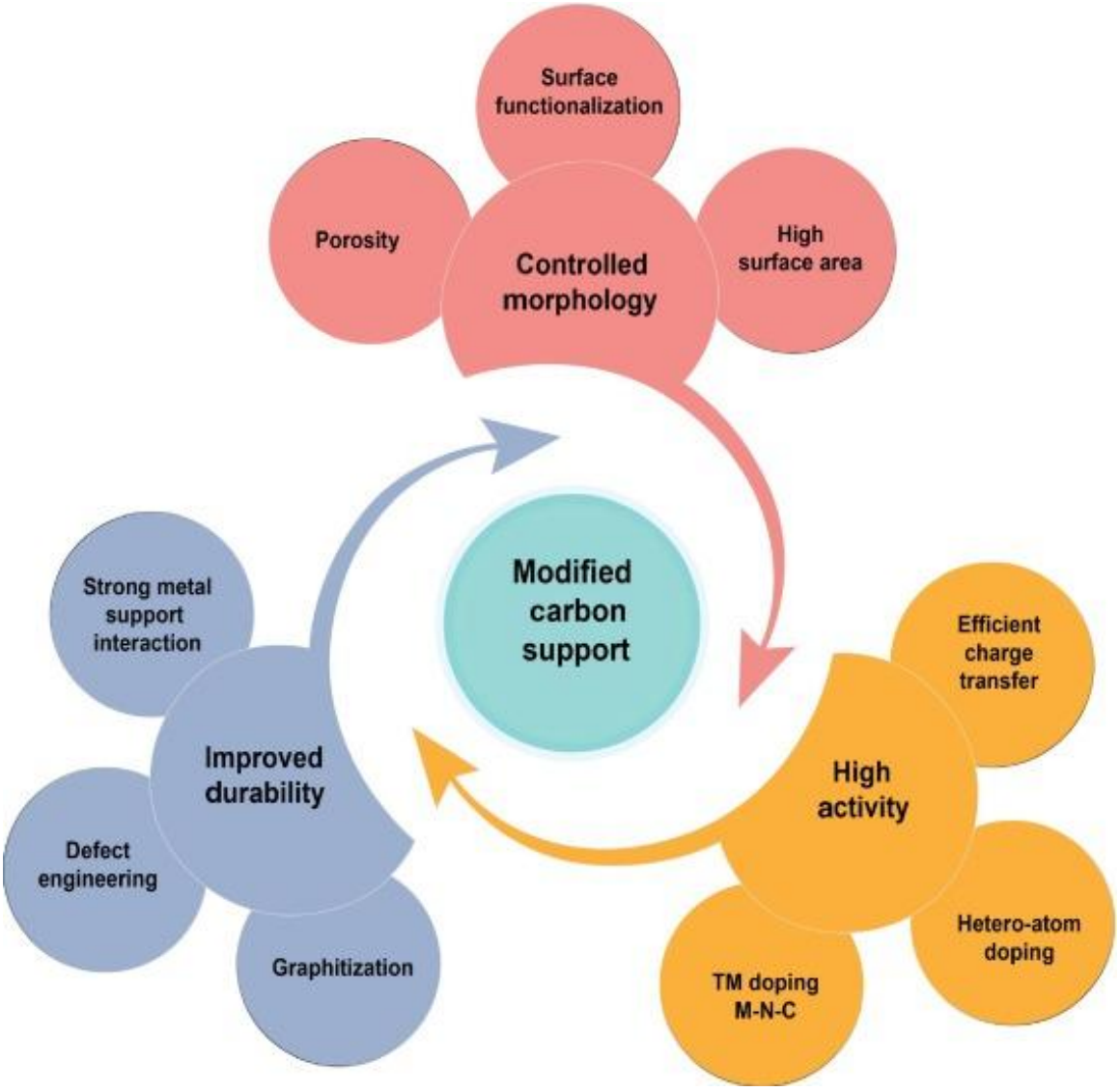


Fig. 3.1 Key parameters of modified carbon supports for heterogenous catalysis, Reprinted from reference[4].

Li *et al.* has been investigating on the effect of carbon structure towards the catalytic activity of ammonia decomposition. They found out that the catalytic activity over supported Ru catalysts is ranked as Ru/CNTs (carbon nanotubes) > Ru/CB-S (carbon black) > Ru/CB-C > Ru/CMK-3 ≈ Ru/AC. A stronger relationship is acknowledged between the graphitic structure of the carbon support nature for the catalytic activity of the carbon-supported catalyst compared to the pore structures and surface area of the carbon supports.[5] Further work by Bell *et al.* proposed that the graphitisation degree

is directly related to the electron donating effect from the support to the active site, which is crucial to ammonia decomposition activity.[6] Yin *et al.* reported a well acknowledged Ru-K-CNT catalyst which showed excellent catalytic performances for the generation of CO_2 free H_2 generation.[7] In depth characterisation revealed that such high activity is mainly attributed to the high dispersion of Ru particles, and to the high graphitization and high purity of the CNTs material. Kinetic studied suggested that the rate determining step lies on the desorption step of N_2, which the activation barrier is significantly lowered by the modification with KOH.[8]

As previously discussed, the electron-donating effect is a key factor in promoting the activity of metal sites in catalysts for ammonia decomposition. In this context, nitrogen doping has emerged as a promising strategy for modifying carbon-based supports. Nitrogen, located one period after carbon in the periodic table, possesses an additional 2p electron, which allows it to introduce localized electron-rich sites when incorporated into a carbon matrix. Based on this, various modified nitrogen doped carbon supports have been studied, including N-CNTs, N- ordered mesoporous carbon, N- nanofibers (N-CNFs) etc.[9–12] These nitrogen functionalities can strengthen metal–support interactions by facilitating charge transfer from the support to the metal nanoparticles (NPs), thereby leading to better metal dispersion, and ultimately enhancing catalytic activity.

Apart from the electron donating effect, incorporation nitrogen in a facile manner may also introduce new reaction mechanisms as discussed in the introduction section. Traditionally, ammonia cracking over monometallic catalysts follows a dissociative process where the N-H bonds of adsorbed ammonia molecules are consecutively dehydrogenated leaving bare nitrogen on the catalytic surface.[13] The subsequent nitrogen triple bond formation and N_2 desorption faces high activation barrier and limits

the rate of the overall reaction.[14] Furthermore, the Brønsted−Evans−Polanyi (BEP) scaling correlation inhibits the reaction as stronger NH_x adsorption energy favours N-H bond dissociation, but is always accompanied by a less thermodynamic favourable N_2 desorption.[15] Thus, if nitrogen doping can open up to a new Mars–van Krevelen (MvK) mechanism, where nitrogen from NH_3 is initially bound to the atomic nitrogen site of the catalyst to form a *N-N-H_2 intermediate. Dinitrogen bond is then formed stepwise and accompanied by the dehydrogenation of the N-H bonds of ammonia.[16] The mix matched reaction pathway leads to a lower activation energy and better catalytic performance at milder reaction condition.

Although nitrogen-doped carbon materials have been widely studied as catalyst supports, the precise nature of the metal–support interaction, particularly the influence of nitrogen content on metal sites, remains insufficiently understood.[17,18] Furthermore, the role of different nitrogen configurations, such as graphitic, pyrrolic, and pyridinic nitrogen, in governing catalytic behaviour during ammonia decomposition is still a subject of ongoing investigation. Each nitrogen species can interact differently with the metal active sites, potentially altering the electronic environment, binding strength, and activation pathways. Not to mention the associative mechanism route introduced, as it is not yet known whether N_2 is formed between weakly bound surface NH_x from pure gaseous ammonia or somehow involving mobile nitrogen from catalyst support as in redox manner. Clarifying these effects is essential for the rational design of N-doped carbon supports with optimized metal-support synergy for enhanced catalytic performance in ammonia decomposition.

To address this gap, we employed a synthesis strategy that enables systematic tuning of nitrogen content and environment in the carbon support. In our recipe, nitrogen doped carbon support is synthesized by calcinating chitosan with urea. Chitosan is a

polymer containing β-linked D-glucosamine and N-acetyl-D-glucosamine which is extracted from the outer skeleton of crab, lobster and shrimp.[19,20] Owing to its nitrogen-rich composition and facile processability, chitosan serves as an ideal carbon precursor for generating nitrogen-doped carbon supports. Urea has an extremely high N content of 46 wt.%, thus, acts as a nitrogen source and can be used to alter the nitrogen content on the catalyst support. The resulting materials are denoted as CNU_x, where x represents the chitosan-to-urea ratio. To gain further control over the nitrogen configuration and thereby investigating on the effect of nitrogen towards the catalysis reaction, the synthetic procedure is modified by addition of $MgCO_3$. Upon calcination, $MgCO_3$ decomposes and releases carbon dioxide while chitosan was carbonized in the presence of urea to yield nitrogen doped carbon. Leading to MgO species wrapped by more exposed edge site nitrogen (namely pyrrolic and pyridinic) doped carbon support. Final acid rinsing was carried out to remove residual MgO and yielding the final material, denoted as P-CNU_x. A schematic illustration of the synthetic process is shown on **Fig. 3.1**.

In this chapter, a nitrogen doped carbon material support with high nitrogen content has been synthesized and presented. Our catalyst, Cs-Ru/P-CNU_3 shows a superior catalytic performance towards ammonia decomposition with an exceptional low activation barrier of 39 kJ mol^{-1}. The strong interactions between edge site nitrogen species on the support (pyrrolic and pyridinic N) and Ru metal sites are studied using a range of characteristic techniques. This work could provide insights on future catalysts design for the heterogeneous activation of ammonia and other potential processes.

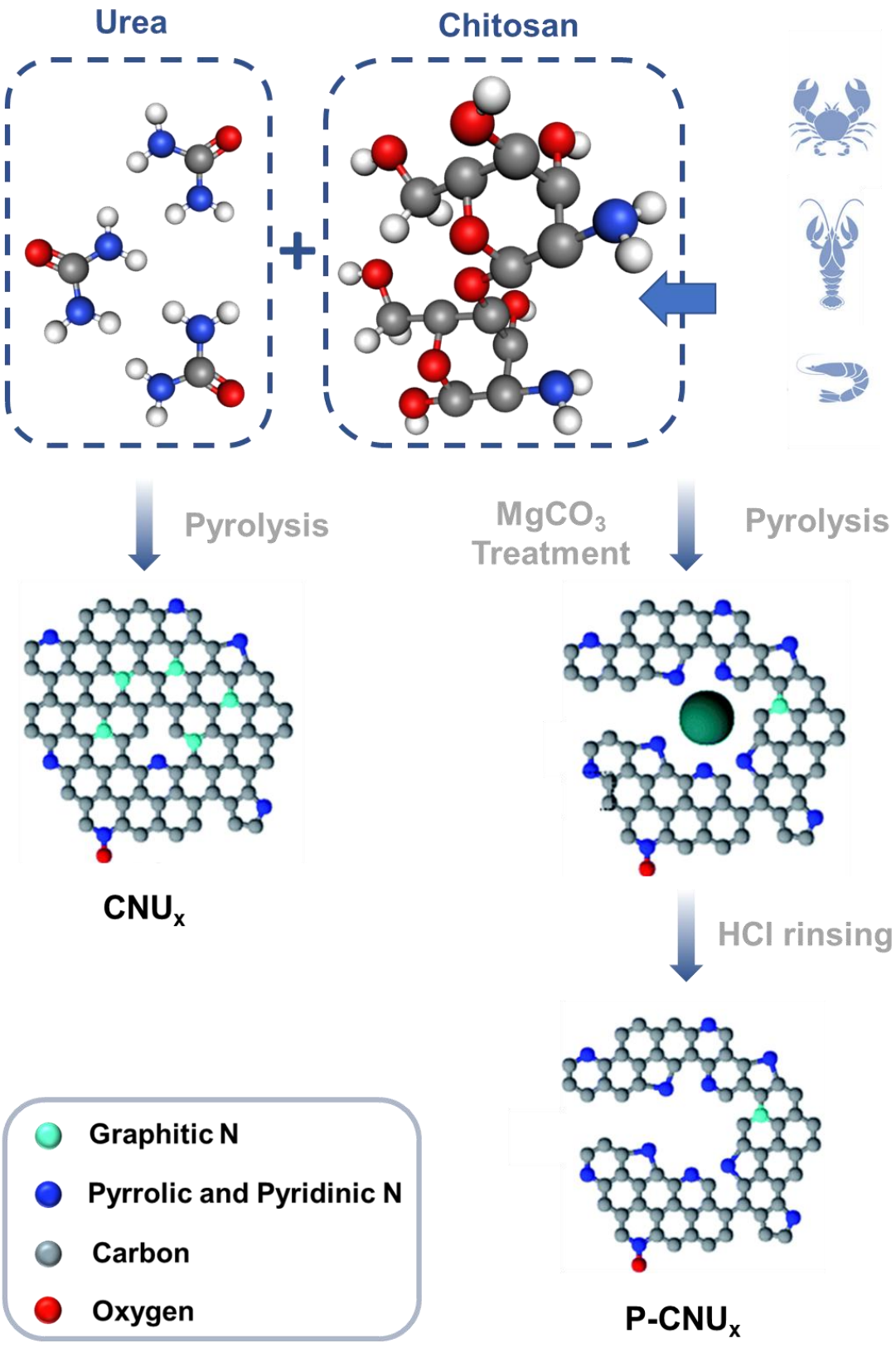


Fig. 3.1 Schematic illustration of the synthetic process of CNU_x and P-CNU_x catalyst support.

3.2 Result and discussion

This section presents the key findings and interprets them in the context of nitrogen effect on nitrogen doped carbon catalysts towards ammonia decomposition.

3.2.1 Effect of nitrogen content

To investigate the effect of nitrogen content towards ammonia decomposition, nitrogen doped carbon with different ratio of chitosan to urea was synthesized and evaluated. As illustrated in **Table 1**, with increasing content of urea in our recipe during the synthesis, the N content of the final carbons indeed increases (4.95, 6.45, 8.95 and 11.95% for CNU_0, CNU_1, CNU_3 and CNU_5, respectively). This is a clear indication of successful doping of nitrogen into the support. However, the distribution of different nitrogen configuration on the support remained relatively constant, with graphitic-N being the major N species.

Table 1 Atomic percentage of O, C and N on the presented material, the relative content of graphitic nitrogen, pyrrolic nitrogen, pyridinic nitrogen and nitrogen oxide species in the material derived from XPS analysis.

Sample	**O (at.%) ±2.4%**	**C (at.%) ±1.4%**	**N (at.%) ±1.8%**	**Specific N configuration**			
				Graphitic (400.8 eV)	**Pyrrolic (399.6 eV)**	**Pyridinic (398.2 eV)**	**N-O (403.1 eV)**
CNU_0	8.6	86.5	5.0	44.0	16.1	30.4	9.5
CNU_1	6.8	86.7	6.5	47.5	8.2	35.0	9.3
CNU_3	5.4	86.1	8.5	48.0	8.2	34.6	9.2
CNU_5	4.9	84.7	10.5	45.7	8.3	36.7	9.3

Note: The measurements were taken for a sample mixture consisting of three different batches; The error bar is calculated based on the deviation of the raw spectrum and the fitted spectrum.

Furthermore, increase in chitosan to urea ration further result an increase in the overall surface area (**Table 2**). A positive progressive correlation has been found between the nitrogen content and the specific surface area/porosity, showing a better exfoliation and larger porous level when more urea has been used during the synthesis.

Table 2 BET result on the specific surface area and pore volume of the analogue sample.

Sample	Specific surface area ($m^2 g^{-1}$)	Pore Volume ($cm^3 g^{-1}$)
CNU_0	7.33	0.0019
CNU_1	41.50	0.1703
CNU_3	120.94	0.1730
CNU_5	217.50	0.3030

To examine the activity relation towards the nitrogen content and surface area, all supports were first impregnated with 5 wt.% Ru and tested in the fixed-bed flow reactor setup described in ***Chapter 2***. As illustrated in **Fig. 3.2a**, an increase in both nitrogen content and surface area generally enhances catalytic performance, as evidenced by the significant rise in the increasing ammonia decomposition activity. The highest conversion was observed at 64.7% for 5 wt.% Ru/CNU_3. However, further increasing the nitrogen content and surface area, as in the case of 5 wt.% Ru/CNU_5, resulted in a reduced conversion of approximately 45%. Among the nitrogen-doped carbon supports, 5 wt.% Ru/CNU_3 demonstrated the highest activity. Consequently, a series of CNU_3 based catalysts with varying Ru loadings were synthesized and tested. A similar trend was observed where higher Ru loading leads to higher activity. Both 5 wt.% and 10 wt.% loaded CNU_3 achieved 99.9% conversion at 550 °C, while conversion for all samples, not surprisingly, decrease at lower temperatures. It is

however noted, that without Ru, no conversion towards ammonia decomposition was observed, indicating that the activity of the catalyst predominantly originates from the Ru metal.

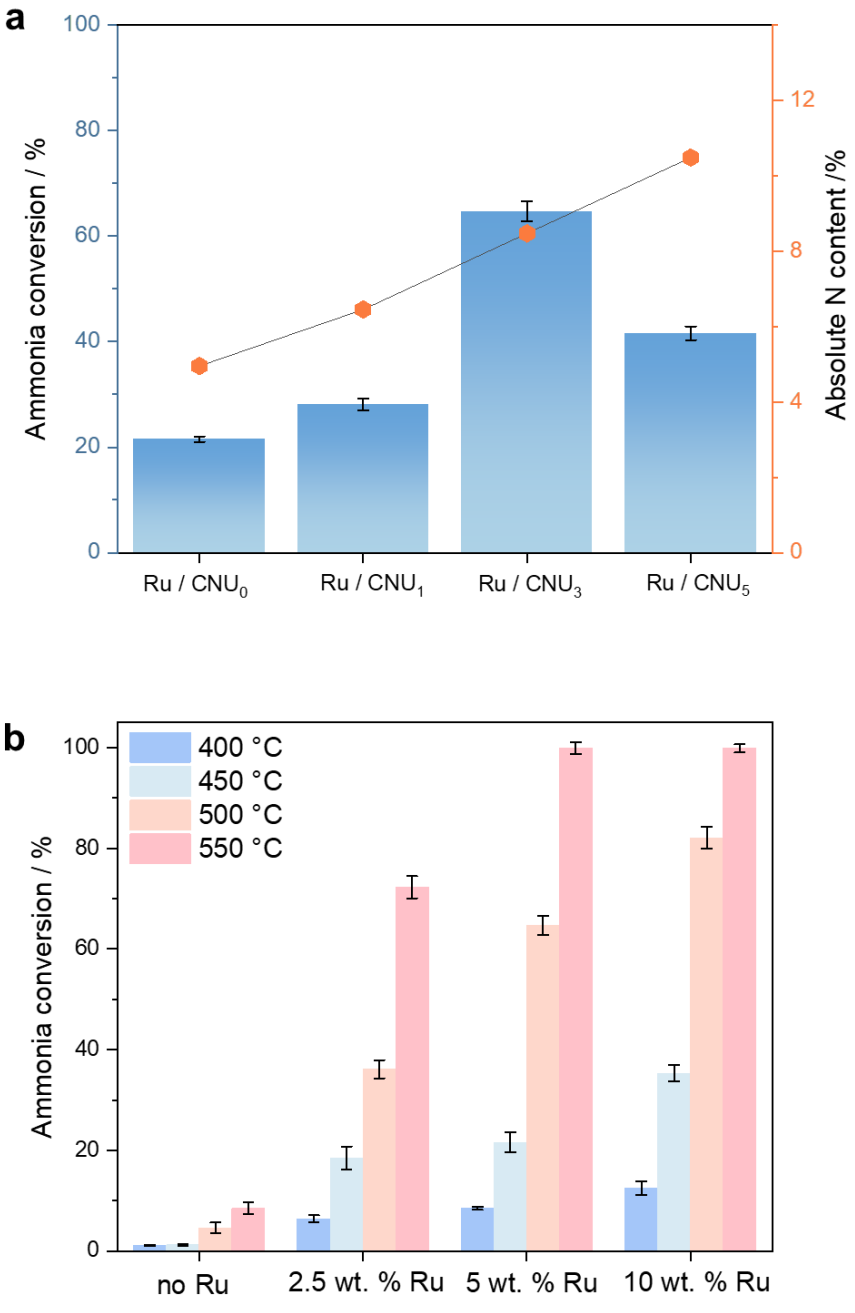


Fig. 3.2 Catalytic activity measurement of the analogue Ru-based catalysts. a. 5 wt.% Ru on nitrogen doped carbon support synthesised based on different chitosan to urea ratio, the test was carried out at 500 °C and WHSV = 30,000 ml g_{cat}^{-1} h^{-1}. b. Different Ru loading on CNU_3 support at various reaction temperature, test carried out at WHSV = 30,000 ml g_{cat}^{-1} h^{-1}.

In the case of a N-doped carbon support impregnated with Ru NPs. When nitrogen atoms substitute for carbon atoms in the graphite lattice, they contribute an additional electron to the delocalized π-electron system. This modification enhances the electron density within the carbon matrix, thereby increasing the electron-donating ability of the support material. As a result, the basicity of the catalyst surface is improved, which is particularly beneficial for ammonia decomposition.[10] The enhanced electron-donating capacity of the N-doped support promotes charge transfer from the support to the Ru NPs. This would lead to an increase in the electron density on the Ru surface. Consequently, resulting in an improved catalytic activity as the electron rich Ru NPs facilitates better back-donation to break the N–H bonds during the decomposition process.[21] However, on the other hand, excessive nitrogen sites with Ru particularly in CNU_5 is not desirable in catalysis. Direct interaction between Ru and the excess N dopants will lead to formation of strong Ru-N interaction, which withdraw electron density from Ru NPs locally.[9,22] This local electron depletion weakens the metal's ability to participate in back-donation with surface-bound nitrogen species, thereby reducing the overall efficiency of the catalytic process. Additionally, excess nitrogen doping will decrease the degree of graphitization, leading to a more disordered carbon structure and a compromised π-conjugated system. This structural degradation reduces both the electrical conductivity and the robustness of metal–support interactions, further diminishing catalytic performance.[23] Thus, resulting in a worse activity as exhibited by 5 wt.% Ru/CNU_5 catalyst.

It is worth noting that increasing surface area would commonly lead to a better metal dispersion, more active sites and thus a better catalytic activity.[24] However, for the 5 wt.% Ru/CNU_5 catalyst, even that it is demonstrated to be the largest surface area

among others, it gives a lower conversion compared to 5 wt.% Ru/CNU_3. This apparent deviation suggests that surface area is not the major governing factor in determining catalytic activity, particularly when other competing effects are present. It is suggested that the higher nitrogen content in CNU_5 may exceed the critical level leading to a negative impact as discussed above. Moreover, increase in nitrogen dopant may result in stronger anchoring effect of Ru NPs leading to a reduced promotion effect from metal dispersion, which typically gives rise to the better activity from larger surface area.[25] Consequently, the expected positive influence of higher surface area is overshadowed by excess nitrogen, contributing to the 'volcano' shaped activity, as shown on **Fig. 3.2a**.

A positive correlation is found between larger Ru loading and ammonia decomposition activity on CNU_3 support (**Fig. 3.2b**). Although 10 wt.% Ru loading on the nitrogen doped carbon support illustrates a higher ammonia conversion rate compared to 5 wt.% Ru loading. Further catalytic experiments were still performed based on 5 wt.% metal loading as the catalytic activity is already comparable to most of our conventional catalysts tested. Additionally, Ru is an expensive ingredient so maintaining high activity at lower metal loading is more desirable.

3.2.2 Effect of metal promotors

To investigate the role of promoters in enhancing catalytic performance, various metal promoters were co-impregnated onto the 5 wt.% Ru/CNU_3 catalyst at a fixed Ru-to-promoter molar ratio of 1:1. As shown in **Fig. 3.3**, the general order of catalytic activity ≤450°C follows the order Ru/Cs CNU_3 > Ru/K CNU_3 > Ru/Li CNU_3 > Ru/La CNU_3 > Ru/Ce CNU_3. This trend aligns well with the increasing electron-donating capability of

the promoters, indicating that electron-rich environments enhance the activity of Ru by facilitating NH_3 activation through more efficient electron back-donation.

However, it is interesting to note that an unexpected activity boost of the catalysts at highest temperature appears. Specifically, the Ru/La CNU_3 and Ru/Ce CNU_3 catalysts exhibit a surprising increase in conversion, deviating from their relatively poor performance at lower temperatures. At low temperature, the rate determine step over Ru on carbon support is the desorption of N_2, however, at higher temperatures, this step shifts to the dissociation of the N-H bond from ammonia.[26] In this contest, H would play a more vital role in the rate equation. Lanthanide elements generally have low adsorption energy of hydrogen, which during ammonia decomposition, would facilitate H transfer and enhance the H spillover effect.[27–29] This will lead to boost in catalytic activity at higher reaction temperature as observed.

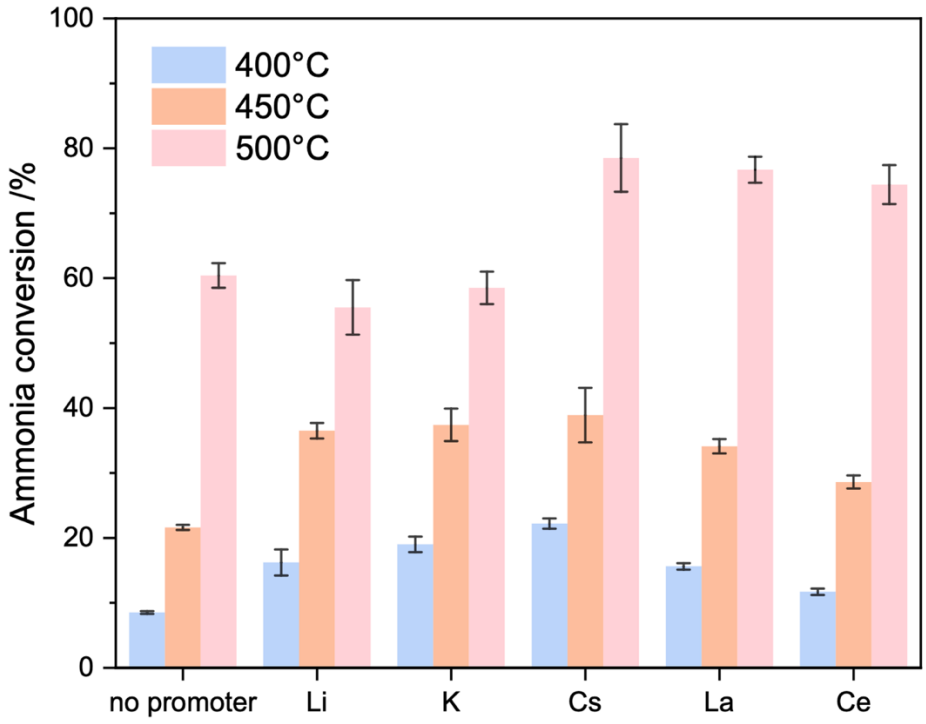


Fig. 3.3 Ammonia decomposition conversion on 5 wt.% Ru/CNU_3 co-impregnated with various promoters. Catalytic test carried out at WHSV = 30,000 ml g_{cat}^{-1} h^{-1}.

Nonetheless, Ru/Cs CNU_3 sample shows the best activity throughout the temperature range. It has been reported that incorporation of alkali metal can decrease the nitrogen desorption energy and hence increases the overall rate of reaction at milder operation condition when N_2 desorption is the rate determining step.[30] Electronic promoters are capable of increasing the electron density of the active metal site, especially for Ru based catalysts.[31–33] Thus, in the case of Ru/Cs CNU_3, the combination of high electron-donating capacity from Cs with the π-conjugated, nitrogen-enriched carbon structure appears to provide an optimal environment for maximizing Ru activity leading to superior ammonia decomposition rate.

3.2.3 Effect of edge site nitrogen configuration control

Since Ru/CNU_3 showed the best activity among other Ru/CNU_x catalysts, nitrogen configuration control was further conducted based on this recipe to reveal the effect of nitrogen configuration towards ammonia decomposition. The nitrogen doped carbon supports CNU_3 and P-CNU_3 are firstly analysed and compared using various characterisation technique.

To start off with, the organic functional group are detected using Fourier transform infrared spectroscopy (FTIR). As shown in **Fig. 3.4a**, distinct peaks are observed at 2850, 2920 and 2960 cm^{-1} which are ascribed to symmetric stretching vibration of C–H bond. The remaining peaks lie within the range of 1300-1700 cm^{-1}, which are mainly accounted towards C–H bending (at 1425 and 1373 cm^{-1}) and the stretching modes of C-N heterocycles in the nitrogen doped carbon (at 1545 and 1649 cm^{-1}).[34,35] The spectrums for CNU_3 and P-CNU_3 are similar with the major peaks ascribed to the C-H and the C-N bonds as described above. This is in agreement with the synthetic

strategy proposed as only the nitrogen configuration is altered, no distinct functional group is introduced.

The structural property of the synthesized carbon supports was examined using X-ray diffraction (XRD). For both supports, two broad characteristic peaks are observed at around 25.8° and 44.0° accounting to the (002) and (100) planes of hexagonal graphite structures on the amorphous carbon nitrogen layers (**Fig. 3.4b**).[36] XRD analysis also served as a qualitative tool to confirm the successful removal of residual inorganic components like MgO and $MgCO_3$ on P-CNU_3 following acid washing. MgO is a crystalline material and even trace amount would display diffraction peaks on XRD. However, as shown, no detectable peaks were observed at 2θ = 36.9°, 42.9°, 62.3°, or 78.6°, which would correspond to the (111), (200), (220), and (222) reflections of crystalline MgO.[37] The absence of these peaks indicates the effective elimination of MgO and unreacted $MgCO_3$ from the final product.

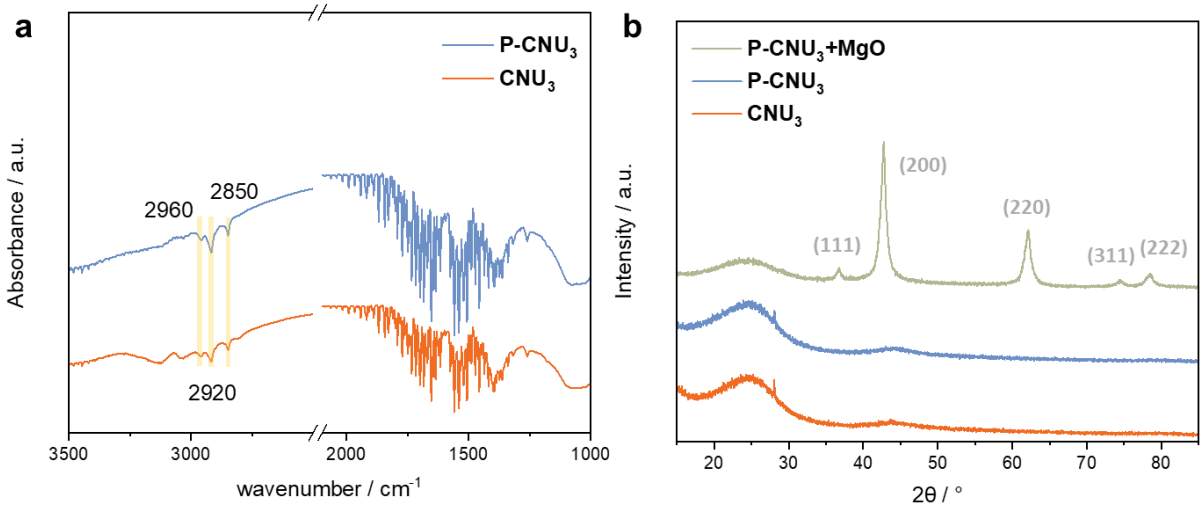


Fig. 3.4 Structural characterisation of the analogue support a. FTIR of CNU_3 and P-CNU_3 b. XRD spectrum of the CNU_3, P-CNU_3 and P-CNU_3 before acid rising, which the distinct peaks are attributed to the MgO phase.

The morphology of the support was revealed by scanning electron microscopy (SEM) and the surface texture properties were evaluated by Brunauer−Emmett−Teller (BET) surface area analysis to better understanding the impact on the nitrogen doped carbon supports upon $MgCO_3$ treatments. As shown in **Fig. 3.5a-d**, the untreated CNU_3 sample exhibits as a dense rigid block with a large aggregated particle size of up to 100 μm. The surface appears relatively smooth and non-porous, suggesting limited textural development during calcination. On the other hand, P-CNU_3 shows a fluffier and sponge-like structure. The carbon layers appear loosely packed, and the particle size is notably smaller. Moreover, the presence of well-developed macropores and mesopores is clearly evident in the P-CNU_3 sample.

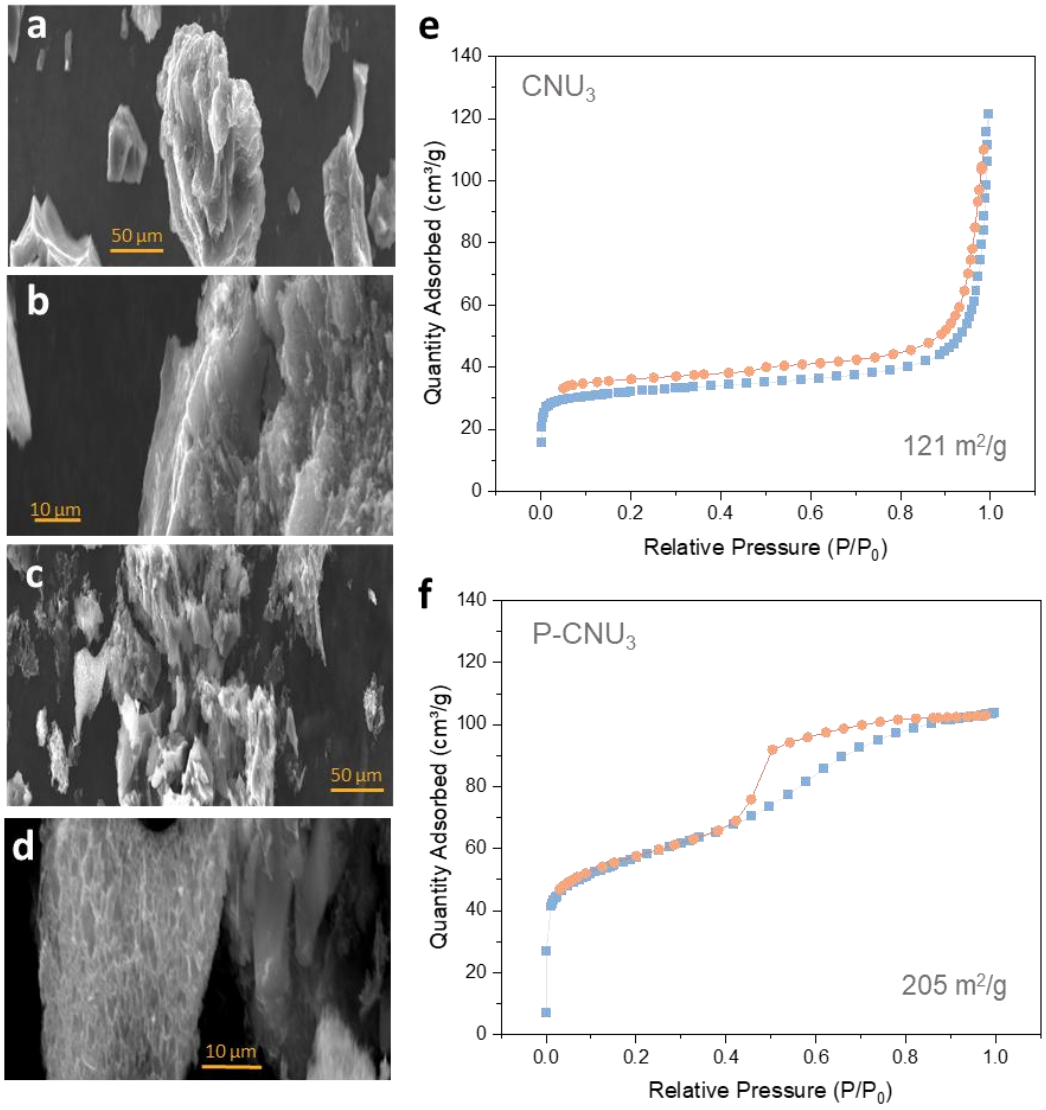


Fig 3.5 Morphology and surface properties of the analogue nitrogen doped carbon support. a-b. SEM imaging of CNU_3 c-d. SEM imaging of P-CNU_3 e-f. N_2 adsorption desorption diagram of the analogue supports from BET measurements.

This feature was confirmed by the BET results. From the nitrogen adsorption desorption diagram, a clear change in the BET isotherm is noted. Specifically, the CNU_3 support shows a hysteresis loop with an II type isotherm while a IV type isotherm for P-CNU_3 support, indicating the presence of distinct meso-pores (**Fig. 3.5e-f**).[38] The additional porous structures lead to spectacular increase in specific surface area from

121 $m^2 g^{-1}$ of CNU_3 to 205 $m^2 g^{-1}$ for P-CNU_3 which is in alignment with the results by SEM discussed above.

Table 3 Atomic percentage of O, C and N on the presented material, the relative content of graphitic nitrogen, pyrrolic nitrogen, pyridinic nitrogen and nitrogen oxide species before and after $MgCO_3$ treatment.

Sample	**O (at.%) ±2.4%**	**C (at.%) ±1.4%**	**N (at.%) ±1.8%**	**Specific N configuration**			
				Graphitic (400.8 eV)	**Pyrrolic (399.6 eV)**	**Pyridinic (398.2 eV)**	**N-O (403.1 eV)**
CNU_3	5.4	86.1	8.5	48.0	8.2	34.6	9.2
P-CNU_3	6.7	84.6	8.8	18.7	25.3	52.3	3.8

To gain insight on the nitrogen configurations present in the synthesized carbon supports, high-resolution N 1s X-ray photoelectron spectroscopy (XPS) was carried out (**Fig. 3.6a-b**). The final spectra of CNU_3 support is deconvoluted into 4 different peaks located at 398.2, 399.6, 400.8 and 403.1 eV, which are assigned to pyridinic-N, pyrrolic-N, graphitic-N (quaternary) and N-oxide (small quantity) species respectively.[39] Among these, graphitic nitrogen dominates the nitrogen environment, accounting for 48.04% of the total nitrogen content, followed by pyridinic-N (34.56%), pyrrolic-N (8.21%), and a small fraction of N-oxide (**Table 3**). Interestingly, a clear shift in the N configuration on the catalyst support has been noted when it was treated with $MgCO_3$. In the P-CNU3 sample, the proportion of graphitic-N decreases markedly from 48.04% to 18.72%. This decrease is accompanied by notable increases in pyridinic-N (from 34.56% to 52.25%) and pyrrolic-N (from 8.21% to 25.28%), indicating that the $MgCO_3$ modified synthesis alters the nitrogen bonding environment. This transformation suggests that nitrogen atoms previously integrated within graphitic

domains may become more exposed and converted into edge-type configurations such as pyridinic and pyrrolic nitrogen. These edge-located nitrogen species are known to interact more strongly with metal particles and may serve as active sites, potentially enhancing catalytic activity in ammonia decomposition, as discussed in a later section.

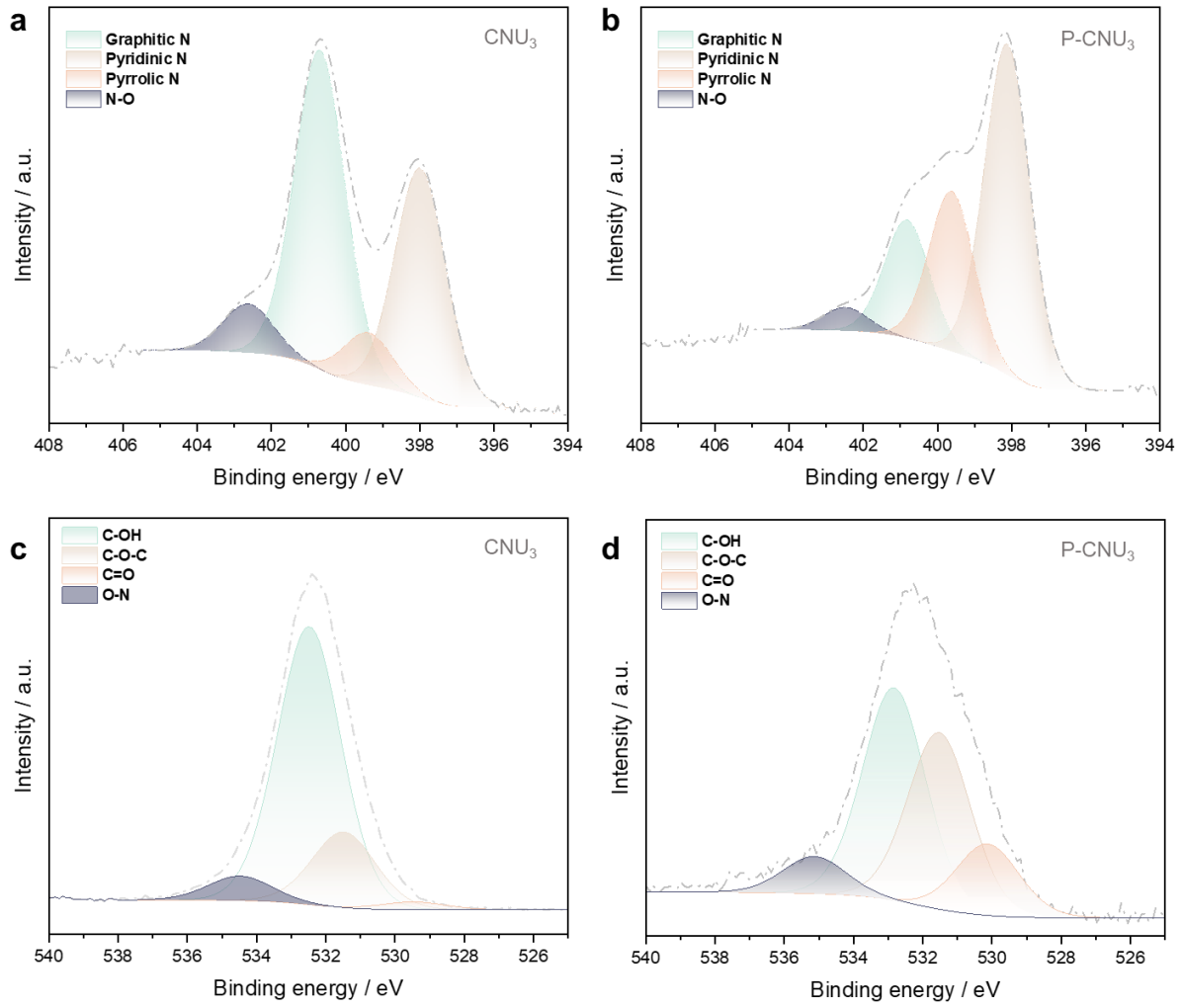


Fig. 3.6 XPS spectrum of the analogue nitrogen doped carbon material. a. N 1s spectrum of CNU_3 b. N 1s spectrum of P-CNU_3 c. O 1s spectrum of CNU_3 d. O 1s spectrum of P-CNU_3.

Additionally, high-resolution O 1s XPS was performed and the spectra for both supports were also deconvoluted into 4 peaks, which corresponds to C=O at 531.2 eV, C−O−C at 532.6 eV, C−OH at 533.9 eV and O-N at 536.2 eV respectively (**Fig. 3.6c-**

d).[40] The total oxygen content remains low and relatively constant, suggesting that oxygen-containing groups are not the primary contributors to catalytic performance in ammonia decomposition.

Although bulk structural analysis based on XRD suggests that both CNU_3 and P-CNU_3 share similar graphitic features, the addition of $MgCO_3$ during synthesis induces distinct morphological and chemical differences, particularly in pore formation and nitrogen speciation. During the preparation process, a gel-like matrix is formed by mixing chitosan and urea in an acetic acid medium. When $MgCO_3$ is introduced into this acidic environment, it partially reacts with acetic acid, releasing carbon dioxide and hydrogen. The localized generation of gas within the gel creates pore templates in the precursor structure. Under further calcination, unreacted $MgCO_3$ would decompose into MgO. This reaction is accompanied with the release of carbon dioxide, which further reacts with adjacent carbon/oxygen atoms to form CO.[41] Physically, this effect enlarges the existing pores and creates new pores. From the chemical point of view, it generates structural defect sites during the pyrolysis process. Increased edge exposure therefore favours the stabilization of edge-type nitrogen functionalities, namely pyridinic and pyrrolic nitrogen, which are typically located at defect sites and graphene sheet terminations. Thus, it explains the increase in pyrrolic and pyridinic nitrogen content at the expense of graphitic nitrogen as the formation of these two types of nitrogen are favoured.

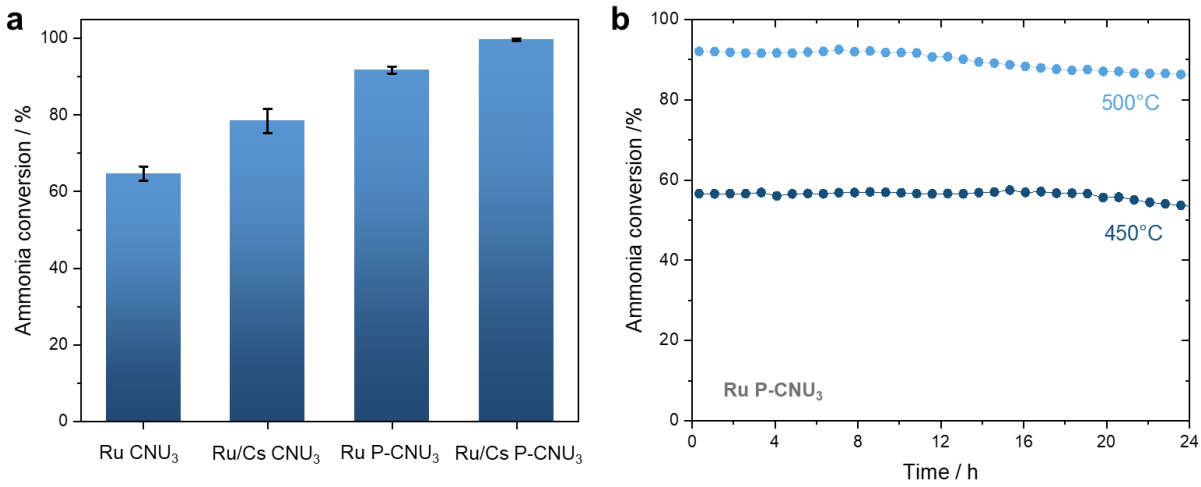


Fig. 3.7 Ammonia decomposition activity measurements, performed at WHSV = 30,000 ml g_{cat}^{-1} h^{-1}. a. Activity of the analogue catalyst measured at 500 °C. b. Stability test of Ru P-CNU_3 catalyst at different temperatures over 24 h.

Further catalytic evaluation revealed a remarkable enhancement in ammonia decomposition performance for nitrogen-doped carbon catalysts enriched with edge-site nitrogen configurations. Specifically, at 500 °C and WHSV=30,000 mL g_{cat}^{-1} h^{-1}, the conversion of 5 wt.% Ru/CNU_3 increased from 64.7% to 91.2% for 5 wt.% Ru/P-CNU_3. Under the same condition Cs promoted Ru/Cs P-CNU_3 catalyst achieved near-complete conversion (99.7%), approaching the thermodynamic limit, yielding an exceptional hydrogen production rate of 31.3 mmol min^{-1} g_{cat}^{-1}. As seen from the **Table 4**, the specific activity of our $MgCO_3$ modified nitrogen doped carbon sample out-performs most of the state-of-the-art carbon based catalysts such as Ru/carbon nano-fibre (Ru/CNFs), Ru/carbon nano-tubes (Ru/CNTs) and Ru/AC.[7,42,43] The 5 wt.% Ru P-CNU3 catalyst was subjected to continuous operation in a flow reactor for 24 h to access long term stability. As shown in **Fig. 3.7b**, no significant decline in NH_3 conversion was observed, indicating excellent stability of both the Ru active sites and

the nitrogen-doped carbon support throughout the catalytic process. Making the catalyst a promising candidate for future CO_2 free hydrogen delivery using NH_3.

Table 4 Catalytic performance of different carbon-based catalysts for NH_3 decomposition.

Catalysts	Metal (wt %)*	T (°C)	WHSV (NH_3 mL g_{cat}^{-1} h^{-1})	Conv. (%)	E_a (kJ mol^{-1})	Reference
Ru CNTs	5	500	60000	ca. 43	71.4	[32]
Ru NOMC	5	450	6000	84.7	n.d.	[12]
Ru N-carbon	5	450	6000	ca. 80	n.d.	[33]
Ru N-CNTs	7	400	6000	48.0	85.3	[34]
Ru Graphitic Carbon	5	550	30000	95.0	n.d.	[5]
Fe-BTC@400	34.7	500	6000	73.8	74.9	[44]
Fe CNFs-mica	3.5	550	6500	92.0	93.5	[45]
CoO_x@C-700-A	18.7	500	15000	55.0	n.d.	[46]
Ru-$ACX_{5\,h}$	1.38	450	2000	95.8	76.1	[47]
Ru CNU_3	4.6	500	30000	64.7	81.3	This work
Ru/Cs CNU_3	4.6	500	30000	79.8	63.8	This work
Ru P-CNU_3	4.6	500	30000	91.2	43.0	This work
Ru/Cs P-CNU_3	4.6	500	30000	99.7	38.8	This work

*Ru metal loading obtained by Inductively coupled plasma mass spectrometry (ICP-MS)

3.2.4 Mechanistic understanding

To further explore the underlying fundamental effects of nitrogen doping, especially the influence of different nitrogen configurations on catalytic activity, Ru P-CNU_3 was particularly synthesised and compared with Ru CNU_3 and commercial Ru carbon catalysts.

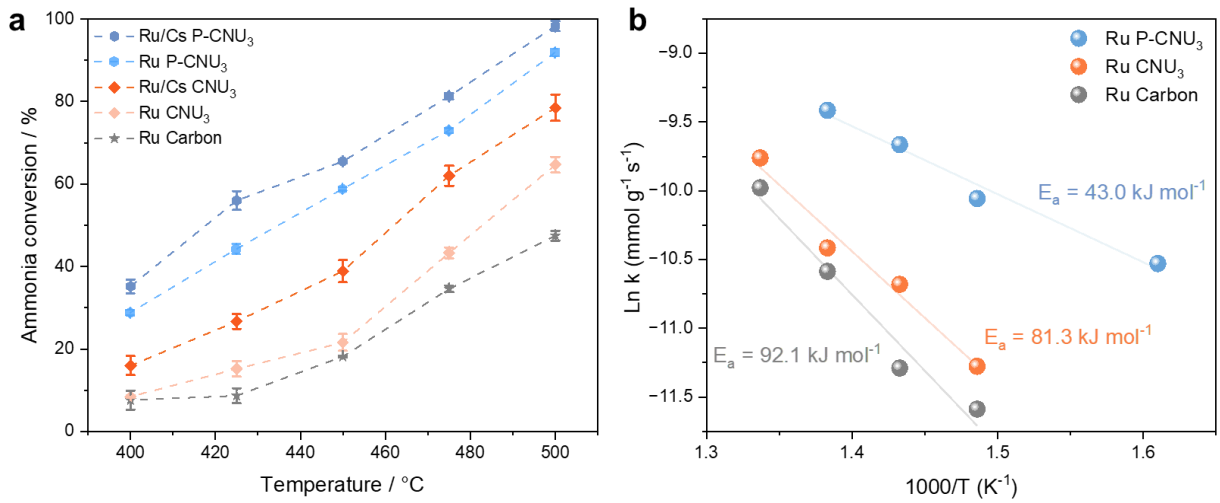


Fig. 3.8 Ammonia decomposition activity measurements and kinetic analysis of 5 wt.% Ru on the analogue carbon supports, performed at WHSV = 30,000 ml g_{cat}^{-1} h^{-1}. a. Catalytic conversion of the analogue catalysts at different temperatures. b. Apparent activation energy derived from the Arrhenius plot for the presented catalysts.

A more detailed comparison of ammonia decomposition activity among the tested catalysts is presented in **Fig. 3.8a**. As shown, the nitrogen doped support, Ru CNU_3 shows a higher conversion rate compared to the commercial Ru on carbon catalyst. This is in agreement with our previous discussion on the beneficial effect of N atoms substitution to replace C atoms in graphitic support which can enhance the overall reaction activity. Further enhancement in the catalytic activity is introduced based on $MgCO_3$ treatment. Even at relatively low temperatures, Ru P-CNU_3 achieves 59% conversion at 450 °C and 20% at 400 °C, outperforming its untreated counterpart. Noticeably, $MgCO_3$ treated sample gives almost 1.5 times larger ammonia conversion rate than the Ru CNU_3 catalyst despite the fact that XPS measurement indicated a similar absolute nitrogen content of ca. 8.5 % for both supports. As discussed, the content of the edge site nitrogen (pyrrolic and pyridinic nitrogen) has significantly increased from 43% to almost 80 % at the expense of graphitic nitrogen due to the

fragmentation of graphite to mesoporous partial graphitic structure. Thus, it is suggested that the prevalence of edge-site nitrogen is critical and beneficial in determining catalytic performance. This conclusion is further supported by a comparison between Ru CNU_5 and P-CNU_3. Despite having comparable surface areas (217.50 m^2 g^{-1} for CNU_5 and 205.64 m^2 g^{-1} for P-CNU_3), their activities differ drastically. Ru CNU_5 reaches only ~40% conversion, while Ru P-CNU_3 achieves ~90% under identical conditions. This disparity reinforces the view that nitrogen configuration plays a more decisive role than surface area in influencing catalytic activity.

To further elucidate the catalytic behaviour, kinetic studies were conducted on three representative catalysts: Ru Carbon, Ru CNU_3 and Ru P-CNU_3. As shown on **Fig. 3.8b**, the apparent activation energy E_a of the nitrogen doped carbon catalyst has decreased from typical 92.1 kJ mol^{-1} for Ru Carbon to 81.3 kJ mol^{-1} for the nitrogen doped sample. Suggesting a positive effect exerted by doping nitrogen towards the support. However, the apparent E_a value is further attenuated to 43 kJ mol^{-1} when $MgCO_3$ treatment was introduced. The unusually low E_a observed for Ru P-CNU_3 implies that it is not simply the dissociative mechanism of ammonia over Ru NPs, which typically lies in the range of 70-110 kJ mol^{-1}.[48]

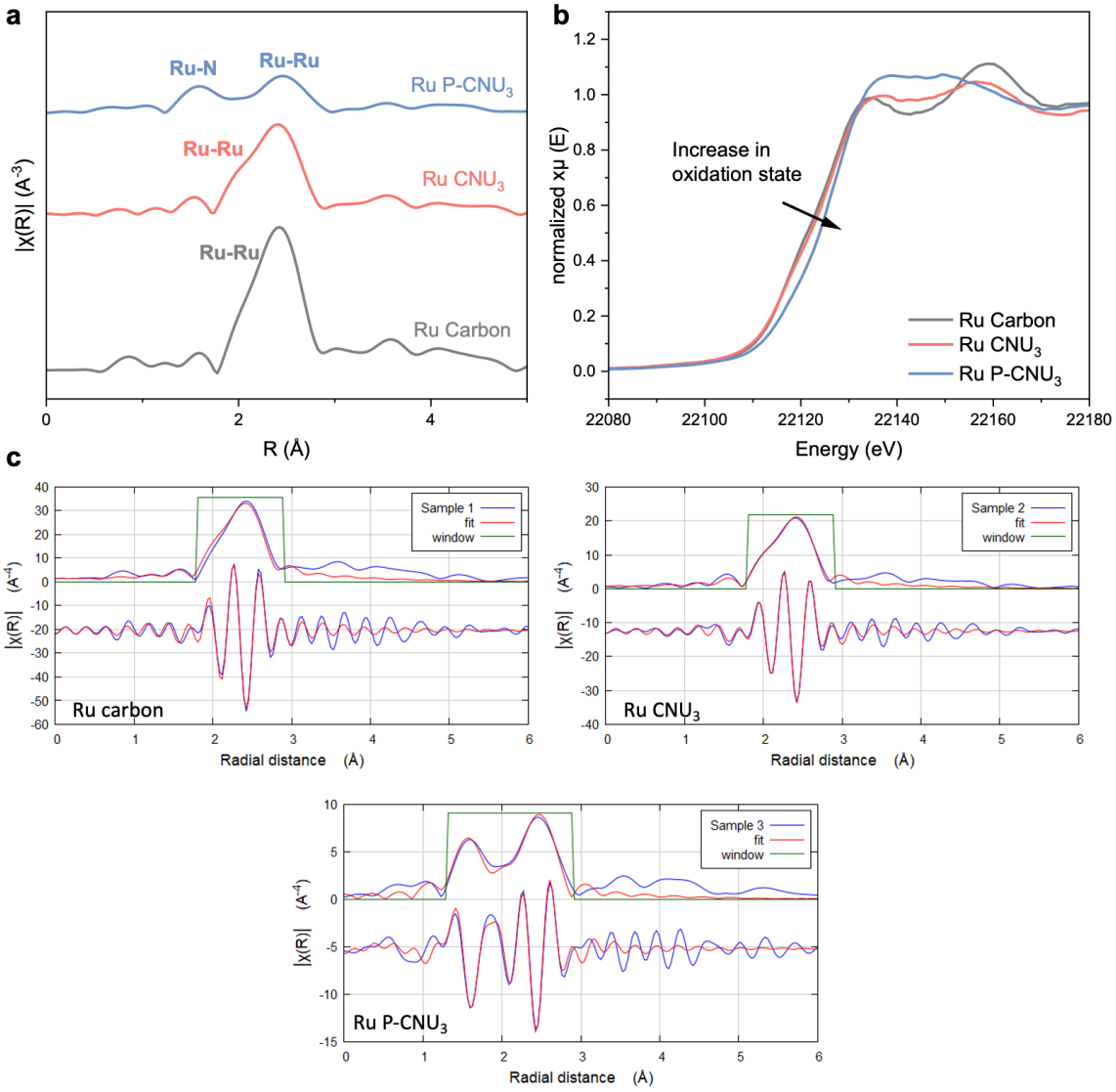


Fig. 3.9 Ru K-edge XAS results for the Ru loaded samples a. Fourier Transform of the EXAFS signals. b. XANES spectra. c. Fitting spectrums of the R space and K space of the analogue materials.

Table 5 EXAFS fitting parameters, related to Fig. 3.9

Composition	Shell	N	R (Å)	σ^2	R factor
Ru Carbon	Ru-Ru	10.50 ± 0.53	2.670 ± 0.003	0.0030	1.02%
Ru CNU_3	Ru-Ru	8.70 ± 0.25	2.670 ± 0.002	0.0044	0.33%
Ru P-CNU_3	Ru-N	4.03 ± 0.48	2.040 ± 0.008	0.0030	1.62%
	Ru-Ru	5.66 ± 0.39	2.690 ± 0.004	0.0070	

N, coordination number; R (Å), bond length; σ^2, Debye-Waller factor

To gain deeper understanding of the chemical state of the active site within this change in morphology and chemical configuration of the support, X-ray absorption spectroscopy (XAS) over the Ru K edge has been carried out. As shown in **Fig. 3.9a**, one main peak at 2.67 Å is observed which is assigned to the typical metallic Ru-Ru in Ru NPs. The intensity of this peak progressively reduces after N doping and $MgCO_3$, reflecting a smaller coordination number (**Table 5**) and a smaller particle size. This is well aligned with the Transmission electron microscopy (TEM) result. As can be seen from **Fig. 3.10**, the averaged Ru NPs size dropped from 10.0 ± 1.6 nm to 7.3 ± 1.4 nm after $MgCO_3$ treatment.

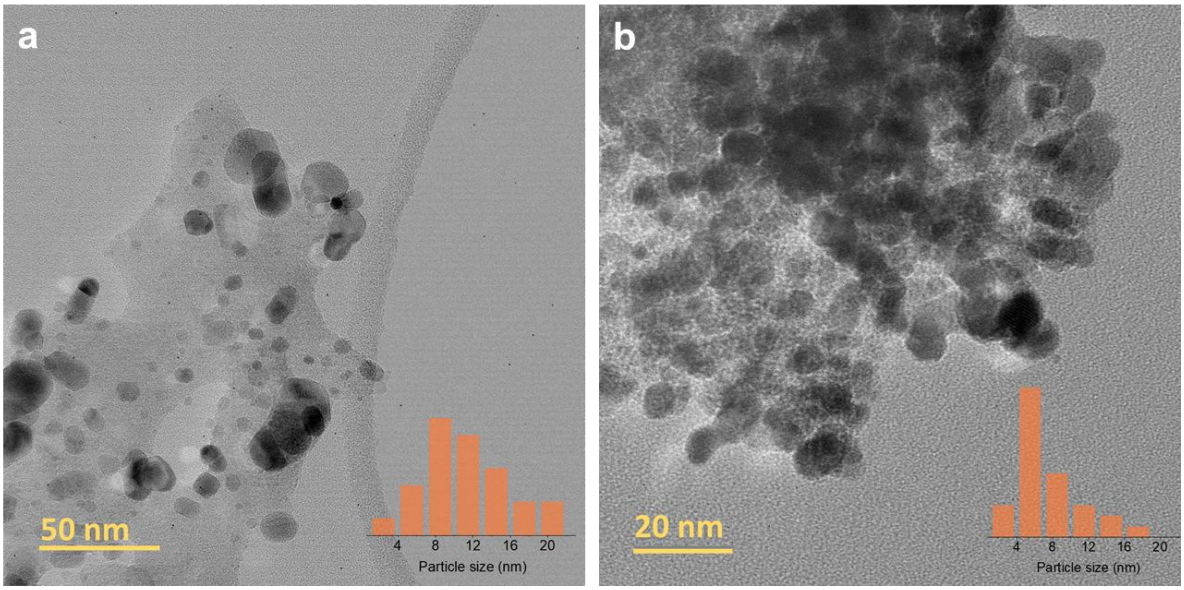


Fig. 3.10 TEM image of the analogue catalysts a. Ru CNU_3 b. Ru P-CNU_3.

As have been illustrated from the XAS data, Ru exhibits predominantly as metallic Ru NPs on all carbon supports. The simple incorporation of N to carbon support (Ru CNU_3) is observed to stabilizes Ru NPs leading to a better metal dispersion and smaller Ru NPs size as concluded from the coordination number derived from Extended X-ray Absorption Fine Structure (EXAFS) analysis. However, this structural improvement does not appear to significantly influence either the apparent activation energy as

calculated from kinetic measurements or the oxidation state of Ru, as evidenced by the Near Edge X-Ray Absorption Fine Structure (XANES) spectra. These observations suggest that the main promotional effect of the nitrogen-doped carbon lies not in altering the electronic state of Ru or changing the reaction pathway. Instead, it is the enhancement of electron donation from the support to the metal site which facilitates the breakage of N-H bonds via traditional dissociative mechanism.

However, the introduction of $MgCO_3$ towards the synthesis significantly alters the nitrogen configuration within the carbon support. Leading to formation of meso-/macro-pores enriched with exposed edge-site nitrogen atoms. These newly formed edge sites can effectively chelate Ru species, promoting the stabilization of isolated Ru ions. This structural transformation is consistent with the emergence of a new Ru–N peak in the EXAFS spectrum at approximately 2.04 Å, indicative of discrete Ru–N coordination environments. Furthermore, the positive shift in the Ru K edge observed in the XANES spectra (**Fig. 3.9b**) reflects a higher oxidation state of Ru, confirming the presence of significant quantities of oxidized Ru species (ca. Ru^{3+}) coexisting with residual metallic Ru^0. Quantitative EXAFS analysis yields an average coordination number of 4.03 ± 0.48 for Ru–N interactions, further supporting the notion that Ru ions are anchored by four nitrogen atoms within the porous matrix. These distinct $Ru–N_4$ species benefit from enhanced metal–support interactions and improved accessibility, which correlates with the substantial increase in catalytic activity observed for the $MgCO_3$-treated sample.

It is well recognised that in Ru based catalysts, the Ru atom arrangement in B5 structure provides the active site for the ammonia synthesis and decomposition reaction. Nonetheless, for such catalysts, the reaction follows a dissociative mechanism and exhibiting slower rate with an activation energy of 70-110 kJ mol^{-1} as

has been mentioned above. Ru Carbon and Ru CNU_3 catalysts with relatively higher E_a falls into this category with dissociative ammonia decomposition being the dominant reaction pathway. In contrast, Ru P-CNU_3 demonstrated an exceptionally high activity and a much lower activation energy, not to mention its discrete Ru ions species do not possess B5 ensembles. Taken together, these findings suggest that the enhanced catalytic performance of $MgCO_3$ treated support is primarily driven by the formation of discrete Ru species coordinated with edge-site nitrogen via a Ru–N_4 configuration.

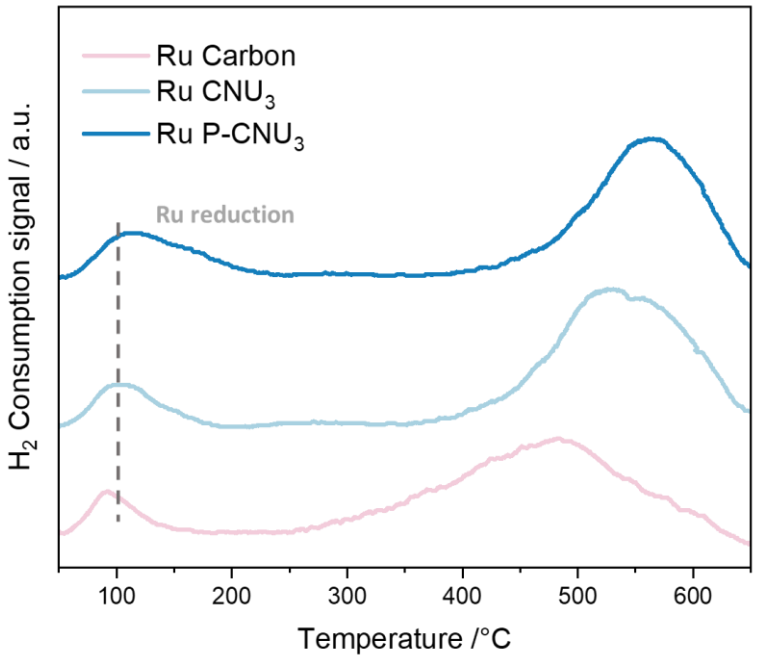


Fig. 3.11 H_2-TPR of analogue samples.

Temperature programmed reduction (H_2 TPR) was used to quantify the strength of interaction between Ru species and the support. As demonstrated in **Fig. 3.11**, there are two peaks observed: one peak in the range of 50-200°C and the other broad peak appearing after 450°C. The first peak corresponds to the reduction of oxidised Ru species while the later one is attributed towards the catalytic methanation and gasification of carbon by H_2 over Ru.[49,50] By doping N on to the support, a remarkable

peak shift and peak size enhancement in the first reduction peak of the Ru species from 90 to 105°C is noted. This effect becomes even more pronounced upon $MgCO_3$ treatment. These trends are consistent with XAS findings, which indicate an increased stabilization of oxidized Ru ions by surface nitrogen sites, particularly edge exposed nitrogen configuration. In this contest, the edge site nitrogen atoms can act as ligands that anchor Ru^{3+} species with their unpaired electron lone pairs, leading to stronger metal support interactions than those provided by graphitic nitrogen. Thereby, underscore the critical role of pyrrolic and pyridinic nitrogen in stabilizing active Ru species, which further result in the enhanced performance of the catalyst in ammonia decomposition.

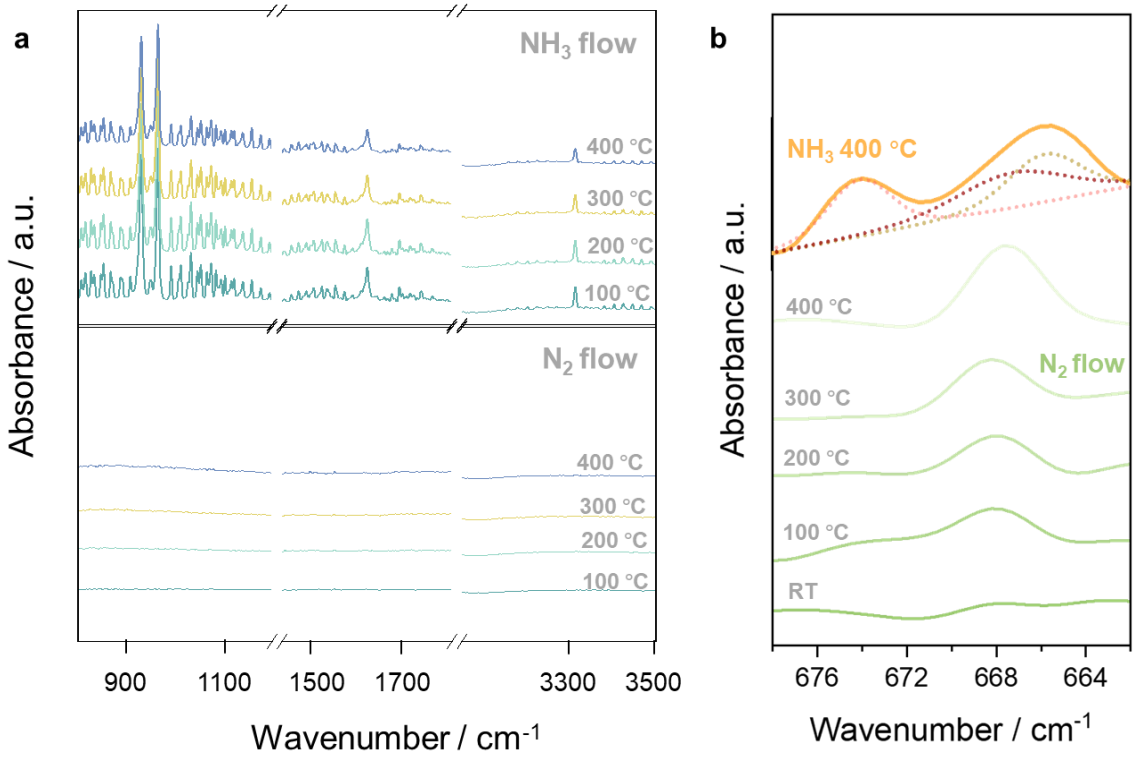


Fig. 3.12 Operando FTIR of Ru P-CNU_3 catalyst at various temperature. a. Full spectrum in N_2 and NH_3 flow respectively. b. spectrum focused in the range 678-662 cm^{-1}.

Operando FTIR was employed on the Ru P-CNU_3 catalyst to follow on the changes of NH_3 and related N containing species during ammonia decomposition. As seen in **Fig. 3.12a**, under ammonia flow, there are 3 NH_3 characteristic peaks, namely symmetric bending of NH_3 at 948.6 cm^{-1} (umbrella mode), one asymmetric bending N-H bending peak located at 1627 cm^{-1} and one symmetric N-H stretching peak at 3334.5 cm^{-1}.[51] Not much difference in peak intensity was noted on the sample under continuous N_2 flow from the full spectrum. However, if we zoom in and focus on the low wavenumber region as illustrated in **Fig. 3.12b**, a peak at 667 cm^{-1} attributable to stretching of Ru-N with pyridine/pyrrole of support becomes visible under nitrogen flow (moisture from the porous material appears to block up such absorption peak).[52] Even at higher temperature, the peak did not attenuate, which suggest their good thermal stability of the catalyst. In this contest, no ammonia is yet purged through the IR chamber, the peak is thus accounted to the interaction between Ru and edge site nitrogen species from the support. This is also in agreement with the reported Ru-N asymmetric stretching peak of Ru (II) bipyridine complex, which further confirms the ionic Ru species being anchored by the support sites with 4 N as stable surface coordination Ru complex.[53,54]

As ammonia is passed over the catalyst, a broadening of the peak at the original 667 cm^{-1} and a new peak at 675 cm^{-1} is observed. Due to limitation of the instrument, it would be too ambiguous to direct separate the broad peak to separate peaks. However, since the broad peak encompasses the original 667 cm^{-1} feature, which remains unchanged in the deconvoluted spectrum. It is suggested that this phenomenon is attributed to new weaker Ru–NH_2 interactions associated with the presence of gaseous NH_3, while retaining the interaction between structural nitrogen from the support and anchored Ru species.[55,56] In addition, there is a simultaneous

detection of stronger Ru-N at 675 cm^{-1} in NH_3 which matches with the formation of Ru=NH during the ammonia decomposition reaction. This further implies the formation of a surface-bound Ru–NH_2 intermediate.[57]

It is not evidence for the direct involvement of the structural N in the N-doped carbon since there is no apparent consumption of 667 cm^{-1} peak during the catalysis. Such structural N is highly conjugated with the 6 member-ring of pyridine or 5 member-ring in pyrrole in graphitic network so they are unlikely to cleave as redox sites under the reaction conditions. This is further confirmed by comparing the nitrogen configuration of Ru P-CNU_3 before and after catalysis. As presented in **Fig. 3.13**, negligible changes were observed on the distribution of the nitrogen configuration. This clearly suggests that the structural nitrogen species does not directly involve in the ammonia decomposition reaction, instead, these edge site nitrogen species would only stabilise the discrete Ru species through 4 coordinated nitrogen configurations.

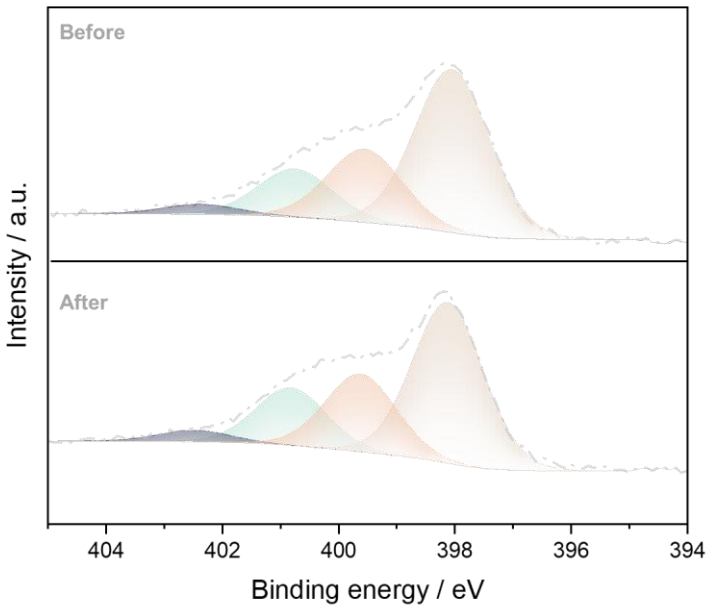


Fig. 3.13 XPS of N 1s spectra on Ru P-CNU_3 catalyst before and after 6h of ammonia decomposition at 500 °C and WHSV = 30,000 ml g_{cat}^{-1} h^{-1}.

Overall, we propose that edge site nitrogen configuration on Ru loaded nitrogen doped carbon support would display better ammonia decomposition activity compared to graphitic N. The lone pairs of exposed pyrrolic and pyridinic N can stabilize Ru as discrete ionic species. Leading to strong metal support interaction as evidenced by FTIR and H_2-TPR. This further results in lower activation barrier of N_2 desorption (rate determining step at milder reaction condition) as discussed above. Since, no change in the N environment is observed after catalysis, it is deduced that such high activity improvement is solely attributed to the structural change and electronic modification.

3.3 Conclusion

In this work, we have successfully synthesized a nitrogen doped carbon material using a simple combustion approach. This approach was further modified using a $MgCO_3$ template to favour the growth of edge site nitrogen configurations (pyridinic and pyrrolic). The activity of different nitrogen content on Ru impregnated nitrogen doped carbon was evaluated. It is concluded that nitrogen content has a greater impact than surface area towards ammonia decomposition and optimal nitrogen content can favour the catalysis by exerting a positively electron donating effect to the active metal site. Further comparison over different nitrogen configuration revealed that by increasing the concentration of edge site nitrogen species, it will induce discrete $Ru\text{-}N_4$ morphology. The effect from this structural change was investigated using kinetic analysis, XAS and operando FTIR. From which we concluded that it is the discrete ionic Ru species responsible for such high activity. Edge site N configuration would greatly enhance the metal support interaction and the electronic structure of the metal, resulting in lower activation barrier for the rate determining N_2 desorption step and thus display better activity.

However, more direct evidence can help to solidify the proposed mechanism. For example, further exploration by ^{15}N labelling experiments, especially using $^{15}NH_3$ would help to track down the origin of the formation of N_2. Since too much of the edge site nitrogen configuration would cause collapse of the support structure. Another avenue worth investigating would be to incorporate theoretical calculations to find the optimal ratio and distribution of N configuration.

It is believed that the results from this Chapter can provide new insights into the fundamental understanding for future catalyst design.

Reference

1. Ljubisa R. Radovic and Rodriguez-Reinoso,F. CARBON MATERIALS IN CATALYSIS. Chem. Phys. Carbon 261–376 (1996)

2. Rodríguez-Reinoso, F. The role of carbon materials in heterogeneous catalysis. Carbon N. Y. 36, 159–175 (1998).

3. Lam, E. & Luong, J. H. T. Carbon materials as catalyst supports and catalysts in the transformation of biomass to fuels and chemicals. *ACS Catal.* **4**, 3393–3410 (2014).

4. Zaman, S. *et al.* Carbon-based catalyst supports for oxygen reduction in proton-exchange membrane fuel cells. *Trends Chem.* **4**, 886–906 (2022).

5. Li, L., Zhu, Z. H., Yan, Z. F., Lu, G. Q. & Rintoul, L. Catalytic ammonia decomposition over Ru/carbon catalysts: The importance of the structure of carbon support. *Appl. Catal. A Gen.* **320**, 166–172 (2007).

6. Torrente-Murciano, L., Hill, A. K. & Bell, T. E. Ammonia decomposition over cobalt/carbon catalysts—Effect of carbon support and electron donating promoter on activity. *Catal. Today* **286**, 131–140 (2017).

7. Yin, S. F., Xu, B. Q., Ng, C. F. & Au, C. T. Nano Ru/CNTs: A highly active and stable catalyst for the generation of CO_x-free hydrogen in ammonia decomposition. *Appl. Catal. B Environ.* **48**, 237–241 (2004).

8. Yin, S. F. *et al.* Carbon nanotubes-supported Ru catalyst for the generation of CO_x free hydrogen from ammonia. *Catal. Today* **93**–**95**, 27–38 (2004).

9. Chen, J. *et al.* Effects of nitrogen doping on the structure of carbon nanotubes (CNTs) and activity of Ru/CNTs in ammonia decomposition. *Chem. Eng. J.* **156**, 404–410 (2010).

10. García-García, F. R., Álvarez-Rodríguez, J., Rodríguez-Ramos, I. & Guerrero-Ruiz, A. The use of carbon nanotubes with and without nitrogen doping as support for ruthenium catalysts in the ammonia decomposition reaction. *Carbon N. Y.* **48**, 267–276 (2010).

11. Bell, T. E., Zhan, G., Wu, K., Zeng, H. C. & Torrente-Murciano, L. Modification of Ammonia Decomposition Activity of Ruthenium Nanoparticles by N-Doping of CNT Supports. *Top. Catal.* **60**, 1251–1259 (2017).

12. Ren, S., Huang, F., Zheng, J., Chen, S. & Zhang, H. Ruthenium supported on nitrogen-doped ordered mesoporous carbon as highly active catalyst for NH_3 decomposition to H_2. *Int. J. Hydrogen Energy* **42**, 5105–5113 (2017).

13. Maciej Serda *et al.* Nitrogen Adsorption and Dissociation on Fe(111). *J. Catal.* **182**, 479 (1999).

14. García-García, F. R. *et al.* TAP studies of ammonia decomposition over Ru and Ir catalysts. *Phys. Chem. Chem. Phys.* **13**, 12892–12899 (2011).

15. Medford, A. J. *et al.* From the Sabatier principle to a predictive theory of transition-metal heterogeneous catalysis. *J. Catal.* **328**, 36–42 (2015).

16. Zeinalipour-Yazdi, C. D., Richard, C., Catlow, A., Hargreaves, J. S. J. & Laassiri, S. A comparative analysis of the mechanisms of ammonia synthesis on various catalysts using density functional theory. *R. Soc. Open Sci*. **8**, 210952 (2021).

17. Chen, Y. *et al.* Atomic Fe Dispersed on N-Doped Carbon Hollow Nanospheres for High-Efficiency Electrocatalytic Oxygen Reduction. *Adv. Mater.* **31**, 1–8 (2019).

18. He, L., Weniger, F., Neumann, H. & Beller, M. Synthesis, Characterization, and Application of Metal Nanoparticles Supported on Nitrogen-Doped Carbon: Catalysis beyond Electrochemistry. *Angew. Chemie - Int. Ed.* **55**, 12582–12594 (2016).

19. Primo, A., Atienzar, P., Sanchez, E. J. D. From biomass wastes to large-area, high-quality, N-doped graphene: catalyst-free carbonization of chitosan coatings on arbitrary substrates. *Chem.Comm.* **48**(74) 9254-9256 (2012)

20. Khan, A., Goepel, M., Colmenares, J. C. & Gläser, R. Chitosan-Based N-Doped Carbon Materials for Electrocatalytic and Photocatalytic Applications. *ACS Sustain. Chem. Eng.* **8**, 4708–4727 (2020).

21. Tiwari, J. N. *et al.* High-Performance Hydrogen Evolution by Ru Single Atoms and Nitrided-Ru Nanoparticles Implanted on N-Doped Graphitic Sheet. *Adv. Energy Mater.* **9**, 1900931 (2019).

22. Ghuman, K. K. *et al.* Tailoring widely used ammonia synthesis catalysts for H and N poisoning resistance. *Phys. Chem. Chem. Phys.* **21**, 5117–5122 (2019).

23. Li, L. *et al.* High oxygen reduction activity on a metal–organic framework derived carbon combined with high degree of graphitization and pyridinic- N dopants. *J. Mater. Chem. A* **5**, 789–795 (2017).

24. Podila, S. *et al.* Hydrogen production by ammonia decomposition using high surface area Mo_2N and Co_3Mo_3N catalysts. *Catal. Sci. Technol.* **6**, 1496–1506 (2016).

25. Zhang, S. L. *et al.* Anchoring Metal-Nitrogen Sites on Porous Carbon Polyhedra with Highly Accessible Multichannels for Efficient Oxygen Reduction. *ACS Appl. Mater. Interfaces* **16**, 44728–44736 (2024).

26. Willhoft, E. M. A. Kinetics of decomposition of ammonia at low pressures on metal surfaces. *Trans. Faraday Soc.* **64**, 1925–1933 (1968).

27. Liu, H., Wang, H., Shen, J., Sun, Y. & Liu, Z. Promotion effect of cerium and lanthanum oxides on Ni/SBA-15 catalyst for ammonia decomposition. *Catal. Today* **131**, 444–449 (2008).

28. Zhang, J., Xu, H. & Li, W. Kinetic study of NH_3 decomposition over Ni nanoparticles: The role of la promoter, structure sensitivity and compensation effect. *Appl. Catal. A Gen.* **296**, 257–267 (2005).

29. Wu, S. *et al.* Removal of Hydrogen Poisoning by Electrostatically Polar MgO Support for Low-Pressure NH_3 Synthesis at a High Rate over the Ru Catalyst. *ACS Catal.* **10**, 5614–5622 (2020).

30. Bamufleh, H. S. & Zaman, S. F. Ammonia Decomposition over Alkali Metal (Li, K, Cs)-Promoted Bulk Mo_2N Catalyst. *Processes* **11**, (2023).

31. Wang, Q., Guo, J. & Chen, P. The impact of alkali and alkaline earth metals on green ammonia synthesis. *Chem* **7**, 3203–3220 (2021).

32. Guo, X. *et al.* Applied Catalysis B : Environment and Energy Alkaline earth metal promoted hydrogen production from ammonia decomposition over Ni / La_2O_3 -based catalysts. *Appl. Catal. B Environ. Energy* **348**, 123844 (2024).

33. Hill, A. K. & Torrente-Murciano, L. Low temperature H2 production from ammonia using ruthenium-based catalysts: Synergetic effect of promoter and support. Appl. Catal. B Environ. 172–173, 129–135 (2015).

34. Luo, E., Xiao, M., Ge, J., Liu, C. & Xing, W. Selectively doping pyridinic and pyrrolic nitrogen into a 3D porous carbon matrix through template-induced edge engineering: enhanced catalytic activity towards the oxygen reduction reaction. *J. Mater. Chem. A*, **5**, 21709 (2017).

35. Chen, X., Oh, W. Da, Zhang, P. H., Webster, R. D. & Lim, T. T. Surface construction of nitrogen-doped chitosan-derived carbon nanosheets with hierarchically porous structure for enhanced sulfacetamide degradation via peroxymonosulfate activation: Maneuverable porosity and active sites. *Chem. Eng. J.* **382**, 122908 (2020).

36. Zhao, Q. *et al.* Single Nickel Atoms Anchored on Nitrogen-Doped Graphene as a Highly Active Cocatalyst for Photocatalytic H_2 Evolution. *ACS Catal.* **8**, 11863−11874 (2018).

37. Fang, H. *et al.* Dispersed surface Ru ensembles on MgO(111) for catalytic ammonia decomposition. *Nat. Commun.* **14**, 647 (2023).

38. He, S. *et al.* Facile preparation of N-doped activated carbon produced from rice husk for CO_2 capture. *J. Colloid Interface Sci.* **582**, 90–101 (2021).

39. Peng, W. *et al.* Facilitating two-electron oxygen reduction with pyrrolic nitrogen sites for

electrochemical hydrogen peroxide production. *Nat. Commun.* **14**, 4430 (2023).

40. Ayiania, M. *et al.* Deconvoluting the XPS spectra for nitrogen-doped chars: An analysis from first principles. *Carbon N. Y.* **162**, 528–544 (2020).

41. Zhao, C. *et al.* Nano-$CaCO_3$ as template for preparation of disordered large mesoporous carbon with hierarchical porosities. *J. Mater. Chem.* **20**, 976–980 (2010).

42. Yin, S. F., Xu, B. Q., Wang, S. J., Ng, C. F. & Au, C. T. Magnesia-carbon nanotubes (MgO-CNTs) nanocomposite: Novel support of Ru catalyst for the generation of CO_x-free hydrogen from ammonia. *Catal. Letters* **96**, 113–116 (2004).

43. Chen, C. *et al.* Ru-Based Catalysts for Ammonia Decomposition: A Mini-Review. *Energy and Fuels* **35**, 11693–11706 (2021).

44. Akarçay, Ö., Kurtoğlu, S. F. & Uzun, A. Ammonia decomposition on a highly-dispersed carbon-embedded iron catalyst derived from Fe-BTC: Stable and high performance at relatively low temperatures. *Int. J. Hydrogen Energy* **45**, 28664–28681 (2020).

45. Duan, X. *et al.* Tuning the size and shape of Fe nanoparticles on carbon nanofibers for catalytic ammonia decomposition. *Appl. Catal. B Environ.* **101**, 189–196 (2011).

46. Li, L. *et al.* Cobalt nanoparticles embedded in a porous carbon matrix as an efficient catalyst for ammonia decomposition. *Catal. Sci. Technol.* **7**, 1363–1371 (2017).

47. Mazzone, S. *et al.* Ruthenium-based catalysts supported on carbon xerogels for hydrogen production via ammonia decomposition. *Appl. Catal. A Gen.* **632**, 118484 (2022).

48. Ye, D. & Tsang, S. C. E. Prospects and challenges of green ammonia synthesis. *Nat. Synth.* **2**, 612–623 (2023).

49. Zhang, X. *et al.* Synergizing Surface Hydride Species and Ru Clusters on Sm_2O_3 for Efficient Ammonia Synthesis. **15**, 49 (2022).

50. Madadi, S. & Kaliaguine, S. Activated Carbon-Supported Ruthenium as a Catalyst for the Solvent- And Initiator-Free Aerobic Epoxidation of Limonene. *ACS Sustain. Chem. Eng.* **9**, 10557–10568 (2021).

51. Kim, J. S., Nam, H., Kim, H. J., Lee, J. H. & Park, B. H. Real-Time Measurement of Ammonia (NH_3) in Artillery Smoke Using a Passive FT-IR Remote Sensor. *ACS Omega* **4**, 16768–16773 (2019).

52. Adeniyi, A. A. & Ajibade, P. A. Exploring the Ruthenium-Ligands Bond and Their Relative Properties at Different Computational Methods. *Journal of Chemistry*, **15**, 3672062 (2016).

53. Munshi, M. U., Martens, J., Berden, G. & Oomens, J. Vibrational Spectra of the Ruthenium-Tris-Bipyridine Dication and Its Reduced Form in Vacuo. *J. Phys. Chem. A* **124**, 2449–2459 (2020).

54. Garza-Ortiz, A., Uma Maheswari, P., Siegler, M., Spek, A. L. & Reedijk, J. A new family of Ru(ii) complexes with a tridentate pyridine Schiff-base ligand and bidentate co-ligands: Synthesis, characterization, structure and in vitro cytotoxicity studies. *New J. Chem.* **37**, 3450–3460 (2013).

55. Dołega, D., Mikuli, E. & Chruszcz-Lipska, K. Experimental (FT-IR and FT-RS) and theoretical (QC-DFT) studies of vibrational modes and molecular structure of new low-temperature phases of $[Ru(NH_3)_6](BF_4)_3$ and $[Ru(NH_3)_6](ClO_4)_3$. *Spectrochim. Acta - Part A Mol. Biomol. Spectrosc.* **98**, 132–141 (2012).

56. Allen, A. D. & Senoff, C. V. Preparation and infrared spectra of some ammine complexes of ruthenium(II) and ruthenium(III). *Can. J. Chem.* **45**, 1337–1341 (1967).

57. Stüker, T., Hohmann, T., Beckers, H. & Riedel, S. Fluoro Nitrenoid Complexes $FN{=}MF_2$ (M=Co, Rh, Ir): Electronic Structure Dichotomy and Formation of Nitrido Fluorides $N{\equiv}MF_3$. *Angew. Chemie* **132**, 23374–23379 (2020).

Chapter 4 Enhanced Associative Ammonia Decomposition on Cerium Oxide via Inducing N Dopants

4.1 Introduction

On conventional Ru-based catalysts for low temperature ammonia decomposition, it is agreed that the rate determining step (RDS) is the cleavage of the three N-H bonds on the ammonia molecule.[1,2] A major challenge arises from the high energy barrier associated with consecutive N-H dissociation, further constrained by the Brønsted−Evans−Polanyi (BEP) scaling relationship, which dictates an inverse correlation between NHx adsorption energy and the N_2 desorption energy on metal surfaces.[3] This further inhibits ammonia decomposition at mild condition and makes carbon free hydrogen delivery using ammonia less promising.

In order to mitigate this high energy barrier and circumvent the scaling limitation, innovative catalyst designs have been explored which enable the catalytic reaction to proceed through an alternative pathway. Li *et al* founded that when the size of Ru dropped to subatomic or even a single atom, the traditional dissociation mechanism (NH_3 is fully dissociated before N recombination to emit N_2) over Ru B5 site is inhibited. Alternatively, the reaction proceeds through an associative mechanism with Ru-N(H)-N(H)-Ru intermediate where adsorbed reactant molecules over two spatially adjacent Ru active sites interact.[4] Under this reaction pathway, the nitrogen is generated with the dehydrogenation of N-H bonds via a step wise manner. Thus, lowers the activation energy of the N-H bond dissociation and leads to better catalytic activity. Yu *et al* introduced a unique chemical looping approach using a Ru-$M(NH_2)_2$ catalysts. The metal amide decomposes into Ru-M(NH) imide, releasing H_2 and N_2, followed by regeneration under NH_3, enabling an efficient decomposition cycle.[5] Other studies on Ru/MgO(111) and Ru/13X zeolite revealed that ammonia decomposition activity can be

promoted by heterolytically rupturing the N-H bond via a $Ru^{\delta+}$–$O^{\delta-}$ Frustrated lewis pair (FLP) mechanism.[6–8]

Among all these novel catalyst and reaction approach studied, incorporation redox active N sites and facilitate associative mechanism has emerged as one most practical and promising route. On one hand, this reaction mechanism has been widely studied in the reverse reaction of ammonia decomposition, which can support some precious guidance on catalyst design.[9–11] On the other hand, unlike chemical looping systems, where ammonia is decomposed via a two-step reaction, this associative pathway is more compatible with continuous reactor designs, making it more suitable for industrial applications.[12,13] Recently, metal nitride-based (MN_x) materials have emerged as effective supports for NH_3 activation via this reaction route, as they provide both nitrogen incorporation capabilities and redox-active lattice sites.[14,15] In these systems, transition metals such as Ni are typically dispersed onto the surface of various metal nitrides to attain high activity. During reaction, ammonia is initially interacting with the nitrogen sites at the interface of the metal nanoparticles (NPs). The metal assists in the progressive dehydrogenation of the adsorbed NH_3, ultimately enabling the release of N_2. The nitrogen atom removed during this process leaves behind a lattice nitrogen vacancy in the support. This vacancy can then be refilled by nitrogen derived from incoming NH_3 molecules, thus completing the redox cycle and sustaining the catalytic activity. Though in general, MN_x materials showed enhanced activity towards the catalysis, exposure to air or moisture can lead to oxidation of the nitride phase, structural degradation, and permanent loss of activity. Therefore, the development of air-stable supports that combine nitrogen incorporation capability with reversible redox behaviour is particularly desirable. Such materials would not only maintain structural integrity under reaction conditions but also enable long-term catalytic performance favoured for real-world industrial applications.

Building upon the need for air-stable supports with redox-active functionality, cerium oxide presents itself as a particularly attractive candidate. Cerium oxide is a rare earth metal oxide which is well recognized for its abundant oxygen vacancies due to the easily interconversion

of Ce^{3+}/Ce^{4+}.[10,16] This unique property makes it highly versatile in catalytic applications, such as ammonia decomposition. Teng *et al* reported an oxygen defect rich CeO_2 nanorod which illustrates exceptional high catalytic activity. They attributed such high activity towards the electron transfer tunnel between Ru and the nanorod support under a Schottky contact model facilitated by oxygen defects of the catalyst.[17] Another group proposed a CeO_2/Ni inverse catalyst with optimal metal support interaction. It have been demonstrated that oxygen vacancies generated at the metal-support interface would favour more NH_3 absorption thus leading to a promoted catalytic effect.[18] More importantly, studies have shown that CeO_2 can also incorporate nitrogen species into its lattice under suitable conditions, enabling N substituted oxygen sites that may mimic the behaviour of metal nitrides while offering superior air stability. This is in great alignment with the previous discussed associative route and Mars–van Krevelen mechanism (MvK) that facilitates lower activation barrier at mild conditions. Furthermore, its strong metal–support interactions and high thermal stability make it an ideal platform for dispersing active metal NPs, enhancing ammonia decomposition activity. These features motivate the exploration of nitrogen-doped CeO_2 as a novel support capable of facilitating associative ammonia decomposition under industrially relevant conditions.

In this chapter, we present a Ru/N-CeO_2 catalyst that demonstrates exceptional NH_3 decomposition activity, achieving a 2–3 times enhancement in catalytic performance compared to undoped Ru/CeO_2. Ceria support is synthesized using a simple soft urea glass (SUG) approach.[19] Prior to metal impregnation, the ceria is annealed under NH_3 at various conditions to introduce nitrogen dopants and systematically investigate the influence of nitrogen content on catalytic behaviour. Following nitrogen doping, ruthenium is introduced using an organometallic precursor dissolved in an organic solvent, a strategy designed to minimize the interaction between hydroxyl groups from water and oxygen vacancies on the ceria support. This approach allows for better control of the metal–support interface and preserves the redox-active features of both ceria and the incorporated nitrogen species.

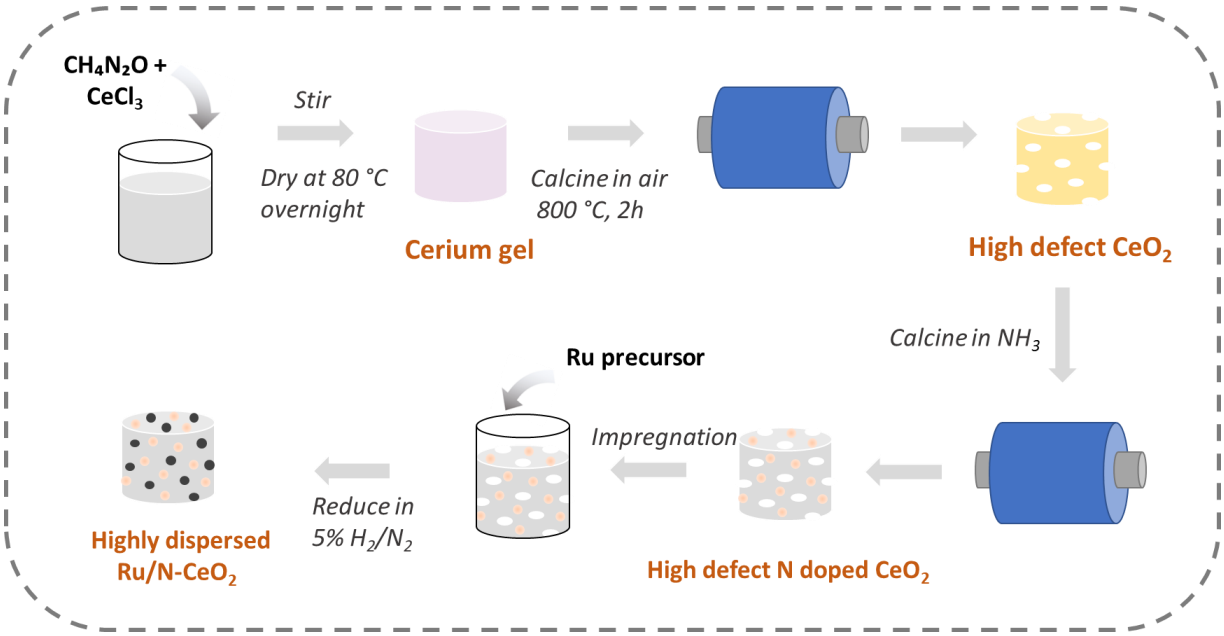


Fig. 4.1 schematic illustration of the synthetic process of Ru/ N-CeO_2.

Kinetic studies indicate a mechanistic shift, with an increased contribution from the associative pathway. This transition has been further confirmed via *in situ* FTIR and isotopic pulse experiments. While nitrogen doping is often considered a method to modify electron density and enhance metal-support interactions.[20,21] Our findings reveal a more profound impact—not only accelerating NH_3 decomposition via electronic effects but also introducing a Mars–van Krevelen mechanism that fundamentally alters the reaction pathway.

Overall, these insights highlight nitrogen doping as a powerful strategy to break scaling limitations, strengthen Ru-support interactions, and enhance NH_3 decomposition kinetics. This work offers a new perspective on catalyst design for heterogeneous ammonia activation, particularly at the metal-support interface.

4.2 Result and discussion

This section presents the key findings and interprets them in the context of nitrogen effect on nitrogen doped cerium oxide catalysts towards ammonia decomposition.

4.2.1 Support optimization

A series of nitrogen doped cerium oxide supports with different NH_3 annealing temperature and time are synthesized to investigate the effect of temperature to nitrogen dopants. The structure of the bulk support is analysed by powder X-ray diffraction (XRD). As illustrated in **Fig. 4.2a**, the synthesized CeO_2 (SUG) exhibits nine peaks at 2θ of 28.20°,32.74°, 47.16°, 56.05°, 58.79°,69.16°,76.44°, 78.82° and 88.20° which are well assigned to the (111), (200), (220), (311), (222), (400), (331), (420) and (422) planes of CeO2, respectively.[22] This XRD pattern matches with the face-centred cubic structure of CeO2 (PDF# 34–0394), indicating a fluorite structure and a crystalline cubic $Fm\bar{3}m$ space group. The nitrogen doped CeO_2 (N-CeO_2) catalysts show identical diffraction pattern reflecting no change in the fluorite structure after annealing in NH_3. However, higher crystallinity was observed for N-CeO_2 synthesized at higher temperature. This is attributed to the elimination of grain boundary defects during calcination at high temperatures, which therefore increases the crystallinity of the N-CeO_2 particles. Similar trend was observed for N-CeO_2 calcined for longer time scale while fixing the annealing temperature (see **Fig. 4.2b**). At elevated temperatures, atoms gain more mobility due to thermal energy input. Thus, extended durations would allow rearrangement of atoms into more energetically favourable, ordered crystal lattices, reducing defects and disorders. This is shown by sharper and more intense XRD peaks as illustrated in **Fig. 4.2**. Although N is slightly larger than oxygen and lattice expansion is expected upon N doping, by refining the lattice parameter, neglectable difference were observed. The lattice parameter (*a*) for all the measured sample gave a value of 5.44 Å. This is accounted to the low concentration of N dopants within the structure.

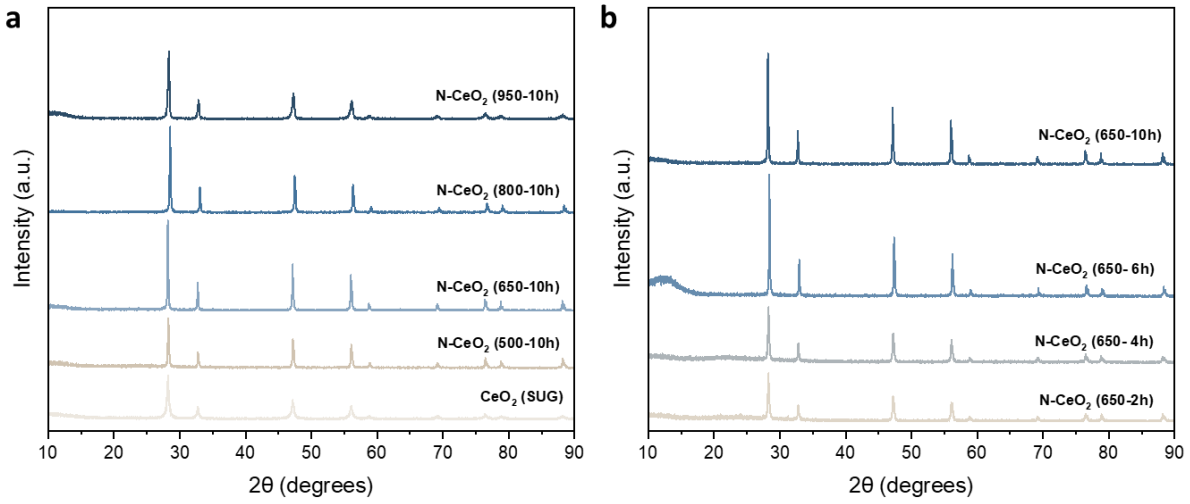


Fig. 4.2 XRD pattern of nitrogen doped cerium oxide synthesized a. At different temperature while fixing the reaction time. b. At 650 °C but different durations.

As depicted from scanning electron microscope (SEM) (**Fig. 4.3 a-f**), the pristine CeO_2 support shows featureless and amorphous structure with few cubic crystallites of size ca. 100 nm. After annealing in NH_3, the structure become more ordered and more cubic crystallites were observed. The size of single cubic crystal further increased from ca. 100 nm for pristine CeO_2 to ca. 750 nm when it is treated in NH_3 gas at 950 °C for 10 h. Moreover, significant aggregation of crystallites was observed at sample annealed at 950 °C. At higher temperature, even under reduction gas flow, crystal growth is induced via Ostwald ripening, smaller particles tend to merge to reduce surface energy and form more thermodynamically stable crystallites.[23] Which is also evidenced by the decrease in surface area measured through BET (Table.1). However, it is interesting to note that there is a less significant change in the BET surface area for nitrogen doped cerium oxide support calcined at different reaction times. It might be that the surface area of the pure ceria is already relatively low ca. 10 $m^2\ g^{-1}$, therefore difference in the surface area upon N doping would lead to even smaller changes which is under the instruments' sensitivity limit.

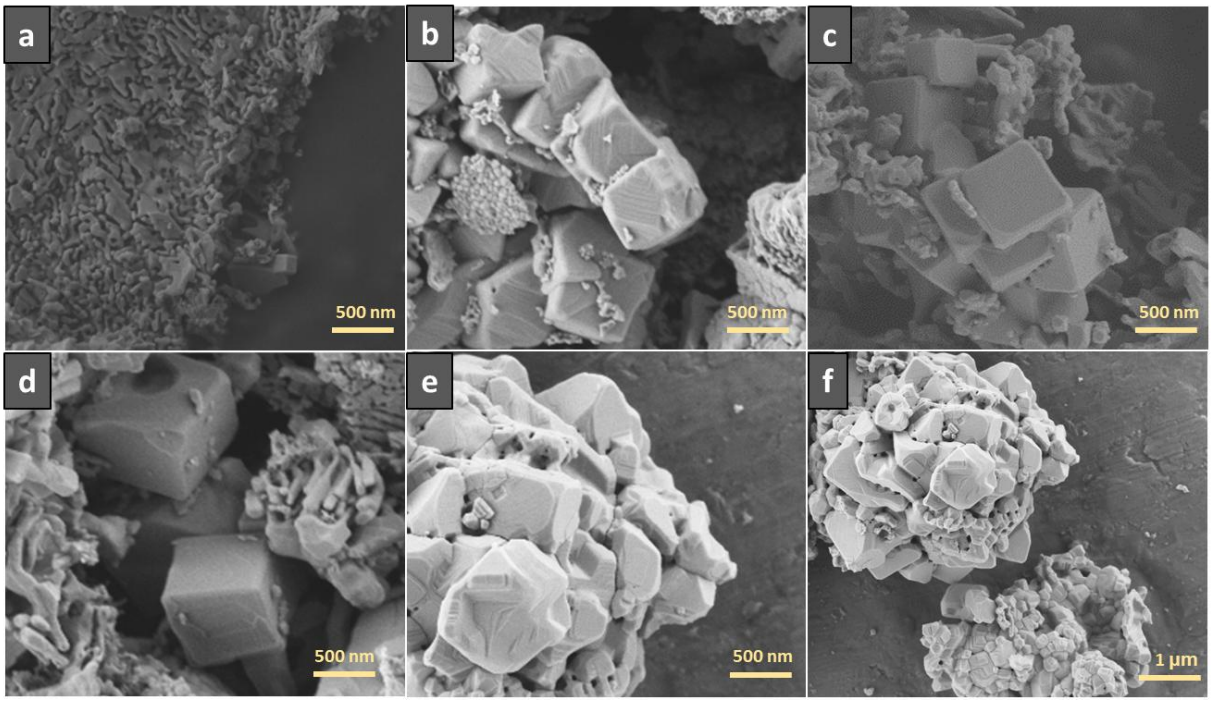


Fig. 4.3 Scanning electron microscopy of Cerium oxide-based supports. d. CeO_2 e. N-CeO_2(500-10h) f. N-CeO_2(650-10h) g. N-CeO_2(800-10h) h. N-CeO_2(950-10h) i. N-CeO_2(950-10h) at Magnification = 5K.

Elemental analysis and chemical properties of the supports were further obtained via X-ray photoelectron spectroscopy. A clear distinct peak shown at 399.2 eV evidences the existence of N and indicates the successfully nitrogen doped cerium oxide catalyst (**Fig. 4.4a**).[24] This alteration in the lattice structure is also accompanied with a change in colour of the finally obtained powder. The pale yellow CeO_2 (SUG) support is turned light grey after annealing in NH_3 at 500 °C (N-CeO_2-500-10h). With higher synthesizing temperature, it further turns white grey (N-CeO_2-650-10h), light blue (N-CeO_2-800-10h) and finally olive green (N-CeO_2-950-10h). Using XPS and Carbon Hydrogen Nitrogen Sulphur (CHNS) analysis, it is noted that the level of N dopants in the lattice is strongly related to the temperature. As presented in **Table. 1**, a 'volcano' shaped trend is illustrated where the highest amount of nitrogen is found for sample annealed at 650 °C with an atomic nitrogen ratio of ca. 2.76 %. This aligns with the optimal temperature used to achieve maximum uptake of N via ammonolysis reported in literature for many other metal oxides supports.[25,26] It is reported that high efficient nitrogen

doping typically takes place in the temperature range of 600 -700 °C. At lower temperature, the process is limited by diffusion as deficient energy for nitrogen and oxygen substitution, while at higher temperature, the nitrogen doping is affected by both excess reduction as well as the thermodynamic ammonia decomposition.[26,27]

Table 1 Structural and elemental analysis of the analogue cerium-based supports

	CHNS analysis	XPS analysis		BET analysis	Lattice parameter[a]
Sample	N content / %	N content / %	$Ce^{3+}/(Ce^{3+}+Ce^{4+})$ / %	BET area / $m^2\ g^{-1}$	*a* / Å
CeO_2 (SUG)	n/a	n/a	15.55	12.76	5.443
N-CeO_2(500-10h)	0.84	n/a	15.48	10.50	5.442
N-CeO_2(650-10h)	2.76	2.57	16.92	10.47	5.446
N-CeO_2(800-10h)	2.28	2.41	19.86	7.36	5.447
N-CeO_2(950-10h)	1.32	1.68	26.16	4.89	5.444
N-CeO2(650-2h)	1.32	n/a	13.95	10.52	5.445
N-CeO2(650-4h)	1.92	2.03	18.49	9.83	5.444
N-CeO2(650-6h)	3.12	3.76	18.29	11.36	5.447

a: lattice parameters are calculated using the Bragg's law, CeO_2 is cubic where a=b=c.

The high-resolution Ce 3d orbital spectrum is highly complicated, 6 distinct peaks, denoted as u0 (901.0 eV), u′ (907.3 eV), u″ (916.6 eV), v0 (882.4 eV), v′ (888.6 eV), and v″ (898.2 eV), are associated with Ce^{4+}. There are further 4 characteristic peaks, namely u0 (900.6 eV), u′ (903.6 eV), v0 (880.1 eV) and v′ (884.9 eV) correspond to Ce^{3+}.[28] By deconvoluting the peaks, it is found with increasing annealing temperature, the Ce^{3+}/Ce^{4+} ratio increases (**Fig. 4.4b**). This phenomenon entails the relinquishment of electrons by lattice oxygen atoms, leading to their departure from the lattice site and subsequently giving rise to the generation of oxygen vacancies, which reveals the formation of more surface oxygen vacancies (O_v) defects associated with the Ce^{3+}- O_v interaction during ammonolysis at higher temperature.[29,30]

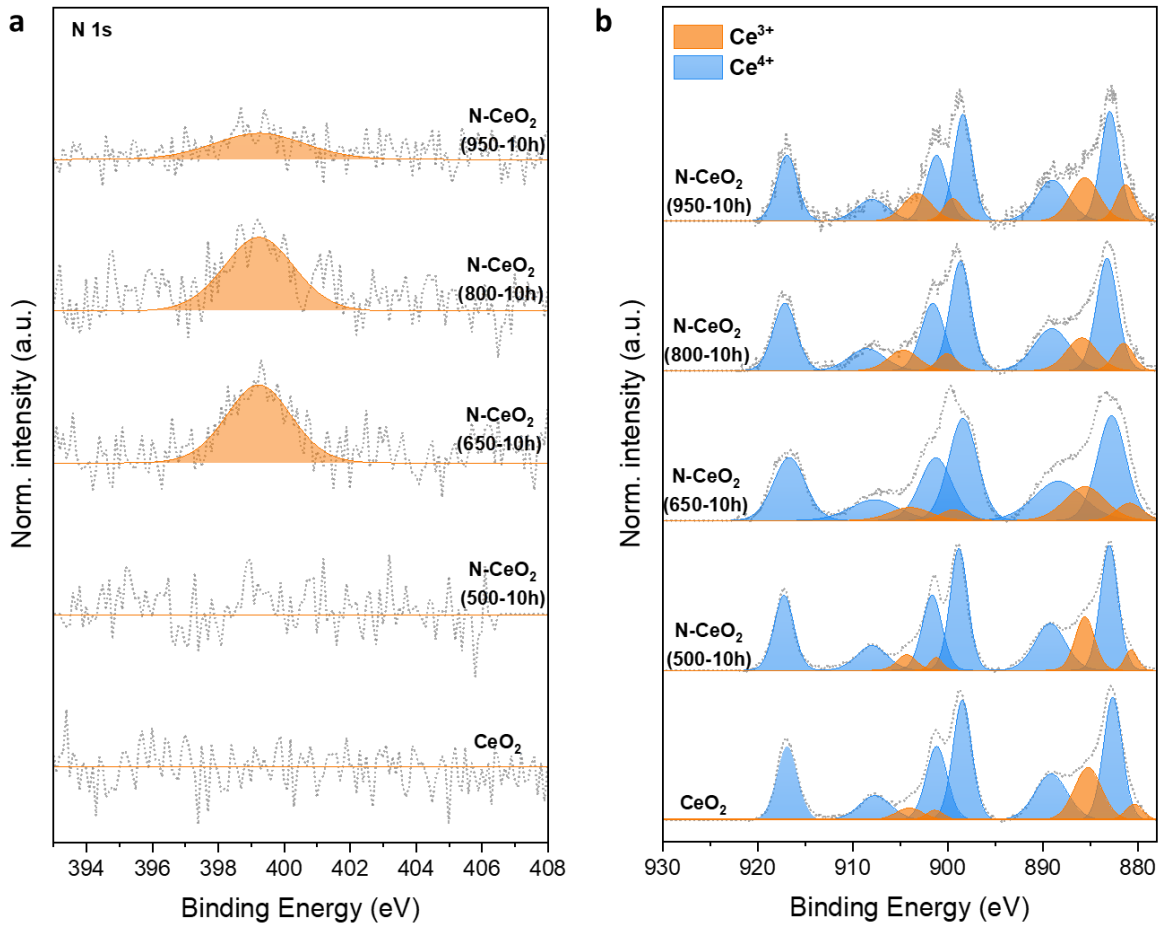


Fig. 4.4 High resolution X-ray photoelectron spectroscopy results of the analogue support samples. a. N 1s orbital spectrum. b. Ce 3d orbital spectrum.

The redox property of the support is further analysed using H_2 temperature programmed reduction analysis (H_2-TPR). As presented in **Fig. 4.5**, two distinct peaks are illustrated, one surface oxygen reduction peak between 200 -300 °C and another reduction peak in the temperature range of 350 -500 °C owing to the outer-layer of CeO_2 to Ce_2O_3.[31,32] The N-CeO_2(650-10h) support exhibits the lowest reduction temperature of the first peak (241 °C). This is followed by N-CeO_2(800-10h) (245 °C), N-CeO_2(500-10h) (250 °C), N-CeO_2(950-10h) (256 °C) and CeO_2 (276 °C). Similar trend was found for the later peak representing reduction of the outer-layer. The reduction temperature range can directly reflect the extent of

involvement of surface-active oxygen species and is intricately linked to the easy of formation of oxygen vacancies. A shift indicated that the N doping could promote the reducibility of neighbouring Ce ions and possess better mobility for oxygen vacancies generation.[33,34] Furthermore, the extend of reduction temperature shift is in well alignment with the amount of nitrogen incorporation into the support as found using XPS and CHNS.

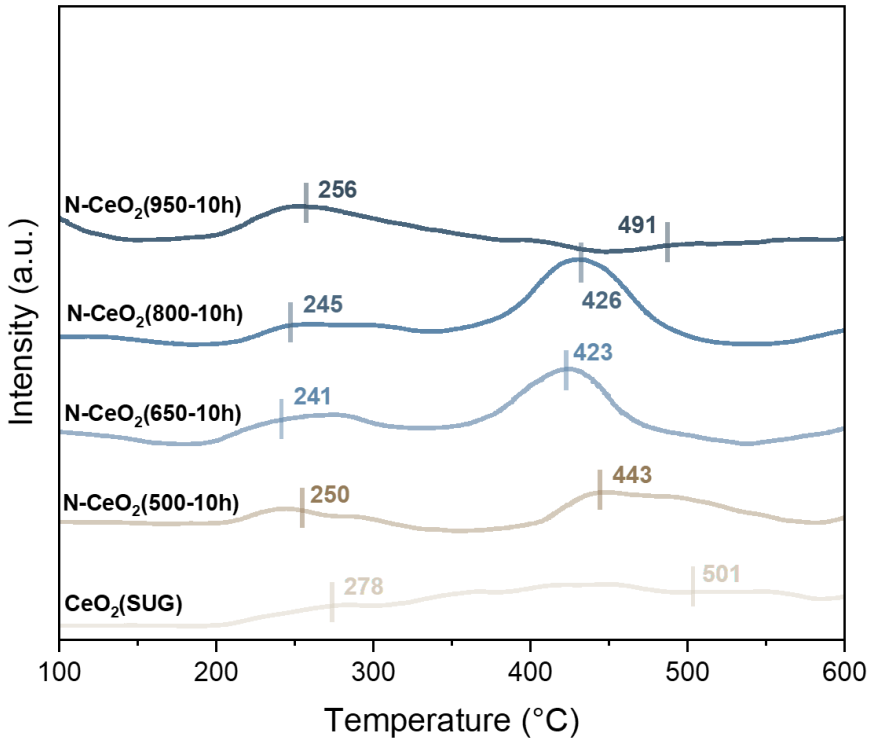


Fig. 4.5 H_2-TPR spectrum of the nitrogen doped cerium oxide calcined at different temperatures.

During the annealing process of CeO_2 under NH_3 flow, N is substituted for oxygen in the lattice structure. Since N is more electronegative compared to oxygen, it would pull electrons away from the lattice oxygen and thereby weaken the surrounding metal-oxygen bonds. Weaker metal oxygen bonds would lower the energy barrier required for one oxygen atom to leave from its lattice state and meaning oxygen vacancy can be easier formed. When a negatively charged oxygen lattice is removed, the support is left with a positively charged vacancy. This charge is compensated by the support via promoting electron redistribution and stabilizing the

Ce^{3+} state (as it has one more electron compared to Ce^{4+}).[Role of N doping in the reduction] This accompanied shift in the Ce^{3+}/Ce^{4+} ratio directly correlates with the formation of oxygen vacancies. Thus, incorporating N dopants would promote the redox property of the support which is favourable for catalytic reactions.

4.2.2 Catalytic measurements

To evaluate the nitrogen dopant effect towards catalysis, catalytic NH_3 decomposition over Ru-loaded cerium oxide and nitrogen doped cerium oxide was tested over pure NH_3 gas flow. It is shown that Ru on NH_3 annealed cerium oxide in general outperforms the pristine Ru/CeO_2 catalyst, furthermore, the catalytic activity is strongly dependent on the annealing temperature and time. As shown in **Fig. 4.6a**, the ammonia conversion significantly increases from ca. 60% at 500 °C and a weight-hour-space-velocity (WHSV) of 30,000 ml g_{cat}^{-1} h^{-1} for Ru/CeO_2 to ca. 95% for Ru/N-CeO_2(650-10h) under the same condition. The catalyst was further promoted and reaching an equilibrium conversion of ca. 99% at the above-stated condition whilst reducing the annealing time to 6 h. Nitrogen doping is commonly considered as an approach to promote catalytic activity of metal-based catalysts due to the electronic donation effect.[35,36] The lone pairs of electron of N atoms replacing O atoms in the cerium oxide structure can increase electronic donating properties over the support surface, hence adding toward the increasing basicity of the support. This will easily allow electron transfer from the nitrogen doped supports to Ru NPs and increasing the activity of Ru for ammonia decomposition. Both XPS and CHNS analysis showed that nitrogen content increase with calcination time and reaches a maximum nitrogen uptake of 3.12 % at 6 h and 650 °C (**Table 1**). This matches with the catalytic result for **Fig. 4.6b**, where higher nitrogen concentration led to higher activity. However, it is interesting to note that the conversion of Ru/N-CeO_2(500-10h) shows comparative ammonia conversion of ca. 80% to Ru/N-CeO_2(800-10h) given that the nitrogen content of the later one is higher. This is ought to the increase in crystal size observed from both XRD and SEM data. Larger crystal size is always accompanied by lower surface area to approach thermodynamic stability, thus worsening the dispersion and lead to growth of larger

Ru NPs size which is another key factor reducing the catalytic activity.[37,38] The promotion effect from extra N incorporation thus cancels out and thereby lead to the volcano shaped trend as presented.

Table 2 Ru loaded metal oxide-based ammonia decomposition catalysts.

Catalyst	Ru content[a]	Reaction Temp.[b]	WHSV[c]	NH_3 Conv.[d]	H_2 formation rate[e]	Reference
Ru/α-Al_2O_3	1.3	400	60,000	ca. 10.0	6.7	[39]
Ru/Sm_2O_3	3.8	450	30,000	84.6	25.9	[40]
Ru/$La_{0.33}Ce_{0.67}$	1.8	450	6,000	99.9	6.7	[41]
Ru/CeO_2	1.0	350	22,000	ca. 32.0	8.1	[42]
Ru/c-MgO	4.7	450	30,000	80.6	26.5	[43]
Ru/MgO (111)	3.4	450	30,000	99.9	32.4	[44]
Ru/C12A7:e^- [b]	2.2	450	15,000	99.9	16.7	[45]
Ru/Ce_5/MgAl(600)	2.0	465	30,000	50.0	16.8	[46]
RuLaCs/Al_2O_3	1.0	450	5,000	99.0	5.2	[47]
Ru/CeO_2NR-v	0.5	450	15,000	ca. 80.0	13.3	[17]
Ru/NH_2-DMSMs	5.0	450	36,000	43.6	17.5	[48]
Ru/CeO_2 (SUG)	1.6	450	30,000	37.5	12.2	**This work**
Ru/N-CeO_2 (650-6h)	1.6	450	15,000	96.0	16.5	**This work**
Ru/N-CeO_2 (650-6h)	1.6	450	30,000	81.0	26.6	**This work**
Ru/N-CeO_2 (650-6h)	1.6	450	72,000	50.6	40.6	**This work**

Note: [a] unit: wt. % ; Ru content of this work obtained using ICP-MS [b] unit: °C [c] unit: ml g_{cat}^{-1} h^{-1} [d] unit: % [e] unit: mmol$g_{cat}^{-1}$$min^{-1}$.

Further catalytic measurements were conducted on the catalyst with best performance Ru/N-CeO_2(650-6h). The WHSV was varied and an almost equilibrium conversion of ca. 96% at

450 °C at a WHSV of 15000 ml g_{cat}^{-1} h^{-1}, which outperforms most of the state-of-the-art Ru based catalysts (**Table 2**), is achieved (**Fig. 4.6c**). It is as expected that ammonia decomposition conversion decreases with the increase of WHSV owning to the shorter residence time for NH_3 absorbed on active sites.

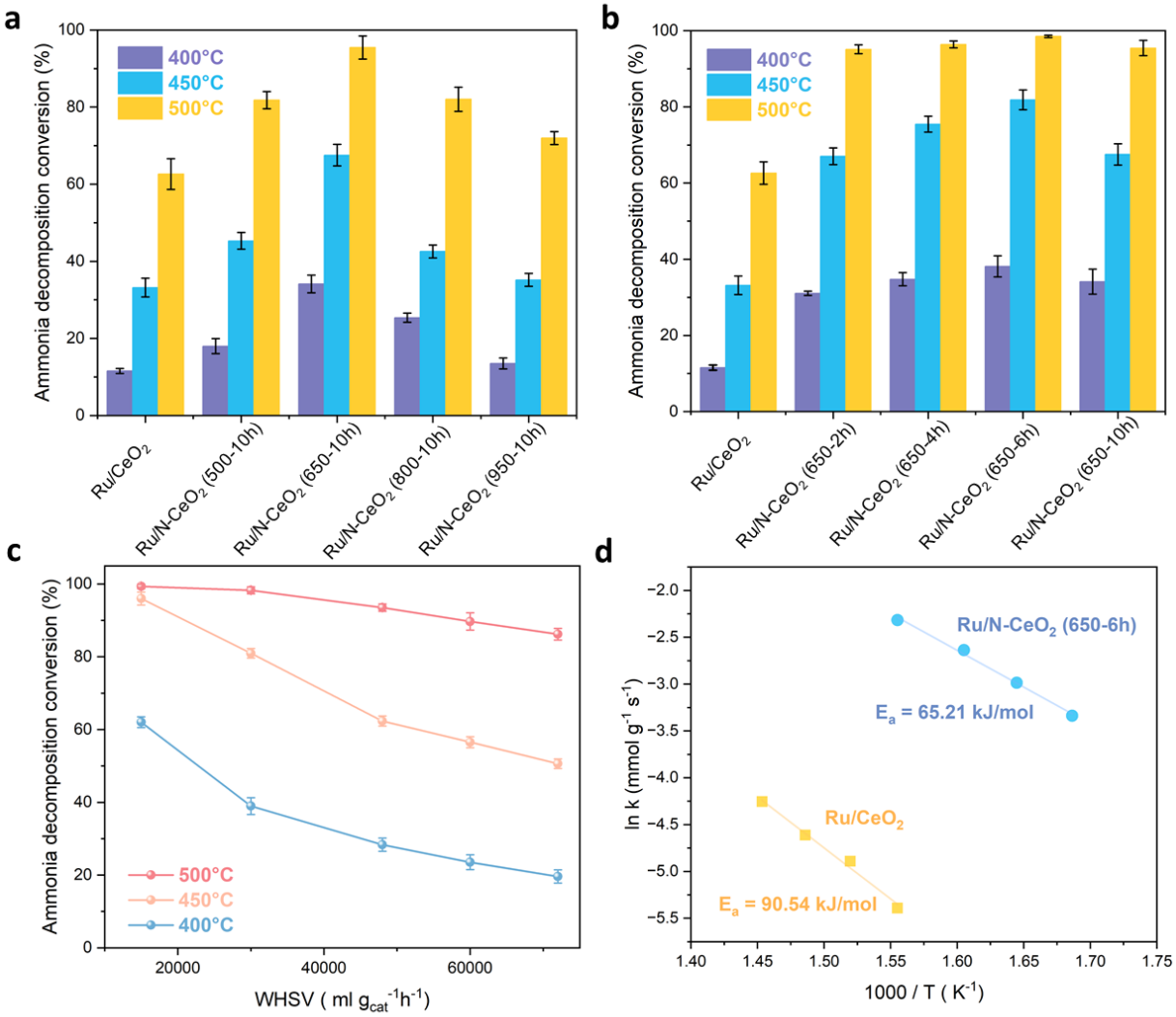


Fig. 4.6 Ammonia decomposition catalysis a-b. ammonia decomposition conversion over Ru on CeO_2 and N-CeO_2 calcined at different temperature and time. c. ammonia decomposition conversion over Ru/N-CeO_2(650-6h) at different weight-hour-space-velocity. d. Arrhenius plot of Ru/CeO_2 and Ru/N-CeO_2(650-6h).

Kinetic studies were performed over Ru/CeO_2 and Ru/N-CeO_2(650-6h) and the results are compared. The Arrhenius plots are obtained by the linear fitting of Ln (rate of ammonia

decomposition) vs 1000/T in the low conversion range (conversion < 15%). This is to keep the system in the kinetic regime and limit the effect of mass transfer on the rate of reaction. The apparent activation energy (Ea) of Ru/CeO_2 is found to be 90.54 kJ mol^{-1}, which lies in the range of 80–115 kJ mol^{-1} for traditional Ru/CeO_2 catalysts (**Fig. 4.6d**).[49,50] However, it is interesting to note that with N doping, the E_a energy of Ru/N-CeO_2(650-6h) drops significantly to 65.21 kJ mol^{-1}. Activation energy is a reflectance over the rate-determining step (RDS) in the overall reaction, which is in general considered to be N recombination for Ru based systems.[2] Thus, the low E_a value for the Ru/N-CeO_2(650-6h) which lies out of the range of typical dissociative ammonia decomposition mechanism over Ru based catalyst would suggest a shift in the overall reaction pathway.

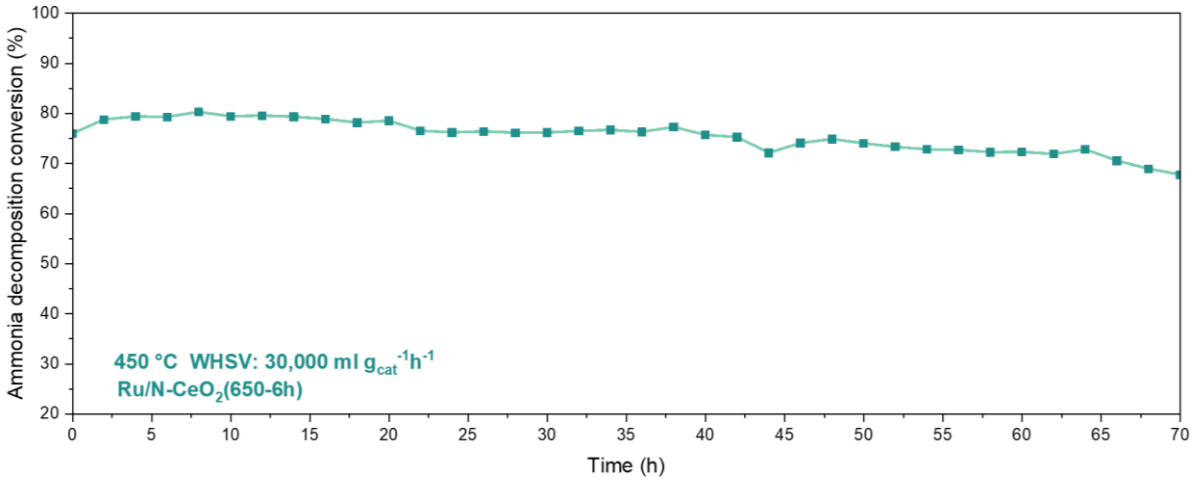


Fig. 4.7 Stability test on ammonia decomposition over Ru/N-CeO_2(650-6h) catalyst at 450 °C and 30000 ml g_{cat}^{-1} h^{-1} for 70 h.

To access long-term stability, the Ru/N-CeO_2(650-6h) sample was placed under continuous flow of NH_3 at 450 °C and 30000 ml g_{cat}^{-1} h^{-1} for 70 h. As illustrated in **Fig. 4.7**, no significant drop in the conversion is observed. Moreover, the XRD, SEM have been carried out over the catalyst after the catalysis (**Fig. 4.8a-c**). No significant change is observed from both its diffraction pattern and the microscopic image. These findings demonstrating the strong

structural stability of N-CeO_2 that holds through-out the catalysis. Thereby, highlight its potential for industrial applications in ammonia decomposition.

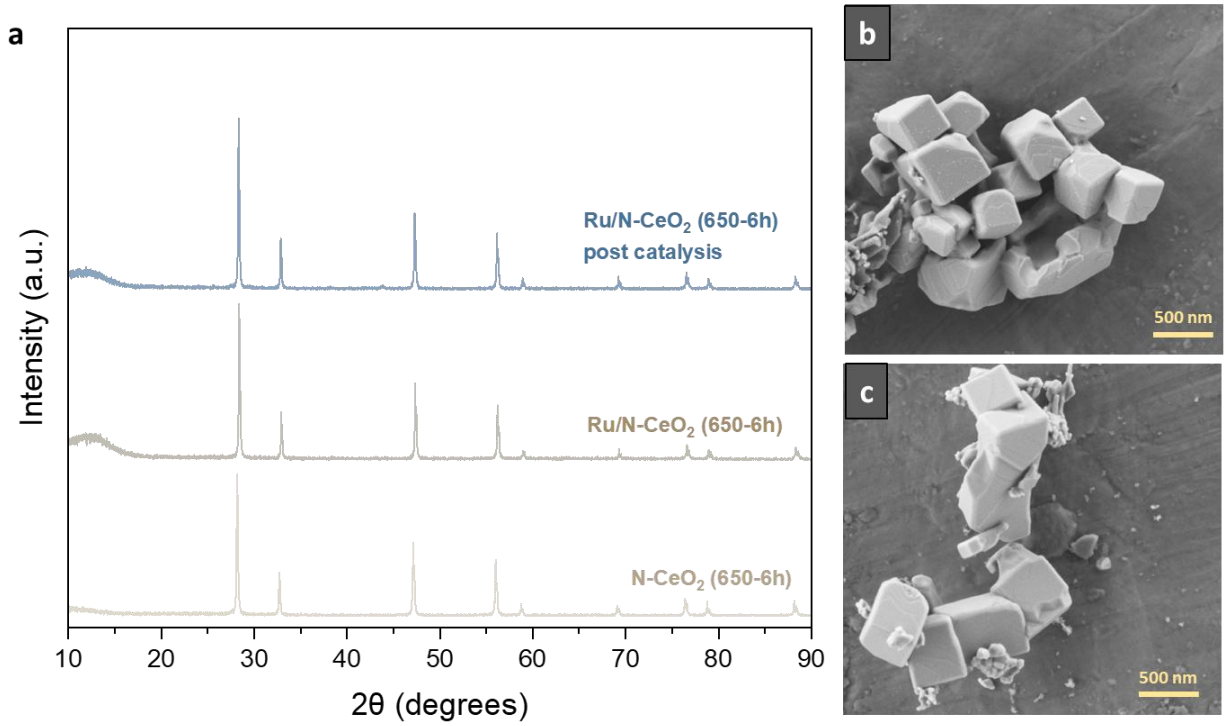


Fig. 4.8 Structural properties of Ru/N-CeO_2(650-6h) catalyst after catalysis. a. XRD patter. SEM image of the sample b. After Ru impregnation and c. After Ru impregnation and ammonia decomposition catalysis.

4.2.3 Metal support interaction

Since Ru/N-CeO_2 (650-6h) exhibits the best catalytic activity, the following sections would investigate the N dopant effect with particular focus on comparing Ru/N-CeO_2 (650-6h) and Ru/CeO_2. Unless otherwise stated, Ru/N-CeO_2 (650-6h) will be referred to Ru/N-CeO_2 for simplicity.

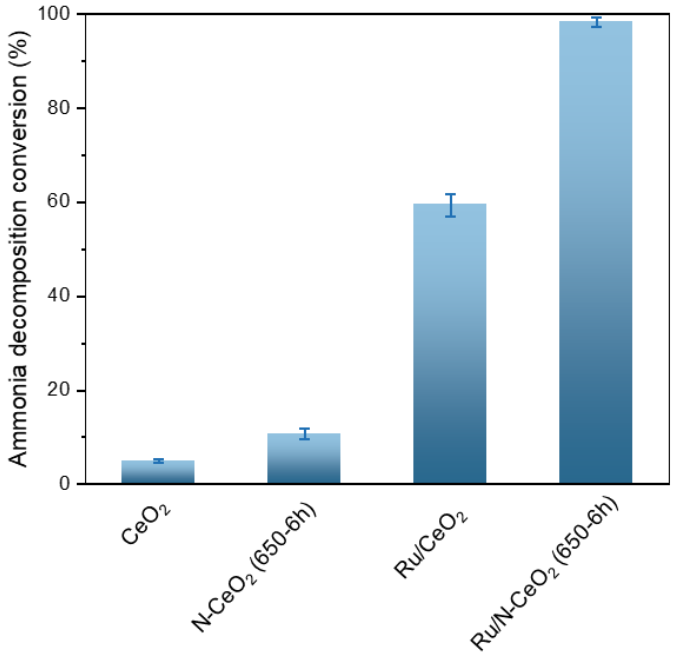


Fig. 4.9 Ammonia decomposition over the analogue support and Ru impregnated catalysts. The conversion taken at 500 °C and WHSV = 30,000 ml g_{cat}^{-1} h^{-1}.

The catalytic activity of plain support CeO_2 and N-CeO_2 as well as their Ru impregnated catalyst has been carried out and compared (**Fig. 4.9**). Not surprisingly, plain Cerium oxide support showed really low activity. The nitrogen doped support exhibits a higher activity than plain CeO_2. The origin of this activity will be discussed in the later section. Since the conversion of ammonia dramatically increased after Ru impregnation, it is believed that the main active site is contributed from the Ru NPs.

To reveal the MSI of different support and relate it to the catalytic activity, H_2-Temperature programmed reduction analysis (H_2-TPR) has been performed. As illustrated in **Fig. 4.10**, a clear peak in the range 90-150 shows up, which is accounted to the reduction peak of oxide Ru species.[51] This peak shifts remarkable from 95 up to 144 °C for Ru on nitrogen doped CeO_2 calcined at different temperature. The exposed surface nitrogen sites offer a stronger interaction accounting for the higher degree of temperature shift.

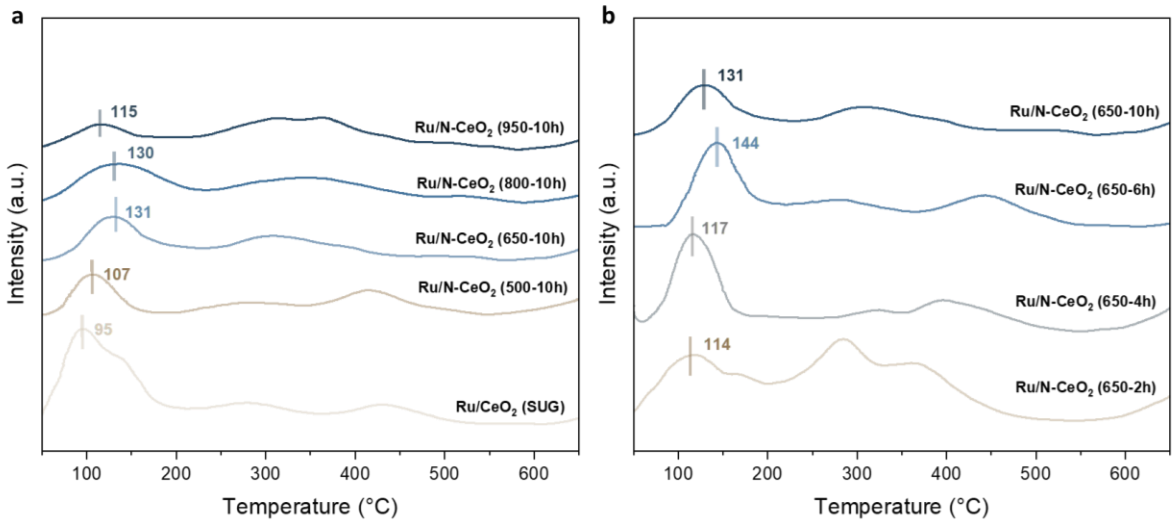


Fig. 4.10 H_2-TPR spectrum of Ru on nitrogen doped cerium oxide calcined at different temperatures and durations.

It is interesting to note that a linear relationship is observed between the calculated nitrogen content on the surface and the reduction temperature of the Ru oxide species (**Fig. 4.11**). The underlying mechanism involves the coordination of nitrogen dopants with Ru species. Nitrogen atoms incorporated into the CeO_2 lattice possess lone electron pairs, which can act as Lewis bases.[52] These electron pairs are capable of forming coordination bonds with cationic Ru species during impregnation, thereby anchoring Ru cations and resulting in the formation of Ru–N interactions. Such bonding increases the stability of the oxidized Ru state, making it more resistant to reduction under hydrogen flow. As a result, higher temperatures are required to reduce Ru^{n+} to metallic Ru^0, which manifests as a positive shift in the TPR peak.

In addition to ligand-type interactions, the presence of nitrogen can also alter the electronic environment of the support, modifying the electron density at the Ru site and strengthening MSI and thus increases the reduction temperature of the metal species.[36]

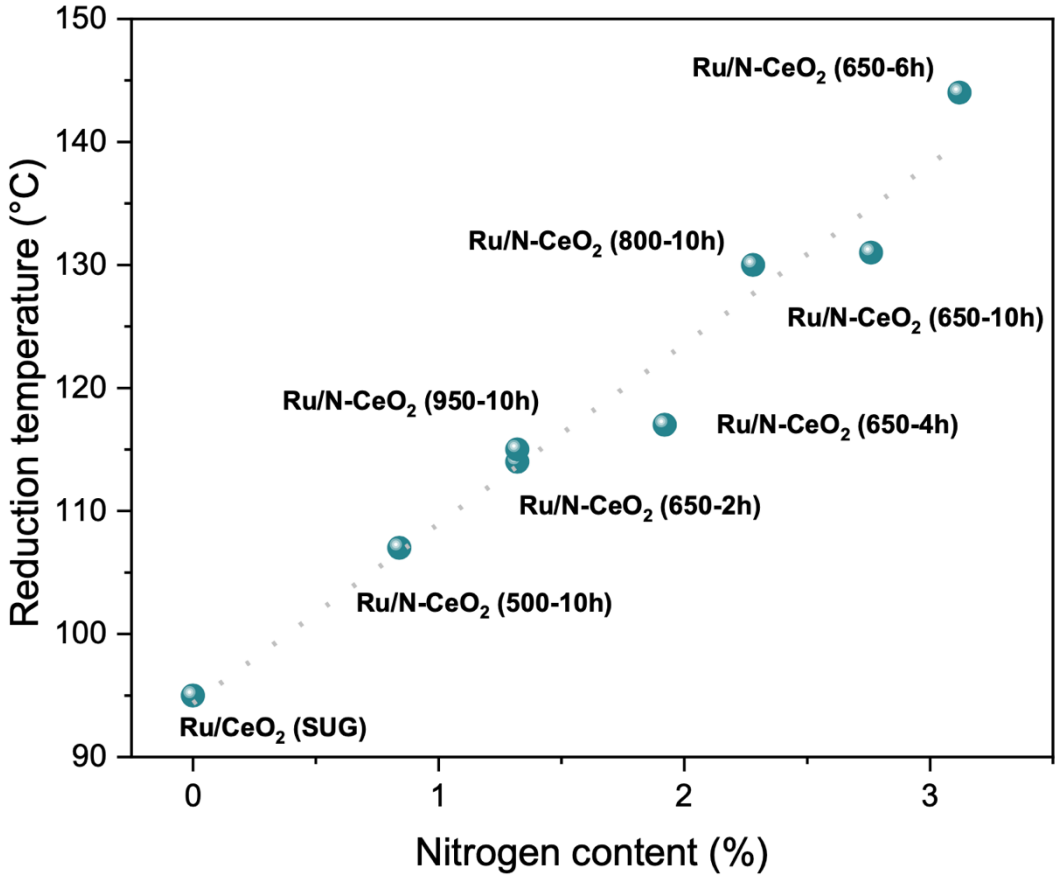


Fig. 4.11 Corelation diagram of the reduction temperature of Ru and the content of the nitrogen dopant.

To gain further insights into the interaction between the Ru NPs and the cerium support, paying particular attention towards the N dopant effect, three different stages of Ru on the catalyst: i) as synthesized after wetness impregnation (AS), ii) after reduction (RED), and iii) after catalysis (AC), were synthesized and analysed. Geometrical and chemical properties of the Ru NPs on the support was investigated using Extended X-ray Absorption Fine Structure (EXAFS) and X-Ray Absorption Near Edge Structure (XANES).

As shown in **Fig. 4.12a-b**, it is noteworthy that for Ru supported on pristine CeO_2 and the nitrogen doped samples (after Ru impregnation but before reduction), a clear shift is observed in the peak position corresponding to Ru–O/Ru–N bonds.[41] It suggests that the Ru NPs upon impregnation, interact with the surface nitrogen dopants possessing a chelating and anchoring

effect. Such interactions are indicative of strong metal–support interaction (MSI), which typically leads to improved metal dispersion and enhanced catalytic performance. Notably, the Ru–N bond exhibits a shorter bond distance compared to Ru–O, consistent with the stronger bond strength of Ru–N. This is also in alignment with the H_2-TPR data mentioned above, where upon N treatments, the Ru requires a higher reduction temperature, further confirming strengthened MSI due to nitrogen incorporation.

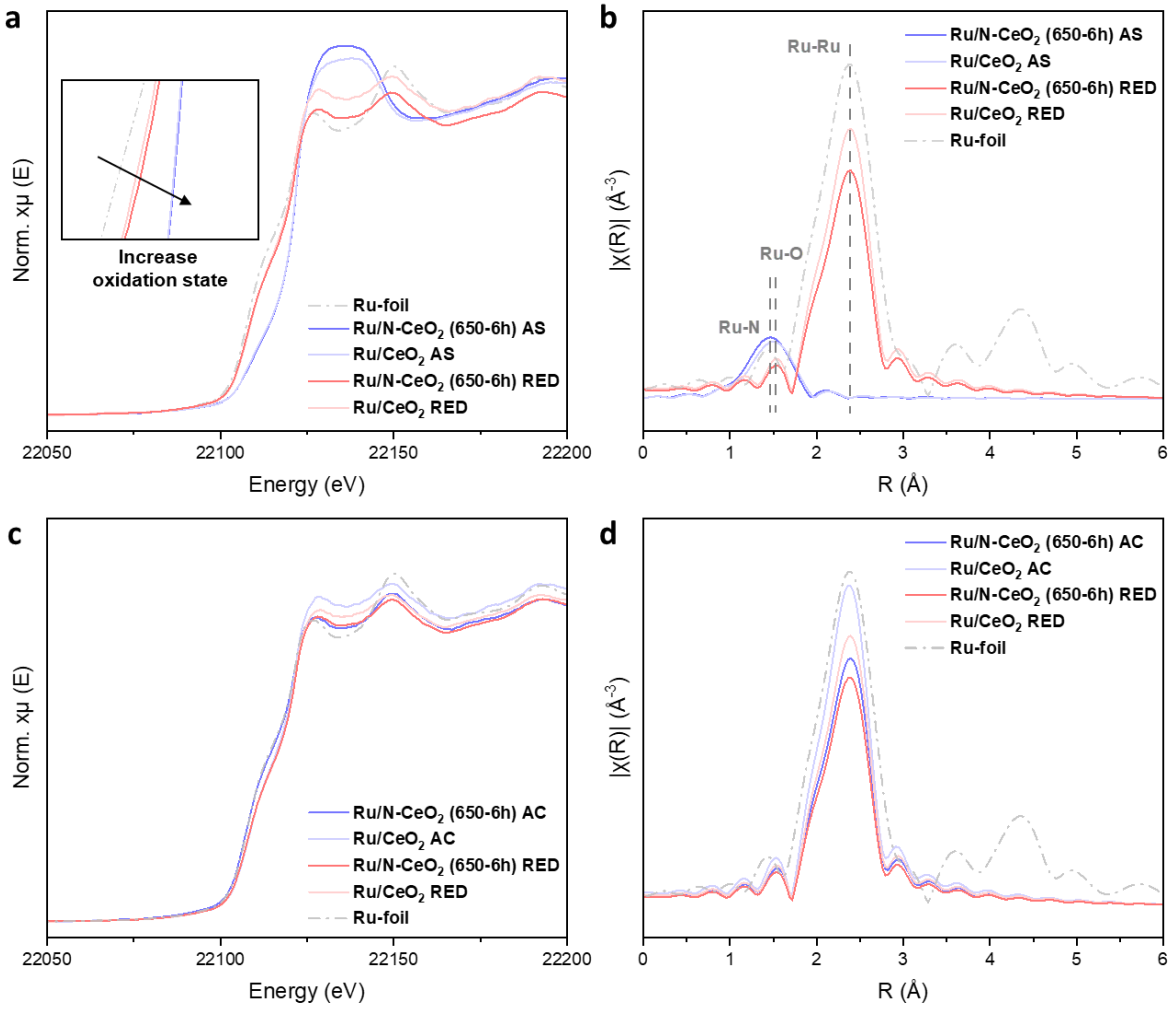


Fig. 4.12 X-Ray adsorption spectroscopy on the Ru K edge of the analogue catalysts. Comparison between catalyst as synthesized and reduced a. XANES and b. R space derived from EXAFS; Comparison between catalyst after reduction and after catalysis c. XANES and d. R space derived from EXAFS.

After reduction, a huge increase in the metallic Ru-Ru bonding peak located at 2.67 Å is observed. This indicates that most of the Ru exists as metallic NPs on the surface. Nevertheless, the reduced samples still exhibit a higher average oxidation state compared to Ru foil. This can be attributed to a small fraction of Ru interacting with the surface oxygen/nitrogen exposed on the support located at the metal support interface. However, since the nitrogen content of the sample is only ca 3%, it renders such effects subtle and difficult to distinguish in the R-space EXAFS spectra.

Table 3 EXAFS fitting parameters, related to Fig. 4.12

Composition	Shell	N	R (Å)	σ^2	R factor
Ru CeO_2 AS	Ru-O	5.931 ± 0.81	2.043 ± 0.017	0.0087	1.92%
Ru N-CeO_2 AS	Ru-O/N	6.729 ± 0.80	2.014 ± 0.015	0.0095	1.41%
Ru CeO_2 RED	Ru-Ru	9.466 ± 1.36	2.670 ± 0.006	0.0042	1.28%
Ru N-CeO_2 RED	Ru-Ru	8.460 ± 1.40	2.670 ± 0.005	0.0043	1.67%
Ru CeO_2 AC	Ru-Ru	11.138 ± 1.59	2.670 ± 0.005	0.0043	1.26%
Ru N-CeO_2 AC	Ru-Ru	8.516 ± 1.18	2.670 ± 0.005	0.0047	1.22%

N, coordination number; R (Å), bond length; σ^2, Debye-Waller factor

Further comparison with samples after catalysis revealed that minimal change in Ru oxidation state is observed, and no signs of Ru nitridation are detected, highlighting the stability and nitridation resistance of Ru under prolonged reaction conditions (**Fig. 4.12c**). However, on the other hand, increase in the Ru-Ru coordination number is found after catalysis (**Table 3**). Particularly for Ru/CeO_2 catalyst, where the coordination number increased from 9.5 to 11. Similar to the phenomenon that larger crystallites are found at higher synthetic temperature, it is indicative of particle sintering under reaction conditions. Such aggregation leads to a reduction in the number of exposed active sites, which is a primary cause of catalyst deactivation. The nitrogen doped sampled showed relatively stable coordination number after

catalysis, indicates that N incorporation can help to stabilize the Ru and inhibit further aggregation. These findings further emphasize the importance of surface nitrogen configuration, as nitrogen dopants help anchor Ru nanoparticles, limiting their mobility and preventing sintering. Thus, nitrogen sites play a key role not only in enhancing metal dispersion but also in maintaining catalyst stability and promoting sustained catalytic activity.

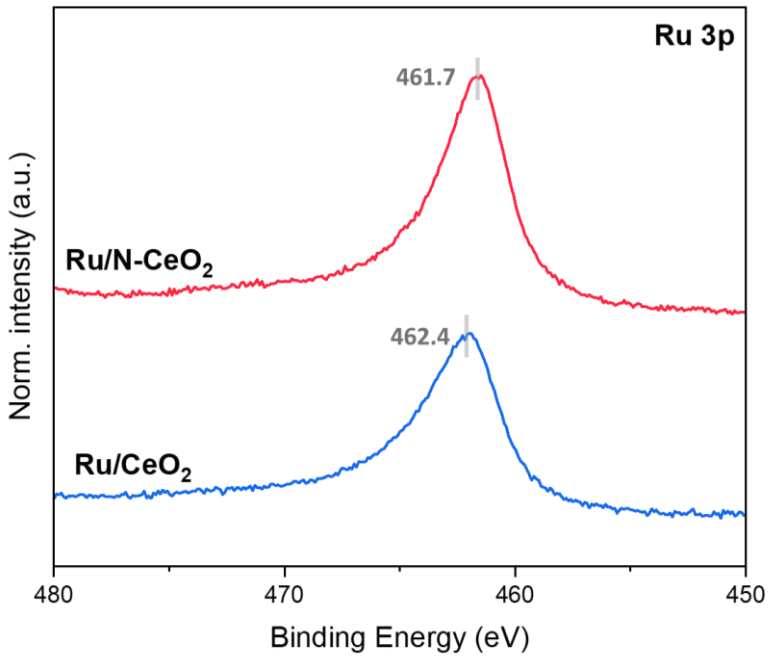


Fig. 4.13 XPS spectrum of the Ru 3p orbital of the analogue reduced samples.

Similar trend in the oxidation state was found by analysing the XPS spectrum of the Ru 3p orbital of the analogue reduced catalyst. A huge peak is raises which corresponds to the Ru^0 species.[53] Suggesting that the predominantly phase of Ru on both supports are metallic Ru, corroborating with the result from XAS spectrum. Nevertheless, it is interesting to note that there is a slight deviation of the experimental tested Ru 3p peak from Ru/N-CeO_2 and the literature value 461.2 eV, this is ought to the slightly partial charge crossing the interphase between the Ru NPs and the cerium oxide support. This interfacial electronic effect is likely due to the different chemical environments created by oxygen and nitrogen coordination. Specifically, nitrogen tends to stabilize Ru in a +3 oxidation state via Ru–N bonding, whereas

oxygen typically coordinates Ru in the +4 state, as in RuO_2.[54,55] As a result, the N doped system exhibits a slightly lower binding energy, reflecting a lower average oxidation state of Ru, as shown in **Fig. 4.13**. This subtle shift provides further evidence of electronic modification of the Ru sites by nitrogen, reinforcing the role of N dopants in tuning metal–support interactions and potentially influencing catalytic behaviour.

To better visualize and analyse the size and morphology of the catalyst, transmission electron microscopy (TEM) was employed. As illustrated in **Fig 4.14**, the image of high-angle annular dark-field scanning transmission electron microscopy (HAADF-STEM) illustrates small bright dots that are due to Ru atoms. As seen from **Fig. 4.14a**, Ru is well dispersed across the surface of N-CeO_2 forming atomic clusters of an average size of 1.75 nm. The corresponding energy-dispersive X-ray spectroscopy (EDS) mapping further manifests the homogeneous distributions of Ce, O, N and Ru on the catalyst. The Ru NPs on pristine CeO_2 shows a slightly higher average particle size of 2.5 nm (**Fig. 4.14f**). This feature is in good agreement with the XAS result, where it displays a higher Ru–Ru coordination number compared to the nitrogen-doped counterpart, indicative of larger metal clusters. These results corroborate our earlier discussion that nitrogen dopants act as anchoring sites for positively charged Ru ions through its lone pair of electrons, thus enhancing metal dispersion and smaller averaged particle size.

Further structural insights can be drawn by comparing the plain CeO_2 and N-CeO_2 support, it is interesting to note that there are many defects which are revealed by the dark spot, existing on the surface (**Fig. 4.14k-l**). It is interesting to note that size of these defects matches in size with the observed Ru (**Fig. 4.14m-n**). During initial calcination of the cerium gel mixture, evaporation and combustion of urea leave behind surface pits and voids. Suggesting that these depressions can also help to form finely and well dispersed NPs by serving as an anchoring site.

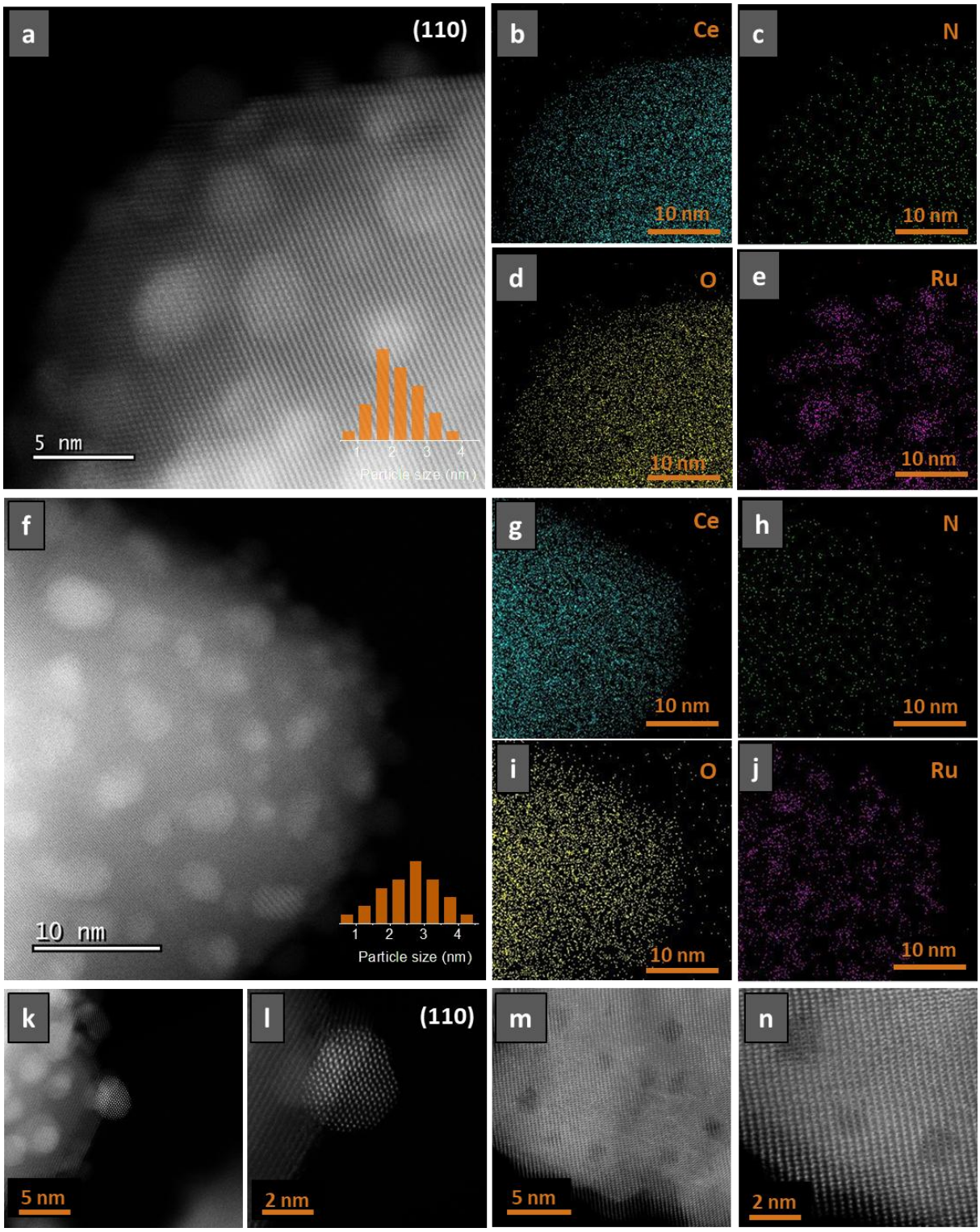


Fig. 4.14 High-angle annular dark-field scanning transmission electron microscopy (HAADF-STEM) of a. Ru/N-CeO_2 after reduction f. Ru/CeO_2 after reduction; Energy-dispersive X-ray spectroscopy (EDS) mapping on the Ce, N, O and Ru elements of b-e. Ru/N-CeO_2 RED and g-j. Ru/CeO_2 RED. K-l. Imaging showing the (110) plane of the Ru NPs on Ru/N-CeO_2 RED. m-n. Imaging showing the plane N-CeO_2 support without Ru impregnation.

Additionally, the removal of urea may also lead to exposure of higher-index crystal planes, which are generally more reactive than the low index planes.[56] This can facilitate nitrogen doping preferentially at defect-rich sites. Given that nitrogen atoms are larger than oxygen atoms, substitutional doping results in local structural distortion.[57,58] This distortion, particularly at the interface between the Ru nanoparticles and the N-doped support, can enhance MSI by modifying the local coordination environment and electronic structure, which is keen to catalytic performance.

4.2.4 Mechanistic understanding

Operando NH_3 DRIFTS measurements were carried out over the following samples to understand the reaction mechanism for ammonia decomposition i) CeO_2 ii) Ru/CeO_2 iii) N-CeO_2 (650-6h) and iv) Ru/N-CeO_2 (650-6h). As being clearly observed from **Fig. 4.15a**, there are 3 peaks that appears for all four samples, symmetric N-H bending of NH_3 at 930.5 and 966.6 cm^{-1}, one asymmetric N-H bending peak located at 1627 cm^{-1} and one symmetric N-H stretching peak at 3334.5 cm^{-1}.[59] It is interesting to note that with increasing temperature, a significant decrease in the above mentioned peaks is observed for Ru impregnated samples. This is due to the effective ammonia decomposition taking place over the sample, resulting in lower retention time of adsorbed -NH species on the surface. At low temperature, a rise in the sharp peak between ca. 1400-1425 cm^{-1} is observed, this is assigned to the adsorption of NH_3 species to the surface of the CeO_2 support.[60,61] This peak vanishes as temperature increases which indicate desorption of the surface attached species at elevated temperature.[60] Furthermore, at higher temperature a broad and weak peak representing N=N bond at 1430 cm^{-1} shows up.[11,62] This peak appears in the spectra for Ru impregnated sample and surprisingly the N-CeO_2 (650-6h) support indicating distinct activity induced by nitrogen dopants. Moreover, it is interesting to note that a few peaks in the area 1900-2200 cm^{-1} are

raised only for the nitrogen doped ceria. As can be seen from **Fig. 4.15b**, 3 distinct peaks are observed, peaks at 2,163 and 1,970 cm^{-1} are attributed to N≡N stretching of N_2 molecules formed by inducing NH_3 decomposition.[11] The peak at 2060 cm^{-1} is ascribed as a key -N_2H intermediate species that is being detected on the surface of the support.[4,63] This feature is only observed for N doped cerium oxide support which suggests that lattice N dopants can serve as active sites binding with incoming NH_3 molecule to form N-N interaction. The phenomenon aligns similarly to the associative route proposed in ammonia synthesis, where N_2 gas is activated by the N vacancies in the catalyst support. For the associative ammonia synthesis pathway, N triple bonds from the gaseous N_2, instead of being directly dissociated, would be step wise hydrogenated via a *N=NH_x intermediate.[3] As for the context of ammonia decomposition, an associative route shall have N-N binding prior of cleaving all the N-H bonds. And the identification of the -N_2H species indicates that the catalyst will proceed the reaction through an associate manner. Furthermore, it is noted that the peak intensity is much smaller for the Ru impregnated sample. We accommodate this to the following reasons: Ru impregnated sample would result in high dispersed Ru NPs covering the surface of the support, which lead to reduced interaction between NH_3 and the lattice N; Incorporation of Ru NPs would significantly accelerate the reaction, resulting in lower retention time on the support to be observed via FTIR; Ru NPs would also adsorb NH_3 and proceed NH_3 cracking via a dissociative mechanism. Under this reaction route, -N_2H is not an intermediate as N triple bond is directly formed between two bare N atoms rather than being hydrogenated. Thus, this competition between the two routes would also result in a less significant peak change.

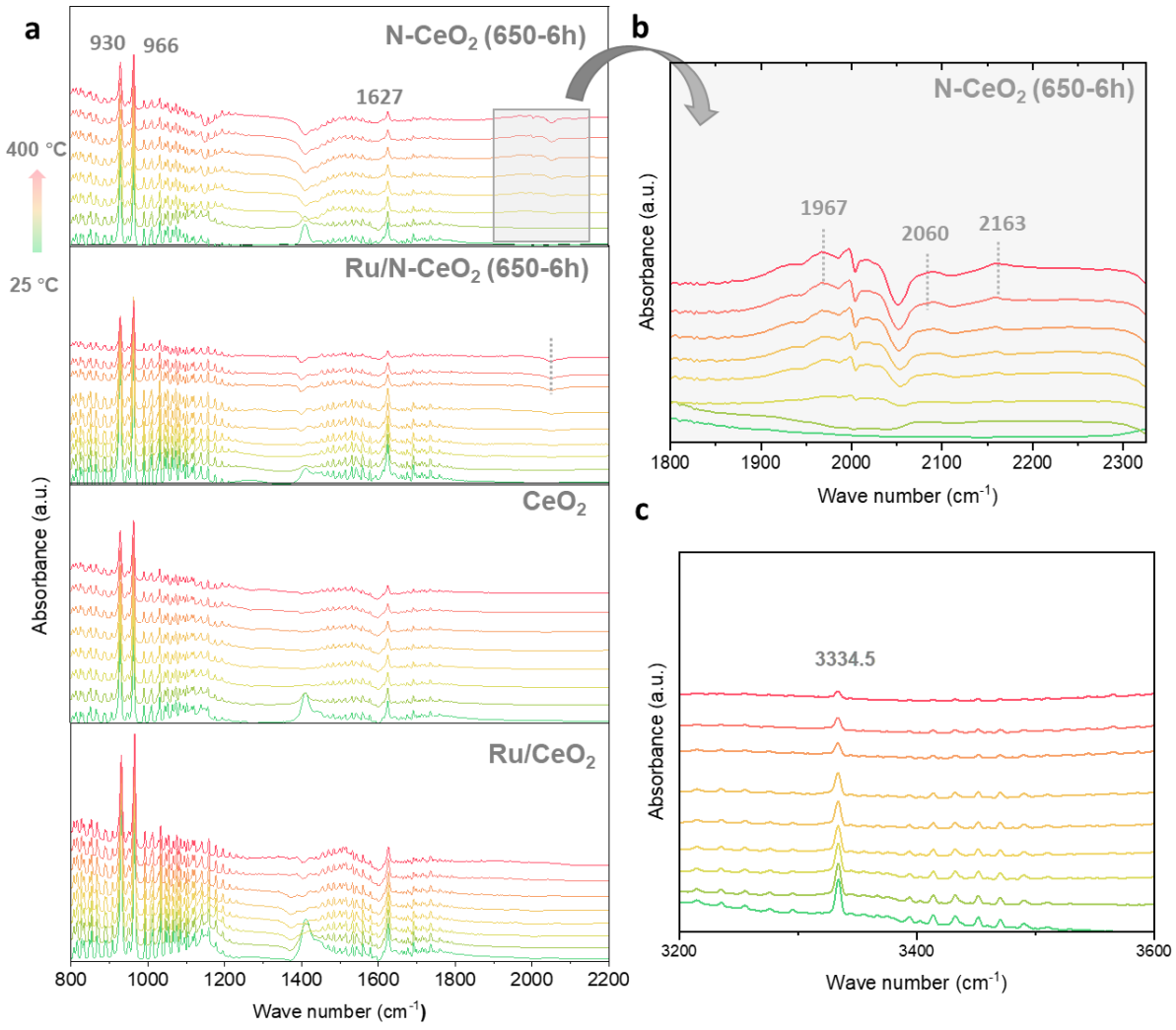


Fig. 4.15 Operando NH_3 FTIR spectroscopy analysis a. NH_3 DRIFTs of the analogue catalysts b. enlarged figure of the NH_3 DRIFT spectrum of N-CeO_2 (650-6h) c. Spectrum in the range 3200 -3600 cm^{-1}, showing the change in intensity of the N-H stretching mode of Ru/N-CeO_2 (650-6h) upon increasing temperature.

Further isotopic $^{15}NH_3$/$^{14}ND3$/$^{14}NH_3$ pulse experiments were carried out on time-resolved FTIR spectroscopy to evaluate the catalytic activity and reaction intermediates to a further extend. This time-resolved approach helps capture short-lived intermediates by introducing reactants in short, controlled bursts, allowing transient species to be observed before they are fully converted to products. As illustrated in **Fig. 4.16a-b**, the same characteristic NH_3 peaks are observed during the $^{14}NH_3$ pulse over the Ru/N–CeO_2 catalyst. These peaks decrease in

intensity over time, consistent with the progressive decomposition of ammonia into nitrogen and hydrogen gas. A particularly notable observation is the emergence of a broad O–H vibrational band around 3500 cm^{-1}, along with a sharp, isolated O–H peak at 3648 cm^{-1}, attributed to surface hydroxyl groups. Both peaks diminish during Ar purging, indicating their transient nature under reaction conditions. Concurrently, a distinct band at 1918 cm^{-1}, assigned to Ru–H stretching, also diminishes over time (**Fig. 4.16b-c**).[44] The synchronous evolution of O–H and Ru–H peaks during NH_3 decomposition suggests that the surface hydroxyls originate from the dissociation of ammonia. The hydrogen atoms generated during decomposition appear to migrate from Ru sites to the CeO_2 support, reacting with surface oxygen to form O–H groups. This hydrogen migration directly indicates that the Ru/N-CeO_2 catalyst exhibits a notable hydrogen spill-over effect. $^{14}ND_3$ pulse experiment further corroborated the idea (**Fig. 4.16d**), where the broad O–H and isolated O–H peaks shift to ~2500 and 2680 cm^{-1}, respectively. These shifts are consistent with expectations from the harmonic oscillator model for isotopic substitution (3500 cm^{-1} × $(\mu_{OH}/\mu_{OD})^{0.5}$ = 2500 cm^{-1} and 3648 cm^{-1} × $(\mu_{OH}/\mu_{OD})^{0.5}$ = 2630 cm^{-1}). Comparative analysis of spectra from $^{14}NH_3$ and $^{15}NH_3$ pulses also reveals a red shift in the N=N stretching region, with the peak moving from 1430 to 1405 cm^{-1} (**Fig. 4.16e**). This shift corresponds to the formation of $^{15}N=^{15}N$ (1382 cm^{-1}) and $^{15}N=^{14}N$ (1406 cm^{-1}) species, supporting the nitrogen exchange between ammonia-derived nitrogen and lattice nitrogen, which was also validated by mass spectrometry results discussed in the later section. Additionally, the Ce–NH_x adsorption peak shifts from 1173 to 1165 cm^{-1}.[64,65] This red shift lends further support to an associative mechanism, where NH_3-derived intermediates engage directly with surface sites on the catalyst and probe further ammonia decomposition.

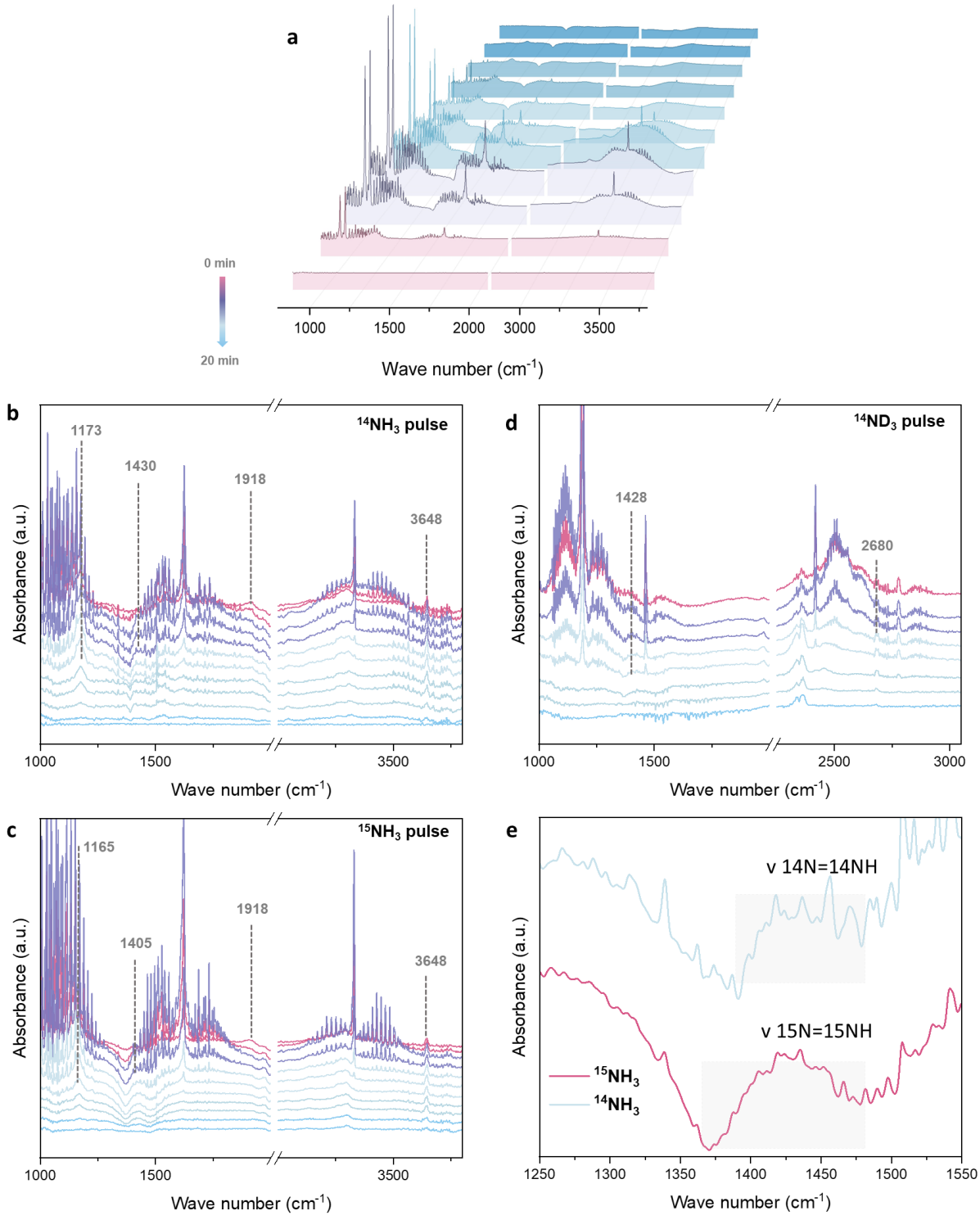


Fig. 4.16 Time resolved FTIR over Ru/N-CeO_2 catalyst under different isotopic pulses. Experiment carried out at 400 °C, 10 ml min^{-1} flow of Ar, each pulse contains 0.6 bar of either $^{15}NH_3$, $^{14}NH_3$ or $^{14}ND_3$. a. 3D waterfall plot of the spectrum over $^{14}NH_3$. Absorbance spectrum recorded under different pulses b. $^{14}NH_3$ c. $^{15}NH_3$ d.$^{14}ND_3$. e. Enlarged absorbance spectrum figure showing the broadening and red shift of the N=N peak upon inducing ^{15}N.

To further verify the reaction mechanism, $^{15}NH_3/^{14}NH_3$ pulse experiments were carried out over mass spectroscopy. As can be seen from Fig. **4.17a**, when $^{14}NH_3$ pulses were initially pumped into the reactor (the first two pumps), only peaks at m/z=28 which represents ^{14}N-^{14}N arises. This is well agreed as no ^{15}N is yet present in the system. However, when $^{15}NH_3$ is pulsed into the system, the signal intensities of 3 different peaks arise, which are accounted for m/z=28 (^{14}N-^{14}N), m/z=29 (^{15}N-^{14}N) and m/z=30 (^{15}N-^{15}N). The peak standing for ^{14}N-^{14}N is relatively small compared to the other two peaks. It is therefore considered as a change in baseline resulted by pulsing extra pressure to the system. Under dissociate mechanism, N_2 molecule is formed by bare N atoms supported by the NH_3 reactants, suggesting only rise in ^{15}N-^{15}N peak is expected. Therefore, a huge increase in m/z=29 peak clearly indicates interaction taking place at the surface of N doped cerium oxide. $^{15}NH_3$ will bond with the lattice ^{14}N from the support leading to the formation of ^{15}N-^{14}N, which well complies the associative mechanism proposed from the discussion above. More interestingly, after pulsing $^{15}NH_3$, the $^{14}NH_3$ pulse right after it would also give rise to a m/z=29 peak signal. Since, operando NH_3 FTIR over the Ru/CeO_2 and $Ru/N\text{-}CeO_2$ (650-6h) already revealed that NH_3 readily desorbs from the catalyst at temperature lower than 300 °C (**Fig. 4.15a**). XAS spectrum of the K-edge of Ru on Ru/CeO_2 and $Ru/N\text{-}CeO_2$ (650-6h) before and after catalysis also confirmed no change on the oxidation state of the Ru NPs, indicating no nitridation taking place (**Fig. 4.12c**). It can be concluded that by flushing argon after each pulse, no physically adsorbed $^{15}NH_3$ or $^{14}NH_3$ would remain on the catalyst, and no residue N from the reactants would be bounded to the active metal site. Based on these results, it is suggested that N exchange takes place at the surface between lattice N and N from ammonia gas. More specifically, $^{15}NH_3$ would drag the lattice ^{14}N out of the support, leading to the formation of nitrogen vacancies (V_N) on the support. Under $^{15}NH_3$ pulse, this V_N is filled by ^{15}N, which results in ^{14}N and ^{15}N exchange in the lattice of the catalyst. Thus, the next $^{14}NH_3$ pulse would also result in the formation of ^{15}N-^{14}N, but this time, it is the ^{14}N from $^{14}NH_3$ which interacts with the lattice ^{15}N. As more $^{14}NH_3$ is pulsed, a decrease in the m/z=29 peak signal is observed, owing to less lattice ^{15}N remaining in the support, thereby explaining the observation. The same experiment was carried out over

Ru/CeO_2 under the same condition, but no significant rise of m/z=29 peak was observed (**Fig. 4.17b**). Indicating that most of this associative pathway is introduced after N doping and further implies the essence of N pre-doping for promoting the catalysis. To sum up, this $^{15}NH_3/^{14}NH_3$ pulse experiment is strong evidence that the N doped cerium oxide catalyst would enable ammonia decomposition not only by the traditional dissociative pathway, but by also introducing an associative mechanism as illustrated in **Fig. 4.17c**.

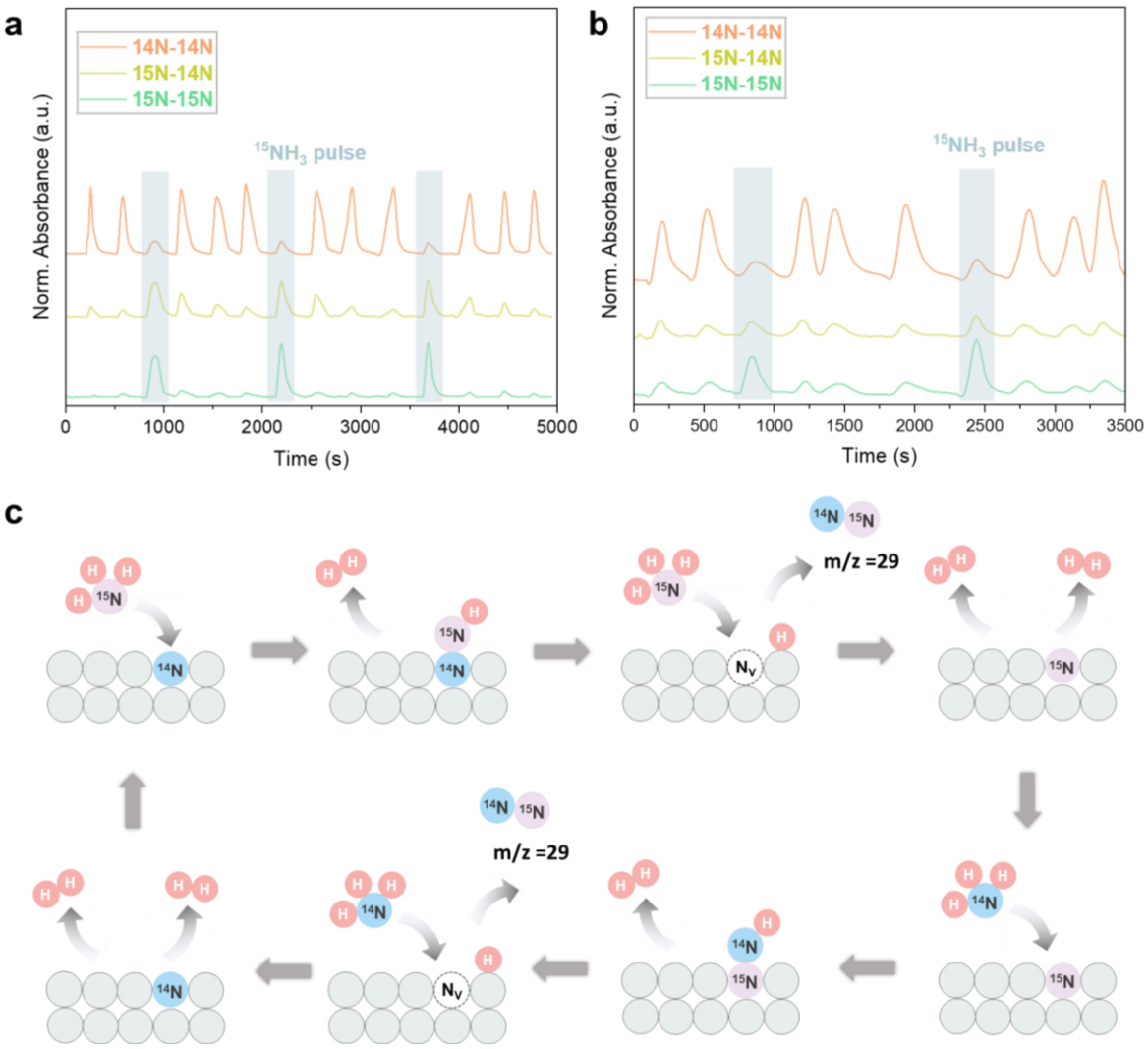


Fig. 4.17 $^{15}NH_3/^{14}NH_3$ pulse experiment operated at 450 °C, 10 ml min^{-1} flow of Ar, each pulse contains 0.6 bar of either $^{15}NH_3$ or $^{14}NH_3$. On a. Ru/N-CeO_2 and b. Ru/CeO_2 catalyst. c. Proposed associative ammonia decomposition pathway following the Mars-van Krevelen mechanism.

4.3 Computational modelling

To further verify the fundamental mechanism and gain in depth understanding on the thermodynamics of the reaction pathway. Computational calculation and analysis have been carried out with collaboration with *Mingyu Luo (Marvin)*.

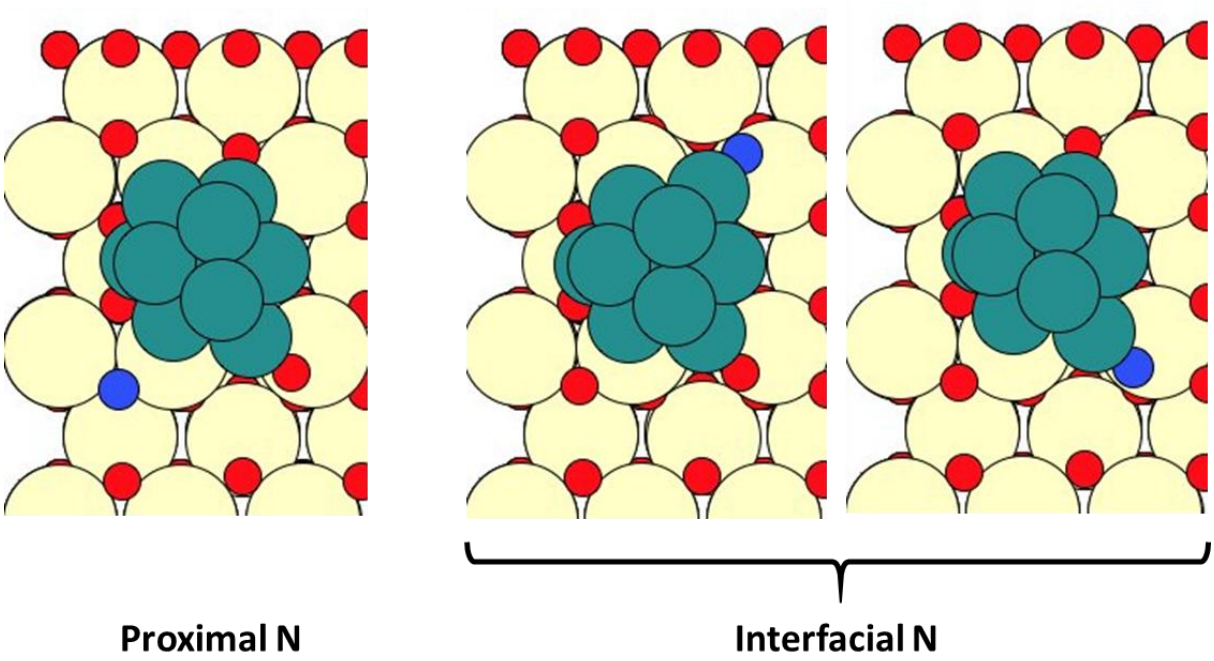


Fig. 4.18 Illustration of different interactive N species on the Ru impregnated N doped cerium oxide catalyst. Yellow circle being Ce; Red circle being O; Blue circle being N and Dark green circle being Ru metal NPs.

As illustrated in **Fig. 4.18**, a CeO_2 (110) plane, which was observed from the TEM result (**Fig. 4.14a.**) was initially created. A Ru_{10} cluster was then placed on the surface of this unit cell for the ease of calculation. Though, Ru possess a high coordination number of 8~9 (**Table 3**), previous studies have confirmed that once the Ru cluster reaches 10, it will share the same property as higher coordinated clusters.[66] To understand the role of doped nitrogen in the associative NH_3 decomposition mechanism, a sterically accessible interfacial N site and a representative proximal N site were evaluated along the Mars–van Krevelen pathway. In

parallel, the dissociative pathway was examined on Ru clusters and the pristine CeO_2 (110) surface for further comparison.

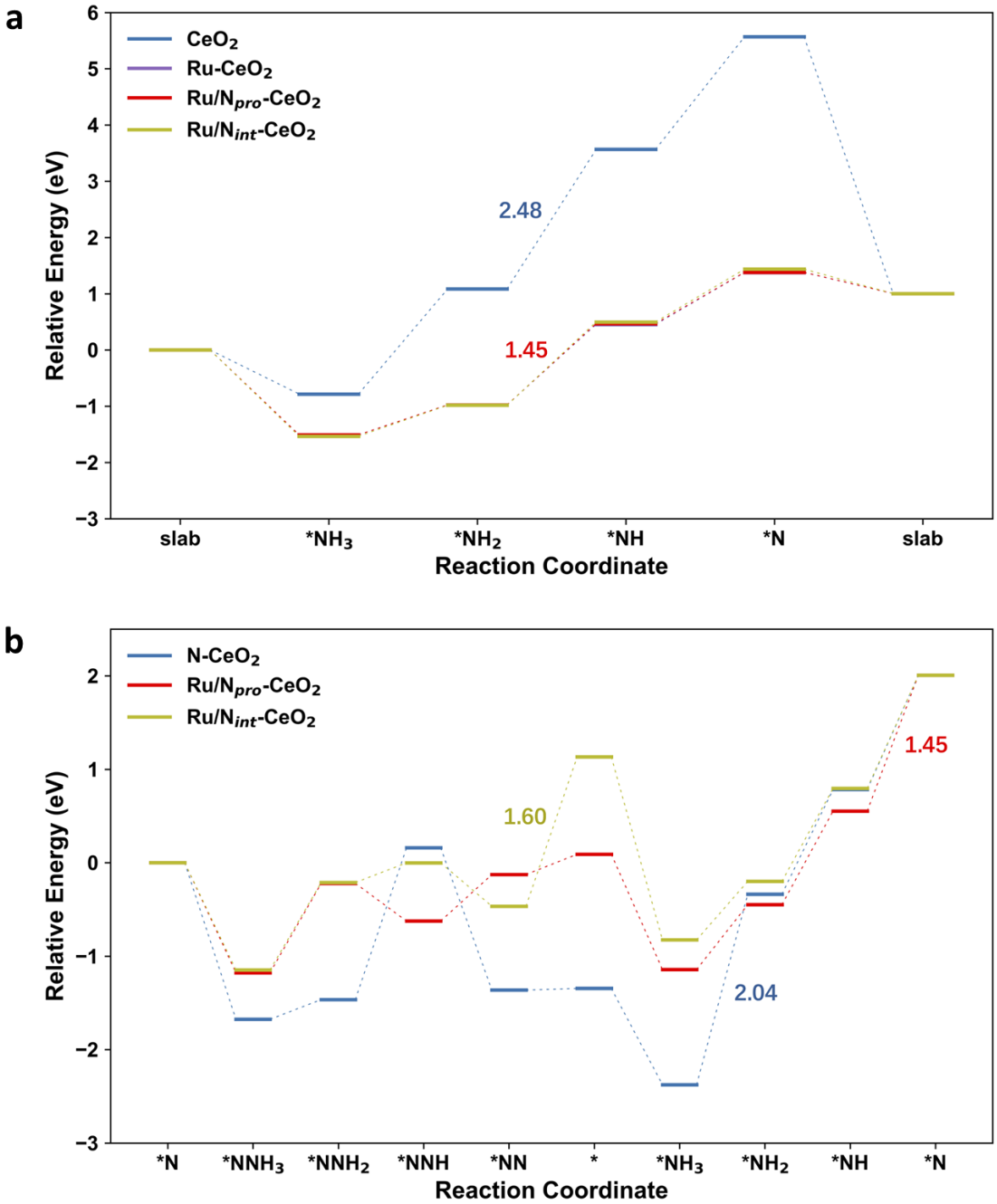


Fig. 4.19 Computed reaction energy profiles for NH_3 decomposition using MACE. a. MvK-type reaction profiles at nitrogen-doped sites under different configurations. b. Traditional dissociative reaction profiles on pristine CeO_2 and on Ru_{10} clusters supported on analogue surfaces.

Traditional dissociative NH_3 decomposition on pristine CeO_2 proceeds with a considerably high thermal barrier of 2.48 eV, as illustrated in **Fig. 4.19a**. This activation barrier dramatically decreased to 1.45 eV upon Ru cluster loading. These results confirm that the Ru cluster remains catalytically active as an independent reaction centre. However, it is interesting to note that there is negligible influence on the activation energy barrier for the dissociative mechanism while having doped different configuration of N to the support.

However, while switching to the associative pathway which proceeds through the MvK mechanism. It is surprising to note that different N configurations possess huge difference on the catalytic activity towards ammonia decomposition. As shown in **Fig. 4.19b**, the MvK pathway on pure N doped CeO_2 without Ru involves a high thermal barrier of 2.04 eV for the dehydrogenation of N-H bonds. Upon Ru cluster loading, the energy required for this step dramatically decreased for both N sites. It shifts the reaction barrier from dehydrogenation towards N_2 desorption as shown for the interfacial N. As for the proximal N site, the highest thermal barrier is reduced to 1.45 eV and located at the final vacancy recovery step. It exhibits a lower barrier compared to the 1.60 eV observed for the interfacial N site, where strong metal–support interactions hinder N_2 desorption.

These results further highlights that the RDS in the MvK mechanism is governed by the spatial proximity between the doped nitrogen and the Ru cluster. Notably, while the metal cluster promotes key surface reactions, excessively strong adsorption imposes kinetic constraints on the desorption step, whereas the proximal configuration avoids this effect and exhibits enhanced reactivity.

Thus, it is rationalised that this enhancement in catalytic activity with N doped cerium oxide originates from this external N active site, particular located at the proximal position. It has been said that metal incorporated on CeO_2 would perturb the electronic structure, thereby favouring the formation of O_v at the interface.[67] Thus, even for undoped Ru/CeO_2, the interaction between Ru and the support may induce the formation of interfacial nitrogen-like active sites to some extent, possibly through adsorption or residual contamination. However,

intentional pre-doping of N into the structure would result in simultaneous presence of interfacial and proximal N on the surface. These proximal N sites are particularly significant, as they participate directly in the reaction by providing alternative activation pathways of low activation energy that are comparable in activity to Ru metal itself. This distinct functionality contributes to the overall improvement in catalytic efficiency and underlines the importance of tailoring surface chemistry via heteroatom doping.

4.4 Conclusion

In this Chapter, a nitrogen doped cerium oxide catalyst is synthesized using a simple soft urea glass method. The synthesis conditions were systematically optimized to maximize nitrogen incorporation, with the most effective doping achieved by annealing the pristine support at 650 °C under flowing NH_3 for 6 h. By evaluating the activity of the catalysis, it is found that nitrogen content doped on the support plays a vital role on the final hydrogen yield from ammonia decomposition. The Ru/N-CeO_2 (650-6h) catalyst demonstrated 2-3 times enhancement in the catalytic activity compared to the undoped counter-part. Further kinetic measurements showed a decrease in apparent activation energy to 65 kJ mol^{-1}, indicating the emergence of an alternative reaction pathway.

The interaction between the Ru NPs and the support has been intensively studied using various techniques. Upon nitrogen pre-doping, nitrogen was found to function as a Lewis base site, anchoring Ru nanoparticles and promoting better dispersion and smaller particle size, both of which are beneficial for the reaction. Spectroscopic analyses, in particular XPS and XAS confirmed that nitrogen dopants act as electron donors, forming Ru–N interfacial bonds that enhance the metal support interaction and contribute significantly to the observed high activity.

Mechanistic insights were further explored through isotopic labelling experiments. These directly confirmed the involvement of lattice nitrogen in the reaction via exchange with NH_3 derived nitrogen. Supporting evidence was provided by isotopic pulse FTIR, where a broadening and red shift of the *N=NH peak is observed after introducing $^{15}NH_3$. Additionally, the appearance of a Ce–N adsorption peak during pulsing offered insight into the spatial location of the alternative reaction pathway.

Finally, the computational calculations were in alignment with our experimental results. It demonstrates that N dopants create external active sites that are thermodynamically favourable for catalysis. A volcano-type relationship was uncovered between the spatial

distance of these nitrogen sites and the Ru nanoparticles: shorter distances facilitate N–H bond activation while inhibiting the final dinitrogen desorption, and vice versa. Therefore, the presence of proximal nitrogen sites is concluded to be the key factor driving the enhanced catalytic performance.

Although this project presents a compelling and well-studied system, there remain several promising branch directions for future research. One key limitation lies in the fact that Ru currently exists as NPs, where the dissociative reaction mechanism is inevitably active. This introduces complexity to the system, making it difficult to isolate and evaluate a single, dominant reaction pathway. To address this, next step would be focussing on the synthesis of single atom Ru catalysts on the same nitrogen doped CeO_2 support. By eliminating the B5-type active sites responsible for N–H bond dissociation in Ru nanoparticles, this approach would suppress the dissociative route and instead favour an associative mechanism.

Building on this concept, a particularly intriguing direction would involve the controlled investigation of the spatial relationship between proximal nitrogen sites and Ru atoms. Although technically challenging, one primary thought on the potential strategy could involve synthesizing a series of Ru/N-CeO_2 catalyst in which the Ru loading is kept constant while maintain its single atomic state. Then further systematically varying the surface concentration of nitrogen dopants. A change in the density of nitrogen sites across the support surface would in theory effect the spatial distance between two neighbouring N sites and allow for a fundamental study of how the proximity influences the associative reaction pathway and catalytic performance.

This Chapter not only demonstrates that nitrogen incorporation into cerium oxide can induce an electronic promotion effect that enhances catalytic ammonia decomposition but also reveals that nitrogen can function as a redox active site, facilitating an associative reaction mechanism. More importantly, this study uncovers a critical foundation: that spatial variations in nitrogen configurations and the active metal sites can lead to significant differences in

catalytic performance. These findings provide valuable insights into the underlying reaction mechanisms and are expected to inspire future strategies for catalyst design.

Reference

1. Su, Z. *et al.* Research progress of ruthenium-based catalysts for hydrogen production from ammonia decomposition. *Int. J. Hydrogen Energy* **51**, 1019–1043 (2024).
2. Im, Y., Muroyama, H., Matsui, T. & Eguchi, K. Investigation on catalytic performance and desorption behaviors of ruthenium catalysts supported on rare-earth oxides for NH_3 decomposition. *Int. J. Hydrogen Energy* **47**, 32543–32551 (2022).
3. Ye, D. & Tsang, S. C. E. Prospects and challenges of green ammonia synthesis. *Nat. Synth.* **2**, 612–623 (2023).
4. Li, L. *et al.* Size sensitivity of supported Ru catalysts for ammonia synthesis: From nanoparticles to subnanometric clusters and atomic clusters. *Chem* **8**, 749–768 (2022).
5. Yu, P. *et al.* Effects of Alkaline Earth Metal Amides on Ru in Catalytic Ammonia Decomposition. *J. Phys. Chem. C* **120**, 2822–2828 (2016).
6. Leung, K. C. *et al.* Confined Ru Sites in a 13X Zeolite for Ultrahigh H_2 Production from NH_3 Decomposition. *J. Am. Chem. Soc.* **145**, 14548–14561 (2023).
7. Li, J., Li, G. & Tsang, S. C. E. Heterogeneous Frustrated Lewis Pair Catalysts: Rational Structure Design and Mechanistic Elucidation Based on Intrinsic Properties of Supports. *Acc. Chem. Res.* **58**, 2 (2025).
8. Wu, S. *et al.* Rapid Interchangeable Hydrogen, Hydride, and Proton Species at the Interface of Transition Metal Atom on Oxide Surface. *J. Am. Chem. Soc.* **143**, 9105–9112 (2021).
9. Ye, T.-N. *et al.* Contribution of Nitrogen Vacancies to Ammonia Synthesis over Metal Nitride Catalysts. *J. Am. Chem. Soc* **142**, 14374–14383 (2020).
10. Ye, T.-N. *et al.* Dissociative and Associative Concerted Mechanism for Ammonia Synthesis over Co-Based Catalyst. *Cite This J. Am. Chem. Soc* **143**, 12857–12866 (2021).
11. Zhang, Z. *et al.* Anion vacancies activate N_2 to ammonia on Ba–Si orthosilicate oxynitride-hydride. *Nat. Chem.* **17**, 679–687 (2025)
12. Yan, H. *et al.* Lithium Palladium Hydride Promotes Chemical Looping Ammonia Synthesis Mediated by Lithium Imide and Hydride. *J. Phys. Chem. C* **125**, 6716–6722 (2021).
13. Gao, W. *et al.* Production of ammonia via a chemical looping process based on metal imides as nitrogen carriers. *Nat. Energy* **3**, 1067–1075 (2018).
14. Miyashita, K. *et al.* Effects of nitrogen vacancy sites of oxynitride support on the catalytic activity for ammonia decomposition. *NPG Asia Mater.* **16**, 54 (2024).
15. Miyazaki, M. *et al.* Ammonia decomposition mediated at nitrogen vacancies on NaCl-type binary metal nitrides supporting transition metal nanoparticles. *Chem. Commun.* **60**, 6447–6450 (2024).
16. Mizoguchi, H., Luo, S., Sasase, M., Kitano, M. & Hosono, H. Ammonia Decomposition Catalyzed by Co Nanoparticles Encapsulated in Rare Earth Oxide. *J. Phys. Chem. Lett.* **16**, 796–801 (2025).
17. Teng, B. *et al.* Ru Dispersed on Oxygen-Defect-Rich CeO_2 Nanorods for Ammonia Decomposition. *ACS Appl. Nano Mater.* **7**, 15012–15024 (2024).
18. Liu, H., Zhang, R., Liu, S. & Liu, G. CeO_2/Ni Inverse Catalyst as a Highly Active and Stable Ru-free Catalyst for Ammonia Decomposition. *ACS Catal.* **14**, 9927–9939 (2024).
19. Yuan, Y. *et al.* Zirconium nitride catalysts surpass platinum for oxygen reduction. *Nat. Mater.* **19**, 282–286 (2019).
20. Shi, Z. *et al.* Metal-Nitrogen-Doped Carbon Materials as Highly Efficient Catalysts: Progress and Rational Design. *Adv. Sci.* **7**, 2001069 (2020).
21. Zhang, J. *et al.* Activating and Optimizing Activity of CoS_2 for Hydrogen Evolution Reaction

through the Synergic Effect of N Dopants and S Vacancies. *ACS Energy Lett.* **2**, 1022–1028 (2017).

22. Li, Y. *et al.* Roles of Oxygen Vacancies in CeO_2 Nanostructures for Catalytic Aerobic Cyclohexane Oxidation. *ACS Appl. Nano Mater.* **6**, 14214–14227 (2023).

23. Kim, M. G. *et al.* Effects of Calcination Temperature on the Phase Composition, Photocatalytic Degradation, and Virucidal Activities of TiO_2Nanoparticles. *ACS Omega* **6**, 10668–10678 (2021).

24. Paick, J. *et al.* Effective Atomic N Doping on CeO_2 Nanoparticles by Environmentally Benign Urea Thermolysis and Its Significant Effects on the Scavenging of Reactive Oxygen Radicals. *ACS Omega* **8**, 22646–22655 (2023).

25. Li, Y. *et al.* Photocatalytic water splitting by N-TiO_2 on MgO (111) with exceptional quantum efficiencies at elevated temperatures. *Nat. Commun.* **10**, 4421 (2019).

26. Jorge, A. B. *et al.* Nitrogen Doping of Ceria. *Chem. Mater.* **20**, 5, 1682–1684 (2008).

27. Jorge, A. B. *et al.* Nanocrystalline N-doped ceria porous thin films as efficient visible-active photocatalysts. *J. Mater. Chem.* **22**, 3220–3226 (2012).

28. Yan, X. *et al.* Cooperatively tailored surface frustrated Lewis pairs and N-doping on CeO_2 for photocatalytic CO_2 reduction to high-value hydrocarbon products. *Appl. Catal. B Environ.* **343**, 123484 (2024).

29. Wang, L. *et al.* Oxygen vacancy clusters essential for the catalytic activity of CeO_2 nanocubes for o-xylene oxidation. *Sci. Reports* **7**, 12845 (2017).

30. Wu, H. *et al.* Investigation into the impact of CeO_2 morphology regulation on the oxidation process of dichloromethane. *RSC Adv.* **14**, 12265–12277 (2024).

31. Wei, Y. *et al.* Catalysts of self-assembled Pt@$CeO_{2-\delta}$-rich core–shell nanoparticles on 3D ordered macroporous $Ce_{1-x}Zr_xO_2$ for soot oxidation: nanostructure-dependent catalytic activity. *Nanoscale* **9**, 4558–4571 (2017).

32. Xu, J. *et al.* Size dependent oxygen buffering capacity of ceria nanocrystalsw. *Chem. Commun.* **46**, 1887-1889 (2010).

33. Yu, Y., Zhong, Q., Cai, W. & Ding, J. Promotional effect of N-doped CeO_2 supported CoO_x catalysts with enhanced catalytic activity on NO oxidation. *J. Mol. Catal. A Chem.* **398**, 344–352 (2015).

34. Wang, F. *et al.* A comparative study about the influence of nitrogen doping and oxygen vacancies on the photocatalytic performance of ceria. *Surfaces and Interfaces* **46**, 103889 (2024).

35. García-García, F. R., Álvarez-Rodríguez, J., Rodríguez-Ramos, I. & Guerrero-Ruiz, A. The use of carbon nanotubes with and without nitrogen doping as support for ruthenium catalysts in the ammonia decomposition reaction. *Carbon N. Y.* **48**, 267–276 (2010).

36. Bueno-Ferrer, C., Parres-Esclapez, S., Lozano-Castelló, D. & Bueno-López, A. Relationship between surface area and crystal size of pure and doped cerium oxides. *J. Rare Earths* **28**, 647–653 (2010).

37. Zhou, Y. *et al.* Unraveling the size-dependent effect of Ru-based catalysts on Ammonia synthesis at mild conditions. *J. Catal.* **404**, 501–511 (2021).

38. Kim, H. B. & Park, E. D. Ammonia decomposition over Ru catalysts supported on alumina with different crystalline phases. *Catal. Today* **411**–**412**, 113817 (2023).

39. Zhang, X. *et al.* Metal–support interaction-modulated catalytic activity of Ru nanoparticles on Sm_2O_3 for efficient ammonia decomposition. *Catal. Sci. Technol.* **11**, 2915–2923 (2021).

40. Le, T. A. *et al.* Ru-supported lanthania-ceria composite as an efficient catalyst for CO_x-free H_2 production from ammonia decomposition. *Appl. Catal. B Environ.* **285**, 119831 (2021).

41. Hu, X. C. *et al.* Ceria-supported ruthenium clusters transforming from isolated single atoms for

hydrogen production via decomposition of ammonia. *Appl. Catal. B Environ.* **268**, 118424 (2020).

42. Ju, X. *et al.* Highly Efficient Ru/MgO Catalyst with Surface-Enriched Basic Sites for Production of Hydrogen from Ammonia Decomposition. *ChemCatChem* **11**, 4161–4170 (2019).

43. Fang, H. *et al.* Dispersed surface Ru ensembles on MgO(111) for catalytic ammonia decomposition. *Nat. Commun.* **14**, 647 (2023).

44. Hayashi, F. *et al.* Ammonia decomposition by ruthenium nanoparticles loaded on inorganic electride C12A7:e^-. *Chem. Sci.* **4**, 3124–3130 (2013).

45. Shin, J. H. *et al.* Elucidating the effect of Ce with abundant surface oxygen vacancies on $MgAl_2O_4$-supported Ru-based catalysts for ammonia decomposition. *Appl. Catal. B Environ.* **340**, 123234 (2024).

46. Wang, Z. *et al.* Promotion of Low-Temperature Catalytic Activity of Ru-Based Catalysts for Ammonia Decomposition via Lanthanum and Cesium Codoping. *ACS Sustain. Chem. Eng.* **12**, 5620–5631 (2024).

47. Tang, S., Ding, J., Li, W., Zhang, S. & Zhang, H. Ultrafine Ru Nanoparticles Supported on Mesoporous Silica for Hydrogen Production via Decomposition of Ammonia. *ChemCatChem* **16**, e202400241 (2024).

48. Yamazaki, K., Matsumoto, M., Ishikawa, M. & Sato, A. NH_3 decomposition over Ru/CeO_2-PrO_x catalyst under high space velocity conditions for an on-site H_2 fueling station. *Appl. Catal. B Environ.* **325**, 122352 (2023).

49. Furusawa, T., Kuribara, H., Kimura, K., Sato, T. & Itoh, N. Development of a Cs-Ru/CeO_2 spherical catalyst prepared by impregnation and washing processes for low-temperature decomposition of NH_3: Characterization and kinetic analysis results. *Ind. Eng. Chem. Res.* **59**, 18460–18470 (2020).

50. Madadi, S. & Kaliaguine, S. Activated Carbon-Supported Ruthenium as a Catalyst for the Solvent- And Initiator-Free Aerobic Epoxidation of Limonene. *ACS Sustain. Chem. Eng.* **9**, 10557–10568 (2021).

51. Zhang, S. L. *et al.* Anchoring Metal-Nitrogen Sites on Porous Carbon Polyhedra with Highly Accessible Multichannels for Efficient Oxygen Reduction. *ACS Appl. Mater. Interfaces* **16**, 44728–44736 (2024).

52. Morgan, D. J. Resolving ruthenium: XPS studies of common ruthenium materials. *Surf. Interface Anal.* **47**, 1072–1079 (2015).

53. Lee, K. R., Haider, A., Park, K., Ahn, S. & Jung, K. D. Sustainable synthesis of N-doped carbon to stabilize Ru species for CO_2 hydrogenation to formic acid. *J. CO_2 Util.* **86**, 102896 (2024).

54. Zhang, C. *et al.* Single-Atomic Ruthenium Catalytic Sites on Nitrogen-Doped Graphene for Oxygen Reduction Reaction in Acidic Medium. *ACS Nano* **11**, 6930–6941 (2017).

55. Li, L. *et al.* Size sensitivity of supported Ru catalysts for ammonia synthesis: From nanoparticles to subnanometric clusters and atomic clusters. *Chem* **8**, 749–768 (2022).

56. Huang, W. Crystal Plane-Dependent Surface Reactivity and Catalytic Property of Oxide Catalysts Studied with Oxide Nanocrystal Model Catalysts. *Top. Catal. 2013 5615* **56**, 1363–1376 (2013).

57. Chen, L. *et al.* Insight into the Improvement Effect of Nitrogen Dopant in Ag/Co_3O_4 Nanocubes for Soot Oxidation: Experimental and Theoretical Studies. *J. Hazard. Mater.* **420**, 126604 (2021).

58. Mondal, S. *et al.* Nitrogen Doping-Induced Structural Distortion in $LaMnO_3$ Enhances Oxygen Reduction and Oxygen Evolution Reactions. *ACS Energy Lett.* **9**, 3440–3447 (2024).

59. Kim, J. S., Nam, H., Kim, H. J., Lee, J. H. & Park, B. H. Real-Time Measurement of Ammonia (NH_3) in Artillery Smoke Using a Passive FT-IR Remote Sensor. *ACS Omega* **4**, 16768–16773 (2019).

60. Duan, C. peng, Guo, R. tang, Wu, G. lin & Pan, W. guo. Selective catalytic reduction of NO_x by NH_3 over $CeVO_4$-CeO_2 nanocomposite. *Environ. Sci. Pollut. Res.* **27**, 22818–22828 (2020).

61. Qi, G. & Yang, R. T. Characterization and FTIR studies of MnO_x-CeO_2 catalyst for low-temperature selective catalytic reduction of NO with NH_3. *J. Phys. Chem. B* **108**, 15738–15747 (2004).

62. Zimmermann, F. *et al.* N=N Vibrational Frequencies and Fragmentation Patterns of Substituted 1-Aryl-3,3-Dialkyl-Triazenes: Comparison with Other High-Nitrogen Compounds. (1993).

63. Ren, J. *et al.* A Scenario for a Carbon-Neutral Ammonia-Fueled Engine Mediated by Catalytic NH_3 Cracking and CO_2 Hydrogenation. *Angew. Chemie Int. Ed.* **64**, e202420292 (2025).

64. Zhang, P., Guo, R. tang, Wu, L. jun & Pan, W. guo. The enhancement of NH_3-SCR performance for CeO_2 catalyst by CO pretreatment. *Environ. Sci. Pollut. Res.* **27**, 13617–13636 (2020).

65. Kubota, H. *et al.* Operando Spectroscopic Study of Reduction and Oxidation Half-Cycles in NH_3-SCR over CeO_2-Supported WO_3. *ACS Catal.* **13**, 9274–9288 (2023).

66. Gao, X., Zhu, S., Dong, M., Wang, J. & Fan, W. Ru/CeO_2 catalyst with optimized CeO_2 morphology and surface facet for efficient hydrogenation of ethyl levulinate to γ-valerolactone. *J. Catal.* **389**, 60–70 (2020).

67. Yan, X. *et al.* Metal/CeO_{2-x} with regulated heterointerface, interfacial oxygen vacancy and electronic structure for highly efficient hydrogen evolution reaction. *Appl. Surf. Sci.* **626**, 157248 (2023).

Chapter 5 Direct Coupling of Ammonia and Carbon Dioxide for Methane Production

5.1 Introduction

Ammonia has always been considered as a 'key species' in the hydrogen economy, primarily due to its favourable physicochemical properties of high hydrogen content by weight (i.e., 17.6 wt%) and ease of liquefaction under mild conditions (i.e., 8 bars at room temperature).[1] These features make ammonia an efficient hydrogen carrier, particularly attractive for long-distance storage and transportation. However, the reconversion of ammonia back to hydrogen, typically through thermal catalytic cracking, is a highly endothermic process requiring elevated temperatures often exceeding 600 °C.[2] Technoeconomic analyses have shown that the cost associated with ammonia cracking can represent 30–50% of the total hydrogen delivery cost, depending on the transport distance, cracking technology, and purification requirements.[3] This substantial cost burden presents a critical bottleneck to the broader implementation of utilizing ammonia in the hydrogen transport chains.

One solution to address this challenge would rely on the development of sustainable and yet active catalyst. Under this approach, the activation barrier for ammonia decomposition is lowered, thereby enabling operation at milder temperatures and reducing overall energy input and system cost. An alternative and increasingly attractive strategy is directly couple ammonia decomposition with downstream hydrogenation reactions (**Fig. 5.1**). Herein, hydrogen is consumed *in situ* as it is released from ammonia in a single reactor system. This approach would eliminate the need for hydrogen cracking and purification units, reduces heat loss associated with standalone systems resulting in lower overall cost of production.

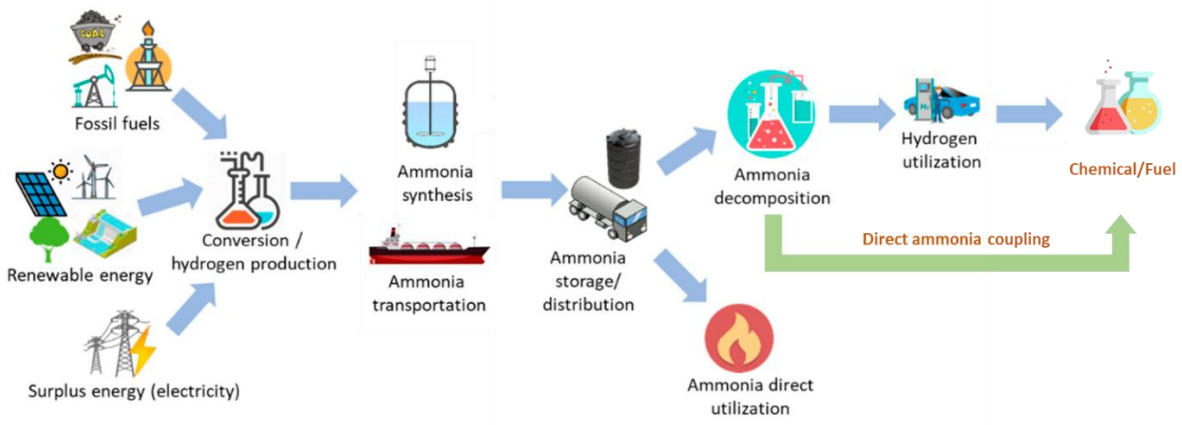


Fig. 5.1 Schematic illustration of the key role ammonia as hydrogen carrier in the hydrogen economy.

Hydrogen plays a vital role in industrial chemical transformations, especially in refining and chemical hydrogenation.[4,5] Notably, a substantial fraction of around 50% of the global hydrogen consumption is dedicated to industrial hydrogenation processes. This includes but is not limited to methanol synthesis, methane formation via CO/CO_2 hydrogenation, hydrocracking of fossil feedstocks and polymer modifications (**Fig. 5.2**). This strong demand motivates the exploration of ammonia coupled hydrogenation reactions that can not only deliver the desired products but also streamline the use of green hydrogen carriers like ammonia.

From an industrial and engineering aspect, such integrated reaction schemes leverage ammonia as both hydrogen source and chemical feedstock, offering advantages in terms of energy efficiency, process intensification, and system compactness. Moreover, this system would reduce the economic and environmental costs associated with conventional cracking, making them highly promising for future industrial applications, particularly under a green hydrogen infrastructure.

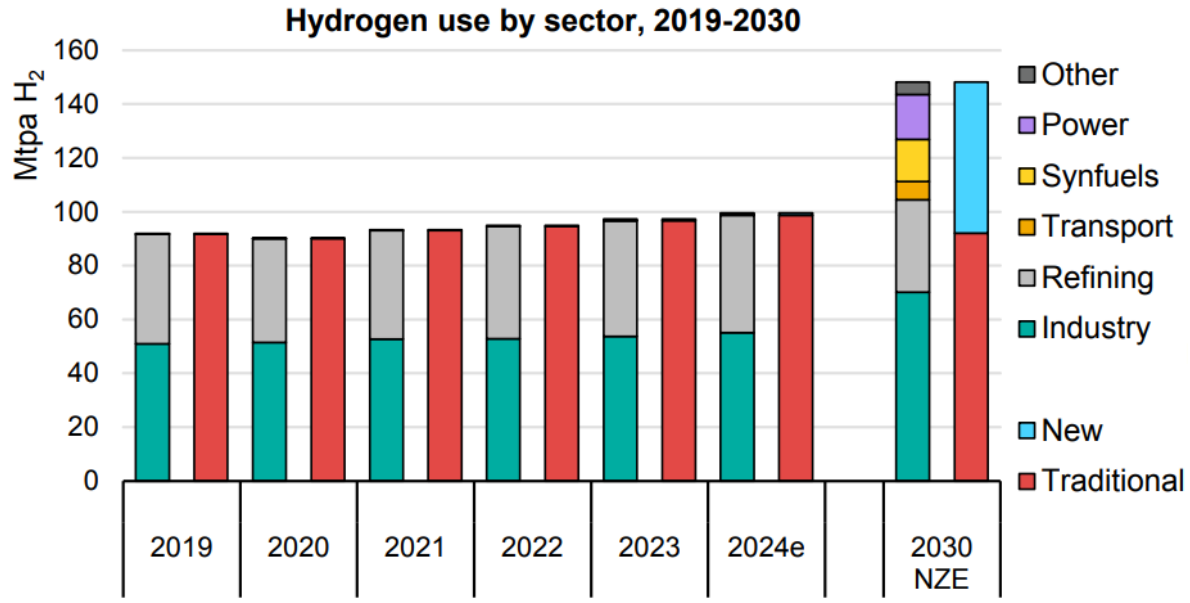


Fig. 5.2 Hydrogen demand by sector from 2019 to 2030. At present, hydrogen is primary used in traditional sectors like oil refinery and other industry applications. In the future, its use is expected to expand into emerging sectors including power generation and transportation. Figure reproduced with permission from reference [6]

From the fundamental chemical perspective, the use of NH_3 as a hydrogen source offers several intrinsic advantages that may enhance reaction kinetics. Ammonia molecules possess a trigonal pyramidal molecular geometry with an extra lone pair of electrons on the N atom, this uneven distribution of electron density and the non-centrosymmetric shape result in a net dipole moment, making ammonia a polar molecule. In general, hydrogen activation catalysts often involve polar surfaces. Thus, by switching the reactant to a more polar molecule would result in more favourable adsorption and facilitating further reactions.[7,8] Thus, the polarity of NH_3 can facilitate its preferential adsorption during the catalytic reaction, which in turn may accelerate surface-mediated reaction rates by increasing local reactant concentrations. Additionally, N-H dissociation energy is 391 kJ mol^{-1} which is lower compared to the H-H bond energy of 432 kJ mol^{-1} in molecular hydrogen.[9] This indicates that initial bond cleavage in NH_3

is thermodynamically more accessible than in H_2, potentially enabling hydrogen delivery under milder conditions.

Moreover, on most catalytic systems, the dissociation of a hydrogen source for cracking reactions lead to the formation of M–H intermediates, with hydrogen atoms adsorbed onto the catalyst surface. In the case of ammonia decomposition, this process is further driven forward by the formation of thermodynamically stable nitrogen gas as a by-product. According to Le Châtelier's principle, if the hydrogen released during NH_3 decomposition is simultaneously consumed in a coupled hydrogenation reaction, the removal of hydrogen from the system will continuously shift the equilibrium toward ammonia decomposition. This creates a favourable thermodynamic environment, where hydrogen-consuming downstream reactions promote further ammonia decomposition, potentially allowing the overall process to proceed efficiently at lower temperatures. In essence, this coupling of decomposition and hydrogenation reactions may enhance ammonia utilization efficiency compared to isolated decomposition and hydrogenation reactions.

As mentioned, ammonia decomposition often requires high temperature exceeding 600 °C to achieve satisfactory conversion. However, with the development of novel catalysts as outlined in earlier chapters, this temperature requirement can be significantly reduced to around 400-450 °C, while still demonstrating moderate activities. In order to enable an integrated reaction system described above, the operation conditions of the down-stream hydrogenation reaction must be compatible with the high temperature required for ammonia cracking. This necessity for thermal compatibility precludes coupling ammonia decomposition with many organic hydrogenation reactions involving long-chain hydrocarbons or functionalized organic molecules, as these compounds predominantly consist of thermally labile C-C covalent bonds. As a result, these materials typically begin to degrade at temperatures above 300 °C, not to mention ammonia decomposition provides a reducing environment which accelerates this degradation process.[10–12] Therefore, such organic systems are unsuitable for high-temperature coupling with ammonia decomposition.

In contrast, carbon dioxide hydrogenation has emerged as a promising candidate for such coupling. CO_2 is not only a major contributor to greenhouse gas (GHG) emissions, accounting for over 70% of global GHG output, but also an abundant and renewable C_1 feedstock.[13] Its utilization as a reactant in catalytic hydrogenation offers both environmental and economic advantages, aligning with global sustainability goals. Moreover, the hydrogenation of CO_2 into carbon-based fuels and chemicals (such as methane, methanol, or higher hydrocarbons) typically occurs under moderate conditions, generally in the range of 200–400 °C and up to 100 bars, depending on the specific product and catalyst system employed.[14,15] Thus, there exists a mismatch between the optimal reaction conditions of ammonia decomposition (450-550 °C, 1 atm) and CO_2 hydrogenation, which would result in overall lower rate of reaction. However, the coupling effect can alter the dynamic equilibrium as discussed above, this shift would drag the equilibrium towards the decomposition of ammonia as hydrogen are consumed *insitu*. Hence, integrating ammonia decomposition with CO_2 hydrogenation offers a synergistic platform: the endothermic cracking of NH_3 is balanced by the exothermic hydrogenation of CO_2, leading to enhanced energy efficiency for the overall process.

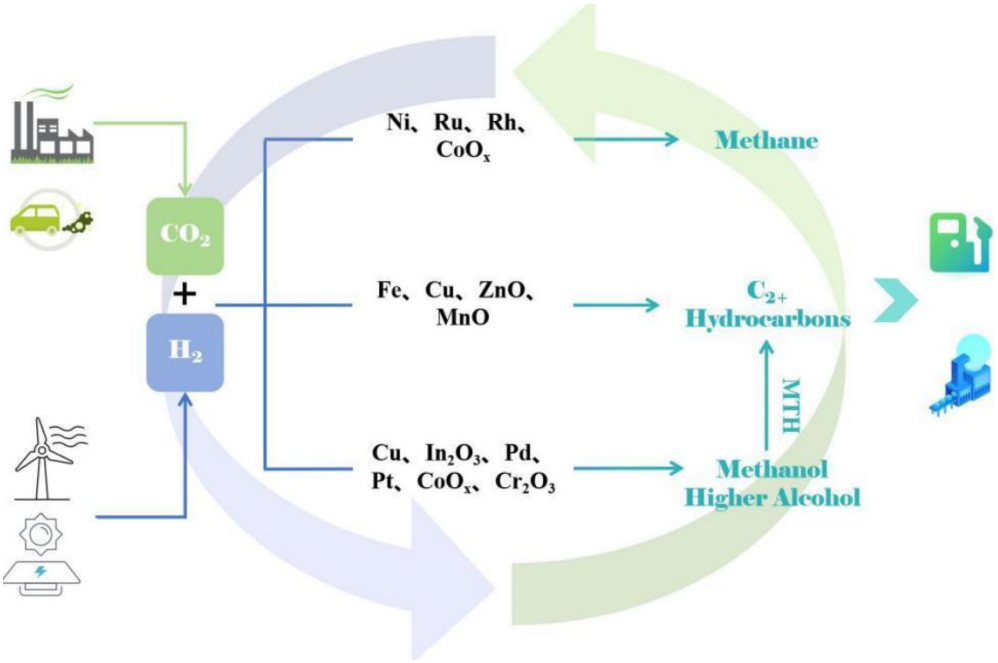


Fig. 5.3 Hydrogenation of CO_2 into different products based on different catalyst applied during catalysis. Figure reproduced with permission from reference [16].

In the context of hydrogenation of CO_2 into hydrocarbon or other carbon-based fuels, two main routes have been proposed. The first proceeds via the formation of methanol as an intermediate, followed by its subsequent conversion into hydrocarbons such as olefins, gasoline-range hydrocarbons, aromatics, and alkanes across multiple stages (**Fig. 5.3**).[17] This route typically employs non-noble metal catalyst such as Cu and Zn, and is typically operated under high pressure condition to favour methanol formation and stability.[18] Since ammonia cracking is an endothermic reaction with low pressure favoured reaction conditions, coupling reaction with hydrogenation reactions proceeding through the methanol mediated route will foreseeable result in poor performance. In the other alternative pathway, the reaction proceeds by emitting CO intermediates via reverse water gas shift (RWGS) reaction and then undergoes further formation of hydrocarbons by hydrogenation of the C-O bond. This route circumvents methanol formation and is generally promoted by noble or semi-noble metal catalysts such as Ru, Co, or Ni, which also happen to be effective for ammonia decomposition, making the operational and catalytic requirements more aligned with NH_3 cracking processes.[19,20]

Given the need for thermal compatibility and potential catalyst synergy, this chapter focuses on CO_2 methanation, one of the simplest CO_2 hydrogenation reactions that avoids formation of methanol and thus can be operated at ambient pressure condition. The Additionally, the reaction condition of methanation closely matches with the operating temperature window of ammonia decomposition (typically 350–450 °C). Furthermore, it also exhibits strong overlap in catalyst design principles, particularly involving Ru based systems. As Ru is the state-of-the-art metal for ammonia decomposition, it favours lower cracking temperatures. It is also one of the most active catalysts for CO_2 methanation, achieving over 90% selectivity for CH_4.[21,22] As such, coupling ammonia decomposition with CO_2 methanation presents a highly promising strategy for efficient, integrated hydrogen and carbon dioxide utilization under unified reaction conditions.

This work is intended as a proof-of-concept case study of the route in which green ammonia, instead of being converted to green hydrogen, is directly utilised for the methanation of CO_2 to methane. The aim is not yet to propose a full commercial system but rather to evaluate the viability, energetic implications, basic catalyst and reaction condition optimisation as well as fundamental understanding on the differences between the two reactions.

In this chapter, we demonstrate an approach to generate methane using ammonia as its hydrogen source. By screening and optimizing the metal loading and catalyst support, an optimized single catalyst system of using 10 wt.% Ru on CeO_2 was obtained, which illustrated comparable CO_2 conversion and CH_4 production rate to those obtained when using molecular hydrogen as the reductant.

Mechanistic studies revealed that such high activity is accounted for by the presence of oxygen vacancies on CeO_2 support which facilitate CO_2 activation and thereby reduce the reliance of Ru active sites. Furthermore, implementation of the previously discussed N doped CeO_2 support yielded even higher performance, underscoring that external support derived active sites can reduce the demand for precious metal sites. Which is crucial in systems where competitive adsorption between NH_3 and CO_2 occurs.

Our energy efficiency evaluation suggests that using ammonia as a hydrogen source for direct CO_2 methanation will give a higher power-to-gas efficiency compared to using pure hydrogen as the reactant.

Overall, these findings present a practical and efficient route for generating green methane directly from ammonia. This work introduces a novel perspective on coupling ammonia decomposition with downstream hydrogenation reactions via *in situ* hydrogen generation.

5.2 Results and discussion

This section presents the key findings on thermo-catalytic CO_2 methanation using NH_3 as the hydrogen source. A wide range of well-studied catalysts have been screened and the best performance catalyst is further evaluated to study the fundamental aspect of this reaction.

5.2.1 Catalyst screening

As has been mentioned in *Chapter 1*, Ru is the state-of-the-art metal that favours ammonia decomposition. In addition, it is also considered as one of the most active metal catalysts for CO_2 hydrogenation, especially in methanation reactions, where it exhibits high selectivity towards methane as the main product. Thus, various supports that are well recognised for thermo-catalytic ammonia decomposition are impregnated with 5 wt.% of Ru to evaluate the catalytic activity towards ammonia methanation reaction.

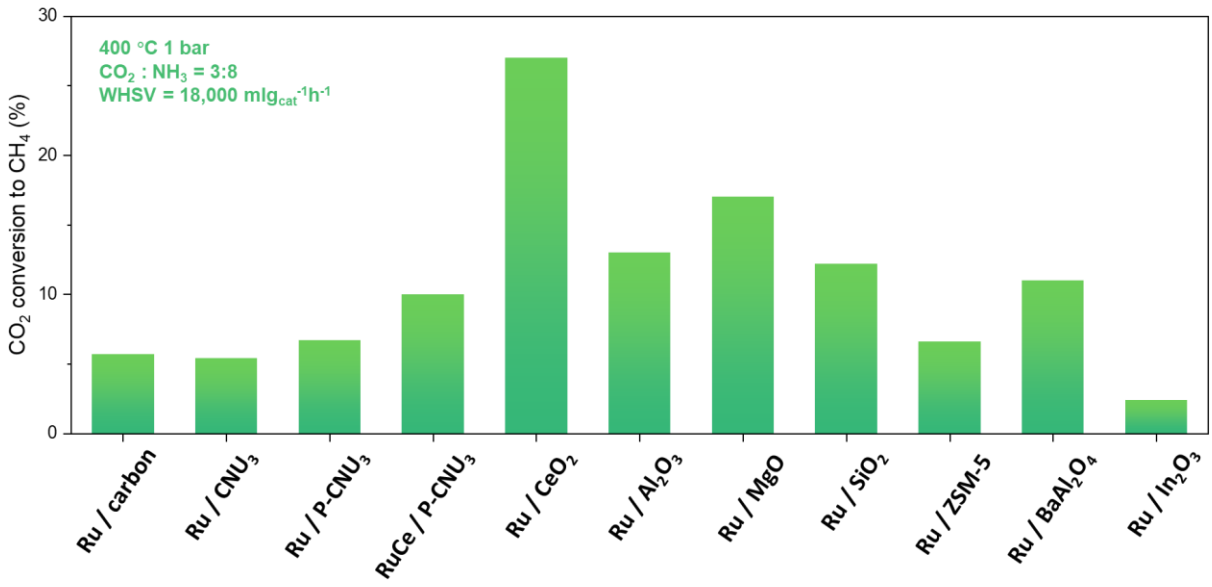


Fig. 5.4 CO_2 conversion to methane for various Ru impregnated support. Reaction condition of 400 °C, 1 bar, CO_2 to NH_3 flow ratio 3:8, WHSV = 18,000 ml g_{cat}^{-1} h^{-1}.

Carbon-based support demonstrates relatively inert activity towards ammonia methanation (**Fig. 5.4**), given that this class of catalyst already illustrated high activity for pure ammonia decomposition in *Chapter 3*. On the other hand, metal oxide-based support shows much better performance with Ru/CeO_2 yielding the highest CH_4 formation rate. For thermal CO_2 methanation, typically two different mechanisms are applied (**Fig. 5.5**).

In the associative mechanism, CO_2 molecules are adsorbed onto the catalyst surface (typically basic sites) and subsequently react with the adsorbed hydrogen atoms to form surface-bound oxygenated intermediates. These intermediates are then hydrogenated stepwise to form methane ultimately. A distinctive feature of this pathway is that no CO intermediate is involved. The rate-determining step (RDS) in this scheme is typically the formation and subsequent hydrogenation of these oxygenates.[23]

In contrast, the dissociative mechanism is triggered by direct dissociation of CO_2 into a surface adsorbed CO and an adsorbed oxygen atom. The reaction further proceeds via a CO methanation pathway, involving stepwise hydrogenation of CO to methane. In this dissociative pathway, the RDS is generally associated with the C–O bond cleavage in H_xCO^* species, which competes with their hydrogenation.[24]

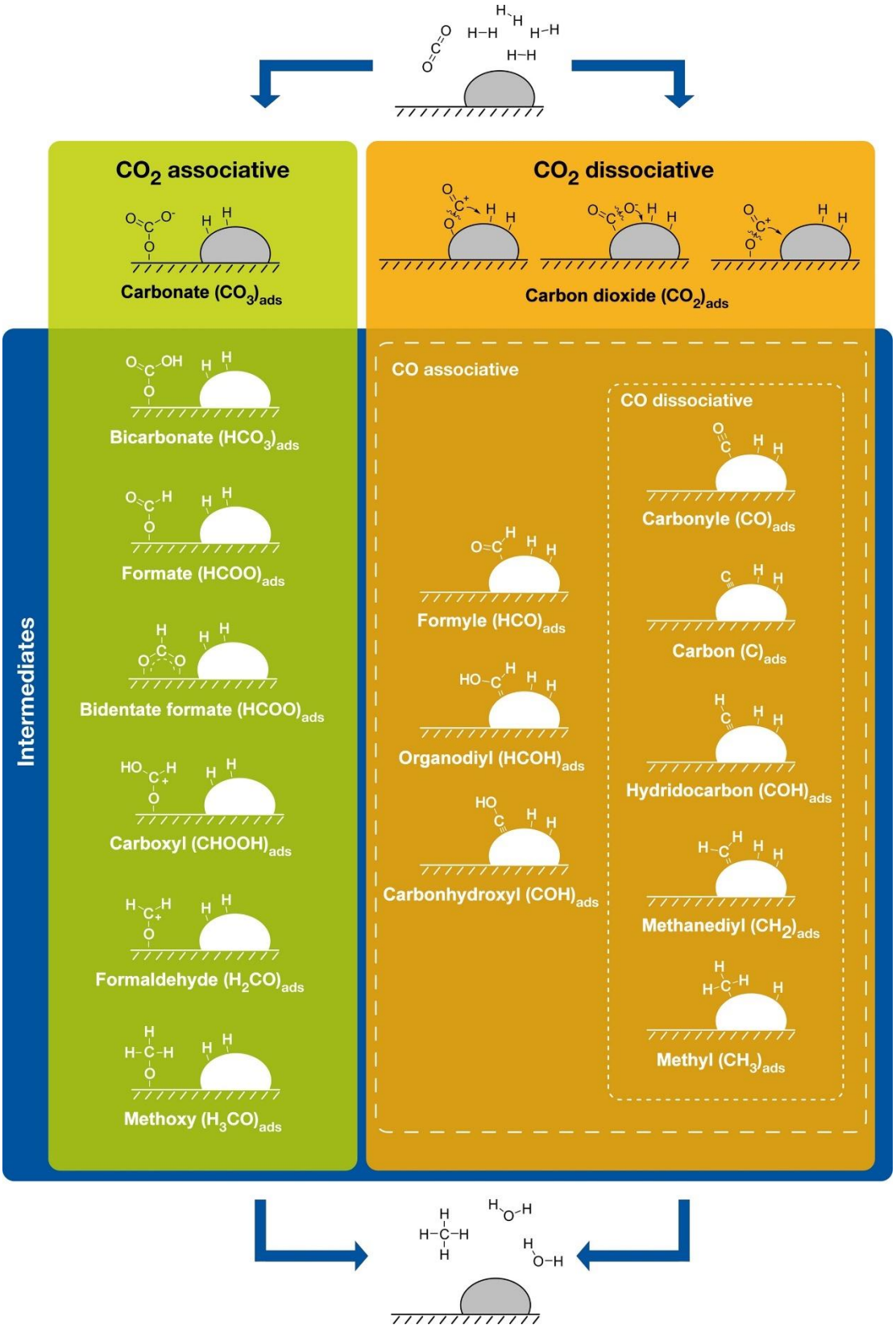


Fig. 5.5 Dissociative and associative pathway of heterogenous CO_2 hydrogenation to methane. Figure reprinted with copyright from reference[25].

For Ru supported on carbon-based materials, the catalyst support typically lacks active sites capable of activating CO_2 via the associative pathway. In this system, the catalytic activity is predominantly attributed to the Ru nanoparticles, which are well dispersed across the surface of the inert carbon support. As a result, during ammonia methanation, both NH_3 and CO_2 molecules compete for adsorption on the limited Ru active sites. This competitive adsorption not only reduces the availability of active sites but also intensifies the energy demand for bond cleavage in both molecules, leading to significant catalyst deactivation. Additionally, CO poisoning and carbon deposition are commonly observed as further deactivation mechanisms, especially over low activity catalysts.[26] CO molecules formed during the methanation process bind strongly to Ru, effectively blocking active sites and inhibiting subsequent NH_3 decomposition. As hydrogen production declines, the system enters a self-reinforcing deactivation cycle in which adsorbed CO species are not adequately hydrogenated or removed, resulting in the progressive loss of active Ru sites and a marked decline in overall catalytic performance.

Metal oxides, in particular CeO_2 demonstrated improved activity, which is attributed to the facilitation of the associative CO_2 activation mechanism proposed above. In these systems, CO_2 molecules, instead of all being bonded to the Ru metal sites, would interact with the oxygen vacancies on the metal oxides, and promote the formation of formats (see Fig. 5.5 green pathway).[27,28] This mitigates competitive adsorption on Ru and reduces site blocking, allowing for more balanced and sustained catalytic activity during ammonia methanation. Consequently, the presence of redox-active oxide supports such as CeO_2 plays a critical role in enhancing catalyst performance by providing alternative activation pathways and minimizing deactivation.

Interestingly, an outlier was observed in the performance of the Ru/In_2O_3 catalyst, which exhibited negligible CO_2 methanation activity. This is unexpected given that indium oxide has been widely studied for its high density of oxygen vacancies, which are typically beneficial for CO_2 activation.[29,30] This phenomenon is explained by a recent article published by Yu *et al*. It

is reported that indium can act as an electron-accepting centre. Thus, when Ru is impregnated onto indium support, electron density is withdrawn from the metal site. This electronic effect would lower the Ru-CO adsorption bond strength and consequently raising the energy barrier of CO hydrogenation. As a result, it will inhibit evolution of complete hydrogenation from CO_2 to CH_4 and illustrate an over tuning selectivity from ~99% CH_4 to 100% selective to CO.[31,32] This fundamental aspect provides new insight for general strategies in terms of catalyst designs with controllable activity and selectivity.[33]

Among the Ru-based catalysts tested, Ru/CeO_2 demonstrated the best performance in terms of ammonia methanation activity. This superior performance is likely due to the synergistic interaction between Ru and the redox-active CeO_2 support, which enables associative CO_2 activation while minimizing site blocking. As such, subsequent investigations into ammonia methanation will focus on the Ru/CeO_2 catalyst system.

5.2.2 Reaction condition optimisation

Thermodynamically, ammonia decomposition is an endothermic reaction, whereas carbon dioxide methanation is highly exothermic (eq. 1 and eq. 2). When these reactions are combined stoichiometrically into the overall ammonia methanation reaction, the net enthalpy change per mole of CH_4 produced becomes moderately exothermic (eq. 3). Under ideal conditions, a CO_2 : NH_3 molar ratio of 3:8 is required to fully convert CO_2 to CH_4, based on hydrogen availability from NH_3 decomposition. However, the actual thermodynamic behaviour is far more complex. At elevated temperatures, the reverse water–gas shift (RWGS) reaction is thermodynamically more favourable, resulting in competition with methanation and reducing CH_4 selectivity. This alteration in the thermodynamics is more complicated when NH_3 is used as the hydrogen source instead of H_2, due to the energy required for NH_3 decomposition and the potential for intermediate species to inhibit downstream hydrogenation steps.

$$2NH_3 \leftrightarrow N_2 + 3H_2 \quad \Delta_f H_0 = +91.8\ kJ\ mol^{-1} \qquad (1)$$

$$CO_2 + 4H_2 \leftrightarrow CH_4 + 2H_2O \quad \Delta_f H_0 = -164.7\ kJ\ mol^{-1} \qquad (2)$$

$$3CO_2 + 8NH_3 \leftrightarrow 3CH_4 + 6H_2O + 4N_2 \quad \Delta_f H_0 = -392.0\ kJ\ mol^{-1} \qquad (3)$$

$$CO_2 + H_2 \leftrightarrow CO + H_2O \quad \Delta_f H_0 = +41.2\ kJ\ mol^{-1} \qquad (4)$$

To evaluate the reaction dynamics, thermodynamic equilibrium of ammonia methanation has been computationally calculated (*HSC 6.0* Software; considering CO_2 and NH_3 as the only reactants; CO, CO_2, NH_3, H_2, H_2O as the only products)

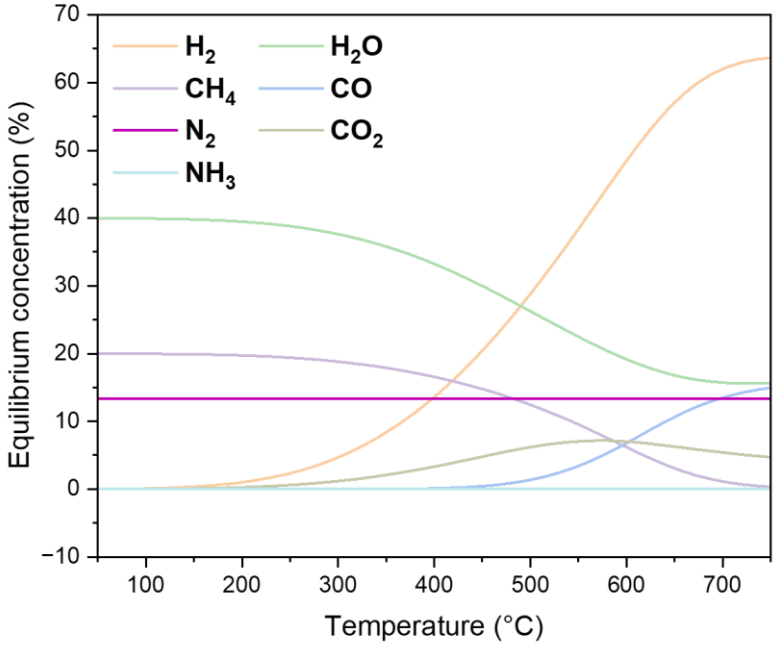


Fig. 5.6 Thermodynamic equilibrium of ammonia methanation calculated with respect of reaction temperature. The reactant CO_2 and NH_3 are fixed at a molar ratio of 3:8, reaction pressure set to 1 bar.

As illustrated in **Fig. 5.6**, the equilibrium concentration of ammonia remains zero throughout the process. This is attributed to the overall exothermic nature of the ammonia methanation reaction, indicating that even at relatively low temperatures, complete conversion of NH_3 is thermodynamically favourable for methane formation. However, as the temperature increases,

the equilibrium shifts toward the RWGS reaction, resulting in CO formation. Concurrently, CH_4 production decreases, and excess hydrogen derived from NH_3 decomposition accumulates and is emitted as H_2.

It is important to note that pure NH_3 decomposition is an endothermic process. Thus, the equilibrium shift affecting CH_4 and CO formation has minimal impact on upstream NH_3 cracking. As a result, the equilibrium concentrations of NH_3 and N_2 remain unchanged, reinforcing that NH_3 decomposition proceeds independently of the downstream methanation and RWGS equilibria under these conditions.

Based on these theoretical calculation findings, further catalytic measurements have been carried out over Ru/CeO_2 over the ammonia methanation reaction. The catalytic reaction is first analysed independently over pure ammonia decomposition and carbon dioxide methanation over different Ru loadings (wt.%).

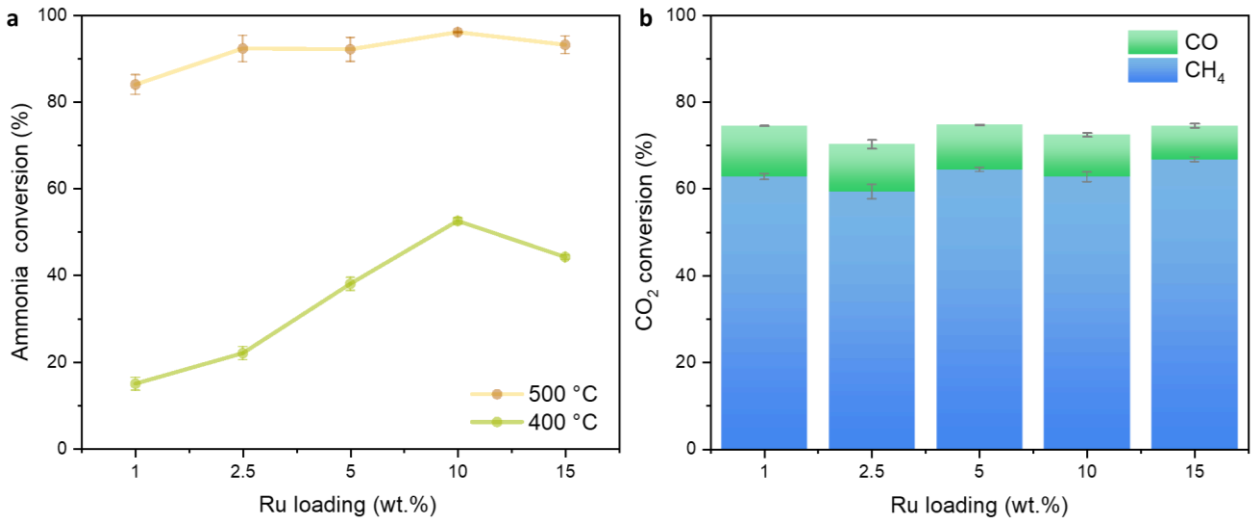


Fig. 5.7 Catalytic measurement of Ru/CeO_2 catalyst with different Ru loadings over a. Pure ammonia decomposition, at different temperatures, WHSV = 18,000 ml g_{cat}^{-1} h^{-1}; b. Pure CO_2 methanation; reaction was conducted at 500 °C with a fixed WHSV of 18,000 ml g_{cat}^{-1} h^{-1}, the molar ratio of CO_2 : H_2 during the methanation is fixed at 1:4.

As illustrated in **Fig. 5.7a**, increasing Ru loading up to 10 wt% would lead to a higher ammonia decomposition conversion. This is simply due to an increase in the number of active sites provided by more Ru metal. A highest activity is noted for this catalyst at an optimal Ru loading of 10 wt.% under 400 °C, achieving a notable NH_3 conversion of 58.6%. Nonetheless, further increasing the Ru content beyond this point leads to a decline in catalytic activity. This decrease is attributed to the overloading effect, where excess Ru leads to agglomeration and the formation of larger Ru particles, thereby reducing the dispersion and number of accessible active sites, as evidenced by the lower ammonia conversion observed.

As for pure CO_2 methanation, minimal variation in activity is observed across the CeO_2 catalyst impregnated with different Ru loadings. They all demonstrate a total CO_2 conversion of ~ 78% with a CH_4 selectivity of ~ 80%. This suggest that at 500 °C, the reaction is largely thermodynamically controlled. The thermal energy at this temperature is sufficient to drive the forward methanation reaction, and the effect of Ru loading on the reaction kinetics becomes less pronounced. Similar trend was also observed for NH_3 decomposition taking place at 500 °C.

The methane formation rate from ammonia methanation over CeO_2 support with varying Ru loadings was investigated at 500 °C. The results are presented in **Fig. 5.8**. A clear semi-volcano trend is observed with increasing Ru content, resembling the catalytic performance trend seen in pure NH_3 decomposition at 400 °C. The highest methane production rate of 0.142 $mmolmin^{-1}$ is achieved with a 10 wt.% Ru loading, indicating this as the optimal Ru concentration for the reaction under the conditions studied.

Although NH_3 decomposition and CO_2 methanation are each thermodynamically driven when carried out individually, the combined reaction system exhibits distinct behaviour. It is hypothesized that at lower Ru loadings, the limited number of active sites becomes a bottleneck, as the catalyst is required to simultaneously facilitate both reactions. In this context, Ru no longer serves solely as the active site for a single reaction but must effectively catalyze both processes, placing higher demands on active site availability. As a result, although low

Ru loading catalysts may perform well in the pure reactions, they are insufficient for the coupled system.

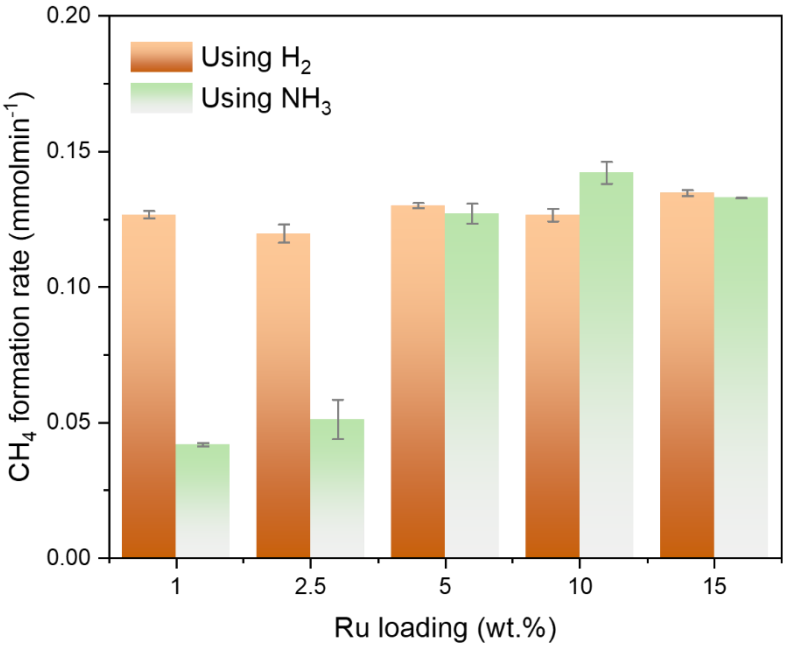


Fig. 5.8 Methane production rate of Ru/CeO_2 catalyst with different Ru loadings over ammonia methanation reaction at 500 °C with a fixed WHSV of 18,000 ml g_{cat}^{-1} h^{-1}, the molar ratio of CO_2 : NH_3 during ammonia methanation is fixed at 3:8.

However, on the other hand, it is interesting to note that at high Ru loadings, the methane production rate from ammonia methanation is comparable to that observed in conventional CO_2 methanation using pure H_2. This significant observation highlights the feasibility of using NH_3 as an alternative hydrogen carrier for *in situ* hydrogen production. Enabling a fully integrated process for green methane synthesis and reinforcing its potential role in sustainable energy applications.

Further catalytic measurements are carried out over the best performance catalyst 10 wt.% Ru on CeO_2 at different reaction conditions. Again, the results are first analysed based on pure individual reactions.

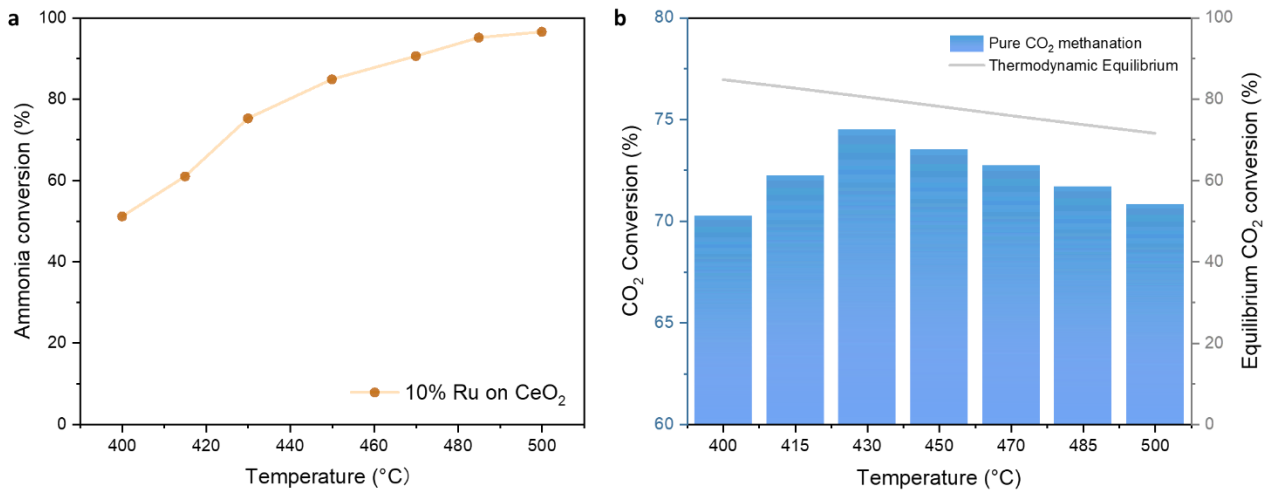


Fig. 5.9 Catalytic measurement of 10 wt.% Ru on CeO_2 catalyst over a temperature range of 400-500 °C a. Pure ammonia decomposition, at WHSV = 18,000 ml g_{cat}^{-1} h^{-1}; b. Pure CO_2 methanation, reaction conducted with a fixed WHSV of 18,000 ml g_{cat}^{-1} h^{-1}, the molar ratio of CO_2 : H_2 during the methanation is fixed at 1:4.

The catalytic conversion for ammonia decomposition shows a consistent increase with temperature (**Fig. 5.9**). This behaviour is attributed to the endothermic nature of the reaction, where higher temperatures thermodynamically shift the equilibrium toward formation of hydrogen and nitrogen. In contrast, the CO_2 methanation reaction exhibits a volcano-shaped conversion profile, with a maximum observed at 430 °C, achieving a conversion of 74.5%. Unlike ammonia decomposition, CO_2 methanation is a highly exothermic, meaning that higher temperatures thermodynamically disfavour methane formation by shifting the equilibrium back toward CO_2 and H_2. However, elevated temperatures simultaneously enhance the kinetics of the reaction, allowing for faster surface reaction rates.[34] The observed volcano trend thus reflects the competition between thermodynamic limitations and kinetic acceleration.

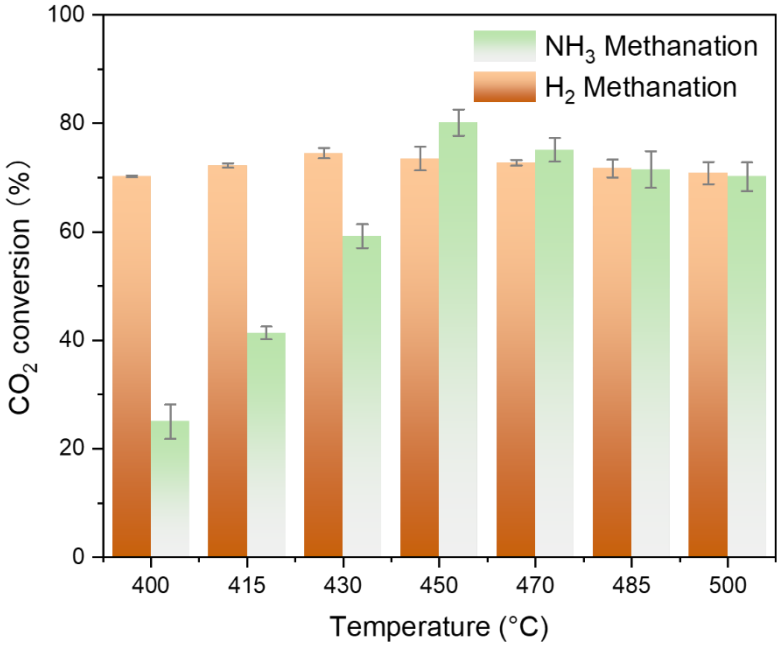


Fig. 5.10 CO_2 conversion of 10 wt.% of Ru on CeO_2 catalyst over a temperature range of 400-500 °C. WHSV set at 18,000 ml g_{cat}^{-1} h^{-1}, the molar ratio of CO_2 : NH_3 during ammonia methanation is fixed at 3:8.

As illustrated in **Fig 5.10**, reaction temperature plays a critical role in determining the overall catalytic performance of the ammonia methanation process. At low temperatures, CO_2 conversion remains low, primarily due to the insufficient *in situ* generation of hydrogen from ammonia decomposition. In this regime, the up-stream NH_3 decomposition step becomes rate-limiting, controlling the overall reaction rate.

With increasing temperature, the endothermic NH_3 decomposition becomes more favourable, leading to greater hydrogen yield. As a result, the rate of methane formation begins to approach that of conventional CO_2 methanation using H_2 as the hydrogen source. In this regime, the overall reaction becomes increasingly influenced by the thermodynamic behaviour of CO_2 methanation, which, as discussed previously, is exothermic and thus limited at higher temperatures.

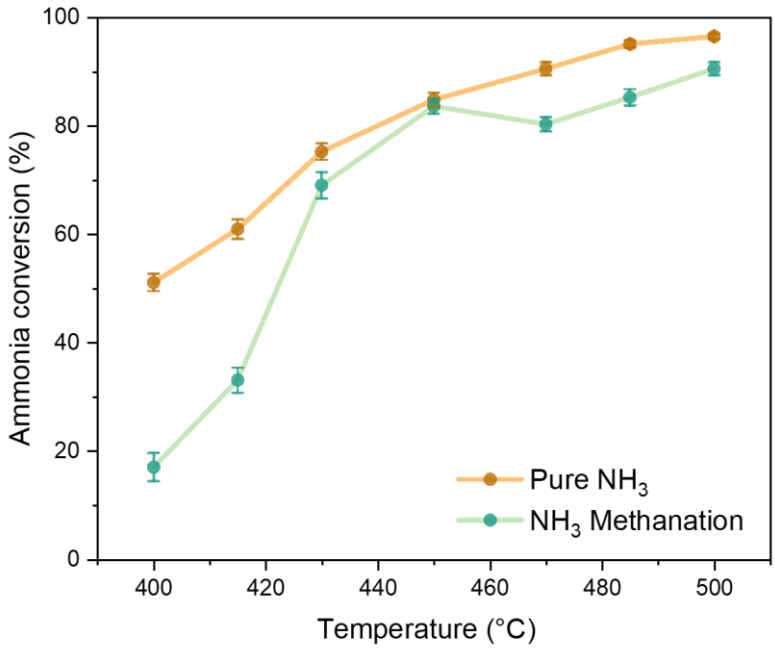


Fig. 5.11 Comparison between the ammonia conversion over 10 wt.% Ru ono CeO_2 for both pure ammonia decomposition and ammonia methanation reaction at different temperatures.

At 450 °C, the highest CO_2 conversion of approximately 80% is achieved. This optimal activity is resulted by balancing the thermodynamic and kinetic constraints of both constituent reactions. Interestingly, this temperature is higher than that for CO_2 methanation using pure hydrogen (430 °C). This shift indicates that the presence of ammonia modifies the overall thermodynamic profile of the system, resulting in a less exothermic net reaction, consistent with the enthalpy change calculated for the stoichiometric ammonia methanation system.

In addition to CO_2 conversion, the behaviour of ammonia conversion provides further insight. For pure ammonia decomposition, the conversion increases as temperature raises, as expected for an endothermic process. However, during ammonia methanation, a distinctly different trend emerges.

Across the temperature range, NH_3 conversion remains generally lower compared to the pure decomposition case. This is likely due to the additional energy demand associated with C–O

bond activation in the CO_2 hydrogenation step. Moreover, a notable rise in NH_3 conversion is observed between 430–460 °C, with a maximum located around 450 °C. At this optimum, NH_3 conversion reaches a level comparable to the pure decomposition case (~80%). It is suggested that this slight enhancement is attributed to a synergistic effect from the exothermic CO_2 methanation, which likely contributes local thermal energy that facilitates NH_3 decomposition. Thus, the interplay between the endothermic and exothermic components creates a self-sustaining thermochemical environment that favours higher conversions at this balanced temperature.

These catalytic findings underscore the importance of co-optimizing thermal conditions when coupling NH_3 with CO_2 over one single catalyst system. Unlike the isolated systems, the combined reaction introduces new kinetic and thermodynamic interdependencies, which must be carefully tuned for efficient operation.

5.2.3 Operando mechanism understanding

To reveal the reaction mechanism over this single catalyst system, *in situ* FTIR has been comprehensively performed and analysed.

As illustrated in **Fig. 5.12**, after purging CO_2/H_2 mixture gas over the catalyst, two sets of CO_2 characteristic peaks are observed. A huge broad peak located at 2350 cm^{-1} is accounted to the asymmetric stretching of the C-O bond of CO_2.[27,35,36] The two sets of peaks in the range of 3500-3750 cm^{-1} represents the formation of hydroxyl groups that are attached to the surface of CeO_2 support.[37] As temperature gradually increases, the intensity of CO_2 decreases indicating progressive CO_2 methanation taking place. This is accompanied by the formation of new peaks at 3015 cm^{-1}, 2005 cm^{-1} 1640 cm^{-1} and 1305 cm^{1}. Which are attributed to the formation of $*CH_4$, Ru-CO, *O-CHO and another stretching mode of C-H respectively.[38–40] Furthermore, there are low intensity peaks formed in the range of 1300-1700 cm^{-1} that corresponds to carbonate and bi-carbonate intermediates.[38,41] These findings provides

fundamental insights into the reaction mechanism that aligns with the literature, indicating that CO_2 methanation proceeds via a concerted route of formate formation and direct CO_2 dissociation.

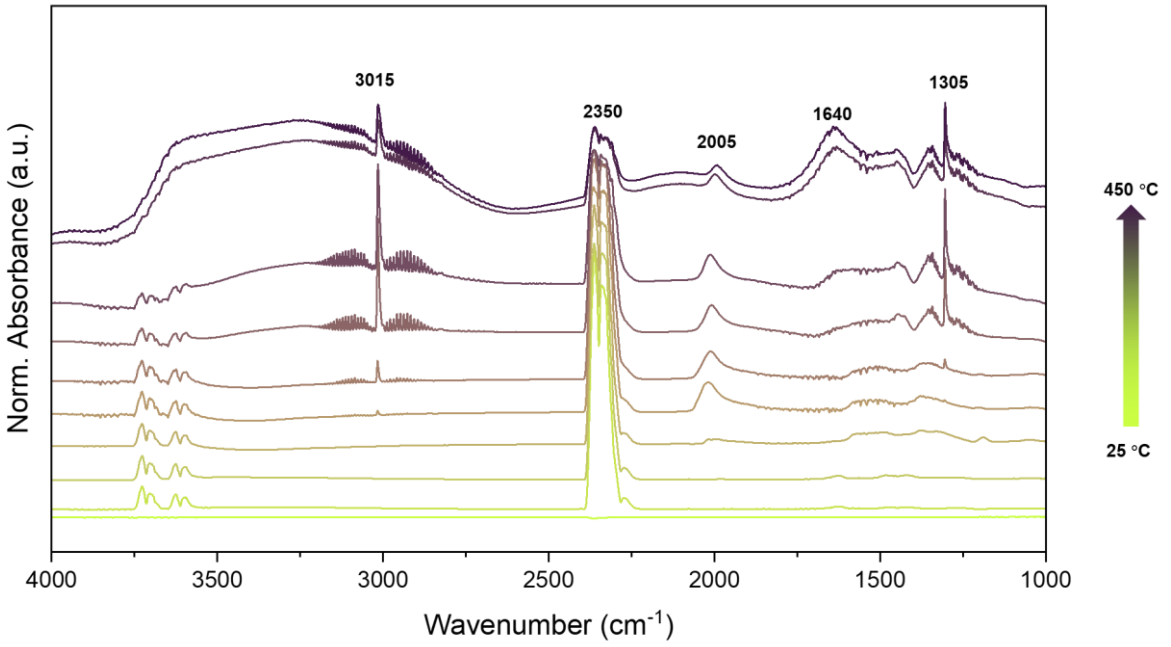


Fig. 5.12 Operando FTIR on 10 wt.% Ru/CeO_2 for CO_2 methanation.

Similar to the results from *Chapter 4*, two characteristic peaks for NH_3 are observed at 3335 and 1627 cm^{-1} owing to the N-H stretching and bending vibration modes, respectively (**Fig. 5.13**).[42–44] As the temperature increases, the intensity of these peaks gradually decrease, accompanied by the emergence of a distinct O-H stretching band at 3630 cm^{-1}, indicating progressive ammonia decomposition.

To gain deeper insight into the underlying reaction mechanism of ammonia methanation, a pulse experiment approach on FTIR was employed, which offers a viable alternative to probe the intrinsic mechanistic aspects of the reaction under transient conditions.

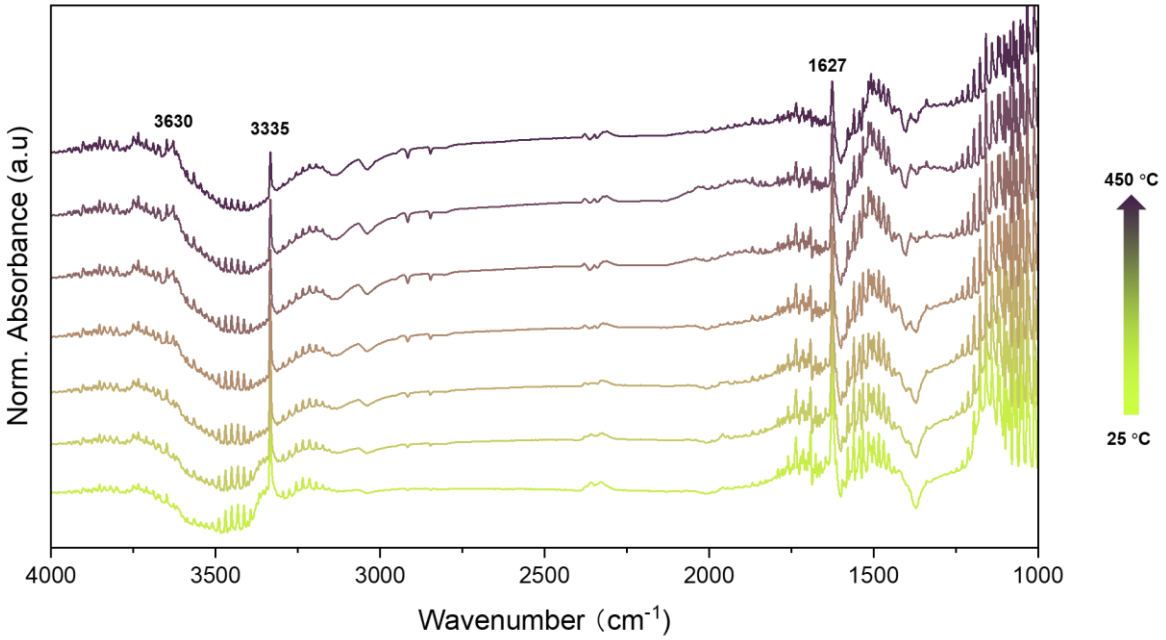


Fig. 5.13 Operando FTIR on 10 wt.% Ru/CeO_2 for ammonia decomposition.

Given that the optimal reaction temperature for ammonia methanation was previously identified as 450 °C, all pulse experiments were carried out at this temperature to ensure relevance to practical performance. Both CO_2 methanation and the combined ammonia methanation reaction were systematically investigated. This approach enables a direct comparison of surface intermediates, product evolution profiles, and the interplay between hydrogen generation and carbon species hydrogenation.

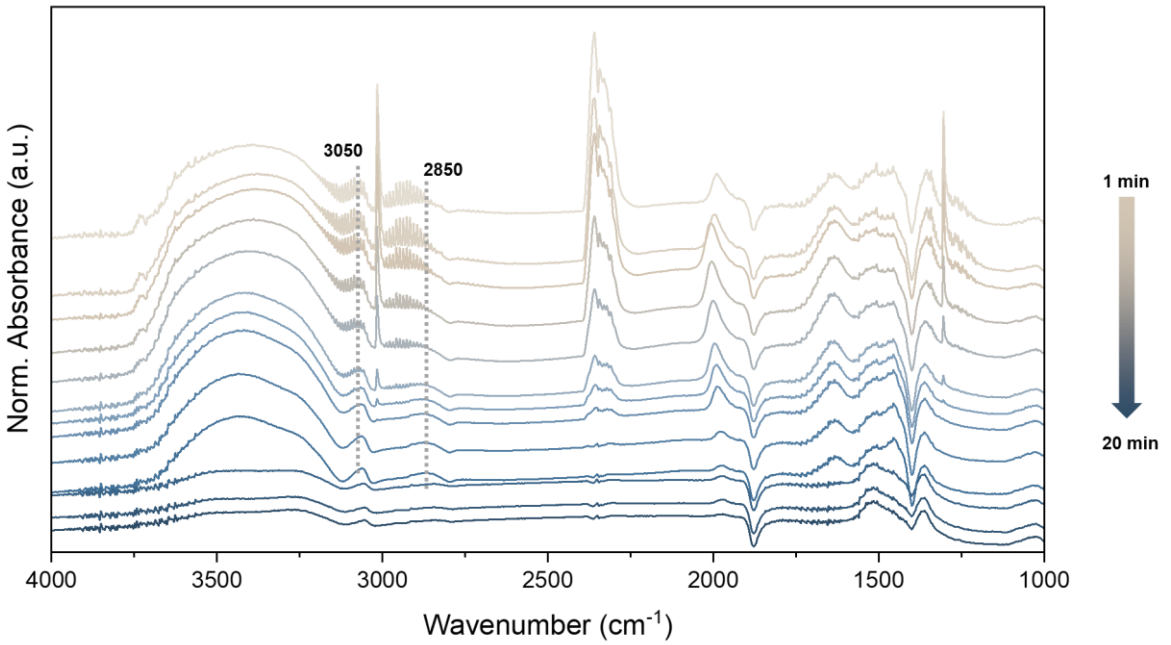


Fig. 5.14 Pulse FTIR on 10 wt.% Ru/CeO_2 for CO_2 methanation at 450 °C, each pulse contains 1 bar of mixture gas CO_2 : H_2 molar ratio = 1:4.

In addition to the characteristic peaks previously identified from the operando FTIR spectra, several distinct vibrational bands were observed in the pulse CO_2 methanation spectrum (**Fig 5.14**). Notably, a peak at ~3050 cm^{-1}, corresponding to C–H stretching vibrations, was detected following the disappearance of the intense $*CH_4$ band.[45] Moreover, a peak at ~2850 cm^{-1}, associated with surface formate species, was also observed.[46] Furthermore, a few transient peak in the range from 1350-1650 cm^{-1} is raised, these peaks are assigned to the formation of bi-carbonate and bidentate carbonate species on the support's surface (**Fig. 5.15** right).[47,48] These features were difficult to detect in the operando FTIR under continuous conditions but became more pronounced in the pulse experiment. These findings further reinforce the proposed reaction mechanism in which CO_2 activation occurs on the support and proceeds via formation of formate along the associative methanation pathway.

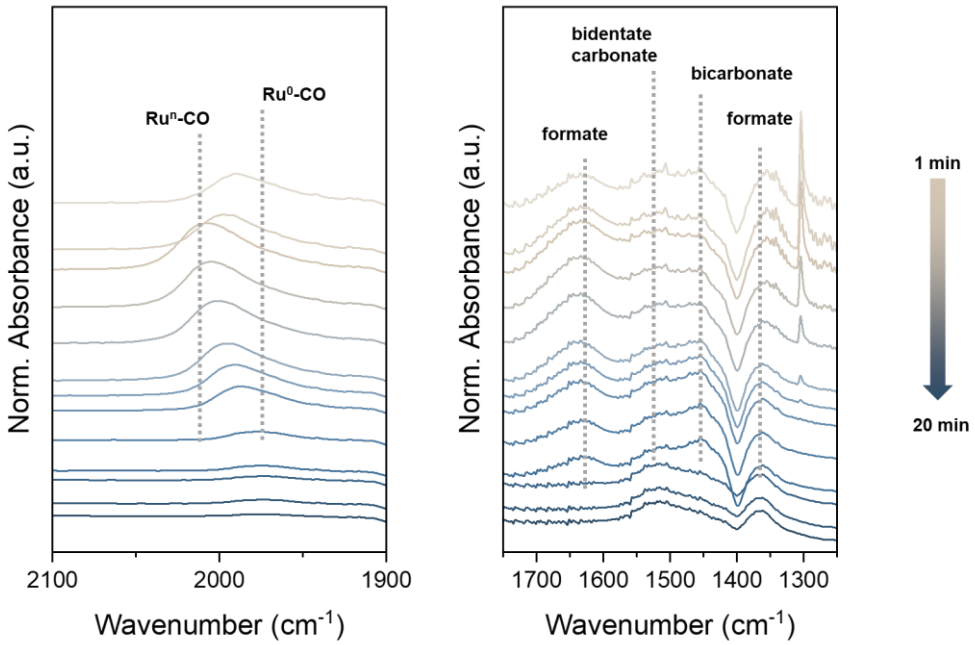


Fig. 5.15 Pulse FTIR on 10 wt.% Ru/CeO_2 for CO_2 methanation at 450 °C, focused on the dynamic of Ru-CO interaction (left) and the surface carbon species (right).

An intriguing observation arises from the dynamic behaviour of the Ru–CO interaction (**Fig 5.15**). A reversible shift in the IR peak positions was recorded during the course of the reaction. In particular, the linear carbonyl species associated with metallic Ru **(**Ru^0–CO) are typically observed around 2000 cm^{-1}, whereas oxidized Ru^{n+}–CO species exhibit dominant bands at higher wavenumbers, near 2050 cm^{-1}.[49–51] During the course of the pulse reaction, a transient blueshift of the carbonyl band to approximately 2015 cm^{-1} was first detected. This shift is attributed to a progressive reduction process of the CO_2 with the aid of Ru. Electrons are donated from the Ru metal site to the C-O bond to facilitate further hydrogenation and thereby oxidize the metal centre. The hydrogen-rich conditions generated *in situ*, in turn decreases and consumes the CO adsorbs on the surface and further proceeds the methanation. As the reaction progresses, a further reverse redshift of the Ru-CO band back to 1980 cm^{-1} is observed, indicating the partial re-oxidation or re-establishment of equilibrium surface coverage. These findings provide strong evidence that Ru is not a passive site but rather plays

an active electronic and catalytic role, with its oxidation state dynamically tuned by the local reaction environment.

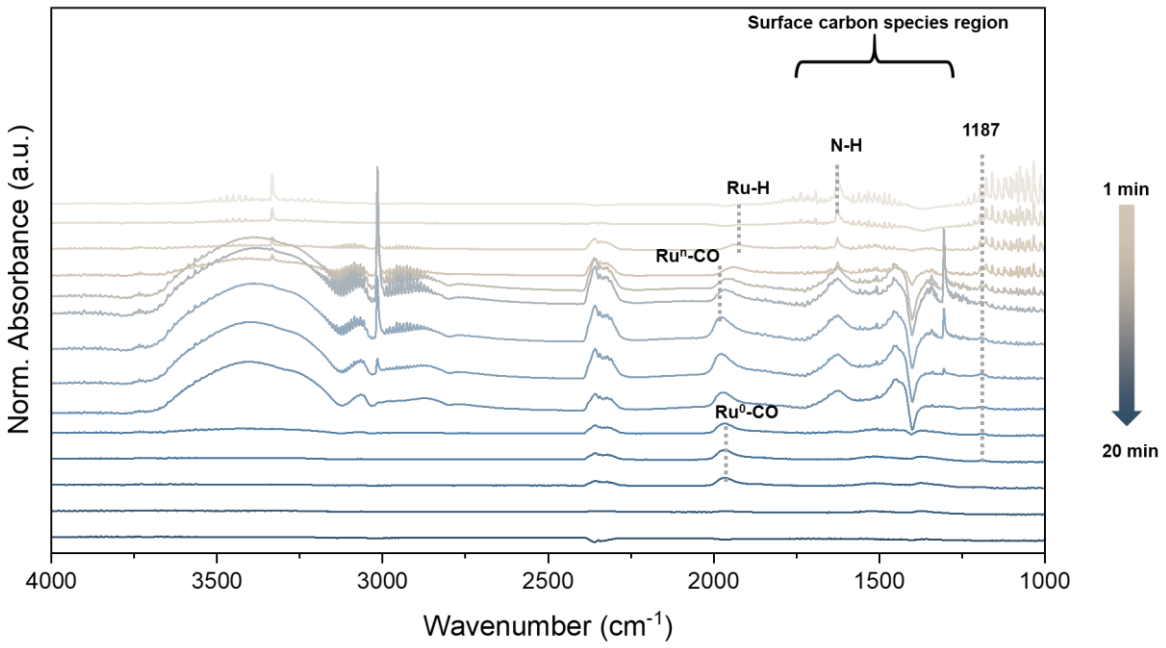


Fig. 5.16 Pulse FTIR on 10 wt.% Ru/CeO_2 for NH_3 methanation at 450 °C, each pulse contains 1 bar of mixture gas CO_2 : NH_3 molar ratio = 3:8.

The operando FTIR spectra for ammonia methanation (**Fig. 5.16**) reveal a profile largely comparable to that observed during pure CO_2 methanation, indicating mechanistic similarities. Apart from the dynamics of the carbonyl species observed and discussed above. Newly introduced N-H characteristic peaks located at 3335 and 1627 cm^{-1} are observed. However, a more pronounced shift in the Ru bonded species band is noted. Specifically, a low wavenumber peak initiated at 1930 cm^{-1} is accounted to the Ru-H species.[52] This peak progressively blueshifts similar to the trend observed for CO_2 methanation. Furthermore, a weak band at 1187 cm^{-1} represents the interaction between NH_3 and surface derived Lewis acid site.[53,54] Among all surface intermediates, CO proves the most persistent, exhibiting strong binding and slow desorption kinetics. This observation is consistent with prior findings

indicating that CO forms stable linear and bridged species on Ru, leading to catalytic site poisoning and long-term deactivation.[55–57]

Based on these findings, an integrated mechanistic framework for ammonia methanation is proposed (**Fig. 5.17**). It appears that the reaction follows two concerted mechanisms over this catalytic system. One direct dissociation mechanism on Ru metal sites, where CO_2 and NH_3 are all adsorbed to the active sites on the metal. NH_3 is decomposed to form H and N atoms, the two nitrogen atoms recombine and emits as N_2 gas. The adsorbed hydrogen facilitates CO_2 hydrogenation and forms Ru-CO as a key intermediate during this mechanism, as have been clearly evidenced from FTIR. The reaction further proceeds via subsequent CO hydrogenation and forms methane.

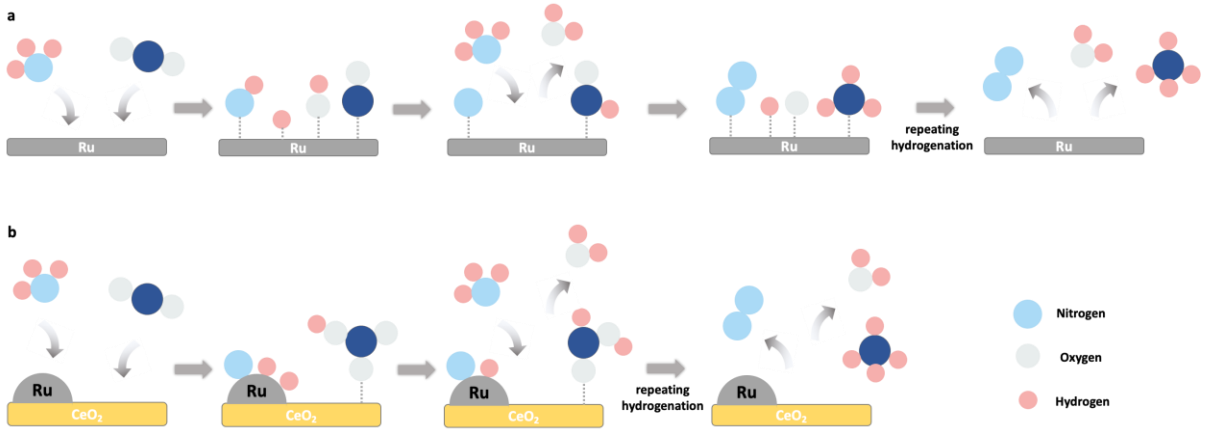


Fig 5.17 Schematic illustration of ammonia methanation over Ru/CeO_2 system. a. The dissociative CO pathway on Ru metal. b. The associative pathway circulates via formation of formate intermediates.

The other pathway proceeds through the formation of formate as key species. As shown in **Fig 5.17b**, ammonia is decomposed on the Ru site, generating surface hydrogen and nitrogen species. Meanwhile, CO_2 is predominantly activated on the cerium oxide support. This is supported by operando FTIR results, which revealed distinct bands associated with surface

formates. Furthermore, pulse spectrums also evidenced the reversible surface oxygen vacancy dynamics on CeO_2, indicating active participation of the support in CO_2 activation.

This bifunctional mechanism, especially the associative pathway significantly reduces the demand on Ru active sites, as NH_3 and CO_2 reactants interact with different catalytic domains. Consequently, less competition is faced between the two reactants over the Ru surface, alleviating the issue of site blocking and improving overall catalytic activity. This is particularly beneficial given that CO binds strongly to Ru and cause site poisoning. The proposed mechanism is consistent with previous studies highlighting the role of oxygen vacancies in CeO_2 for CO_2 activation to proceeds via formate intermediate formation and the role of Ru for typically dissociative ammonia decomposition.[28,58]

5.2.4 N doping evaluation

Building on the findings presented in *Chapter 4*, where nitrogen-doped cerium oxide exhibited enhanced catalytic activity for ammonia decomposition, we employed this optimized support for further catalytic evaluation in ammonia methanation. The presence of nitrogen dopants was previously shown to modulate the electronic structure and defect chemistry of the ceria lattice, leading to an increased concentration of surface oxygen vacancies. On one hand, this structural alteration promotes ammonia decomposition by inducing an associative mechanism taking place over the support surface. On the other hand, increasing oxygen vacancies facilitate more CO_2 adsorption and favours the formate mechanism. Given these advantages, the N-CeO_2 support would reduce the demand for Ru active sites during ammonia methanation and is expected to promote the activity of the combined reaction. In the following section, the performance of 10 wt.% Ru/N–CeO_2 under ammonia methanation conditions is examined in detail and benchmarked against its undoped counterpart.

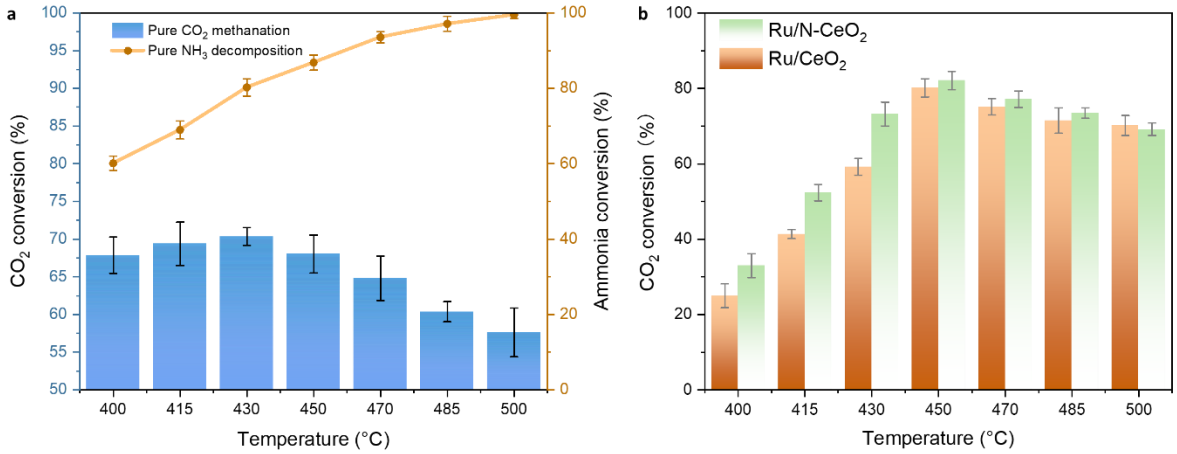


Fig. 5.18 Catalytic evaluation of the Ru/N-CeO_2 catalyst over a different temperature range. a. CO_2 to CH_4 conversion and ammonia decomposition conversion. Both catalytic reactions were performed at a fixed WHSV of 18,000 ml g_{cat}^{-1} h^{-1}. b. CO_2 conversion of the analogue catalysts. WHSV set at 18,000 ml g_{cat}^{-1} h^{-1}, the molar ratio of CO_2 : NH_3 during ammonia methanation is fixed at 3:8.

Surprisingly, despite the superior performance of the N doped CeO_2 supported catalyst in pure ammonia decomposition, the catalytic activities of both the doped and undoped systems are found to be comparable for CO_2 methanation and ammonia methanation under high-temperature conditions (**Fig. 5.18**). This is consistent with the fact that the reaction is thermodynamically controlled at elevated temperatures, where the influence of the support becomes less significant due to the dominant role of thermal energy in driving the forward reaction. However, at lower temperatures for ammonia methanation, the Ru/N–CeO_2 catalyst displays noticeably higher activity than its undoped counterpart. This enhancement could be attributed either to the electronic promoting effect from N dopants for ammonia decomposition or more specifically to the contribution of the associative NH_3 and CO_2 activation mechanism enabled by nitrogen doping.

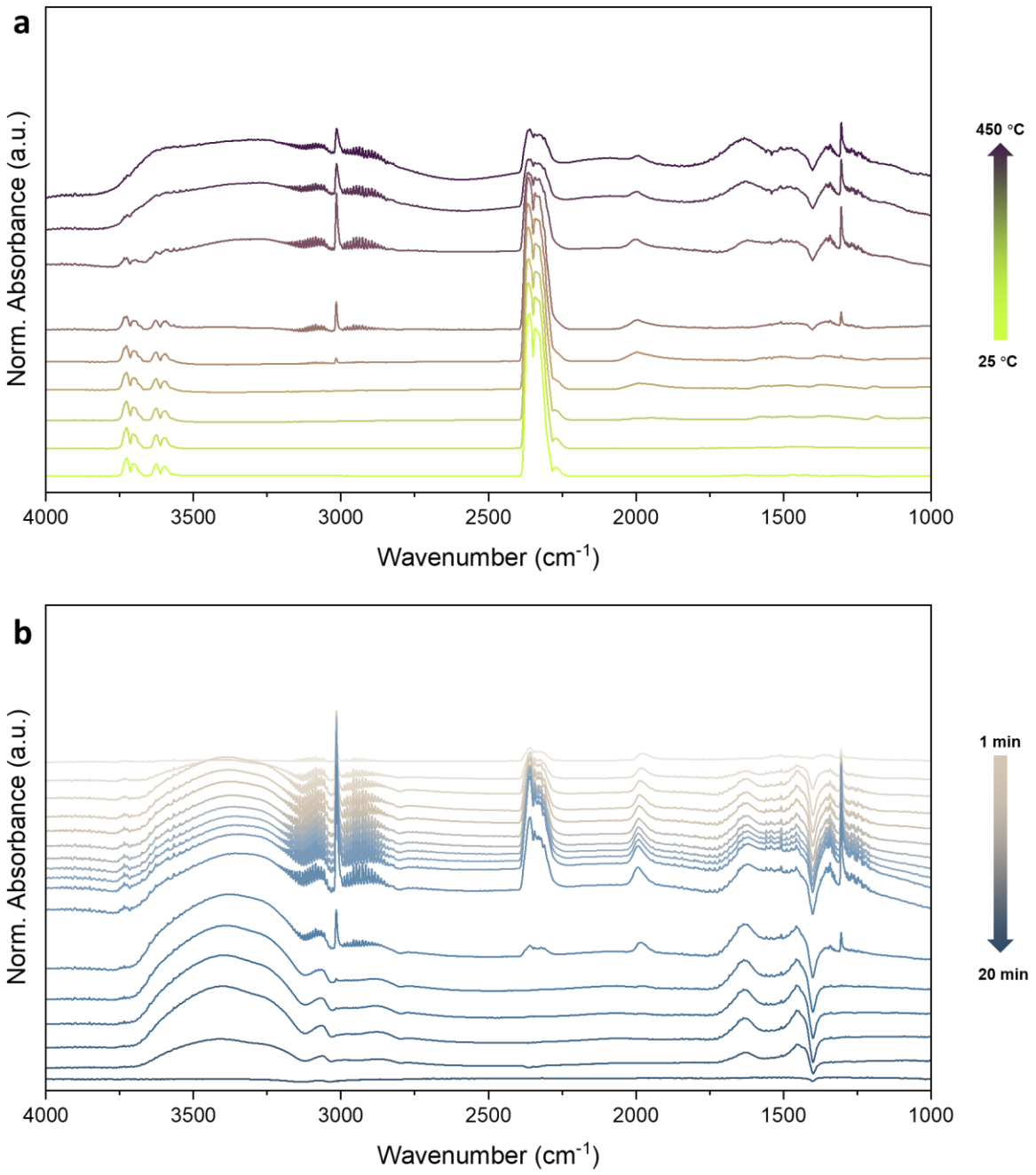


Fig. 5.19 Operando FTIR on Ru/N-CeO_2 for CO_2 methanation. a. Operando experiments. b. Pulse experiments carried out at 450 °C, each pulse contains 1 bar of mixture gas (CO_2 : H_2 molar ratio = 1:4).

To gain further understanding on this system. Operando and pulse FTIR were carried out and compared (**Fig. 5.19**). Both the N doped and undoped CeO_2 systems exhibited nearly identical spectral trends, suggesting that the associative ammonia decomposition pathway does not play a dominant role in the overall reaction mechanism under the investigated conditions. This

reduction may be interpreted as a relative decrease in the contribution of the dissociative CO_2 methanation pathway, and a corresponding increase in the involvement of the associative mechanism. Such a shift is consistent with the higher concentration of oxygen vacancies typically found in heteroatom doped ceria, which are known to facilitate the activation of CO_2 via the formation of surface formates.[59]

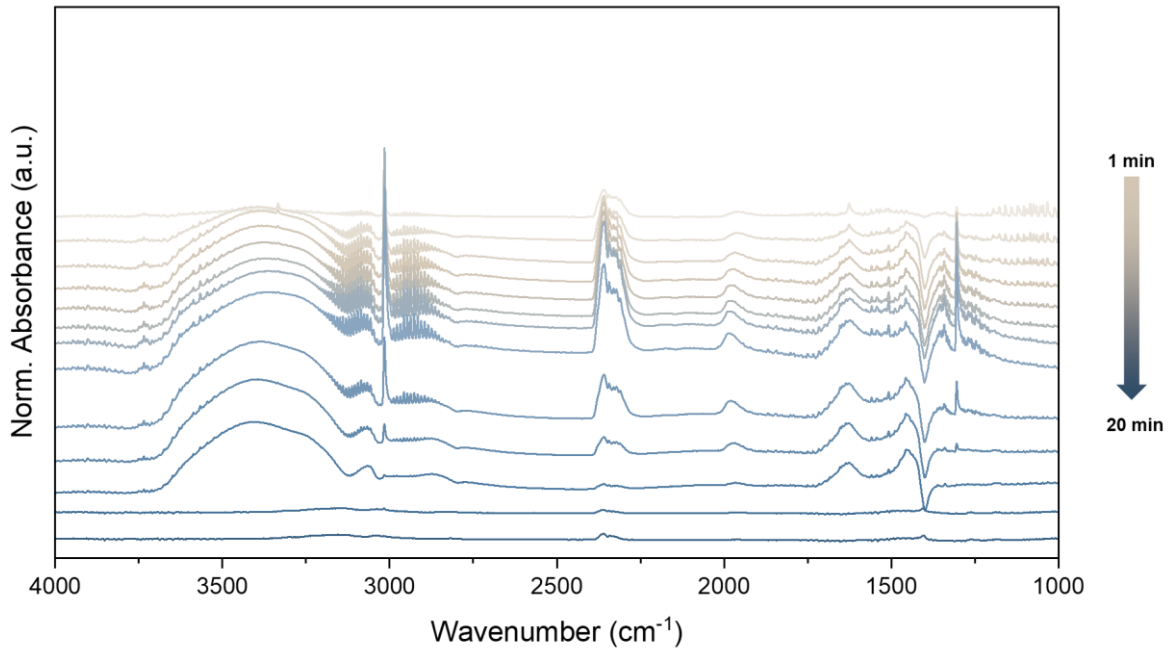


Fig. 5.20 Pulse FTIR on 10 wt.% Ru/N-CeO_2 for NH_3 methanation at 450 °C, each pulse contains 1 bar of mixture gas CO_2 : NH_3 molar ratio = 3:8.

As illustrated in **Fig. 5.20**, a trend nearly identical to that of the undoped counterpart is observed. This further confirms that both catalysts facilitate a dual-pathway mechanism for CO_2 methanation, involving both dissociative and associative routes. However, in the presence of N dopant, more oxygen vacancies are formed, leading to an enhanced contribution of the associative formate mediated mechanism, as being supported by the lower Ru-CO peak intensity.

Additionally, prior findings from *Chapter 4* have shown that NH_3 can also be activated at nitrogen sites via an associative decomposition mechanism. Thus, in the N doped system, the

activation of both reactants on the support would partially shift the reaction away from the Ru metal surface, thereby alleviating the demand on Ru active sites. This redistribution of reaction responsibilities enhances not only the activity but also the long-term stability of the catalyst by mitigating surface poisoning effects and improving resistance to site saturation under operating conditions.

5.2.5 Techno-economic evaluation

As demonstrated by the catalytic performance results discussed in the preceding sections, Ru-loaded CeO_2 exhibits strong potential as an effective catalyst for the ammonia methanation reaction. Notably, this catalyst achieves comparable CH_4 production rates when using either pure H_2 or NH_3 as the hydrogen source at 450 °C, highlighting the technical feasibility of employing ammonia as an alternative hydrogen source in CO_2 methanation. To further assess the process viability, the energy efficiency of both the hydrogen and ammonia pathways for green methane production was evaluated, combining experimentally derived conversion data with literature-based process energy standards.

For the process model developed, several key assumptions were applied: (1) all reactions proceed under quasi-static and continuous operation; (2) ammonia and hydrogen are stored at their respective boiling points under 1 bar (−34 °C for NH_3 and −253 °C for H_2)[60]; (3) storage duration is 30 days, with negligible aging or leakage losses; and (4) the Haber–Bosch process achieves a 90% molar conversion, while the CO_2 methanation reaction reaches 80% conversion under the tested conditions. The energy demand for the individual process units was taken from standard literature values.[61–63] As illustrated in Figure 5.21, hydrogen is produced via water electrolysis, requiring approximately 216 MJ $kg_{(hyd)}^{-1}$. In the direct hydrogen methanation route, subsequent stages include liquefaction, cryogenic storage, vaporization, and CO_2 methanation to yield CH_4. The overall power-to-gas efficiency for this route is estimated at 40.7%, assuming the higher heating value (HHV) of methane is 55 MJ kg^{-1}.[64]

In contrast, the ammonia-based route introduces additional energy requirements for the Haber–Bosch synthesis of NH_3 but significantly reduces the energy penalty associated with hydrogen liquefaction and cryogenic storage, since ammonia can be stored and handled under milder conditions. Based on the process model and catalyst performance, the overall round-trip energy efficiency of the ammonia pathway is calculated to be 42.9%, exceeding that of the direct hydrogen route. This suggests that, from an energy-conversion perspective, ammonia-mediated methanation presents a more favourable pathway for green methane production.

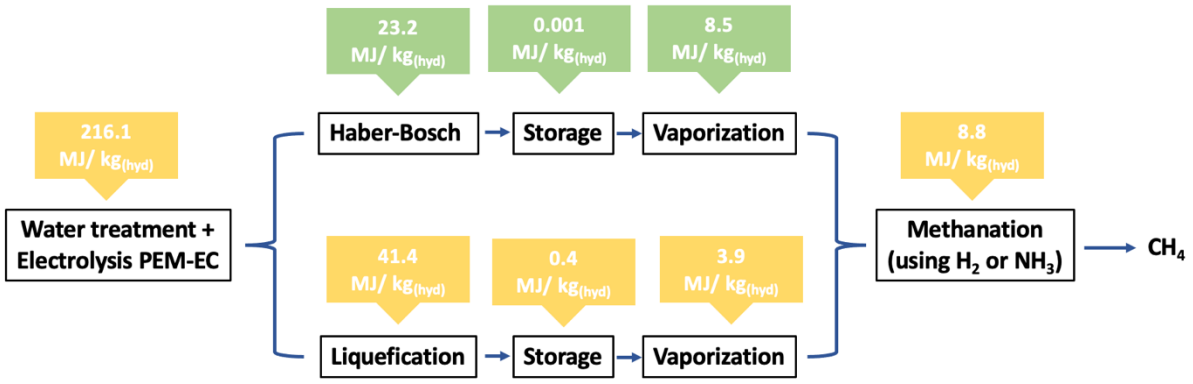


Fig. 5.21 Pathway of green hydrogen (yellow) and green ammonia (green) and their energy demand for CO_2 methanation process.

Despite the promising energetic performance, a comprehensive economic assessment remains essential. The Haber–Bosch process itself is energy-intensive and requires continuous nitrogen separation and compression, representing significant operational costs. Moreover, during ammonia methanation, undesirable by-products such as NO_x, urea, or other nitrogen-containing compounds may form. These species can be hazardous or environmentally persistent, necessitating downstream purification and emission control, thereby adding both capital and operational costs to the process chain. Nonetheless, given that ammonia benefits from a well-established global storage and transport network, the balance between additional synthesis costs and logistic advantages will be strongly location dependent.[65] Consequently, the overall economic feasibility is not straightforward and

depends on multiple context-specific factors, including electricity price, feedstock availability, transportation infrastructure, and scale of operation. Future work integrating life-cycle assessment (LCA) and techno-economic modelling (TEA) would therefore be required to provide a more conclusive evaluation of the overall sustainability and competitiveness of the ammonia methanation route.

5.3 Conclusion

In this chapter, methane was successfully synthesized through the integrated catalytic conversion of using carbon dioxide and ammonia as the reactants. A comprehensive screening of reaction conditions and catalyst systems was performed to gain a broader picture regarding this thermo-catalytic process. Among all systems studied, the Ru/CeO_2 catalyst demonstrated the highest performance. Mechanistic investigations using operando and pulsed FTIR spectroscopy provided critical insights into the reaction pathway. The redox-active CeO_2 support plays a crucial role by facilitating the formation of surface oxygen vacancies, which serve as active sites for CO_2 activation. This promotes a formate mediated hydrogenation pathway, effectively lowering the reliance on Ru metal sites for both NH_3 and CO_2 activation and enhancing overall catalyst efficiency. Results from *Chapter 4* indicated an increase in associative mechanism for ammonia decomposition on CeO_2 by N doping. This modified support was implemented in the integrated ammonia methanation reaction and exhibited higher activity. However, the fundamental reaction mechanism remained largely consistent with the undoped system. A minor shift toward greater formate pathway contribution was observed, as indicated by reduced Ru–CO spectral features, suggesting enhanced surface oxygen activation due to N doping.

Energy evaluation simulation states that the energy efficiency of ammonia methanation, if only considered from power-to-gas, is higher than just using hydrogen. Suggesting the strong techno-energy feasibility for this reaction. Yet, there are external cost associated with the process and its economic feasibility cannot be easily concluded without considering the cost, operation mode, location and feedstock availability.

Despite the breadth of investigation conducted in this chapter, further research opportunities remain. In particular, exploring bimetallic catalytic systems, especially those that promote CO hydrogenation. This could offer additional performance gains and mechanistic advantages. Another future work could focus more on the N doped systems. As the Ru loading

implemented in this project is ~10 wt.%, so the effect of N doping is minimal. Thus, the same set of experiment can be carried out over lower loading Ru/N-CeO_2 systems.

Overall, the findings from this work offer a promising framework for designing future integrated catalytic systems, especially those leveraging ammonia as a sustainable hydrogen carrier for *in situ* hydrogen generation.

Reference

1. Ye, D. & Tsang, S. C. E. Prospects and challenges of green ammonia synthesis. *Nat. Synth.* **2**, 612–623 (2023).
2. Bell, T. E. & Torrente-Murciano, L. H_2 Production via Ammonia Decomposition Using Non-Noble Metal Catalysts: A Review. *Top. Catal.* **59**, 1438–1457 (2016).
3. Restelli, F. *et al.* Detailed techno-economic assessment of ammonia as green H_2 carrier. *Int. J. Hydrogen Energy* **52**, 532–547 (2024).
4. Aziz, M., TriWijayanta, A. & Nandiyanto, A. B. D. Ammonia as Effective Hydrogen Storage: A Review on Production, Storage and Utilization. *Energies* **13**, 3062 (2020).
5. Energy Agency, I. Ammonia Technology Roadmap Towards more sustainable nitrogen fertiliser production.(2021) URL:https://www.iea.org/reports/ammonia-technology-roadmap
6. Energy Agency, I. Global Hydrogen Review 2024. (2024). URL: https://www.iea.org/reports/global-hydrogen-review-2024
7. Zhang, J. *et al.* Tuning Polarity of Cu-O Bond in Heterogeneous Cu Catalyst to Promote Additive-free Hydroboration of Alkynes. *Chem* **6**, 725–737 (2020).
8. Shiraishi, Y., Sugano, Y., Inoue, D. & Hirai, T. Effect of substrate polarity on photocatalytic activity of titanium dioxide particles embedded in mesoporous silica. *J. Catal.* **264**, 175–182 (2009).
9. Wu, S., Salmon, N., Li, M. M. J., Bañares-Alcántara, R. & Tsang, S. C. E. Energy Decarbonization via Green H_2 or NH_3? *ACS Energy Lett.* **7**, 1021–1033 (2022).
10. Scholes, D. T. *et al.* The Effects of Crystallinity on Charge Transport and the Structure of Sequentially Processed F_4TCNQ-Doped Conjugated Polymer Films. *Adv. Funct. Mater.* **27**, 1702654 (2017).
11. Huang, L. *et al.* Porous Semiconducting Polymers Enable High-Performance Electrochemical Transistors. *Adv. Mater.* **33**, 2007041 (2021).
12. Alexander, R., Kralert, P. G. & Kagi, R. I. Kinetics and mechanism of the thermal decomposition of esters in sediments. *Org. Geochem.* **19**, 133–140 (1992).
13. Global Emissions - Center for Climate and Energy SolutionsCenter for Climate and Energy Solutions. URL:https://www.c2es.org/content/international-emissions/.
14. Zhong, J. *et al.* State of the art and perspectives in heterogeneous catalysis of CO_2 hydrogenation to methanol. *Chem. Soc. Rev.* **49**, 1385–1413 (2020).
15. Bao, J., Yang, G., Yoneyama, Y. & Tsubaki, N. Significant Advances in C1 Catalysis: Highly Efficient Catalysts and Catalytic Reactions. *ACS Catal.* **9**, 3026–3053 (2019).
16. He, X., Wang, X. & Xu, H. Advancements in Cobalt-Based Catalysts for Enhanced CO_2 Hydrogenation: Mechanisms, Applications, and Future Directions: A Short Review. *Catal.* **14**, 560 (2024).
17. Sharma, P., Sebastian, J., Ghosh, S., Creaser, D. & Olsson, L. Recent advances in hydrogenation of CO_2 into hydrocarbons via methanol intermediate over heterogeneous catalysts. *Catal. Sci. Technol.* **11**, 1665–1697 (2021).
18. Jiang, X., Nie, X., Guo, X., Song, C. & Chen, J. G. Recent Advances in Carbon Dioxide Hydrogenation to Methanol via Heterogeneous Catalysis. *Chem. Rev.* **120**, 7984–8034 (2020).
19. Visconti, C. G., Martinelli, M., Falbo, L., Fratalocchi, L. & Lietti, L. CO_2 hydrogenation to hydrocarbons over Co and Fe-based Fischer-Tropsch catalysts. *Catal. Today* **277**, 161–170 (2016).
20. Jiang, Y. *et al.* Recent advances in thermocatalytic hydrogenation of carbon dioxide to light olefins and liquid fuels via modified Fischer-Tropsch pathway. *J. CO_2 Util.* **67**, 102321 (2023).

21. Chen, L., Filot, I. A. W. & Hensen, E. J. M. Computational Study of CO_2 Methanation on Ru/CeO_2 Model Surfaces : On the Impact of Ru Doping in CeO_2. *ACS Catal.* **13**, 15230-15247 (2023)

22. Hatta, A. H. *et al.* A review on recent bimetallic catalyst development for synthetic natural gas production via CO methanation. *Int. J. Hydrogen Energy* **47**, 30981–31002 (2022).

23. Mebrahtu, C. *et al.* CO_2 Methanation: Principles and Challenges. *Stud. Surf. Sci. Catal.* **178**, 85–103 (2019).

24. Kattel, S., Liu, P. & Chen, J. G. Tuning Selectivity of CO_2 Hydrogenation Reactions at the Metal/Oxide Interface. *J. Am. Chem. Soc.* **139**, 9739–9754 (2017).

25. Memon, M. A. *et al.* Heterogeneous Catalysts for Carbon Dioxide Methanation: A View on Catalytic Performance. *Catal.* **13**, 1514 (2023).

26. Miao, B., Ma, S. S. K., Wang, X., Su, H. & Chan, S. H. Catalysis mechanisms of CO_2 and CO methanation. *Catal. Sci. Technol.* **6**, 4048–4058 (2016).

27. Sharma, S., Hu, Z., Zhang, P., McFarland, E. W. & Metiu, H. CO_2 methanation on Ru-doped ceria. *J. Catal.* **278**, 297–309 (2011).

28. Wang, F. *et al.* Active Site Dependent Reaction Mechanism over Ru/CeO_2 Catalyst toward CO_2 Methanation. *J. Am. Chem. Soc.* **138**, 6298–6305 (2016).

29. Shen, C. *et al.* CO_2 Hydrogenation to Methanol on Indium Oxide-Supported Rhenium Catalysts: The Effects of Size. *ACS Catal.* **12**, 12658–12669 (2022).

30. Dang, S. *et al.* Rationally designed indium oxide catalysts for CO_2 hydrogenation to methanol with high activity and selectivity. *Sci. Adv.* **6**, 2060–2077 (2020).

31. Xie, Y. *et al.* Overturning CO_2 Hydrogenation Selectivity by Tailoring the Local Electron Density of Ru/CeO_2 Catalysts. *ACS Catal.* **14**, 12214–12224 (2024).

32. Yang, H. *et al.* Tuning the selectivity of CO_2 hydrogenation to alcohols by crystal structure engineering. *Chem* **10**, 2245–2265 (2024).

33. Wang, L., Xiao, F. Tuning product selectivity in CO_2 hydrogenation over metal-based catalysts. *Chem. Sci.*, **12**, 14660 (2021)

34. Gao, J. *et al.* A thermodynamic analysis of methanation reactions of carbon oxides for the production of synthetic natural gas. *RSC Adv.* **2**, 2358–2368 (2012).

35. Wang, C. *et al.* Low-temperature CO_2 methanation over Ru/CeO_2: Investigation into Ru loadings. *Fuel* **345**, 128238 (2023).

36. Garbarino, G., Bellotti, D., Finocchio, E., Magistri, L. & Busca, G. Methanation of carbon dioxide on Ru/Al_2O_3: Catalytic activity and infrared study. *Catal. Today* **277**, 21–28 (2016).

37. López-Rodríguez, S. *et al.* Elucidating the Role of the Metal Catalyst and Oxide Support in the Ru/CeO_2-Catalyzed CO_2 Methanation Mechanism. *J. Phys. Chem. C* **125**, 25533–25544 (2021).

38. Cárdenas-Arenas, A. *et al.* Isotopic and in situ DRIFTS study of the CO_2 methanation mechanism using Ni/CeO_2 and Ni/Al_2O_3 catalysts. *Appl. Catal. B Environ.* **265**, 118538 (2020).

39. Jin, B., Li, S. & Liang, X. Enhanced activity and stability of MgO-promoted Ni/Al_2O_3 catalyst for dry reforming of methane: Role of MgO. *Fuel* **284**, 119082 (2021).

40. A. Álvarez, M., Bobadilla, L. F., Garcilaso, V., Centeno, M. A. & Odriozola, J. A. CO_2 reforming of methane over Ni-Ru supported catalysts: On the nature of active sites by operando DRIFTS study. *J. CO_2 Util.* **24**, 509–515 (2018).

41. Aksoylu, A. E., Akin, A. N., Önsan, Z. I. & Trimm, D. L. Structure/activity relationships in coprecipitated nickel-alumina catalysts using CO_2 adsorption and methanation. *Appl. Catal. A Gen.* **145**, 185–193 (1996).

42. Kim, J. S., Nam, H., Kim, H. J., Lee, J. H. & Park, B. H. Real-Time Measurement of Ammonia in Artillery Smoke Using a Passive IR Remote Sensor. *ACS Omega* **4**, 16768–16773 (2019).

43. Duan, C. peng, Guo, R. tang, Wu, G. lin & Pan, W. guo. Selective catalytic reduction of NO_x by NH_3 over $CeVO_4$-CeO_2 nanocomposite. *Environ. Sci. Pollut. Res.* **27**, 22818–22828 (2020).

44. Qi, G. & Yang, R. T. Characterization and FTIR studies of MnO_x-CeO_2 catalyst for low-temperature selective catalytic reduction of NO with NH_3. *J. Phys. Chem. B* **108**, 15738–15747 (2004).

45. Scarano, D., Bertarione, S., Spoto, G., Zecchina, A. & Otero Areán, C. FTIR spectroscopy of hydrogen, carbon monoxide, and methane adsorbed and co-adsorbed on zinc oxide. *Thin Solid Films* **400**, 50–55 (2001).

46. Chuang, C. C., Wu, W. C., Huang, M. C., Huang, I. C. & Lin, J. L. FTIR Study of Adsorption and Reactions of Methyl Formate on Powdered TiO_2. *J. Catal.* **185**, 423–434 (1999).

47. Yan, X. *et al.* Cooperatively tailored surface frustrated Lewis pairs and N-doping on CeO_2 for photocatalytic CO_2 reduction to high-value hydrocarbon products. *Appl. Catal. B Environ.* **343**, 123484 (2024).

48. Liu, H., Zhang, R., Liu, S. & Liu, G. CeO_2/Ni Inverse Catalyst as a Highly Active and Stable Ru-free Catalyst for Ammonia Decomposition. *ACS Catal.* **14**, 9927–9939 (2024).

49. Elmasides, C., Kondarides, D. I., Grünert, W. & Verykios, X. E. XPS and FTIR study of Ru/Al_2O_3 and Ru/TiO_2 catalysts: Reduction characteristics and interaction with a methane-oxygen mixture. *J. Phys. Chem. B* **103**, 5227–5239 (1999).

50. Panagiotopoulou, P. & Verykios, X. E. Mechanistic Study of the Selective Methanation of CO over Ru/TiO_2 Catalysts: Effect of Metal Crystallite Size on the Nature of Active Surface Species and Reaction Pathways. *J. Phys. Chem. C* **121**, 5058–5068 (2017).

51. Brown, M. F. & Gonzalez, R. D. An infrared study of the adsorption of carbon monoxide on the reduced and oxidized forms of silica supported ruthenium. *J. Phys. Chem.* **80**, 1731–1735 (1976).

52. Fang, H. *et al.* Dispersed surface Ru ensembles on MgO(111) for catalytic ammonia decomposition. *Nat. Commun.***14**, 647 (2023).

53. Zhang, P., Guo, R. tang, Wu, L. jun & Pan, W. guo. The enhancement of NH_3-SCR performance for CeO_2 catalyst by CO pretreatment. *Environ. Sci. Pollut. Res.* **27**, 13617–13636 (2020).

54. Kubota, H. *et al.* Operando Spectroscopic Study of Reduction and Oxidation Half-Cycles in NH_3-SCR over CeO_2-Supported WO_3. *ACS Catal.* **13**, 9274–9288 (2023).

55. Lee, M. J. *et al.* Understanding the Bifunctional Effect for Removal of CO Poisoning: Blend of a Platinum Nanocatalyst and Hydrous Ruthenium Oxide as a Model System. *ACS Catal.* **6**, 2398–2407 (2016).

56. Sato, K. *et al.* Operando Spectroscopic Study of the Dynamics of Ru Catalyst during Preferential Oxidation of CO and the Prevention of Ammonia Poisoning by Pt. *JACS Au* **2**, 1627–1637 (2022).

57. Xu, S. *et al.* CO Poisoning of Ru Catalysts in CO_2 Hydrogenation under Thermal and Plasma Conditions: A Combined Kinetic and Diffuse Reflectance Infrared Fourier Transform Spectroscopy-Mass Spectrometry Study. *ACS Catal.* **10**, 12828–12840 (2020).

58. García-García, F. R., Guerrero-Ruiz, A. & Rodríguez-Ramos, I. Role of B5-type sites in Ru catalysts used for the NH_3 decomposition reaction. *Top. Catal.* **52**, 758–764 (2009).

59. Hussain, I. *et al.* A review of the indispensable role of oxygen vacancies for enhanced CO_2 methanation activity over CeO_2-based catalysts: Uncovering, influencing, and tuning strategies. *Int. J. Hydrogen Energy* **48**, 24663–24696 (2023)..

60. Kojima, Y. Safety of ammonia as a hydrogen energy carrier. *Int. J. Hydrogen Energy* **50**, 732–739 (2024).

61. Müller, M., Pfeifer, M., Holtz, D. & Müller, K. Comparison of green ammonia and green hydrogen pathways in terms of energy efficiency. *Fuel* **357**, 129843 (2024).

62. Kojima, Y. Round-trip efficiencies of green ammonia and green hydrogen. *Next Energy* **8**, 100340 (2025).

63. Wang, L. *et al.* Greening Ammonia toward the Solar Ammonia Refinery. *Joule* **2**, 1055–1074 (2018).

64. Friend, D. G., Ely, J. F. & Ingham, H. Thermophysical Properties of Methane. *J. Phys. Chem. Ref. Data* **18**, 583–638 (1989).

65. Smith, C. & Torrente-Murciano, L. Cost efficiency versus energy utilization in green ammonia production from intermittent renewable energy. *Nat. Chem. Eng.* **2**, 261–272 (2025).

Chapter 6 Conclusion

6.1 Summary of work

This thesis examines various catalyst systems for thermal ammonia decomposition, with a particular emphasis on the associative decomposition mechanism. As have been comprehensively discussed throughout the thesis, traditional dissociative mechanism is constrained by the BEP (Brønsted–Evans–Polanyi) correlation. It demonstrates a positive correlation between the M-N adsorption energy and the N-H dissociation energy, indicating that stronger M-NH_3 interaction would result in faster N-H breaking but limit the final M-N_2 desorption. According to this correlation, the rate-determining step is often either N–H bond cleavage or N_2 desorption. In contrast, the associative decomposition mechanism involves simultaneous N–H dehydrogenation and N–N bond formation in a single elementary step. Thermodynamically, this approach merges the two steps and results in a lower overall energy barrier, thereby reducing the activation energy and enabling improved activity at lower temperatures. This mechanism requires the interaction between NH_3 derived nitrogen species and nitrogen from the catalyst support and is thus discussed in relation to nitrogen doping effects.

In *Chapter 3*, different N configuration within N doped carbon support was investigated. Catalytic results indicated that pyrrolic and pyridinic N sites (sp^2 hybridized N) significantly enhance thermal ammonia decomposition. Using various techniques including XAS, operando FTIR, H_2-TPR etc, it is further concluded that pyrrolic and pyridinic N dopants favours the formation of Ru^{n+}-N_4 coordination structure due to higher availability of the lone pairs at edge site. Based on these observations, we propose a non-dissociative ammonia decomposition facilitated by the two spatial interactable Ru^{n+}-N_4 coordination site on our amorphous support. This mechanism closely resembles the associative pathway and bypasses the BEP limitations, resulting in enhanced catalytic performance. Building on the insights from *Chapter 3*, it is realised that redox active N dopants is necessary for associative

ammonia decomposition. Thus, in *Chapter 4*, a N doped cerium oxide support where the N dopants mimic the redox behaviour in CeN_x is synthesized. Catalytically, this catalyst illustrates outstanding performance, comparable to the state-of-the-art catalyst Ru/MgO(111). Comprehensive structural analysis revealed improved Ru nanoparticle dispersion and stronger metal-support interactions due to the N dopants. Moreover, isotopic labelling experiment confirmed fast interaction between lattice derived N and NH_3 derived N exists, which directly supports the idea of associative mechanism. Further pulsed FTIR experiments and isotopic pulsed FTIR experiments provided a broader picture of this overall associative ammonia decomposition reaction. Complementary MACE and DFT calculations validated the experimental findings, indicating that N dopants can act as independent active sites with comparable thermodynamic barriers to Ru metal sites but proceeding via distinct mechanisms and kinetics.

After intensively studied structural-activity-mechanism relationship of the two systems in ammonia decomposition, *Chapter 5* shifted to a broader application. Instead of focusing on ammonia decomposition for hydrogen generation, we investigated CO_2 methanation reactions that could replace H_2 by NH_3 as the only hydrogen source. It is observed that both reactants compete over the same Ru metal site, limiting catalytic activity. This subsequent leads to the formation of CO, which binds strongly with Ru and result in blockage of further available active sites and catalyst deactivation. However, the use of CeO_2 support significantly mitigates this issue by introducing a formate-mediated reaction route, activated by oxygen vacancies on the redox-active support. Further implementation of N–CeO_2 from *Chapter 4* strengthened this concept. As not only was CO_2 activated on the support, but NH_3 activation also partially shifted away from Ru sites. This reduced the demand on precious metal active sites and enhanced overall catalytic performance.

These three interconnected chapters present a cohesive investigation into thermal ammonia decomposition, with a particular focus on the associative reaction mechanism. Together, they provide valuable fundamental insights into catalyst design, structure–activity relationships, and reaction engineering for efficient hydrogen generation and utilization from ammonia.

6.2 Future perspective

Ammonia decomposition has been intensively studied over the past few years for on-site hydrogen generation. This process still faces challenge on the operation condition as the reaction is endothermic and energy consuming. In this thesis, we focused on structure modification at catalyst supports to induce an associative ammonia decomposition route. This pathway allows lower overall activation energy and novel fundamental mechanistic aspects.

For future study branched from this thesis, research should focus on the following:

- Further optimize N doped redox active metal oxide support materials that can stabilize nitrogen coordination environments while providing high redox activity. More specifically, maximizing the N dopants concentration, surface area of the overall support, size and morphology of the crystallites. One ongoing research direction includes screening the reactivity of N-doped materials across the lanthanide series to identify optimal support candidates.
- Another more fundamental direction should focus on the synthesis of different spatial configurations of N dopants on N-CeO_2. As validated by the computational analysis in *Chapter 4*, proximal N site serves as the most effective active sites for associative ammonia decomposition, due to the striking balance between Ru-N interaction and N-H activation. However, this has not been experimentally validated yet. Future work should investigate the structure–activity relationships of spatially separated Ru–N sites, which will require carefully controlled synthesis to ensure consistent Ru cluster sizes, N dopant concentrations, and support morphologies for reliable comparisons.
- From a broader application perspective, given its hydrogen-rich nature, ammonia can in principle be coupled with a wide range of hydrogenation reactions. Especially with the aid of processing the cracking process associatively, which generates different reaction intermediates and may have certain effects on the final product selectivity. A promising future direction involves investigating coupling strategies where ammonia

serves as a hydrogen carrier for downstream hydrogenation (e.g., CO_2 methanation), as demonstrated in Chapter 5. This should be followed by comprehensive fundamental analysis, exploring the role of associative ammonia mechanism to the downstream reaction product selectivity.

Overall, the concept of support-driven associative ammonia decomposition not only advances the understanding of ammonia decomposition but also opens up new opportunities in catalyst design for sustainable hydrogen technologies. This approach holds the potential to make ammonia a more versatile and efficient vector for clean energy applications.